Study of photoactive materials and structures based on compounds of the In-S system and in Silicon Rich Oxides

By

Enrique Quiroga González

Thesis advisors:

Prof. Dr. Wolfgang Bensch
Dr. Mariano Aceves Mijares

Thesis submitted in fulfillment of the requirements for the degree of:

Doctor rerum naturalium

in

Institute for Inorganic Chemistry,
Christian-Albrechts-University of Kiel

Kiel, Germany, May 2010

Declaration

I declare that the work presented here was performed by me under the supervision of my advisors, who checked it in form and content. We followed the rules of the DFG for good scientific praxis. For the research I have used only the devices, software and materials mentioned in the thesis. This thesis has been only submitted to the University of Kiel.

Enrique Quiroga González Kiel, May 2010

Examiner: **Prof. Dr. Wolfgang Bensch**

Co-examiner: **Prof. Dr. Norbert Stock**

Date of the examination: **June 25th, 2010**

Approved for printing on: **June 25th, 2010**

The Dean

“¿Será que soy fotoactivo?

Los fotones de los luceros de tus ojos

son absorbidos en la capa activa de mi corazón;

así luego se electriza mi mente

encendiendo la máquina de mi amor.”

Enrique Q. G.

To God,

the one who exists from the very beginning

and gives order to the universe through the chaos.

To him,

who shines in my life through the hugs of my beloved

and always surprises me even with the smallest things.

Aknowledgements

To my wife Alina, my partner in the good and in the better times, the girl who wanted to take with me this boat for two sailing till the end of time.

To my parents Olivia and Enrique, my sister Diana and my brother Angel, for all their unconditional support and love. Also to my whole family, including my family in law, for being always there for me.

To my doctoral assessors Prof. Dr. Wolfgang Bensch and Dr. Mariano Aceves Mijares, for all their time, advices and friendship.

To all my scientific collaborators during my doctoral project, especially Prof. Dr. Lorenz Kienle and his collaborators, Dr. Zhenrui Yu and Dr. Christian Näther who worked together with me in various articles. Also the productive collaborations with Prof. Dr. J. Janek, Dr. D. K. Lee, Prof. Dr. M. Martin, Dr. R. A. De Souza, Prof. Dr. F. Faupel, Dr. V. Zaporojtchenko, Dr. J. P. Savy, Dr. M. Haeckel, Prof. Dr. A. Lechner, Dr. K. Monfil-Leyva and Dr. R. López-Estopier are gratefully acknowledged.

To all my friends, the ones from my childhood, the ones from my studies, the ones from my everyday, and the ones sharing with me the office now, for bringing light in cloudy days. You all know that “mi casa es su casa.”

To the Discalced Carmelites from Tulpetlac and father Francisco Vargas for all their prayers.

To CONACyT and DAAD for their economic support through a scholarship. Also to Stefanie Büchl from DAAD for all her time and help with multiple proceedings.

To the Christian-Albrechts-University of Kiel, where I had the opportunity to materialize scientific thoughts.

To the National Institute for Astrophysics, Optics and Electronics (Mexico), especially to the people of the microelectronics lab, for the support provided in different projects.

Abstract

In the present doctoral thesis the results of the study of photoactive materials and structures in different length scales will be presented. The thesis consists of two parts and base on 4 published manuscripts, 4 submitted papers and 1 paper being in preparation:

1. The preparation of new materials based on thioindates and indium sulfides with possible photoactive properties. The synthesized materials were tested in the areas of photovoltaics, photocatalysis and/or photoluminescence. Thioindates were prepared under solvothermal conditions. Selected compounds are $(C_{13}H_{28}N_2)_5[Cu_2In_{18}S_{33}]\bullet x(H_2O)$, $[In(en)_2S]_2\bullet 2Cl$, and $[Mg(en)_3][In_2S_4]$. These starting materials were used as single-source precursors and were thermally treated producing nanocrystals of indium sulfides like In_2S_3, Cu-containing In_2S_3, $CuInS_2$ or $MgIn_2S_4$ depending on the treatment conditions and chemical compositions. The photoconductive properties of the obtained nanocrystalline powders or films were studied, finding these materials good candidates for photovoltaic applications.

In additional experiments, the element In was substituted by Sb and thioantimonates were obtained. Due to the increasing price of In, this could be a possibility to decrease the costs to prepare photoactive materials.

2. The second part of the work deals with the fabrication of multilayers of SRO (Silicon Rich Oxide) with high Si contents and SiO_2 prepared by LPCVD (Low Pressure Chemical Vapor

Deposition) as well as with studies on their structural, morphologic, optical and luminescent properties. According to previous reports there are no reported multilayer structures based on SRO with high Si contents prepared by LPCVD. SRO is an extensively studied material due to its interesting optoelectronic properties related to the Si nanocrystals embedded in it. The studied multilayers exhibit photoluminescence (luminescence stimulated with light) in the visible range, ascribed to defects located at the interfaces between the layers. A full study of the structural and compositional characteristics of the multilayers was performed gaining more insight in the emission mechanism. Additionally, an alternative evaluation and interpretation of Raman spectra of the samples is proposed to determine the size of the Si nanocrystals in the films.

Zusammenfassung

In der vorliegenden Arbeit werden die Ergebnisse der Untersuchungen an photoaktiven Materialien und Strukturen auf verschiedenen Längenskalen präsentiert. Die Dissertation umfasst zwei Teile und besteht aus 4 publizierten, 4 eingereichten Artikeln und einem Artikel, der in Vorbereitung ist.

1. Die Darstellung neuer Materialien auf Basis von Thioindaten und Indiumsulfiden, die photoaktive Eigenschaften aufweisen können. Die hergestellten Materialien wurden auf den Gebieten der Photoelektronik, Photokatalyse und/oder Photolumineszenz getestet. Thioindate wurden unter Solvothermalbedingungen dargestellt. Ausgewählte Verbindungen sind $(C_{13}H_{28}N_2)_5[Cu_2In_{18}S_{33}]\bullet x(H_2O)$, $[In(en)_2S]_2\bullet 2Cl$, und $[Mg(en)_3][In_2S_4]$). Diese wurden als Precursoren eingesetzt und thermisch zersetzt, wobei sich je nach gewählten Bedingungen Nanokristalle von Indiumsulfiden wie In_2S_3, Cu-haltige In_2S_3, $CuInS_2$ oder $MgIn_2S_4$ bildeten. Die Untersuchungen der photoleitenden Eigenschaften der nanokristallinen Pulver und Filme zeigen, dass sie für photoelektrische Anwendungen geeignet sind.

Bei weiteren solvothermalen Experimenten wurde das Element In durch Sb ausgetauscht und auf diesem Weg konnten neue Thioantimonate synthetisiert und charakterisiert werden. Aufgrund des stetig steigenden Preises für In könnte so eine Möglichkeit geschaffen werden, die Kosten für photoaktive Verbindungen zu senken.

2. Der zweite Teil der Arbeit beschäftigt sich mit der Darstellung von Multi-Schichten aus SRO (Silicon Rich Oxide) mit hohem Si-Gehalt und SiO_2 durch die LPCVD-Methode (Low Pressure Chemical Vapor Deposition) sowie den Untersuchungen ihrer strukturellen, morphologischen, optischen und lumineszierenden Eigenschaften. Bis jetzt sind in der Literatur keine Multi-Schichtstrukturen beschrieben, die auf SRO mit hohem Si-Gehalt basieren und mit LPCVD dargestellt wurden. Aufgrund der interessanten optoelektronischen Eigenschaften in Bezug auf Si-Nanokristalle ist SRO ein häufig untersuchtes Material. Die dargestellten Multi-Schichten zeigen eine Photolumineszenz (Licht-Stimulierte Lumineszenz) im sichtbaren Bereich, was auf Defekte an der Grenzfläche zwischen den Schichten zurückzuführen ist. Um ein tieferes Verständnis über den Emissionsmechanismus zu erlangen, wurde eine vollständige Untersuchung der strukturellen Eigenschaften und der Zusammensetzung der Multi-Schichten durchgeführt. Zusätzlich wurde erstmals die Größe der Si-Nanokristalle der Multi-Schichten durch eine alternative Evaluation und Interpretation der Raman-Spektren bestimmt.

Contents

1. Introduction

Photoactive materials are materials exhibiting photoconductive, photocatalytic, or photoluminescent properties. These materials transform luminous energy into other kinds of energy like electric, mechanic, thermal, chemical or to light with a different frequency. These materials are applied in very different fields of daily life, ranging from optical sensors, solar cells, photocatalytic production of H_2, to illumination. Among the photoactive materials, of especial interest are those suitable for the transformation of solar energy into electricity. There is more than enough solar radiation available all over the world to satisfy a vastly increased demand for power systems. The sunlight reaching the earth's surface is enough to provide 2850 times as much energy as what is currently used. On a global average, each square meter of land is exposed to enough sunlight to produce 1700 kWh of power every year. The average irradiation in Europe is about 1000 kWh per square meter, however, compared with 1800 kWh in the Middle East [1]. Photovoltaic (PV) cells are being used increasingly to take advantage of this huge resource and will play a key role in future sustainable energy systems. Our present needs could be met by covering 0.1 % of the Earth's surface with PV installations that achieve a conversion efficiency of 10 % [2].

Some of the best known photoactive compounds belong to the family of the thioindates and indium sulfides. The indium sulfides are of the most promising candidates to be used in PV cells. For example, compounds like $AgInS_2$, $CuIn_5S_8$ and $CuInS_2$, with band-gaps of 1.9 [3], 1.31 [4] and 1.5 eV [5, 6] are used as the absorber layers in the PV cells. The band-gaps of these materials display the optimum value for solar energy conversion (1.5 eV) [5]. On the other hand, compounds like β-In_2S_3, with a band-gap of 2 eV [6, 7], are used as buffer layers [8]. Thioindates and indium sulfides also exhibit good photocatalytic properties for H_2 evolution from water splitting. Some examples are the open framework thioindates like $[Na_{14}In_{17}Cu_3S_{35}]\cdot xH_2O$ [9] or solid solutions of $AgInS_2$ or $CuInS_2$ with ZnS [10, 11]. In_2S_3 nanocrystals deposited in mesoporous molecular sieves also present comparable photocatalytic characteristics [12]. Hydrogen may play an important role in the future energy supply because it is a clean energy source and can be used e.g. in fuel cells [13]. Talking about illumination, In_2S_3 nanoparticles have been found exhibiting good photoluminescent (PL) properties. In_2S_3 nanocrystals present PL emission of green light produced by band-to-band transitions [14-16], blue light coming from deep trap states [17] and orange light due to interstitial In defects [16]. In addition, open framework thioindates containing transition metal cations have been found as a family of phosphors whose PL covers the whole visible spectrum [18].

Of great importance are also photoactive devices based on Si, because Si is a cheap and abundant semiconductor. In the area of photovoltaics, solid-state junction devices based on crystalline or polycrystalline Si are the dominant technology with 94% of the market share [2]. The fabrication technology of Si-based PV cells is one of the most developed, and an efficiency of about 25% was achieved in the last years using such Si-based cells [19, 20]. The benchmark is about 40 % efficiency from PV cells based on more expensive and complicated technologies [21]. On the other hand, the area of illumination is also of importance and since the discovery of porous Si a transition to Si-based devices can be observed [22]. Porous Si opens new opportunities to Si-based optoelectronics, proving that it is possible generating luminescence from Si nanocrystals (Si-nCs). Besides porous Si the photoluminescent properties of other materials with low dimensional Si particles have been also studied.

Different fabrication techniques have been used to prepare such materials, like direct deposition of Si quantum dots [23, 24], implantation of Si in an amorphous matrix (principally SiO_2) [25, 26], and deposition of Silicon Rich Oxides (SRO) for the further nucleation of Si-nCs by thermal treatments [27, 28]. Among these materials SRO is very easy to prepare, and it is extensively studied due to its photoluminescence in the visible range [29, 30], which is ascribed to quantum confinement effects in the agglomerates of Si (commonly Si-nCs) or to defects at the interfaces between Si-nCs and the silicon oxide matrix. Other possibilities to prepare low dimensional Si particles are the fabrication of superlattices (SLs) or multilayer structures (MLs) composed of Si layers and other materials like e.g. SiO_2. These arrays allow a one-dimensional quantum confinement in the Si layers when their thickness is limited to some nanometers [31-33] being then able to produce PL.

Motivated by the interesting photoactive properties of thioindates and indium sulfides, as well as of multilayer structures with Si nanocrystals, the objective of the present work was to study these systems, preparing new compounds with new crystal structures that could bring new light to the area of photoactive materials. To achieve this general objective the following specific tasks were undertaken:

- New thioindates were synthesized by the solvothermal synthesis method. This approach allows the preparation of compounds with structures that cannot be easily obtained by conventional experimental procedures.
- Different methods like Pulsed Laser Deposition were tested for the preparation of nanocrystalline indium sulfides, using thioindates as single source precursors.
- The substitution of In by Sb or other elements was explored in solvothermal syntheses to obtain cheaper photoactive materials.

- Multilayer structures based on SRO were prepared and analyzed to combine the properties of the multilayers and SRO. For this purpose cheap and conventional methods like LPCVD (Low Pressure Chemical Vapor Deposition) for the deposition of the films were used.
- The photoactive properties of the prepared compounds and structures were investigated.

2. Synthesis techniques and characterization methods

In the following short paragraphs, some details of the synthetic and characterization techniques used in the doctoral project are described. Additional techniques are mentioned in the publications that compose the thesis. A description of standard and basic methods used for the characterization of solid materials is not given because they are well-known in inorganic solid state chemistry.

2.1. Chemical Vapor Deposition

Chemical Vapor Deposition (CVD) is defined as the formation of a solid film on a substrate by the reaction of vapor-phase chemicals (reactants) that contain the required constituents [34]. The reactant gases are introduced into a reaction chamber and are decomposed and/or reacted at a heated surface to form the thin film. In CVD supported reactions the reactant gases do not react with (and therefore do not consume) any substrate surface material. A wide variety of thin films utilized in ULSI (Ultra Large Scale Integration) fabrication are formed by CVD [35, 36].

A CVD process can be summarized as consisting of the following sequence of steps [34], schematically shown in Fig. 1:

1. Reactant gases - often diluted by mixing with an inert carrier or diluent gas - are introduced by forced convection into a reaction chamber. These gaseous materials move in the chamber

from the inlet to the outlet, what is referred to as the main gas-flow region. As these gases flow through the chamber, they come into the vicinity of the wafers/substrates loaded in the chamber.

2. The reactant-gas species are transported to the wafer surface through a sector of the gaseous volume referred to as the boundary layer. This transport occurs by gas-phase diffusion, i.e., a boundary layer in the gas exists between the main gas-flow region and the surface of the wafer/substrate.

3. The reactants are adsorbed on the substrate surface. These adsorbed species are named ad-atoms.

4. The ad-atoms undergo surface migration to the growth sites, where the film-forming chemical reactions take place. These reactions are responsible for creating the solid film and gaseous by-products. In some cases, a gas-phase reaction leading to the formation of film precursors or even the final product occurs somewhere in the gas prior to the reactants reaching the substrate surface.

5. The gaseous by-products of the reaction are desorbed from the surface. These products must diffuse through the boundary layer near the surface into the main gas-flow region, and from there they are removed from the chamber as the main gas-flow moves toward the outlet.

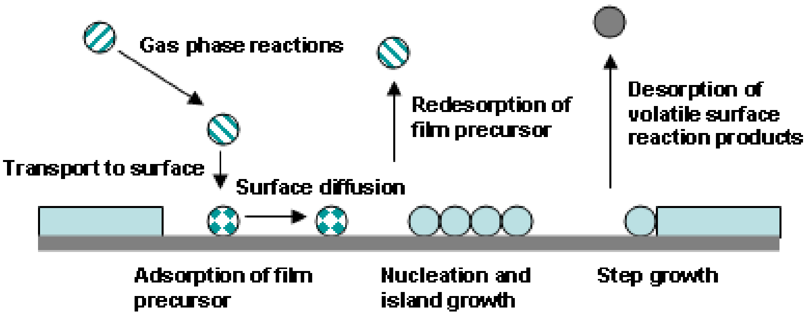

Fig. 1. Scheme of the five sequential steps occurring during a CVD process.

The CVD reactors can be categorized in several ways according to a variety of factors. The first distinction between reactor types is if they are hot-wall or cold-wall reactors. The next criterion is the pressure regime of operation, i.e., atmospheric pressure versus reduced pressure reactors. The reactors operating at atmospheric pressure are commonly called APCVD. Reactors operating at reduced pressures can be divided into: a) low-pressure reactors, the so-called low-pressure CVD or LPCVD reactors, in which the energy input is entirely thermal; and b) reactors in which energy is partially supplied by a plasma as well as by thermal energy. The latter are known as plasma-enhanced CVD or PECVD reactors.

The type of CVD used for the experiments presented in this thesis is LPCVD. The properties of this deposition technique will be now described. The LPCVD system at INAOE which was used for the experiments is shown in Fig. 2.

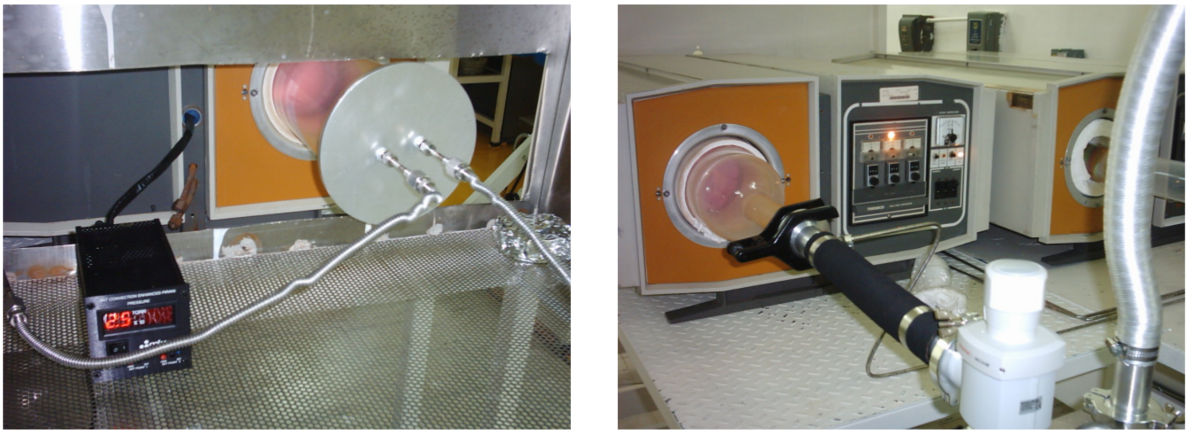

Fig. 2. LPCVD system of INAOE. Left: Front view; right: rear view.

2.1.1. Low Pressure Chemical Vapor Deposition

Films deposited by Low Pressure Chemical Vapor Deposition (LPCVD) present better uniformity and step coverage as well as low particulate contamination than those deposited by APCVD systems [37]. These systems operate with vacuum in the range of 30 - 250 Pa (0.25 - 2 torr) and moderate temperatures (550 - 750 °C), thus they typically deposit films in the reaction-rate-limed regime. At reduced pressure the diffusivity of the reactant gas molecules is sufficiently high so that the mass-transfer to the substrate no longer limits the growth rate. On the other hand, the surface reaction rate is very sensitive to temperature, but precise temperature control is relatively easy to achieve. For example, near the temperature commonly used to deposit polysilicon by LPCVD (625 °C), the deposition rate changes by 2-2.5 % every degree change in temperature. The elimination of mass-transfer constraints in the reactors allows the optimization for high wafer capacity. Low pressure operation also decreases gas-phase reactions, making LPCVD films less subject to particulate contamination. LPCVD is used for depositing many types of films, including poly-Si [38, 39], Si_3N_4 [40], SiO_2 [41, 42], SRO [43], among others.

The two main disadvantages of LPCVD processes are their relatively low deposition rates and relatively high operating temperatures. Attempting to increase deposition rates by increasing the reactant partial pressures tends to initiate gas phase reactions, and attempting to operate at lower temperatures results in unacceptably slow film deposition.

2.2. Pulsed Laser Deposition

The Pulsed Laser Deposition (PLD) method is a physical vapor deposition (PVD) approach, where the target material is vaporized with a high power pulsed laser beam. The deposition of films by this method is performed under ultra high vacuum or in the presence of a background gas such as oxygen when depositing oxides. When the laser radiation is absorbed by the target material the energy is first converted to electronic excitation and then into thermal, chemical and mechanical energy resulting in evaporation, ablation, plasma formation and even exfoliation [44]. The ejected species like atoms, molecules, electrons, ions, clusters, particles and molten globules form a plasma plume and expand in the vacuum chamber to then deposit on a typically hot inert substrate.

The PLD process is very complex but can be generally divided in four stages [45]:

First, atoms of the surface of the target material are vaporized. The penetration depth of the laser beam is around 10 nm, depending on the material. The surface is heated to high temperatures due to the laser, and the non-equilibrium causes a Coulomb explosion that evaporates the substance within the penetration depth. This process occurs within the laser pulse duration (around 10 ps).

In the second stage the plasma of the material expands parallel to the normal vector of the target surface towards the substrate due to Coulomb repulsion and recoil from the target surface. The spatial distribution of the plasma plume is dependent on the background pressure inside the PLD chamber. The most important consequence of increasing the background pressure is the slowing down of the high energetic species in the expanding plasma plume. It has been shown that particles with kinetic energies around 50 eV can re-sputter the film already deposited on the substrate. This results in a low deposition rate and can furthermore alter the stoichiometry of the already deposited film.

In the third stage, the high energetic species ablated from the target bombard the substrate surface and may cause damage of the substrate surface by sputtering of atoms. The sputtered species from the substrate and the particles emitted from the target form a collision region, which serves as a source for condensation of particles. When the condensation rate is high enough, a thermal equilibrium can be reached and the film grows on the substrate surface at the expense of the direct flow of ablation particles and the thermal equilibrium is obtained.

The last stage is the nucleation process and growth of the film on the substrate. The nucleation and film growth kinetics depend on the laser parameters [46, 47], surface temperature [48], background pressure, and on the quality of the substrate’s surface [49].

2.3. Current-voltage characterization of materials

A current-voltage (I-V) plot of a material could be considered as the simplest electrical characterization. Nevertheless the I-V characteristics depend on different factors related to the material and the contacts. The simplest array for such a measurement is shown in Fig. 3. The material is contacted at two points where a voltage is applied. Then the produced current passing through the material is measured. An alternative array consists of applying a certain current and measuring the potential between the two points.

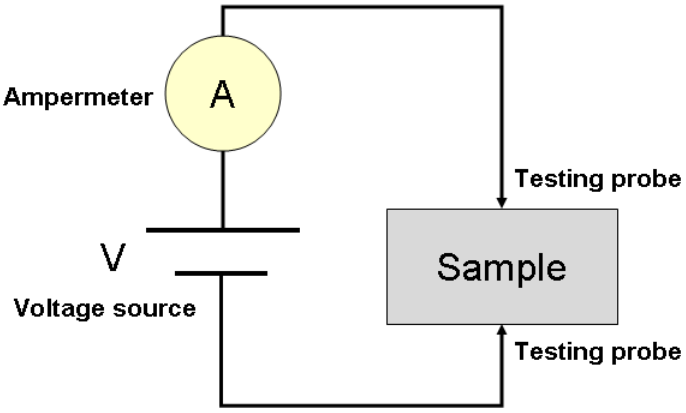

Fig. 3. Electric diagram of the testing circuit.

The obtained I-V plots follow Ohm's law but with the total resistance (R_T) consisting of various components [50]:

$$R_T = \frac{V}{I} = 2R_p + 2R_c + 2R_{sp} + R_m \qquad (1)$$

where R_p is the probe resistance, R_c the contact resistance at each metal probe/semiconductor contact, R_{sp} the spreading resistance under each probe, and R_m is the material resistance. R_{sp} is the resistance encountered by the current flowing from the small metal probe to the measured material, and from the material to the probe. For the determination of R_m the preferred measuring technique is the four-probe method. In this method two probes carry the current and other two probes sense the voltage.

The ability of the contacts to replenish carriers to maintain charge neutrality in the material (properties of an Ohmic contact) if carriers are drawn out of the opposite contact by an electric field plays a key role in determining the kind of observed phenomena in the I-V plots. The general effect of electrical contacts between a metal and a material can be described in terms of three classes of behavior [51]: blocking contacts, Ohmic contacts, and injection contacts. The characteristic dependence of the current on applied voltage for these three types of contacts is shown in Fig. 4.

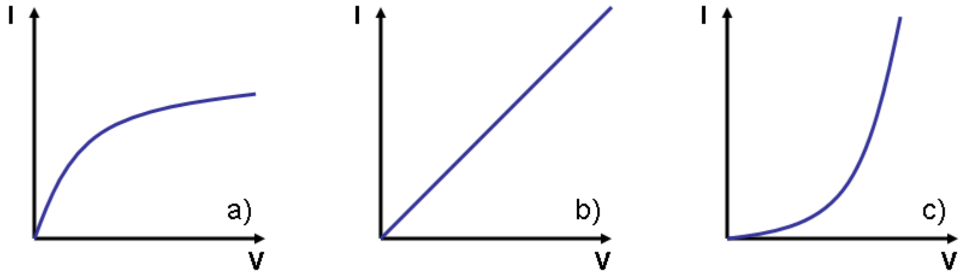

Fig. 4. I-V plots when the contacts are a) blocking, b) Ohmic, c) injecting.

A blocking contact is unable of supplying carriers when they are extracted from the material by an applied electric field. The current varies less than linearly with the applied voltage, and may become saturated.

An Ohmic contact is able to supply carriers. In this case the contacts contribute negligible electrical resistance, and the current varies linearly with the applied voltage with a slope equal to the reciprocal of the resistance of the bulk material. This kind of contacts is the preferred one for the electrical characterization of a material.

An injecting contact is an Ohmic contact being operated under sufficiently high electric fields that allow the carriers from the contact to cross the material before it reaches charge neutrality by dielectric relaxation.

Having Ohmic contacts one can separate the phenomena observed for the measured material. Nevertheless, even with Ohmic contacts the I-V plot could present a non-linear behavior. Depending on the composition of the material one can identify charge trapping [43], tunneling through the material [42], or other interesting effects like current oscillations as found in nanocomposite materials [52].

From electrical measurements using the four-probe technique it is possible to determine the resistivity ρ (the specific resistance) of a material. In semiconductors, the resistance depends on the free electron and hole densities n and p, and the electron and hole mobilities μ_n and μ_p according to the relation [50]:

$$\rho = \frac{1}{q\left(n\mu_n + p\mu_p\right)} \qquad (2)$$

The resistivity is a very important parameter in semiconductor devices contributing to the series resistance, capacitance and threshold voltage of the devices ultimately determining the performance.

3. Thioindates and indium sulfides

The main difference between indium sulfides and thioindates is the charge located on the different basic building units. An indium sulfide is charge neutral, with the composition RSR ($R \neq H$) [53], and a thioindate is any complex anion containing at least one indium cation surrounded by sulfur anions. The thioindates are usually charge compensated by alkali metal cations [54, 55] or protonated organic molecules [55].

The RT-stable (RT = Room Temperature) binary indium sulfides are InS, In_6S_7, $In_{2.8}S_4$, and β-In_2S_3 [56]. InS crystallizes in the orthorhombic space group *P*mnn with unit cell parameters a = 3.94, b = 4.44, c = 10.64 Å [57]. The unit cell of In_6S_7 belongs to the monoclinic space group $P2_1$/m with lattice parameters a = 9.09, b = 3.887, c = 17.705 Å, β = 108.2° [57]. The phase $In_{2.8}S_4$ is identical to the high temperature modification of In_2S_3, specifically the modification α-In_2S_3 [56]. In_2S_3 is polymorphic and can crystallize either in the α, β or γ type structures [58-61]. The structures of the α and β phases can be described as spinel-like. But contrary to a normal spinel structure, one third of the tetrahedral sites remains empty, which leads to the quasi-quaternary compound with formula: $[In_2]_O[In_{2/3}h_{1/3}]_TS_4$ (h represents the vacant sites and T and O represent the tetrahedral and octahedral sites, respectively) [60]. The α-modification is stable above 420 °C and has a cubic structure (a_α = 10.77 Å). Below that temperature the material transforms into tetragonal β-In_2S_3 due to the ordering of the vacancies. The cell parameters of this structure are $c_\beta = 3c_\alpha$ = 32.322 Å, and $a_\beta = a_\alpha/(2)^{1/2}$ = 7.619 Å (space group $I4_1$/amd). Nevertheless if In_2S_3 is prepared with an excess of In larger than 0.5 % the α–modification is stable even at room temperature [61]. Above 754 °C all In atoms change into octahedral interstices of the close-packed sulfur sub-lattice, forming the trigonal phase γ-In_2S_3 [58, 59]. This structural modification is stable at room temperature if about 5 at % of the elements As or Sb are incorporated in the structure.

Within the indium sulfide crystalline matrix, indium and/or sulfur atoms can be substituted by other elements, allowing the synthesis of ternary or quaternary indium sulfides [60]. The case that will be treated in this thesis is mainly the substitution with Cu. The only known single crystal phases in the Cu-In-S system are $CuIn_5S_8$ and $CuInS_2$ [56], even when other phases like $CuIn_3S_5$ have been found as secondary phases in thin films of $CuInS_2$ [62]. $CuIn_5S_8$ crystallizes in the cubic space group *F*-43m, a = 10.6858 Å [63, 64]. $CuInS_2$ crystallizes usually in the chalcopyrite structure type, tetragonal *I*-42d, with a = 5.517 and c = 11.06 Å [65]. But a polymorphic modification of $CuInS_2$ has been reported which has a structure with an ordering observed in the binary alloy CuAu (space group: *P*-4m2) [66]. The addition of Cu to β-In_2S_3 leads to the formation of $CuIn_5S_8$, and a small excess of Cu compared to this composition yields $CuInS_2$ [60].

Thioindates were initially prepared applying high-temperature melts or solid-state reactions, or they were synthesized from aqueous sulfide solutions [54]. Anhydrous thioindates of the alkali metals prepared by these methods have the composition $MInS_2$ (M = Li, Na, K, Rb, Cs) [67, 68]. But when more unconventional chemical synthesis methods are applied, other novel thioindates like $Rb_4In_2S_5$ or $Rb_6In_2S_6$ could be also obtained [69]. High temperature syntheses lead to dense thermodynamically stable products rather than to metastable phases with open network or framework structures. The cations fill the cavities of the anionic sub-lattices producing effectively dense materials. However, after the synthesis of such dense compounds, strategies for creating more space in the structures may be achieved by e.g. ion exchange of large cations by smaller ones [55].

The introduction of structure directing and charge compensating organic molecules applying solvothermal synthesis conditions has allowed the preparation of new compounds with structures containing larger cavities. Due to the interesting structural and optical properties of these hybrid thioindates they have been considered as an alternative to Zeolites in the past decades [70]. The structures may be regarded as open frameworks consisting of interconnected tetrahedral thiometalate clusters [70]. The most common type of tetrahedral cluster is composed of nets of four-coordinated metal cations, emulating a fragment of the zinc-blende type lattice [71, 72] realized with post-transition metals like In [73]. These clusters are called supertetrahedral clusters denoted as Tn (n = 2, 3, 4, 5, …) with the general formulas for isolated clusters being M_4E_{10}, $M_{10}E_{20}$, $M_{20}E_{35}$ and $M_{35}E_{56}$ for n equal to 2, 3, 4 and 5 respectively (with M = Metal and E = chalcogenide anion) [72]. The structures of these clusters are shown in Fig. 5. For T4 and T5 clusters it is necessary to substitute In^{3+} cations by M^+ or M^{2+} metal cations ($M^+ = Cu^+$; $M^{2+} = Mn^{2+}$, Co^{2+}, Fe^{2+}, Zn^{2+}, Cd^{2+}) in some structural positions to reach a local charge balance [72].

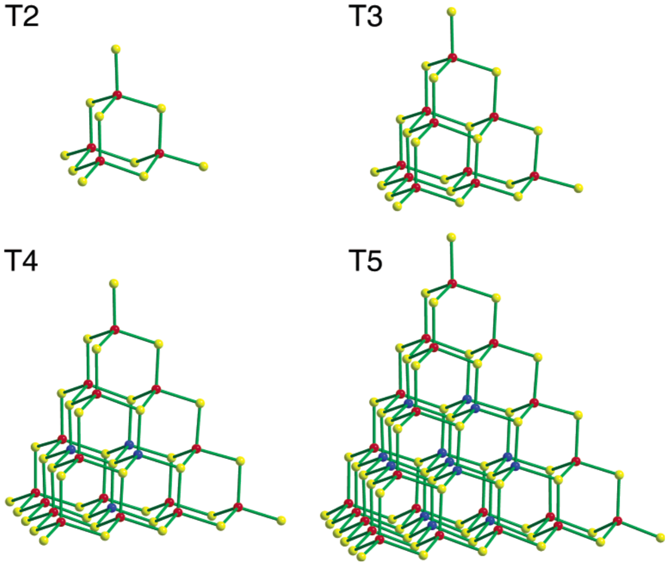

Fig. 5. Ball-and-stick diagrams of T2, T3, T4 and T5 supertetrahedral clusters according to [72]. The yellow and red spheres represent S^{2-} and In^{3+} ions respectively. The blue balls are positions generally occupied by M^+ or M^{2+} cations.

Additionally, other series of tetrahedral clusters have been described in literature and one is the series of pentasupertetrahedral clusters denoted as Pn, which are an assemblage of 4 Tn clusters at the faces of an anti-Tn cluster [74, 75]. There are also capped supertetrahedral clusters which are called Cn. These are based on Tn clusters with a shell of atoms with stoichiometry closely related to the Tn clusters [76].

Structures containing building units not related to supertetrahedral clusters are very scarce, like those composed of layers containing corner and edge-sharing InS_4 tetrahedra [77], helical chains of corner-sharing InS_4 tetrahedra [78], or distorted adamantane-like clusters [79]. Additionally there are reports of one-dimensional (1-D) thioindates, which contain one-dimensional $\{[InS_2]^-\}_\infty$ chains formed by edge-linked InS_4 tetrahedra charge compensated either with protonated amine molecules or with complexes of transition metals [80, 81].

In the present work different thioindates have been synthesized by solvothermal synthesis. Some of them present new architectures and compositions, like the compounds $[In(en)_2S]_2\cdot 2Cl$, and $[Mg(en)_3][In_2S_4]$, which represent the first cationic thioindate and the first thioindate charge compensated with an earth alkaline metal complex (section 3.1). The first compound is a 0-D thioindate whose main structural motif is the centro-symmetric rhomboidal $[In(en)_2S]_2^{2+}$ ring which is formed by S-S edge-sharing of two symmetry related $[InN_4S_2]$ octahedra. A positively charged chalcogenoindate unit has only been observed in a selenoindate with similar structure. The second compound ($[Mg(en)_3][In_2S_4]$) is a 1-D thioindate composed of a straight $\{[InS_2]^-\}_\infty$ chain surrounded by $[Mg(en)_3]^{2+}$ complexes. The presence of an earth alkaline complex is new in thioindates, and opens new possibilities applying new structure directing complexes in future syntheses. An additional trend of the described thioindates is that they are good candidates to be used as single-source precursors for the preparation of indium sulfides. In_2S_3 crystals and $MgIn_2S_4$ nanocrystallites are produced by thermal treatment of the compounds $[In(en)_2S]_2{\cdot}2Cl$ and $[Mg(en)_3][In_2S_4]$ in an inert atmosphere.

The Cu-containing thioindate $(C_{13}H_{28}N_2)_5[Cu_2In_{18}S_{33}]\bullet x(H_2O)$ was also synthesized and was used as single source precursor for the preparation of indium sulfides by two different techniques. The precursor compound is composed of supertetrahedral T4 clusters. Such a compound composed of large inorganic clusters has not been tested as single source precursor before. First, a nanocomposite film of In and $CuInS_2$ nanoclusters has been prepared by PLD (section 3.2). The large amount of In present in the precursor allowed the formation of In clusters in the nanosized range and $CuInS_2$ nanocrystals. The average sizes of the In and $CuInS_2$ nanoparticels were estimated from the X-ray powder pattern and are about 36 and 17 nm respectively. These values match well with the sizes observed in TEM micrographs. The film presents good electrical conductivity, comparable with the one reported for n-type $CuInS_2$, despite the presence of some organic contamination. Extensive EDX studies performed on several areas of the film demonstrate a large variation of the Cu:In:S ratio in a stochastic fashion which can be attributed to amorphous inter-particle regions (dimension about 1 nm). The electric performance seems to be dominated by the $CuInS_2$ islands in the film as can be concluded by the electrical resistance which is rather that of a semiconductor than that of a metal like In. The film also exhibits good photoelectric characteristics. The characterization of the photoelectric properties demonstrate that only light in the wave-length region from 515 to 850 nm yields an increased conductivity under irradiation. Using the rapid pyrolysis method instead of PLD produces Cu-containing In_2S_3 nanocrystals (section 3.3). There is an increasing interest in introducing Cu in the void spaces of In_2S_3, since in this way the photosensitivity and photoconductivity of the material can be varied. The produced In_2S_3 nanocrystals have a cubic structure (the high-temperature modification), probably due to the Cu incorporation in the voids. Two In_2S_3 phases coexist with one being Cu-poor and the other having a larger Cu content. The coexistence of these two compounds is reflected by the Raman and UV-vis spectra. The results of the experiments with PLD and rapid pyrolysis demonstrate the strong dependence of the composition, morphology and structure of the materials on the synthetic method.

Additional work in the field of indium sulfides was the solvothermal preparation of nanocrystalline mixtures of compounds of the Cu-In-S system for photocatalytic applications (section 3.4). Three different compounds could be identified in the mixtures with ratios of these compounds depending on the ratio of the starting materials Cu:In:S. The compounds display different morphologies like micron-sized plates, nano-walls and nanobelts. Whereas the microcrystalline compound could be unambiguously identified as $CuInS_2$ with the chalcopyrite structure type, the structures of the two other compounds with compositions $CuIn_3S_5$ and $CuIn_7S_{11}$ are still not fully clear. Further characterizations with special HRTEM techniques are required to determine the crystal structures of the materials. The mixtures were tested in the photocatalytic production of H_2 from water using sacrificial reagents yielding a H_2 evolution which is comparable to that reported for $CuInS_2/AgInS_2$ in solid solution with a wide-gap semiconductor like ZnS. The catalytic activity of the mixtures depends on the ratio of the three compounds and the most active mixture was obtained using Cu:In:S = 1.3:5:9.5 in the reaction slurry. Note that this mixture contains the largest amount of the compound with approximate composition $CuIn_7S_{11}$ (nanobelts). The results suggest that the morphology and size of the catalyst particles strongly influence the photocatalytic activity.

3.1.

Submitted to J. Solid State Chem. 28.Apr.2010

Zero- and one-dimensional thioindates synthesized under solvothermal conditions yielding α-In_2S_3 or $MgIn_2S_4$ as thermal decomposition products

E. Quiroga-González[1], L. Kienle[2], C. Näther[1], V.S.K. Chakravadhanula[2], W. Bensch[1*]

[1] Institute for Inorganic Chemistry of the University of Kiel, Max-Eyth-Str. 2, 24118 Kiel, Germany.
[2] Institute of Material Science of the University of Kiel, Synthesis and Real Structure, Kaiserstr. 2, 24143 Kiel, Germany.

*Corresponding author: wbensch@ac.uni-kiel.de, Tel.: +49 431 8802094

Abstract

The first cationic thioindate with composition $[In(en)_2S]_2 \cdot 2Cl$ (zero-dimensional) and the first thioindate being charge compensated by a main group metal complex with composition $[Mg(en)_3][In_2S_4]$ (one-dimensional) have been prepared with ethylenediamine under solvothermal conditions. The main structural motif of $[In(en)_2S]_2 \cdot 2Cl$ is the centro-symmetric rhomboidal $[In(en)_2S]_2^{2+}$ ring which is formed by S-S edge-sharing of two symmetry related $[InN_4S_2]$ octahedra. The structure of $[Mg(en)_3][In_2S_4]$ is composed of a straight one-dimensional $\{[InS_2]^-\}_\infty$ chain surrounded by $[Mg(en)_3]^{2+}$ complexes. Both compounds are wide band-gap semiconductors. The thermal decomposition reaction of $[In(en)_2S]_2 \cdot 2Cl$ yielded cubic α-In_2S_3 and $MgIn_2S_4$ in the case of $[Mg(en)_3][In_2S_4]$. The $MgIn_2S_4$ crystals are in the nanometer range as evidenced by a pronounced broadening of the reflections in the powder pattern and with transmission electron microscopy.

Keywords: Cationic thioindate, solvothermal synthesis, crystal structure, thermal decomposition, single source precursor, nanocrystalline $MgIn_2S_4$

1. Introduction

Inorganic-organic hybrid chalcogeno-indates are mainly prepared under solvothermal conditions in the presence of an organic amine as a structure-directing agent. The structures are usually based on the $[InQ_4]$ tetrahedra (Q = S, Se, Te) which are interconnected to form supertetrahedral clusters (Tn) as building units [1], or some variants like pentasupertetrahedral [2, 3] and capped supertetrahedral clusters [4], respectively. Chalcogeno-indates with structures containing other building units are rare, cf. the compounds $[(C_3H_7)_2NH_2]_3[In_6S_{11}H]$ ($(C_3H_7)_2NH$ = dipropylamine) [5] and $[C_{13}H_{28}N_2]_{6.5}[In_{33}S_{56}]$ ($C_{13}H_{26}N_2$ = 4, 4'-trimethylenedipiperidine) [6]. The structure of the first is composed of $[In_6S_{11}]$ chains linked by edge-sharing $[InS_4]$ tetrahedra [5], while the structure of the second compound is a three-dimensional framework constructed from the cross linking of helical chains of corner-sharing $[InS_4]$ tetrahedra [6]. Recently, a one-dimensional (1-D) thioindate with composition $[C_{10}N_4H_{26}]_{0.5}[InS_2]$ ($C_{10}N_4H_{24}$ = 1,4-bis(3-aminopropyl)piperazine) was reported, which contains one-dimensional $\{[InS_2]^-\}_\infty$ chains formed by edge-linked $[InS_4]$ tetrahedra [7]. Other 1-D thioindates like $[Ni(dien)_2]_{0.5}[InS_2]$ (dien = diethylenetriamine) and $[Ni(dap)_3]_{0.5}[InS_2]$ (dap = 1,2-diaminopropane) have the same $\{[InS_2]^-\}_\infty$ chains, but are charge-compensated with complexes of transition metals [8]. Recently, cationic inorganic-organic hybrid seleno-indates have been also reported, namely ($[In(en)_2Se]_2 \cdot 2I$ and $[In(teta)Se]_2 \cdot 2I$, en = ethylenediamine, teta = triethylenetetramine) [9]. These compounds are composed of isolated clusters and hence they may be regarded as zero-dimensional (0-D) with respect to the clusters' substructure.

Besides these hybrid compounds the binary inorganic compound In_2S_3 is in the focus of research because it may replace toxic CdS buffer layers in highly efficient solar cells [10, 11]. Additionally, the crystal structures of α- or β-In_2S_3 present a large amount of vacancies that can serve as host for a number of metal ions to form semiconducting and/or magnetic materials [12]. These structural and chemical features distinguish In_2S_3 from II-VI compounds, which tend to expel guest ions [13], and offer possibilities for tuning the optical and electrical properties according to the type and concentration of the guest cations. For example, the optical band gap can be continuously tuned when

In cations are partially replaced by a metal cation like Cu^+ or Na^+ [14, 15], thus obtaining compounds with formulas $[In_{16}]_O[In_{5.23-x/3}M_xh_{2.67-2x/3}]_TS_{32}$ where M is the substituting metal, h represents the vacant sites and T and O be a symbol of the tetrahedral and octahedral sites, respectively. The maximum substitution level is achieved for MIn_5S_8 with x ~ 4 [16].

For In_2S_3 or its derivatives, the optical, electronic, and catalytic properties can be adjusted by the size and shape of the crystals [13, 17]. Nanocrystalline In_2S_3 has been prepared applying a wide range of methods like hydrothermal synthesis [17-19], solution reactions [13, 20] and pyrolysis of single source molecular compounds [21] producing either the cubic (α) modification [22, 23] or the tetragonal (β) modification [13, 18, 24]. Among these approaches the use of single molecular source precursors is most studied. Frequently, the synthesis of such precursors is simple and they contain the elements of the desired product homogenously distributed on an atomic scale, however, the size of the organic molecules should be small to keep the contamination with organic constituents as low as possible when fabrication techniques like pyrolysis or thermal decomposition are used.

In our ongoing work in the field of solvothermal synthesis of thiometalate compounds we synthesized a 0-D thioindate with composition $[In(en)_2S]_2{\cdot}2Cl$ (**1**) and the 1-D thioindate $[Mg(en)_3][In_2S_4]$ (**2**). The two compounds were tested as precursors for the preparation of In_2S_3 and $MgIn_2S_4$ using thermal decomposition in inert atmosphere. $MgIn_2S_4$ was obtained in nanocrystalline form whereas good crystalline α-In_2S_3 was obtained as decomposition product of **1**. In the paper, the syntheses, crystal structures, thermal and optical properties of the two compounds are reported. The nanocrystals were investigated with Transmission Electron Microscopy (TEM) and X-ray powder diffractommetry.

2. Experimental

2.1. Synthesis of ($[In(en)_2S]_2{\cdot}2Cl$) (1)

For the solvothermal synthesis 0.7 mmol of In and 0.7 mmol of S were used. The precursors were mixed with 4.75 mL of en (ethylenediamine) and 0.25 mL CH_2Cl_2 in a 35 mL Teflon-lined stainless steel autoclave. The sealed vessel was then heated at 190 °C for 5 days. After cooling down to room temperature, the product was filtered off, and washed first with water, then with ethanol and finally with acetone. Colorless needles in a yield of around 40 % based on In were obtained. C-H-N-S analysis (in %): Calculated: C, 15.88; H, 5.33; N, 18.52; S, 10.60%. Measured: C, 16.02; H, 5.36; N, 18.28; S, 10.45 %. The FTIR spectrum of the compound exhibits the characteristic peaks for en at 506 (m), 1038 (s), 1100 (m), 1324 (w), 1382 (vw), 1452 (w), 1576 (m), 1631 (vw), 2937 (w), and 3116 cm^{-1} (w). Additionally the presence of hydrogen bonds is evidenced by the peaks at 3238 (s) and 3425 cm^{-1} (s).

2.2. Synthesis of ($[Mg(en)_3][In_2S_4]$) (2)

This compound was prepared using 0.52 mmol of Mg, 1 mmol of In, and 2.1 mmol of S. The starting materials were mixed with 4 mL of en in a 35 mL Teflon-lined stainless steel autoclave. The sealed vessel was then heated at 190 °C for 10 days. After cooling down to room temperature, the product was filtered off, and washed with water, ethanol and acetone. Prismatic colorless crystals in a yield larger than 80% based on In were obtained. C-H-N-S analysis (in %): Calculated: C, 12.81; H, 4.30; N, 14.94; S, 22.80%. Measured: C, 12.17; H, 4.24; N, 14.04; S, 22.78 %. The FTIR spectrum of this compound presents also the characteristic peaks for en: 494 (m), 1009 (s), 1108 (m), 1337 (w), 1392 (vw), 1453 (w), 1572 (m), 1641 (vw), 2920 (w), and 3138 cm^{-1} (w). The presence of hydrogen bonds is evidenced with the peaks at 3236 (s) and 3285 cm^{-1} (s).

2.3. Thermal decomposition of 1 and 2

Compounds **1** and **2** were crushed and the obtained powders were thermally treated in Argon atmosphere at a rate of 2 °C/min until 500 °C yielding dark red powders. For descriptive purposes, the powders are named **1x** (from compound **1**) and **2x** (from compound **2**). **1x** contains 6.48 wt% of organic residue (C-H-N analysis (in %): C, 4.91; H, 0.0; N, 1.57), and **2x** contains 2.63 wt% (C-H-N analysis (in %): C, 1.9; H, 0; N, 0.73).

2.4. Characterization methods

X-ray single-crystal analysis of **1** and **2** were performed using an Imaging Plate Diffraction System (IPDS1) from Stoe & CIE with MoK_α radiation). The raw data were corrected for Lorentz-polarization effects. The structures were solved with Direct Methods using SHELXS-97 [25]. Structure refinement was performed with SHELXL-97 [25]. All non-hydrogen atoms were refined with anisotropic displacement parameters. All hydrogen atoms were positioned with idealized geometry and refined isotropically using a riding model. For **2**, The C-H and N-H atoms were positioned with idealized geometry and also refined using a riding model. In this compound both crystallographically independent en molecules are disordered over two positions. Selected crystal data and results of the structure refinements of **1** and **2** are summarized in Table 1. Selected bond lengths and angles of the structures are shown in Tables 2 (**1**) and 3 (**2**).

Crystallographic data (excluding structure factors) have been deposited with the Cambridge Crystallographic Data Centre as supplementary publication no. CCDC xxxxx. Copies of the data can be obtained, free of charge *via* www.ccdc.cam.ac.uk/data_request/cif.

DTA-TG measurements of **1** and **2** were performed in Al_2O_3 crucibles using a STA-409CD thermobalance from Netzsch. The measurements were performed in Al_2O_3 crucibles under an Argon atmosphere with a heating rate of 2 °C/min. C-H-N-S analyses was performed using a EURO EA Elemental Analyzer by EURO VECTOR Instruments and Software. Additionally, MIR spectra (450-3000 cm^{-1}) were recorded with a spectrometer ATI Mattson Genesis.

UV/Vis spectroscopic investigations were conducted at room temperature using a UV/Vis-NIR two-channel spectrometer Cary 5 from Varian Techtron Pty., Darmstadt. The optical properties of the compound were investigated by studying the UV/Vis reflectance spectrum of the powdered sample. The absorption data were calculated with the Kubelka-Munk relation for diffuse reflectance data. $BaSO_4$ powder was used as reference material.

The thermal decomposition products were investigated with X-ray powder diffractommetry (Stoe STADI P diffractometer, Ge monochromator, *CuK* radiation, λ = 1.54056 Å). For Transmission Electron Microscopy (TEM) investigations, the powders obtained after thermal annealing of the thioindates were transferred to aluminium grids which were fixed in a side-entry, double-tilt holder with the tilting limited to a maximum of ± 25° in two directions. High resolution transmission electron microscopy (HRTEM) was performed with a Philips CM30ST (300 kV, LaB_6 cathode). EDX (energy dispersive X-ray spectroscopy) was conducted in the scanning and nanoprobe mode of the CM30ST instrument using a Si/Li-EDX detector (Noran, Vantage System).

Table 1
Selected data, technical details of data collection and of the refinement results for compounds **1** and **2**.

	Compound 1	**Compound 2**
Empirical formula	$C_8H_{32}Cl_2In_2N_8S_2$	$C_6H_{12}In_2MgN_6S_4$
Formula weight / gr	605.08	550.41
Color	colorless	colorless
Crystal size / mm^3	0.11 x 0.09 x 0.07	0.1 x 0.08 x 0.08
Crystal system	monoclinic	orthorhombic
Space group	$P2_1/n$	*Cmcm*
a / Å	6.4859(3)	9.7196(7)
b / Å	11.1962(9)	15.1887(10)
c / Å	14.2509(8)	13.1473(7)
β / deg	93.763	90
Volume / $Å^3$	1032.63(11)	1940.9(2)
Z	4	4
Density (calculated) / mg/m^3	1.946	1.884
Wavelength / Å	0.71073	0.71073
Absorption coefficient / mm^{-1}	2.702	2.833
F(000)	600	1056
Reflections collected	9459	13834
Independent reflections	2423 [R(int) = 0.0339]	1239 [R(int) = 0.0365]
Completeness to theta = 28.03°	97.0 %	96.0 %
Data / restraints / parameters	2423 / 0 / 101	1239 / 0 / 73
Goodness-of-fit on F^2	1.027	1.129
Final R indices [I>2sigma(I)]	R1 = 0.0213, wR2 = 0.0532	R1 = 0.0285, wR2 = 0.0785
R indices (all data)	R1 = 0.0249, wR2 = 0.0544	R1 = 0.0335, wR2 = 0.0806

Extinction coefficient	0.0073(6)	0.0015(3)
Largest diff. peak and hole / e.Å^{-3}	0.760 and -0.767	0.843 and -0.731

Table 2. Selected bond lengths [Å] and angles [deg] for compound **1**.

In(1)-N(1)	2.3078(17)	In(1)-N(2)	2.4110(17)
In(1)-N(11)	2.3184(18)	In(1)-S(1)#1	2.4731(5)
In(1)-N(12)	2.3330(18)	In(1)-S(1)	2.5040(5)
N(1)-In(1)-N(11)	88.14(6)	N(2)-In(1)-S(1)#1	94.03(4)
N(1)-In(1)-N(12)	151.56(6)	N(1)-In(1)-S(1)	101.06(4)
N(11)-In(1)-N(12)	75.84(7)	N(11)-In(1)-S(1)	88.27(4)
N(1)-In(1)-N(2)	74.60(6)	N(12)-In(1)-S(1)	101.76(4)
N(11)-In(1)-N(2)	84.20(6)	N(2)-In(1)-S(1)	171.39(5)
N(12)-In(1)-N(2)	80.44(6)	S(1)#1-In(1)-S(1)	93.882(15)
N(1)-In(1)-S(1)#1	96.97(4)	In(1)#1-S(1)-In(1)	86.118(15)
N(11)-In(1)-S(1)#1	173.96(5)	C(1)-N(1)-In(1)	112.47(12)
N(12)-In(1)-S(1)#1	98.18(5)	C(2)-N(2)-In(1)	106.22(13)
C(12)-N(12)-In(1)	110.21(13)	C(11)-N(11)-In(1)	106.62(13)

Table 3. Bond lengths [Å] and angles [deg] for compound **2**.

In(1)-S(1)	2.4477(12)	S(1)-In(1)#2	2.4477(12)
In(1)-S(3)	2.4745(9)	S(2)-In(1)#2	2.4773(11)
In(1)-S(3)#1	2.4745(9)	S(3)-In(1)#1	2.4745(9)
In(1)-S(2)	2.4773(11)		
In(1)-In(1)#1	3.2647(6)	S(2)-In(1)-In(1)#1	138.01(3)
S(1)-In(1)-S(3)	113.364(19)	S(1)-In(1)-In(1)#2	47.20(3)
S(1)-In(1)-S(3)#1	113.364(19)	S(3)-In(1)-In(1)#2	131.014(18)
S(3)-In(1)-S(3)#1	97.45(4)	S(3)#1-In(1)-In(1)#2	131.014(18)
S(1)-In(1)-S(2)	95.04(4)	S(2)-In(1)-In(1)#2	47.83(2)
S(3)-In(1)-S(2)	119.360(18)	In(1)#1-In(1)-In(1)#2	174.157(11)
S(3)#1-In(1)-S(2)	119.360(18)	In(1)-S(1)-In(1)#2	85.59(5)
S(1)-In(1)-In(1)#1	126.95(3)	In(1)#2-S(2)-In(1)	84.33(5)
S(3)-In(1)-In(1)#1	48.726(18)	In(1)-S(3)-In(1)#1	82.55(4)
S(3)#1-In(1)-In(1)#1	48.726(18)		

3. Description of the structure of the thioindates

3.1. Structure of [In(en)$_2$S]$_2$·2Cl (1)

Compound **1** consists of zero-dimensional (0-D) thioindate clusters (Fig. 1) crystallizing in the monoclinic space group P2$_1$/n with all atoms being located on general positions. The In^{3+} cation is coordinated by four N atoms of two en molecules and two S^{2-} anions in a slightly distorted octahedral geometry. The In-N bond lengths ranging from 2.3078(1) to 2.4110(17) Å are significantly longer than in e.g. {[In(C$_6$H$_{14}$N$_2$)$_2$]$_2$Sb$_4$S$_8$}Cl$_2$ (2.272 – 2.299 Å) [26], In$_2$Ge$_6$O$_{15}$(en)$_2$ (2.261 – 2.285 Å) [27], [In(APTSC)$_2$](PF$_6$) (2.230 – 2.297 Å; APTSC = 2-acetylpyridine-thiosemicarbazone) [28], or [HB(2,5-Me$_2$pz)$_3$]In(S$_4$)(3,5-Me$_2$pzH) (2.271-2.341 Å; pz = pyrazolyl) [29], but are in the range reported for {O[In(HDAPTSC)(OH)]$_2$}·5MeOH (2.292 - 2.391 Å) (HDAPTSC = 2-acetylpyridine-thiosemicarbazone) [28], [In(en)$_2$Se]$_2$·2I (2.309 – 2.410 Å) [9] and [In(teta)Se]$_2$·2I (2.313 – 2.368 Å) [9]. The In-S bonds of 2.4731 and 2.5040 Å are comparable with those determined for the above mentioned S-containing compounds or [DEAH]$_7$[In$_{11}$S$_{21}$H$_2$] [30].

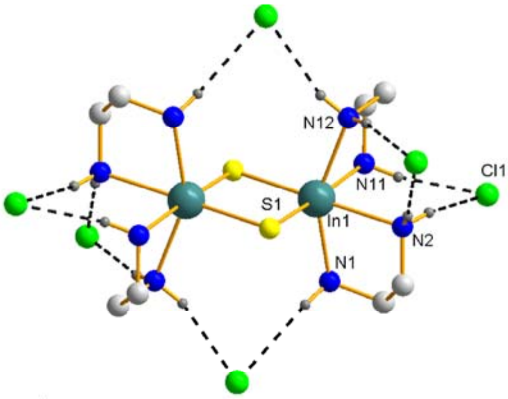

Fig. 1. The central $[In(en)_2S]_2^{2+}$ core with atom numbering and its surrounding by Cl^- anions. Note that H-atoms are not numbered and dotted lines indicate N-H···Cl interactions.

The distortion of the $[InN_4S_2]$ octahedron is obvious analyzing the *trans*-angles that vary from 151.56(6) to 173.96(5)° and the *cis*-angles ranging between 74.60(6) and 101.76(4)° (Table 2). The cationic $[In(en)_2S]_2^{2+}$ core is constructed by edge-sharing of two symmetry related $[InN_4S_2]$ octahedra via the S-S edge forming a centro-symmetric rhomboidal In_2S_2 ring. The two cationic seleno-indates $[In(en)_2Se]_2{\cdot}2I$ and $[In(teta)Se]_2{\cdot}2I$ have been previously reported [9] and compound **1** which is isostructural to the former compound represents the first cationic thioindate. Charge compensation is achieved by Cl^- anions and each $[In(en)_2S]_2^{2+}$ cation is surrounded by six Cl^- anions (Fig. 1). The Cl^- ions are connected to the central structural motif via weak H-bonds (Cl···H distances ranging from 2.32 to 2.94 Å with corresponding N-H···Cl angles between 157.22 and 168.25°). The complexes of **1** are linked into chains that run parallel to the [100] direction through N-H···S hydrogen bonding interactions (S···H distances: 2.40 -2.74 Å), as shown in Fig. 2. The extended S···H and Cl···H interactions generate a three-dimensional framework (Fig. 3). Each $[In(en)_2S]_2^{2+}$ cation is surrounded by six further $[In(en)_2S]_2^{2+}$ groups generating tunnels along [100] hosting the Cl^- anions.

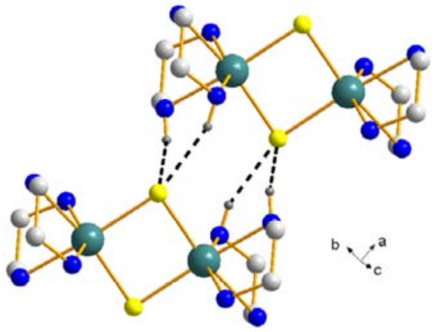

Fig. 2. The S···H bonding interactions (dotted lines) in **1** generating chains running along the [100] direction.

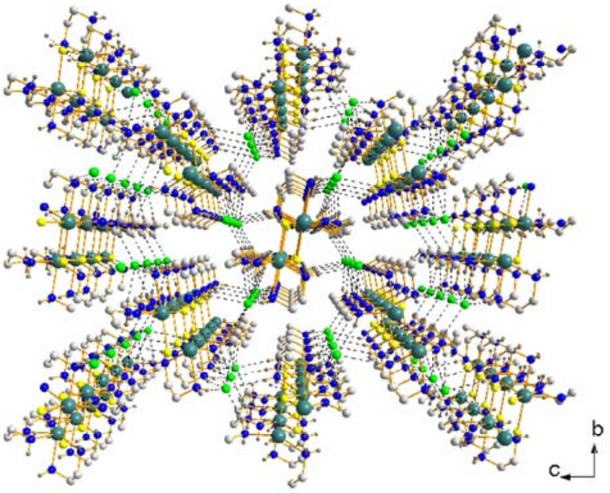

Fig. 3. 3-D framework made by linking the zero-dimensional thioindates through N-H···S and N-H···Cl H-bonds.

3.2. Structure of $[Mg(en)_3][In_2S_4]$ (2)

The 1-D thioindate **1** crystallizes in the orthorhombic space group *Cmcm* with In, Mg, S and N atoms being located on special positions. The structure consists of linear 1-D $\{[InS_2]^-\}_\infty$ chains that run parallel to the [001] direction (Fig. 4). The chains are formed by $[InS_4]$ tetrahedra sharing opposite edges (In-S bond lengths: 2.47 and 2.50 Å, Table 2) with S-In-S angles ranging from 95.04(4) to 119.36(18)°, significantly deviating from the tetrahedral geometry. The connection mode generates In_2S_2 rings and neighboring rings are rotated by 90 ° to each other. The shortest In-In distance of 3.265 Å and the other geometric parameters are similar to those reported for other 1-D thioindates [7, 8]. An identical linkage mode of MQ_4 tetrahedra is observed for SiS_2 [31] or $K_2HgSnTe_4$ [32].

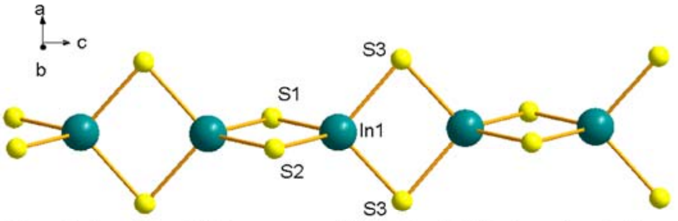

Fig. 4. 1-D $\{[InS_2]^-\}_\infty$ chain of **2**, which runs parallel to the [001] direction. It is composed of edge-sharing $[InS_4]$ tetrahedra.

The polymeric anion is charge compensated by a $[Mg(en)_3]^{2+}$ complex (Fig. 5a). There have been some reports about 1-D thioindates charge-compensated with protonated amine molecules [7] and with transition metal complexes [8], but this is the first time that charge compensation is achieved by an earth-alkaline metal complex. The Mg-N bond lengths of 2.20 and 2.22 Å are comparable with data recently published for $[Mg(en)_3][Sb_4S_7]$ in [33]. Like in the thioantimonate, the octahedral environment around Mg^{2+} is strongly distorted as evidenced by the N-Mg-N angles (see Table 3).

The linear chains are arranged on a rectangular net with channels running along [001] being occupied by the $[Mg(en)_3]^{2+}$ complexes (Fig. 5b). The structure of **2** is stabilized by numerous weak N-H···S H-bonds (bond lengths ranging from 2.55 to 2.98 Å) between the Mg complexes and the anionic chains.

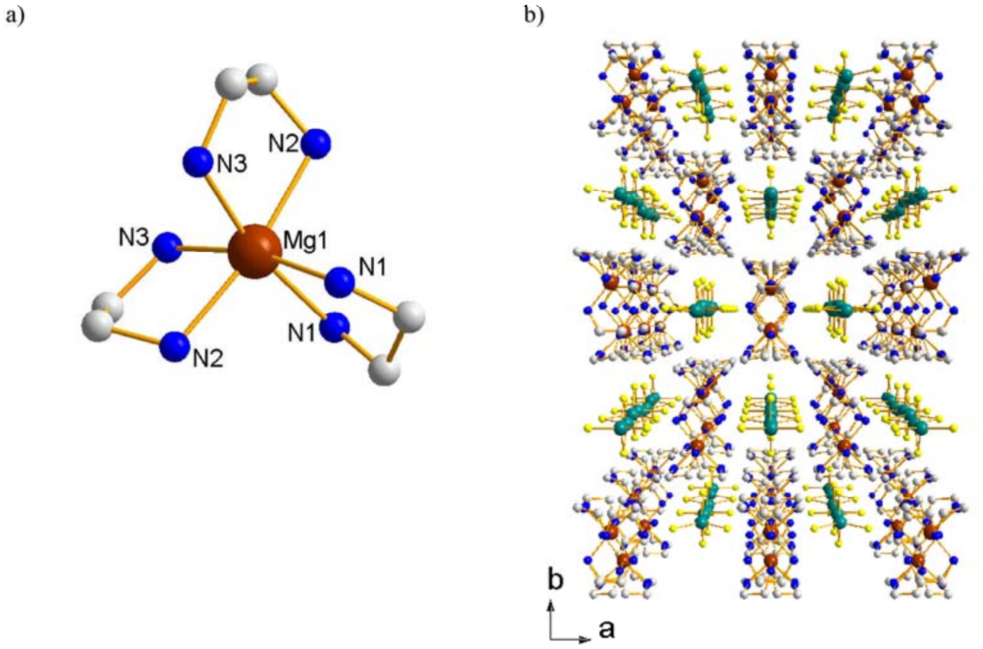

Fig. 5. a) View of the $[Mg(en)_3]^{2+}$ complex in **2**. b) 3-D view of the structure of **2**. The 1-D $\{[InS_2]^-\}_\infty$ chain running parallel to the [001] direction.

4. Thermal and optical characterization of the thioindates

4.1. Thermal properties

The DTA, TG and DTG curves of compounds **1** and **2** are shown in Fig. 6a) and b). According to the TG curve compound **1** undergoes a complex decomposition process with endothermic events in the DTA curve with T_{onset} at around 215, 235, 266, 288 and 365 °C. The total mass loss until 500 °C is about 42.1 %, and about 9.3 % lower than expected for the emission of the amine and Cl (expected: 51.4 %). As can be seen in Fig. 6a, the mass loss is not finished at the final temperature and some organic contamination as well as some chlorine remains in the residue. The presence of Cl in the residue was corroborated by EDX measurements. The chemical composition of some white microparticles at the surface of the product after thermal decomposition was determined with EDX to In:Cl = 1:3 (supporting material), suggesting that $InCl_3$ was formed during the reaction processes. The TG curve of **2** displays three well resolved steps accompanied by three endothermic peaks in the DTA curve at about 195, 268 and 310 °C. The total mass loss until 500 °C is about 30.2 %, and 1.8 % less than expected for the emission of the amine molecules (expected: 32 %).

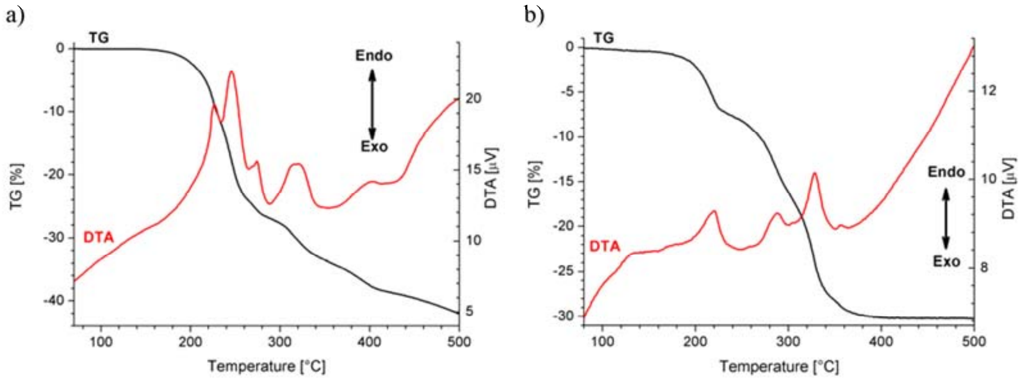

Fig. 6. DTA/TG curves of a) **1**, b) **2**.

4.2. Optical properties

The Kubelka-Munk plots for the determination of the optical band gaps of **1** and **2** are shown in Fig. 7a) and b) respectively. In the curve α^2/s^2 is plotted against energy with α being the absorption coefficient and s the scattering coefficient [34]. The optical band gap of the compounds was determined to $E_g = 3.47$ (**1**) and $E_g = 3.59$ eV (**2**). Because these values are very similar the absorption edge may be assigned to electronic transitions between levels of the In and S atoms. The In-S-In angles and the In-S bond-lengths in both compounds are very similar with small differences (see Tables 2 and 3) which may account for the slightly differing values for E_g.

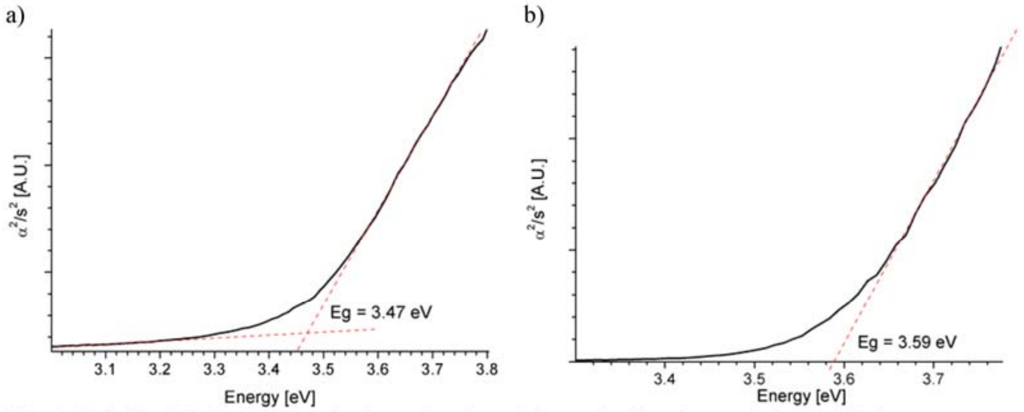

Fig. 7. Kubelka-Munk plots for the determination of the optical band gap of a) **1** and b) **2**.

5. Structural characterization of the decomposition products

The X-ray powder diffractograms (PDs) of **1x** and **2x** are shown in Fig. 8. The reflections in the powder pattern of **1x** match well with those of the pattern of α-In_2S_3 (cubic) [35] and the absence of the (112) reflection at about 17° 2θ according to β-In_2S_3 [36] indicates the that the cubic modification is formed during the thermal decomposition process. The size of the coherent scattering domains was evaluated applying the Scherrer equation. The quantification yields about 29 nm for the most intense reflection. α-In_2S_3 is a high temperature modification of In_2S_3 and according to data presented in the literature this modification can be stabilized at room temperature in the presence of an In excess [37]. In the case of **1x** the formation of α-In_2S_3 seems to be reasonable because it is obtained from an In-rich precursor compound with In:S = 1:1, and stoichiometric In_2S_3 would require the removal of one-third of In. According to literature data the α-phase is stable with the composition $In_{2+x}S_3$ ($0.01 < x < 0.18$) [37]. But there is also a report were the α-modification was obtained for very small deviation of the exact stoichiometry (In:S = 1.01:1) [38]. Additionally In-S films having an In/S ratio between 0.79 and 0.94 have been described as a combination of the α- and β-modifications [39]. The amount of $InCl_3$ in **1x** is either to small to be detected in the powder pattern or the compound is amorphous. Nevertheless, the formation of $InCl_3$ reduces the In:S ratio and the nonstoichiometric α-In_2S_3 modification is formed during the thermal decomposition process.

The diffraction pattern of **2x** can be described on the basis of the cubic spinel-type structure of $MgIn_2S_4$ [40]. Because no additional crystalline phases were detected in the pattern the remaining organic components must be amorphous. The presence of Mg, In, and S in the 1:2:4 ratio was confirmed with EDX analysis. The reflections of the decomposition product are significantly broadened, which is caused by particle size effects. The average particle size calculated with the Debye-Scherrer formula using the most intense reflections (no correction was made for instrumental broadening) is about 9 nm, evidencing the nanocrystalline nature of this material.

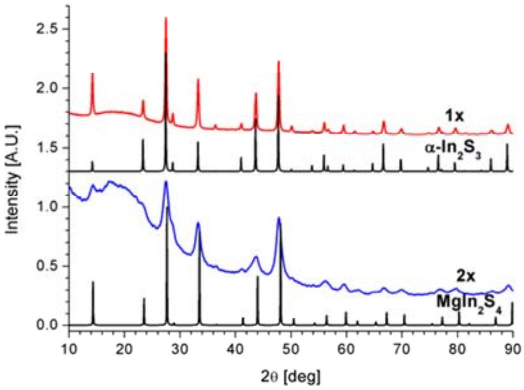

Fig. 8. X-ray powder diffractograms of **1x** and **2x**. The calculated diffractograms of α-In_2S_3 $MgIn_2S_4$ are shown for comparison. No secondary phases are detected.

The TEM micrographs of **2x** show that the sample is composed of nanocrystals randomly oriented (Fig. 9) separated by thin amorphous regions possibly composed of the organic residue. The electron diffraction patterns (ED) recorded inside selected areas of the nanosized crystals can be indexed assuming the structure of $MgIn_2S_4$ [40], as specified in Fig. 10. The d values calculated from the ED pattern are summarized in Table 4. The presence of reflections on concentric circles confirms random orientation of the crystalline grains.

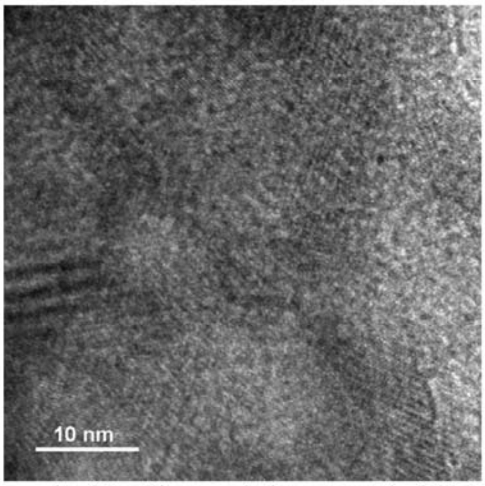

Fig. 9. Typical TEM micrograph of **2x**. The sample is composed of $MgIn_2S_4$ nanocrystals randomly oriented.

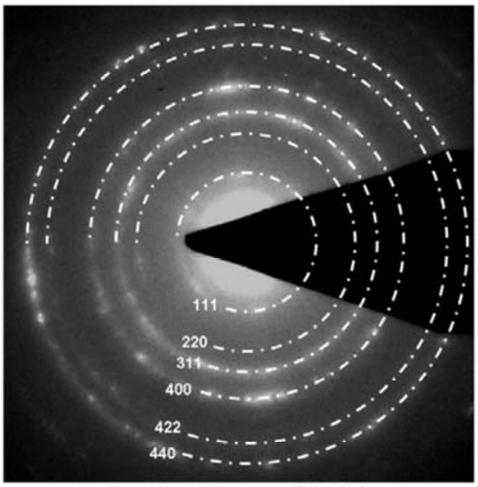

Fig. 10. Electron diffraction pattern of a selected area of **2x**. The observed rings can be indexed with the cubic structure of $MgIn_2S_4$.

Table 4
d-values in the ED pattern of sample **2x** [Å]

2x	$MgIn_2S_4$	hkl
6.2	6.17	(111)
3.88	3.78	(220)
3.27	3.22	(311)
2.69	2.67	(400)
2.14	2.18	(422)
1.9	1.88	(440)

5. Conclusions

A zero- (compound **1**) and a one-dimensional (compound **2**) thioindate have been prepared under solvothermal conditions. Compound **1** consists of isolated complexes linked via H-bonding interactions and represents the first example for a cationic thioindate. The structure of compound **2** contains linear $\{[InS_2]^-\}_\infty$ chains, charge compensated by $[Mg(en)_3]^{2+}$ complexes. Like in compound **1** an extended hydrogen bond network is observed to form a three-dimensional S···H connected network. We note that examples of thiometallates with complexes of earth-alkaline metal complexes are rare and was only reported for a thioantimonate(III) compound [33]. The optical band-gaps of **1** and **2** are very similar demonstrating the small influence of the charge compensating counterparts. Therefore, it is most likely that the absorption is due to electronic transitions between In based and S atom based atomic levels. The thermal reactivity of the two compounds is complex and totally different. For **1** the thermal decomposition is not finished at 500 °C whereas for **2** no weight loss is observed above about 400 °C until the final temperature of 500 °C. During the thermal decomposition reactions of **1** the cubic modification α-In_2S_3 is formed despite the starting In:S ratio of 1:1. The thermal decomposition product of compound 2 was identified as nanocrystalline $MgIn_2S_4$.

Acknowledgements

The authors acknowledge the support of Conacyt and DAAD.

Submitted to J. Solid State Chem. 28.Apr.2010

References

[1] P. Feng, X. Bu, N. Zheng, Acc. Chem. Res. 38 (2005) 293.
[2] N. Zheng, X. Bu, P. Feng, Angew. Chem. 116 (2004) 4857.
[3] Q. Zhang, X. Bu, L. Han, P. Feng, Inorg. Chem. 45 (2006) 6684.
[4] N. Zheng, X. Bu, H. Lu, L. Chen, P. Feng, J. Am. Chem. Soc. 127 (2005) 14990.
[5] C.L. Cahill, B. Gugliotta, J.B. Parise, Chem. Commun. (1998) 1715.
[6] C. Wang, X. Bu, N. Zheng, P. Feng, Angew. Chem. Int. Ed. 41 (2002) 1959.
[7] P. Vaqueiro, J. Solid State Chem. 179 (2005) 302.
[8] J. Zhou, G.Q. Bian, Y. Zhang, Q.Y. Zhu, C.Y. Li, J. Dai, Inorg. Chem. 46/16 (2007) 6347.
[9] C.Y. Li, J. Zhou, Y. Zhang, Z.X. Lei, G.Q. Bian, J. Dai, Z. Anorg. Allg. Chem. 635 (2009) 151.
[10] T.T. John, M. Mathew, C.S. Kartha, K.P. Vijayakumar, T. Abe, Y. Kashiwaba, Sol. Energy Mater. Sol. Cells 89 (2005) 27.
[11] N. Kamoun, S. Belgacem, M. Amlouk, R. Bennaceur, J. Bonnet, F. Touhari, M. Nouaoura, L. Lassabatere, J. Appl. Phys. 89/5 (2001) 2766.
[12] S.H. Choe, T.H. Bang, N.O. Kim, H.G. Kim, C.I. Lee, M.S. Jin, S.K. Oh, W.T. Kim, Semicond. Sci. Technol. 16 (2001) 98.
[13] D.K. Nagesha, X. Liang, A.A. Mamedov, G. Gainer, M.A. Eastman, M. Giersig, J.J. Song, T. Ni, N.A. Kotov, J. Phys. Chem. B 105 (2001) 7490.
[14] N. Barreau, J.C. Bernède, C. Deudon, L. Brohan, S. Marsillac, J. Cryst. Growth 241 (2002) 4.
[15] N. Barreau, C. Deudon, A. Lafond, S. Gall, J. Kessler, Sol. Energy Mater. Sol. Cells 90 (2006) 1840.
[16] N. Barreau, Sol. Energy 83 (2009) 363.
[17] Y. Xing, H. Zhang, S. Song, J. Feng, Y. Lei, L. Zhao, M. Li, Chem. Commun. (2008) 1476.
[18] Y. He, D. Li, G. Xiao, W. Chen, Y. Chen, M. Sun, H. Huang, X. Fu, J. Phys. Chem. C 113 (2009) 5254.
[19] Y. Xiong, Y. Xie, G. Du, X. Tian, J. Mater. Chem. 12 (2002) 98.
[20] X. Cao, L. Gu, L. Zhuge, W. Qian, C. Zhao, X. Lan, W. Sheng, D. Yao, Colloids and Surfaces A: Physicochem. Eng. Aspects 297 (2007) 183.
[21] D.P. Dutta, G. Sharma, A.K. Tyagi, S.K. Kulshreshtha, Mater. Sci. Eng. B 138 (2007) 60.
[22] H.X. Bai, L.X. Zhang, Y.C. Zhang, Mater. Lett. 63 (2009) 823.
[23] W. Chen, J.O. Bovin, A.G. Joly, S. Wang, F. Su, G. Li, J. Phys. Chem. B 108 (2004) 11927.
[24] K.H. Park, K. Jang, S.U. Son, Angew. Chem. 118 (2006) 4724.
[25] G.M. Sheldrick, Acta Crystallogr. A 64 (2008) 112.
[26] E. Quiroga-González, C. Näther, W. Bensch, Solid State Sci. (2010).
[27] D. Pitzschke, W. Bensch, Angew. Chem. 115 (2003) 4525.
[28] S. Abram, C. Maichle-Mossmer, U. Abram, Polyhedron 17 (1998) 131.
[29] D.L. Reger, P.S. Coan, Inorg. Chem. 34 (1995) 6226.
[30] D. Pitzschke, C. Näther, W. Bensch, Solid State Sci. 4 (2002) 1167.
[31] E. Zintl, K. Loosen, Z. Phys. Chem. 174 (1935) 301.
[32] S.S. Dhingra, R.C. Haushalter, Chem. Mater. 6 (1994) 2376.
[33] E. Quiroga-González, C. Näther, W. Bensch, Z. Naturforsch. 64b (2009) 1312.
[34] D. Gal, Y. Mastai, G. Hodes, J. Appl. Phys. 86/10 (1999) 37.
[35] C. Adenis, J. Olivier-Fourcade, J.C. Jumas, E. Philippot, Rev. Chim. Min. 24 (1987) 10.
[36] G.A. Steigmann, H.H. Sutherland, J. Goodyear, Acta Crystallogr. 19 (1965) 967.
[37] R. Diehl, R. Nitsche, J. Cryst. Growth 28 (1975) 306.
[38] N. Revathi, P. Prathap, K.T. Ramakrishna Reddy, Appl. Surf. Sci. 254 (2008) 5291.
[39] R. Bayón, J. Herrero, Appl. Surf. Sci. 158 (2000) 49.
[40] H. Hahn, W. Klingler, Z. Anorg. Allg. Chem. 263/4 (1950) 177.

3.2.

Submitted to J. Solid State Sci. 28.Apr.2010

In-$CuInS_2$ nanocomposite film prepared by Pulsed Laser Deposition using a single source precursor

*Quiroga-González Enrique,[a] Kienle Lorenz,[b] Duppel Viola,[c] Lee Doh-Kwon,[d] Janek Jürgen[d] and Bensch Wolfgang[a]**

[a]Institute for Inorganic Chemistry of the University of Kiel, Max-Eyth-Str. 2, 24118 Kiel, Germany.
[b]Institute of Material Science of the University of Kiel, Kaiserstr. 2, 24143 Kiel, Germany.
[c]Max Planck Institue for Solid State Research, Heisenbergstr. 1, 70569 Stuttgart, Germany.
[d]Institute for Physical Chemistry of the University of Giessen, Heinrich-Buff-Ring 58, 35392 Giessen,Germany.

*wbensch@ac.uni-kiel.de
Tel.: +49 431 8802094

Abstract

An In-$CuInS_2$ nanocomposite film has been prepared by Pulsed Laser Deposition applying a single source precursor. X-ray powder diffraction, Raman spectroscopy and transmission electron microscopy observations evidence that the film consists of nanocrystals of elemental In and chalcopyrite type $CuInS_2$ with sizes of 36 and 17 nm respectively. A detailed analysis of the electrical performance of the film suggests that the nano-particles are in Ohmic contact and that the resistivity is mainly caused by the $CuInS_2$ nanocrystals which are less conducting than the pure In metal. Irradiation of the film with light shows a photoconductive effect mainly with wavelengths larger than 515 nm and smaller than 850 nm.

Keywords: In-$CuInS_2$; nanocomposite film; single source precursor; pulsed laser deposition; electrical properties; photoconductivity

1. Introduction

$CuInS_2$ crystallizing in the chalcopyrite structure type is a material that has been extensively studied due to its good photoelectric properties [1, 2]. It has a direct band-gap of around 1.5 eV being in the optimum range for solar energy conversion [3], and can be prepared as both n- and p-type conducting material. Despite many efforts the energy conversion efficiencies of solar cells prepared with this material have so far been limited to around 12% due to the difficulties to prepare films with very high quality [4, 5]. Based on the pioneering work by Grätzel et al., Heeger et al. and others [6-10] new solar cell designs based on nanometre scale blends or so-called interpenetrating systems have been investigated. In many cases such nanosized or nanostructured cells work with dye-electrolyte couples or organic materials. The disadvantages of these cells are the risk of leakage and degradation. Therefore, there is a need of pure inorganic materials for such nanostructured solar cells and one approach is the usage of inorganic nanoclusters together with $CuInS_2$. For example, nanocomposite films of TiO_2 and $CuInS_2$ have been prepared by chemical spray deposition to produce a nanocomposite 3D solar cell. The TiO_2 nanoparticles reduce the migration distance of the minority carriers during photoconduction and in that way also the recombination rate resulting in an improvement of the efficiency [11, 12]. The performance of such nanocomposite solar cells is strongly influenced by several parameters like buffer layer thickness or morphology of the TiO_2 nanoparticles [12]. Despite some promising results on this kind of nanocomposites, they have not been much explored, even when there are other good candidates to form nanoclusters in $CuInS_2$.

Very recently it was demonstrated that In metal deposited on $CuInS_2$ films shows the lowest specific contact resistivity which is of great importance for solar device properties [13]. On the other hand, tandems of nanometric layers of metals with semiconductors exhibit interesting photoconductive properties with ballistic transport of photo-excited carriers through the metal layers [8, 14]. These observations encouraged us to synthesize nanocomposite films containing $CuInS_2$ and In nanoparticles. Our main aim at the beginning of investigations is only the preparation and characterization of the films and to test their photoelectric properties. For this purpose a single source inorganic-organic precursor was used, since in this state the elements are mixed on atomic level. The precursor material $Cu_{2.1(1)}In_{17.9(1)}S_{33}(C_{13}H_{28}N_2)_5$ was selected because it contains only Cu, In and S besides the organic molecules. Furthermore, the In:Cu ratio is high increasing the possibility of deposition of elemental In besides a Cu-In-S phase. In addition, the present investigation should show whether such a compound composed of large inorganic clusters is suitable as a single source precursor. The selected deposition method was PLD where the fast ablation of the target material by the excimer laser minimizes the preferential vaporization of the different elements, allowing the production of homogeneous films in a broad range of thicknesses [15].

During the deposition process of the film $CuInS_2$ and In nanoparticles regularly distributed were formed. The structural, optical and photoelectric properties of this film are presented and discussed. The film was analyzed by Raman spectroscopy, X-ray diffraction (XRD), high resolution transmission electron microscopy (HRTEM), UV-vis spectroscopy and by means of I-V (current-voltage) measurements.

2. Experimental details

2.1. Preparation of the precursor

An hybrid (organic-inorganic) Cu-In open framework thiometalate with composition $Cu_{2.1(1)}In_{17.9(1)}S_{33}(C_{13}H_{28}N_2)_5$ (**1**), isostructural to the known framework with composition $Cd_4In_{16}S_{33}(C_{13}H_{28}N_2)_5$ [16] was prepared. Note that the estimated variation of the composition of the compound is based on the average of several analyses performed on different batches. For the synthesis, 0.7 mmol of CuS, 4.2 mmol of In, 6.9 mmol of S and 13.46 mmol of 4, 4'-trimethylenedipiperidine were used. The precursors were mixed with 2.5 mL of water and 2.5 mL of ethyleneglycol in a 35 mL Teflon-lined stainless steel autoclave and stirred for 15 min. The sealed vessel was then heated at 190 °C for 5 days. After cooling down to room temperature, the product was filtered off, and washed with water, ethanol and acetone. Prismatic yellow crystals in a yield larger than 90% based on In were obtained. Details of the structure and properties of the compound $Cu_{2.1(1)}In_{17.9(1)}S_{33}(C_{13}H_{28}N_2)_5$ will be published elsewhere.

The product was then crushed and the obtained powder was thermally treated in Argon atmosphere at 330 °C for 2.5 hr. After decomposition of the precursor material elemental analysis gave 15 weight% of C. The black amorphous product was finally pressed isostatically to form a pellet being 1.5 cm long and 1 cm in diameter. This pellet was used as the single source precursor for the deposition of the film.

2.2. Deposition of the film

The film was deposited by pulsed laser deposition (PLD) on a (111) Si substrate with resistivity $100 \cdot 10^3$ Ωcm heated at 500° C, under vacuum. We used a vacuum chamber (minimum pressure $p = 5 \cdot 10^{-3}$ Pa) equipped with a turbomolecular pump and a cold trap (liquid nitrogen) to avoid a sulfur contamination of the pumping system. A Kr-F excimer laser (λ = 248 nm, Compex 201, Lambda-Physik, Göttingen, Germany) was used for the ablation process. For the deposition, the optimized conditions for the preparation of good quality films of other chalcogenide composites were used [15, 17]. We chose pulse energy of 160 mJ, corresponding to approximately 4 J/cm^2. The repetition rate was adjusted to 5 Hz, the pressure of the background gas was fixed to 1 Pa, and the substrate temperature was 500 °C. Argon was used as the background gas. The distance between the target and the substrate was adjusted to 40 mm. The thickness of the films was estimated as approx. 3 μm.

2.3. Characterization methods

For Transmission Electron Microscopy (TEM) investigations, the film was scratched from the substrate and the resulting micro-particulates were transferred to aluminium grids which were fixed in a side-entry, double-tilt holder with the tilting limited to a maximum of ± 25° in two directions. High resolution transmission electron microscopy (HRTEM) was performed with a Philips CM30ST (300 kV, LaB_6 cathode). EDX (energy dispersive X-ray spectroscopy) was performed in the scanning and nanoprobe mode of the CM30ST instrument using a Si/Li-EDX detector (Noran, Vantage System).

XRD (X-ray Diffractometry) measurements were performed with a PANalytical X'PERT-PRO diffractometer in reflection mode using Cu-Kα radiation. The diffractogram was collected from 2θ = 31 to 58° to avoid the reflections from the Si substrate. The Raman spectrum of the film was measured with a HORIBA Jobin Yvon Xplora microscope, using 638 nm laser excitation, a 100x Olympus objective with 0.9 numerical aperture, and an 1800 groove/mm grating with a spectral resolution of about 1.2 cm^{-1}. Approximately 10 mW laser light was focused on the sample in order to avoid artefacts in the measurements due to heating. Measurements of optical reflection were carried with a Cary 5000 UV-Vis-NIR spectrophotometer in the range of 200-900 nm, using a halogen lamp as light source and a photomultiplier as detector. The I-V characteristics of the film were measured with a source-measure-unit Keithley 236 in sweep mode under darkness and under illumination. A 250 Watt Long Life Metal-Halogenide lamp was used as light source, providing a light power of 4 mW/cm^2 to the surface of the sample. A two probe arrangement was used for the measurements with every probe serving as a current and as a voltage probe, contacting directly the surface of the film. The diameter of the probes was around 0.2 mm. The distance between probes for the measurement was either 0.5 or 2.5 mm.

3. Results and discussion

3.1. Structural and chemical characterization

Microprobe EDX analyses performed in the scanning electron microscope show the atomic ratio of Cu : In : S as expected from the precursor. However, according to nanoprobe EDX measurements performed in TEM, the ratio of the constituting elements Cu, In, S varies strongly and unsystematically at the nanoscale. Hence, nanoprobe analyses were undertaken to figure out the reason for the large compositional fluctuations. In the TEM images displayed in Fig. 1a and 1b the different numbered spots indicate the areas where EDX analyses were carried out. The image Fig. 1a was recorded in an In-rich area whereas the picture shown in Fig. 1b was taken in a S rich region. The results of the analyses summarized in Table 1 clearly evidence that in the In-richest regions only small amounts of S and Cu are present. The large compositional variation is caused by the nanodisperse distribution of the components well seen in the TEM micrographs, e. g. CuInS$_2$, In and amorphous S. The latter together with remaining carbon might represent the amorphous areas between the nanocrystals. No evidence for secondary crystalline phases in the film were obtained as described below.

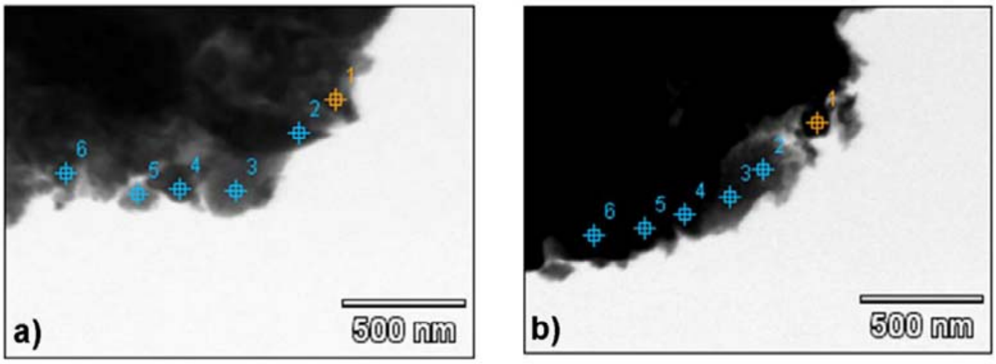

Fig. 1. TEM micrographs of a) an In-rich zone and b) a S-rich zone. EDX analyses were done in the indicated points and the results are summarized in Table 1.

Submitted to J. Solid State Sci. 28.Apr.2010

Table 1
EDX analyses in a) an In-rich zone and b) a S-rich zone, which are illustrated in Fig. 1 a) and b)

Zone	*Point*	*S-K*	*Cu-K*	*In-L*
a)	1	25.8	9.4	64.8
	2	6.0	2.0	92.0
	3	35.3	13.8	51.0
	4	10.3	4.0	85.7
	5	34.2	9.9	56.0
	6	9.3	2.8	87.9
b)	1	29.3	4.6	66.2
	2	47.7	8.0	44.3
	3	51.8	8.2	40.0
	4	51.4	8.4	40.2
	5	40.1	5.8	54.0
	6	50.5	7.4	42.0

A part of the Raman spectrum of the film is shown in Fig. 2. The Raman peak centered at 310 cm^{-1} is blue-shifted with respect to the position of the A$_1$ phonon mode of bulk CuInS$_2$ positioned at around 290 cm^{-1} [18]. This effect has been reported for In-rich CuInS$_2$ films [19]. In the present film the shift of the mode is due to the nanosized In particles found together with CuInS$_2$. The width of the peak is an indication of the nanocrystalline nature of the material, and the asymmetry is caused by the size distribution of the nanocrystals, as in the case of nanocrystalline Si [20]. The presence of CuIn$_5$S$_8$ which is a common byproduct in CuInS$_2$ films [21] could be discarded since its Raman line is located at 362 cm^{-1} [22], exactly at the edge of the Raman peak centered at 310 cm^{-1}. On the other hand, CuInS$_2$ with CuAu structure type presents a Raman peak at 305 cm^{-1} [5] which is very close to the experimentally determined position of 310 cm^{-1}. Nevertheless this structure type of CuInS$_2$ is not in accordance with the XRD and electron diffraction (ED) patterns.

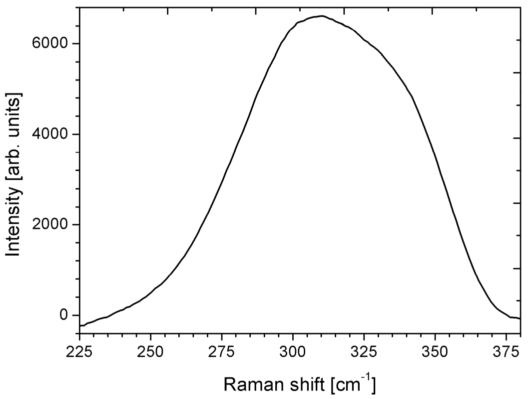

Fig. 2. Raman spectrum of the film. The peak centred at 310 cm^{-1} is due to the A$_1$ phonon mode of CuInS$_2$. The broadness of the peak indicates the nanocrystalline nature of the film.

The TEM bright-field image (Fig. 3a) shows an area containing CuInS$_2$ nanocrystals (nCs). The crystalline particles are enclosed in white lines in the figure, an as can be seen they are randomly oriented. Fourier transforms of different TEM micrographs were performed yielding patterns with the d-values of CuInS$_2$ with chalcopyrite structure. The nCs are uniformly distributed and are separated by amorphous regions (thinner than 1 nm), which contain carbon and possibly sulfur. The sizes of the nCs range between 13 and 20 nm. In Table 2 are compiled the *d*-values calculated from the ED pattern of Fig. 3b and those of bulk chalcopyrite CuInS$_2$ [23] and CuInS$_2$ with CuAu structure [24]. A comparison of the data clearly demonstrates that the $CuInS_2$ crystallites in the film have very similar lattice parameters like bulk $CuInS_2$ with the chalcopyrite structure type [23]. A further comparison with the *d*-values expected for the CuAu structure type of $CuInS_2$ [24] evidences the absence of this kind of structure type in the film material, especially because the observed *d*-value close to 0.32 nm is not present in the CuAu structure type. Therefore, the analysis of the ED pattern supports that the nCs are $CuInS_2$ with chalcopyrite structure and that the Raman peak at 310 cm^{-1} corresponds to the A_1 phonon mode of this material. This conclusion is further evidenced by the detailed analysis of the XRD pattern.

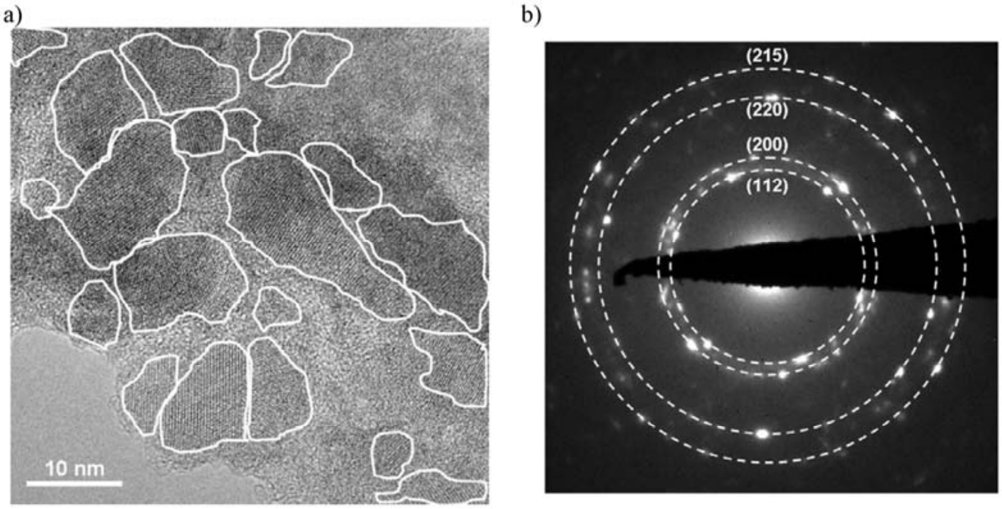

Fig. 3. a) TEM micrograph of a a region of the film containing $CuInS_2$. This material consists of randomly oriented nanocrystals (enclosed in white lines). b) Electron diffraction pattern measured in this region.

Table 2
d-values extracted from the electron diffraction pattern together with those of chalcopyrite and CuAu type $CuInS_2$.

d [nm] meas.	Planes $CuInS_2$ chalc.	d [nm] $CuInS_2$ chalc.	Planes $CuInS_2$ CuAu type	d [nm] $CuInS_2$ CuAu type
0.317	(112)	0.3157		
0.305	(103)	0.3037	(002)	0.3078
0.192	(220)	0.1938	(003)	0.2053
0.164	(215)	0.1658	(004)	0.1538

The XRD pattern of the film is displayed in Fig. 4. The most intense reflections located at 2θ = 32.9, 36.3, 39.2, 54.5 and 56.6°, correspond to the (101), (002), (110), (112) and (220) planes of elemental In [25]. The reflections are significantly broadened, which could be caused by strain and/or particle size effects. The particle size of the coherent scattering domains of the In clusters calculated with the Debye-Scherrer formula is about 36 nm using the (101) reflection (no correction was made for instrumental broadening). The two Bragg peaks located at 46.8 and 55.4° can be indexed with the (220) and (215) reflections of chalcopyrite $CuInS_2$ which were reported to occur at 46.84 and 55.36° 2θ [23]. Several intense reflections of $CuIn_5S_8$ like the (511/333) at 43.99 and the (440) at 48.13° 2θ are not seen in the pattern [26], highly suggesting the absence of this material in the film. Again, the full-width at half maximum was used to calculate the crystallite size and a value of 17 nm is obtained.

The crystallite sizes determined from the powder pattern are in good agreement with the sizes estimated from the TEM picture. The very broad feature in the pattern located around 51.2° 2θ cannot be explained by any Cu-In-S, In-S and/or Cu-S phase, and its origin is still not clear. Considering the areas of the most intense reflection peaks of In and $CuInS_2$ an approximated ratio of 7:1 of In:$CuInS_2$ is calculated, in good agreement with the expected ratio of 8:1.

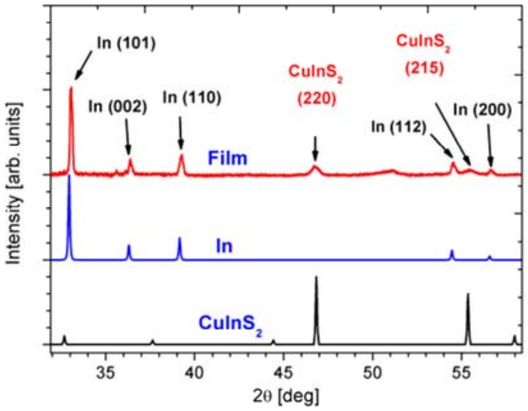

Fig. 4. X-ray powder pattern of the $CuInS_2$/In film. The most intense reflections originate from In nanoclusters. The broad Bragg peaks at 46.8 and 56.4° are due to nanocrystals of chalcopyrite $CuInS_2$.

3.2. Optical and photoelectrical characterization

From the optical reflectance measurements and considering zero transmission, the percentage of absorption is calculated with the simple relation

$$A = 100(1 - R) \tag{1}$$

with A being the percentage of absorption and R the reflectance. The optical absorption spectrum of the sample is shown in Fig. 5 and the inset of the figure displays the absorption spectrum from the Si substrate for comparison. In the considered energy range the absorption of the Si substrate decays monotonically with increasing energy, contrary to what is found for the sample. Despite the contribution of the substrate to the absorption spectrum, an absorption edge is evident in the plot caused by the material of the film. The absorption edge at around 1.46 eV is close to the optical band gap E_g of bulk $CuInS_2$ of 1.5 eV [2]. We note that the value for E_g reported in literature scatters between 1.4 and 1.77 eV depending on the synthesis conditions, Cu:In ratio, particle size, or post-synthesis treatments. $CuInS_2$ nanocrystals prepared by a solution-based method exhibit E_g values either smaller than 1.5 eV (1.47 eV) [27] or much larger (1.65 - 1.77 eV) [28]. It has been also reported that the value of E_g of $CuInS_2$ films could vary from 1.4 to 1.47 eV increasing the annealing temperature [29]. Such a large variation has been also observed for films changing the Cu:In ratio between 1.2 and 0.9 [30]. Some examples for the variation E_g depending on the synthesis method are 1.51 eV for films prepared by sulfuration of Cu/In stacks [31], 1.53 eV for crystalline powders prepared by a sintering method [32] and 1.4 eV for sprayed films [33]. The E_g value for $CuIn_5S_8$ is lower than the values for $CuInS_2$, commonly around 1.3 eV [34, 35].

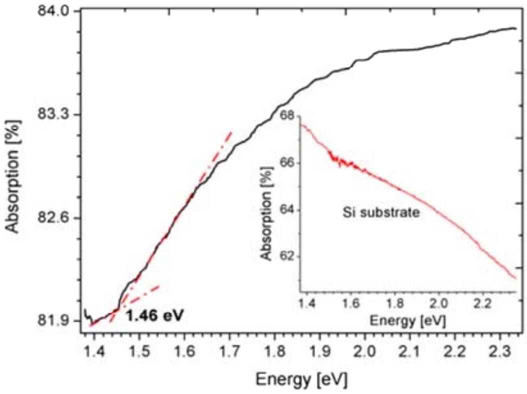

Fig. 5. Absorption spectrum of the film. The absorption edge is at around 1.46 eV. The absorption spectrum from the Si substrate is shown in the inset of the figure, for comparison.

The current-voltage (*I-V*) characteristics of the film under darkness and illumination are displayed in Fig. 6. The shape of both curves is typical for ohmic behavior, i.e. the contacts and the In nanoclusters in the film present a negligible electrical resistance [36], allowing the control of the current by the resistivity of $CuInS_2$. The photosensitivity $\Delta I/I_0$ with ΔI being the photocurrent and I_0 the dark current, both determined applying the same voltage, calculated from the curves yields 0.455. Examples of reported values of the photosensitivity of Cu-poor $CuInS_2$ are 0.1 for single crystals [2] and 1 for sprayed pyrolized films [37]. This parameter is not affected when a filter of 515 nm is used in front of the lamp. This result suggests that the film exhibits photoconductive effects mainly under light with wavelengths larger than 515 nm and smaller than 850 nm (1.46 eV, the band gap of the material). This photoresponse band is close to that of $CuInS_2$ films reported in other works [1].

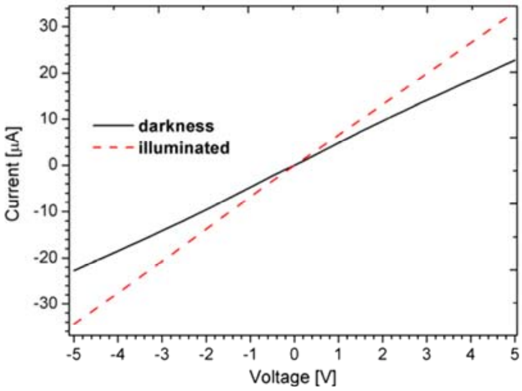

Fig. 6. *I-V* curves from the film under darkness and under illumination. The distance between contacts was 0.5 mm.

The resistance of the film, calculated from the *I-V* plot under darkness is 219.4 kΩ. This resistance (R_t) of the sample combines the contributions of the probe resistance (R_p), the contact resistance (R_c), spread resistance (R_{sp}) and the resistance of the film (R_s), as described in equation (2).

$$R_t = 2\,R_p + 2\,R_c + 2\,R_{sp} + R_s \qquad (2)$$

The values for R_p, R_c and R_{sp} are independent of the distance between the contacts, while R_s varies linearly with the contact distance. This dependence was checked by measuring the resistance with a distance between contacts 5 times larger (2.5 mm) yielding a value for R_t of 371.4 kΩ (R_{t1}). With this distance the value for R_s is supposed to be 5 times larger, and equation (1) can be rewritten as:

$$\mathrm{R}_{t1} = 2\,R_p + 2\,R_c + 2\,R_{sp} + 5\,R_s \qquad (3)$$

Submitted to J. Solid State Sci. 28.Apr.2010

Solving the system of equations (1) and (2) gives $R_s = 38$ kΩ. The rest of the resistance is due to the other contributions, but as the resistance R_p is around 5 Ω and $R_c << R_{sp}$ because the contact is ohmic, R_{sp} could be considered to be the major contribution for the resistance, and for a value $R_{sp} \approx 181.4$ kΩ is derived. From this value it is possible to estimate the resistivity. For semi-infinite thick films, the resistivity can be calculated with the relation [38]:

$$R_{sp} = \rho/4r \qquad (4)$$

where r is the radius of the probe. The estimated electrical resistivity using relation (4) amounts to $7.2 \cdot 10^3$ Ωcm, which is in the range of values reported for stoichiometric and In-rich $CuInS_2$ films (n-type films) [39, 40]. We want to mention that according to some reports the value of the resistivity may be overestimated by a factor that depends on the ratio r/th, with th being the thickness of the film [41]. In the present case an overestimation of the resistivity by up to two orders of magnitude cannot be excluded, and therefore the calculated value of the resistivity should be regarded as an approximation. It is also worthy to mention that a survey of resistivity data published in literature for $CuInS_2$ demonstrates that the data scatter over a relatively wide range. Important factors controlling the resistivity are the synthesis method, chemical composition and type of material, i.e., whether experiments were conducted on bulk or films. For instance, a n-type $CuInS_2$ film deposited on glass using thermal evaporation of suitable ingots in a high-vacuum chamber exhibits a resistivity of $5.5 \cdot 10^2$ Ωcm [42] which could vary up to three orders of magnitude varying the annealing temperature from 300 to 500°C [43]. A strong dependence of the electrical resistivity on the Cu:In ratio was observed for films deposited by spray pyrolysis [24] and other methods. By this technique In-rich $CuInS_2$ films composed of very small crystallites contain In_6S_7, In_2S_3 and $CuIn_5S_8$ as impurity phases. Such films show electrical resistivity values around 10^6 Ωcm. A significant drop of the resistivity to about 0.06 Ωcm occurs for Cu:In ratios around 0.9 – 1.2 where the impurity phases could not be detected in X-ray powder patterns, and additionally the material becomes p-type conducting (In poor) [24]. Using chemical bath deposition for the preparation of p-type $CuInS_2$ films yields 51 Ωcm after annealing of the film at 450 °C in a sulfur atmosphere [5]. For sputter deposited p-type films the electrical resistivity has been reported ranging from 10^{-1} to 10^1 Ωcm depending on the post-treatment of the as-deposited films [23]. Other groups have reported a change of n-type to p-type in sputtered films upon aging in air, having then a change in resistivity of $2\cdot 10^4$ to 10^{-1} Ωcm [44]. For stoichiometric polycrystalline $CuInS_2$ bulk material prepared under high-pressure high-temperature conditions the electrical resistivity is roughly 30 Ωcm [4]. On the other hand, highly densified and oriented stoichiometric $CuInS_2$ single-crystal fragments synthesized by sintering at 1050 °C have a resistivity of 50 Ωcm [45].

In the present film a larger value for the resistivity could be expected considering the large amount of defects due to the grain boundaries of the $CuInS_2$ nCs [39], and due to the presence of amorphous C at the interfaces. But it seems that In nanoclusters and the $CuInS_2$ particles have a reasonable good contact so that scattering phenomena of the carriers at the large number of interfaces is relatively low. Because the resistivity of In metal is much smaller than the resistivity of $CuInS_2$, the main contribution to the resistivity should be due to the $CuInS_2$ nanocrystals.

A temperature-dependent I-V study of the film was done to confirm the semiconducting behavior. For semiconductor materials it is well known that the conductivity σ varies exponentially with the temperature according to:

$$\sigma = \sigma_0 \exp \frac{-E_g}{2kT} \qquad (5)$$

where σ_0 is an overall constant that depends on the mobility, E_g is the band gap, k is the Boltzmann constant and T is the Temperature in K. When plotting ln(σ) versus 1/T the obtained curve is linear. Changes of the slope occur if impurities are present in the material. These impurities need less energy to be activated.

In Fig. 7 a plot of ln(conductance) of the film versus temperature is presented. As can be seen, the curve is linear from 300 to 230 K. In this region the conductivity is dominated by band-to-band transitions. Below 230 K the slope changes and below this temperature the impurities start to be important for the electrical conduction. The transition at 230 K is in good agreement with the value of

250 K reported for n-type $CuInS_2$ [2], and such a transition was also observed in the material with p-type conductivity [46, 47].

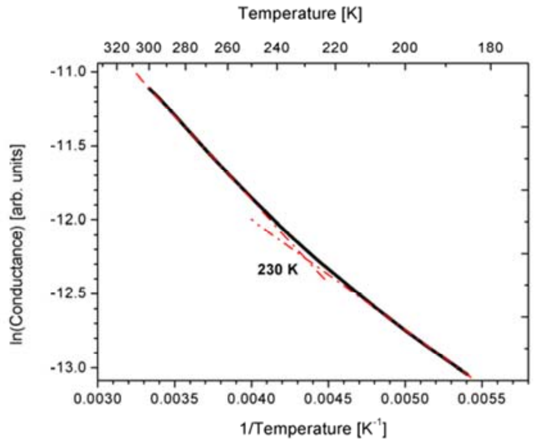

Fig. 7. Plot of ln(conductance) of the film *versus* 1/Temperature. There is a transition of the slope around 230 K. Above this temperature the conductivity is dominated by band-to band transitions. Below 230 K the impurities of the material start to be important for the electrical conduction.

4. Conclusions

A nanocomposite film consisting of nanocrystals (nCs) of $CuInS_2$ with chalcopyrite structure and of In nanoclusters was prepared by PLD using a single source precursor. The precursor was synthesized using a two-step approach. A Cu-In-S-containing thiometalate was prepared solvothermally in the first step followed by controlled thermal decomposition. According to the TEM and X-ray diffraction experiments the size of the $CuInS_2$ crystallites in the film is around 17 nm. The X-ray powder pattern indicates that the In particles are slightly larger than those of $CuInS_2$. An interesting aspect of the synthetic approach is the occurrence of $CuInS_2$ and elemental In despite the large deviation of the Cu:In ratio from 1:1 in the precursor material. In several contributions it was demonstrated that small deviations from the stoichiometric 1:1 ratio for Cu:In leads to the formation of different sulfides as impurity phases thus significantly changing the electrical characteristics of the films. At the moment we have no simple explanation for our experimental finding.

Despite the nanoscale crystals and the large number of defects and grain boundaries the electrical and photoelectrical properties of the film are comparable with $CuInS_2$ films prepared with different synthesis methods and without In nanocrystals. Especially the electrical resistivity is in the same order reported in literature for high quality $CuInS_2$ films. This result is somewhat surprising and one possible reason for the relatively good conductivity is the presence of In nanoparticles being in good contact with the $CuInS_2$ crystallites (the scattering at the particle interfaces is low). Additionally, as the resistivity of In metal is much smaller than the one of $CuInS_2$, the main contribution to the resistivity should be due to the $CuInS_2$ nanocrystals. Further experiments are under way for the synthesis and characterization of thin films using different precursors and applying the PLD technique.

Acknowledgement

The authors appreciate the support of CONACyT and DAAD. The TEM experiments were enabled by Prof. Dr. Dr. h.c. mult. A. Simon at the Max Planck Institute for Solid State Research.

References

[1] Kazmerski L.L., Shieh C.C., Thin Solid Films 41 (1977) 35.

[2] Cybulski D., Opanowicz A., Cryst. Res. Technol. 32/6 (1997) 813.

[3] Bucher E., Appl. Phys. 17 (1978) 1.

[4] Yoshino K., Nomoto K., Kinoshita A., Ikari T., Akaki Y., Yoshitake T., J. Mater. Sci.: Mater. Electron. 19 (2008) 301.

[5] Cui F., Wang L., Xi Z., Sun Y., Yang D., J. Mater. Sci.: Mater. Electron. 20 (2009) 609.

[6] O'Regan B., Grätzel M., Nature 353 (1991) 737.

[7] Pei Q., Yu G., Zhang C., Yang Y., Heeger A.J., Science 270 (1995) 719.

[8] McFarland E.W., Tang J., Nature 421 (2003) 616.

[9] Bach U., Lupo D., Comte P., Moser J.E., Weissörtel F., Salbeck J., Spreitzer H., Grätzel M., Nature 395 (1998) 583.

[10] Wang P., Zakeeruddin S.M., Moser J.E., Nazeeruddin M.K., Sekiguchi T., Grätzel M., Nat. Mater. 2 (2003) 402.

[11] Nanu M., Schoonman J., Goosens A., Nano lett. 5/9 (2005) 1716.

[12] O'Hayre R., Nanu M., Schoonman J., Goosens A., Nanotechnology 18 (2007) 055702.

[13] Peza-Tapia J.M., Morales-Acevedo A., Ortega-López M., Sol. Energy Mater. Sol. Cells 93 (2009) 544.

[14] Willens R.H., Appl. Phys. Lett. 49/11 (1986) 663.

[15] Mogwitz B., Korte C., Kienle L., von Kreutzbruck M., Janek J., J. Appl. Phys. 101 (2007) 043510.

[16] Wang C., Li Y., Bu X., Zheng N., Zivkovic O., Yang C.S., Feng P., J. Am. Chem. Soc. 123 (2001) 11506.

[17] Janek J., Mogwitz B., Beck G., Von Kreutzbruck M., Kienle L., Korte C., Prog. Solid State Chem. 32 (2004) 179.

[18] Bacewicz R., Gebicki W., Filipowicz J., J. Phys.: Condens. Matter. 6 (1994) L777.

[19] Morell G., Katiyar R.S., Weisz S.Z., Walter T., Schock H.W., Balberg I., Appl. Phys. Lett. 69 (1996) 987.

[20] Quiroga E., Bensch W., Aceves M., Yu Z., Savy J.P., Haeckel M., Lechner A., 10th International Conference on Ultimate Integration of Silicon (ULIS 2009), IEEE, Aachen, Germany, 2009, p. 349.

[21] Winkler M., Tober O., Penndorf J., Szulzewsky K., Röser D., Lippold G., Otte K., Thin Solid Films 361-362 (2000) 273.

[22] Gasanly N.M., Magomedov A.Z., Melnik N.N., Salamov B.G., Phys. Stat. Sol. B 177 (1993) K31.

[23] Hwang H.L., Cheng C.L., Liu L.M., Liu Y.C., Sun C.Y., Thin Solid Films 67 (1980) 83.

[24] Guillén C., Herrero J., Gutiérrez M.T., Briones F., Thin Solid Films 480-481 (2005) 19.

[25] Moshopoulou E.G., Ibberson R.M., Serrao J.L., Thompson J.D., Fisk Z., Acta Crystallographica B 62 (2006) 173.

[26] Gastaldi L., Scaramuzza L., Acta Cryst. B36 (1980) 2751.

[27] Norako M.E., Franzman M.A., Brutchey R.L., Chem. Mater. 21 (2009) 4299.

[28] Nose K., Soma Y., Omata T., Otsuka-Yao-Matsuo, Chem. Mater. 21 (2009) 2607.

[29] Ben Rabeh M., Kanzari M., Rezing B., Thin Solid Films 515 (2007) 5943.

[30] Peng S., Cheng F., Liang J., Tao Z., J. Chen, J. Alloys Comp. 481 (2009) 786.

[31] Abou-Ras D., Jahn U., Nichterwitz M., Unold T., Klaer J., Schock H.W., J. Appl. Phys. 107 (2010) 014311.

[32] Wanga Z., Mo X., Li J., Sun D., Chen G., J. Alloys Comp. 487 (2009) L1.

[33] Sebastian T., Gopinath M., Sudha Kartha C., Vijayakumar K.P., Abe M., Kashiwaba Y., Sol. Energy 83 (2009) 1683.

[34] Qasrawi A.F., Gasanly N.M., Cryst. Res. Technol. 38/12 (2003) 1063.

[35] Qasrawi A.F., Gasanly N.M., Cryst. Res. Technol. 36 (2001) 1399.

[36] Bube R.H., Photoelectronic properties of semiconductors, Cambridge University Press, Cambridge, 1992.

[37] John T.T., Sebastian T., Sudha Kartha C., Vijayakumar K.P., Abe M., Kashiwaba Y., Physica B 388 (2007) 1.

[38] Schroder D.K., Semiconductor material and device characterization, John Wiley & Sons, Inc., New York, 1998.

[39] Peza-Tapia J.M., Morales-Acevedo A., Ortega-López M., 4th International Conference on Electrical and Electronics Engineering (ICEEE), IEEE, Mexico City, 2007, p. 326.

[40] Park G.C., Chung H.D., Kim C.D., Park H.R., Jeong W.J., Kim J.U., Gu H.B., Lee K.S., Sol. Energy Mater. Sol. Cells 49 (1997) 365.

[41] Read M.B., Lang J.H., Slocum A.H., 55th IEEE Holm Conference on Electrical Contacts, IEEE, Vancouver, Canada, 2009, p. 303.

[42] Ben Rabeh M., Chaglabou N., Kanzari M., Chalcogenide Lett. 6 (2009) 83.

[43] Akaki Y., Komaki H., Yoshino K., Ikari T., J. Vac. Sci. Technol. A 20 (2002) 1486.

[44] He Y.B., Krämer T., Österreicher I., Polity A., Meyer B.K., Hardt M., Semicond. Sci. Technol. 20 (2005) 685.

[45] Yamamoto N., Ogihara J., Horinaka H., Jpn. J. Appl. Phys. 29 (1990) 650.

[46] Mobarak M., Shaban H.T., Elhady A.F., Mater. Chem. Phys. 109 (2008) 287.

[47] Amara A., Rezaiki W., Ferdi A., Hendaoui A., Drici A., Guerioune M., Bernède J.C., Morsli M., Sol. Energy Mater. Sol. Cells 91 (2007) 1916.

3.3.
ARTICLE

Submitted to Z. Anorg. Allg. Chem. 11.Mar.2010

DOI: 10.1002/zaac.200((will be filled in by the editorial staff))

Transmission Electron Microscopy study of Cu-containing spinel-type In_2S_3 nanocrystals prepared by rapid pyrolysis of a single molecular precursor

E. Quiroga-González,[a] W. Bensch,[a] V. Duppel,[b] L. Kienle[c]*

Keywords: Indium sulfide; nanocrystals; pyrolysis; single precursor; microscopy

Cu-containing spinel-type In_2S_3 nanocrystals have been prepared by rapid pyrolysis (RP) from a single source inorganic-organic hybrid molecular precursor with an initial Cu:In:S ratio of 1:9:16.5. The precursor was synthesized in a one-step hydrothermal reaction with high yield. After a treatment of the precursor for 10 s at 1000 °C a powdered material was obtained. The X-ray powder pattern exhibits broad reflections indicative for the spinel-type and crystallites in the nanometer range, however, the positions of the reflections match well with different compounds of the In-S and Cu-In-S systems. High resolution transmission electron microscopy (HRTEM) studies in connection with EDX analyses evidence the presence of cubic spinel-type Cu-containing In_2S_3. Two such In_2S_3 phases coexist with one being Cu-poor and the other having a larger Cu content. The coexistence of these two compounds is reflected by the Raman and UV-vis spectra.

1. Introduction

Semiconducting materials at the nanoscale are of great interest because they offer a rich palette of optical, electronic, and catalytic properties which can be tuned by particles' size and shape [1, 2]. Such scenario is well known for In_2S_3 nanoparticles [2]. This compound is polymorphic and can crystallize either in the α, β or γ structures [3-6]. The structures of the α and β phases can be described as spinel-like. But contrary to a normal spinel structure, one third of the tetrahedral sites remains empty, which leads to the quasi-quaternary compound with formula: $[In_2]_O[In_{2/3}h_{1/3}]_TS_4$ (h represents the vacant sites and T and O represent the tetrahedral and octahedral sites, respectively) [5]. The α modification is stable above 420 °C and has a cubic structure (space group Fd-3m, a_α = 1.077 nm). Below that temperature the material transforms into the tetragonal β-In_2S_3 due to the ordering of the vacancies. The cell parameters of this structure are $c_\beta = 3c_\alpha$ = 3.2322 nm, and $a_\beta = a_\alpha/(2)^{1/2}$ = 0.7619 nm (space group $I4_1$/amd). Nevertheless if In_2S_3 is prepared with an excess of In larger than 0.5 % the α modification is stable even at room temperature [6]. Above 754 °C all In atoms change into octahedral interstices of the close-packed sulfur sub-lattice, forming the trigonal γ-In_2S_3 [3, 4]. This structural modification is stable at room temperature if about 5 at % of the elements As or Sb are incorporated in the structure.

In_2S_3 may replace the toxic CdS buffer layer in high efficient solar cells [7-13]. This material is also of importance due to its photoluminescent (PL) properties, which are enhanced for crystallites with reduced sizes [14]. Nanoparticles of In_2S_3 could emit green light produced by band to band transitions [14-16], blue light coming from deep trap states [2] and orange light due to interstitial In defects [16]. The defect chemistry of In_2S_3 is of importance for the PL properties as was shown in [17]. Additionally other applications like degradation of organic pollutants under visible light irradiation have been reported [18]. Nanocrystalline cubic and tetragonal In_2S_3 have been prepared applying a wide range of methods like hydrothermal synthesis [19], solution reactions [1, 16], pyrolysis of molecular compounds [20], among others leading to particles exhibiting a variety of morphologies.

The crystal structure of α- or β-In_2S_3 presents a large amount of vacancies that can serve as host for a number of metal ions to form semiconducting and/or magnetic materials [21]. This structural and chemical speciality distinguishes it from II-VI compounds, which tend to expel guest ions [1]. Lately it has been reported that the effective optical band gap of this material decreases upon partial diffusion of Cu in it, increasing then the density of states towards the near infrared [5]. This example of band engineering allows the use of this material as active layer in solar cells and photodetectors. Actually in the recent time a high-sensitivity (photon-to-electron gain > 40), high-speed (video-frame-rate-compatible) photoconductive photodetector based on Cu-doped In_2S_3 has been reported [22]. The material was synthesized via a solution route applying butylamine and oleylamine as solvents. Another possible approach for the preparation of such nanocrystalline compounds is the use of single molecular precursors [20, 23, 24], nevertheless there are no reports of Cu-doped In_2S_3 nanocrystals fabricated in this way. The search for suitable precursors and their applications is a topic of intense actual research because the elements of interest are homogeneously distributed in the precursor. A variety of fabrication methods that use molecular single sources have been studied, ranging from Chemical Vapor Deposition (CVD) [23] to simple pyrolysis [20] or spray pyrolysis [24]. In these studies compounds like metallic thiocarboxylates, or other Indium complexes like $[MeIn(SCH_2CH_2S)]_n$ were applied. An interesting class of molecular precursors could also be the In-containing inorganic-organic hybrid open framework compounds reported recently [25, 26]; these materials are promising candidates for the synthesis of nano-sized products because they are composed of clusters with nano-dimensions and they exhibit a variable chemical composition concerning the metal types and ratios. Furthermore,

---

* Corresponding Author
E-mail: lk@tf.uni-kiel.de
Tel: +49(431)8806196
[a] Institute for Inorganic Chemistry of the University of Kiel. Max-Eyth Str. 2. 24118 Kiel, Germany.
[b] Max Planck Institute for Solid State Research. Heisenbergstraße 1, 70569 Stuttgart, Germany
[c] Institute for Material Science of the University of Kiel. Kaiserstr. 2, D-24143 Kiel, Germany

the samples can be prepared by a simple one-pot method and they are obtained in high yields. To the best of our knowledge the potential of these materials as single source precursors for the preparation of nanostructures was not explored until now.

Here we report the first results of the preparation of Cu-containing In_2S_3 nanocrystals obtained by heating the single source precursor $Cu_2In_{18}S_{33}(C_{13}H_{28}N_2)_5(H_2O)_x$ (x ~ 17) containing Cu and In with a 1:9 ratio. The products were synthesized by heating the starting material for only a few seconds (rapid pyrolysis –RP). Such a low Cu : In ratio enhances the chance for doping of In_2S_3 rather than for formation of a stoichiometric Cu-In-S compound. The method presented here is easy and fast with no elaborated equipment being required. A detailed microstructural analysis with high resolution transmission electron microscopy evidences the formation of two In_2S_3 phases containing different amounts of Cu.

2. Experimental

2.1. Preparation of the precursor

An hybrid (organic-inorganic) Cu-In open framework thiometalate with composition $Cu_2In_{18}S_{33}(C_{13}H_{28}N_2)_5(H_2O)_x$ (x ~ 17) (**1**), isostructural to the known framework with composition $Cd_4In_{16}S_{33}(C_{13}H_{28}N_2)_5$ [26] was prepared using 0.7 mmol of CuS (99%, Aldrich), 4.2 mmol of In, 6.9 mmol of S and 13.46 mmol of 4, 4'-trimethylenedipiperidine. The precursors were mixed with 2.5 mL of water and 2.5 mL of ethylene glycol in a 35 mL Teflon-lined stainless steel autoclave and stirred for 15 min. The sealed vessel was then heated at 190 °C for 5 days. After cooling down to room temperature, the product was filtered off, and washed with water, ethanol and acetone. Prismatic yellow crystals in a yield larger than 90% based on indium were obtained. Details of the structure and further properties of (**1**) will be published elsewhere. The chemical composition of **1** was determined with C-H-N-S analysis and AAS.

2.2. Preparation of the nanocrystals

The product (100 mg) was crushed and the obtained powder was introduced in quartz ampoules which were evacuated and sealed. The ampoules were then introduced in an oven pre-heated at 1000 °C for 5 and 10 s, from which brown (**RP5**) and black (**RP10**) particles were obtained respectively. The experiments were performed several times and the results of the analyses demonstrate the high reproducibility of the synthetic method. According to EDX, the obtained powders have the same Cu:In:S ratio as the precursor with slight variations typical for the EDX method. Elemental C-H-N analysis for **RP5**: C, 15.43; H, 2.56; N, 2.60 wt %. For **RP10**: C, 7.79; H, 0.57; N, 1.02 wt %. For **1**: C, 16.22; H, 3.03; N, 3.14 wt %.

2.3. Characterization methods

For high resolution transmission electron microscopy, HRTEM (Philips CM 30ST, LaB_6 cathode, 300 kV, CS = 1.15 mm), the samples **1**, **RP5** and **RP10** were crushed and the resulting micro-particulates were transferred to carbon/aluminum grids. SAED (selected area electron diffraction) and PED (precession electron diffraction) [27, 28] were carried out using a diaphragm that limited the diffraction to a circular area of 2500 Å in diameter. All HRTEM micrographs were evaluated (including Fourier filtering) with the programs Digital Micrograph 3.6.1 (Gatan) or Crisp (Calidris). Chemical analyses by EDX were performed in the scanning and nanoprobe mode of the CM30ST instrument using a Si/Li-EDX detector (Noran, Vantage System).

X-ray powder diffractometry measurements were performed with a STOE STADI-P diffractometer in transmission mode using a position sensitive detector and a Ge monochromator, Cu $K\alpha_1$ radiation (λ = 1.54056 Å).

The Raman measurements were performed with a Dilor X-Y Raman spectrometer. For this purpose an Ar-Kr Laser RA2018 of Spectra Physics working in the range of 454.5 to 647.1 nm was used. The 488 nm line was selected, and the laser power was limited to approximately 10 mW in order to avoid artefacts in the measurements due to heating.

Measurements of optical reflection were carried with a Cary 5000 UV-vis-NIR spectrophotometer. The instrument uses a tungsten halogen lamp and a photomultiplier as light source and detector respectively in the range of 200-850 nm. For the range from 850 to 3300 nm a deuterium lamp as light source is used and a cooled lead sulfide cell as detector.

3. Results and discussion

3.1. X-ray powder diffractometry

Figure 1 shows the X-ray powder patterns of the three different studied materials. From the figure it is obvious that the parent material **1** is transformed after the very short heat treatment yielding a sample with a very low crystallinity (**RP5**). Increasing the reaction time leads to a new crystalline material (**RP10**). The positions of the reflections of this material indicate a relatively small unit cell, and the broadness of the reflections indicates the nanocrystalline nature of this material.

The size of coherent scattering domains of **RP10** was calculated from the full-width at half-maximum of the most intense reflection at around 27.6 ° 2θ applying the Scherrer formula yielding about 15 nm (no correction for instrumental broadening). A detailed analysis of the positions of the reflections in the powder pattern of **RP10** shows a good match with those of α-In_2S_3 [29], β-In_2S_3 [30] and $CuIn_5S_8$ [31] (Fig. 2). But due to the broadness of the reflections a definite decision about the structure of the nanocrystals of **RP10** cannot be made. We note that there is some confusion in literature concerning the α- and β-modifications of In_2S_3 with respect to the correct space group. Most authors use the tetragonal space group $I4_1$/amd for β-In_2S_3 and the cubic space group Fd-3m for α-In_2S_3. There is one crystallographic study where cubic symmetry (Fd3m) was observed for nonstoichiometric In_2S_3 whereas the tetragonal superstructure was found for the stoichiometric sample [32]. In any case the differences of the powder patterns of the two modifications are very small and the tetragonal indiumsulfide could only be identified due to the presence of weak superstructure reflections. The present material consists of nano-sized crystallites and despite a very long counting time the powder pattern does not show any reflection indicative for the presence of tetragonal In_2S_3. This is in full agreement with electron diffraction (see below) where also no superstructure reflections could be observed. The situation becomes more complex assuming the presence of small amounts of $CuIn_5S_8$ (space group F-43m) or the cubic variant crystallizing in Fd3m reported recently for $NaIn_5S_8$ [33]. Simulation of powder patterns with all four compounds and using the FWHM of the experimental pattern demonstrates the difficulty of a rigorous analysis (see figure 2).

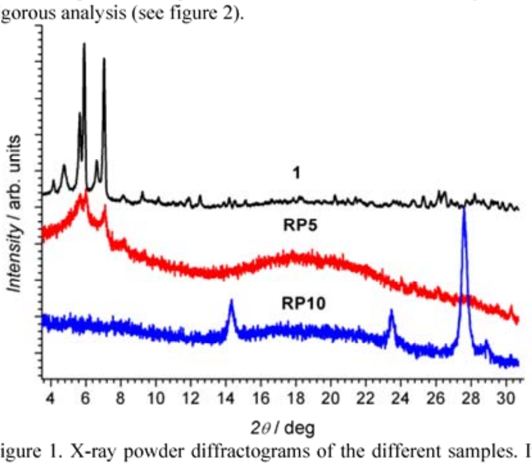

Figure 1. X-ray powder diffractograms of the different samples. It can be observed that **1** reduces its crystallinity upon annealing time (**RP5**) to finally crystallize forming a new material (**RP10**).

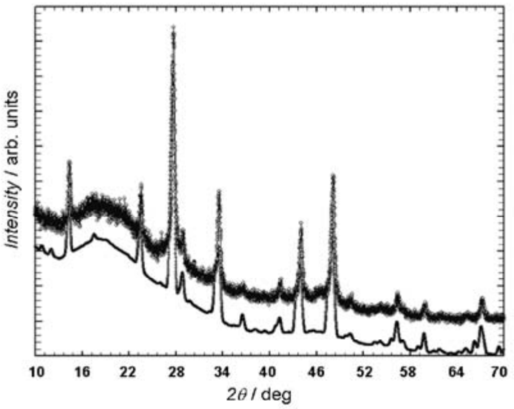

Figure 2. Convoluted simulated powder patterns of In_2S_3 and $CuIn_5S_8$ each calculated for two different space groups (bottom trace) and the experimental powder pattern (top trace). The experimental pattern is shifted for clarity.

In addition, recent reports mentioned that there is a transition from the tetragonal space group of β-In_2S_3 (the most common room-temperature modification) to cubic symmetry when In is partially replaced with a metal cation like Cu^+ or Na^+ at different levels [33, 34], obtaining compounds with formula $[In_{16}]_O[In_{5.23-x/3}M_xh_{2.67-2x/3}]_TS_{32}$ where M is the substituting metal. The maximum substitution level is reached when x = 4, resulting in a compound with formula MIn_5S_8 [5]. In the present case the cubic modification is most likely due to the presence of small amounts of Cu (see also below). Because the analysis of the X-ray powder pattern gives no clear picture about the constituents in the material **RP10**, a TEM analysis was performed.

3.2. Transmission electron microscopy investigations

3.2.1. The precursor material. The samples of this material contain two components with distinct chemical composition and structure. The first component (**W**) consists of strongly disordered crystals as evidenced by HRTEM and electron diffraction patterns, cf. figure 3a. The disordering is based on layered structural motifs as verified by the diffuse streaks seen in FFTs of high resolution micrographs and the electron diffraction pattern (see inset in figure 3a). EDX analysis identifies **W** as a binary phase In-S with an atomic ratio close to In : S ~ 2 : 3. The characteristic high d-values, e.g. d = 9.42 Å calculated from the diffraction pattern of figure 3a, indicate that the present structure can not be assigned to one of the known binary bulk phases. The second and most abundant component (**X**) is a ternary phase of the Cu-In-S system with a stoichiometry close to the specified nominal composition of the precursor, i.e. $Cu_2In_{18}S_{33}$ when neglecting the molecular constituents. The average of four EDX point analyses performed on distinct particles gave an atomic ratio Cu : In : S = 6.12 (0.78): 32.46(0.95) : 61.42(1.35) compared to 3.7 : 33.9 : 62.2 for $Cu_2In_{18}S_{33}$ (**1**). As demonstrated via HRTEM and electron diffraction (figure 3b) the particles are amorphous even without significant structural ordering inside nanoscale areas. According to the X-ray powder pattern the starting material **1** is crystalline in the as prepared state and no hints are seen for the presence of In_2S_3. One possible explanation for the present observation is that **1** is partially decomposed under ultra high vacuum conditions and just after switching of the electron beam some material crystallized (component **W**).

Taking the amorphous chalcogenide based phase change materials [35] as examples, we checked whether the degree of structural ordering in **X** changes under the influence of electron beam impact, particularly whether crystallization occurs [36].

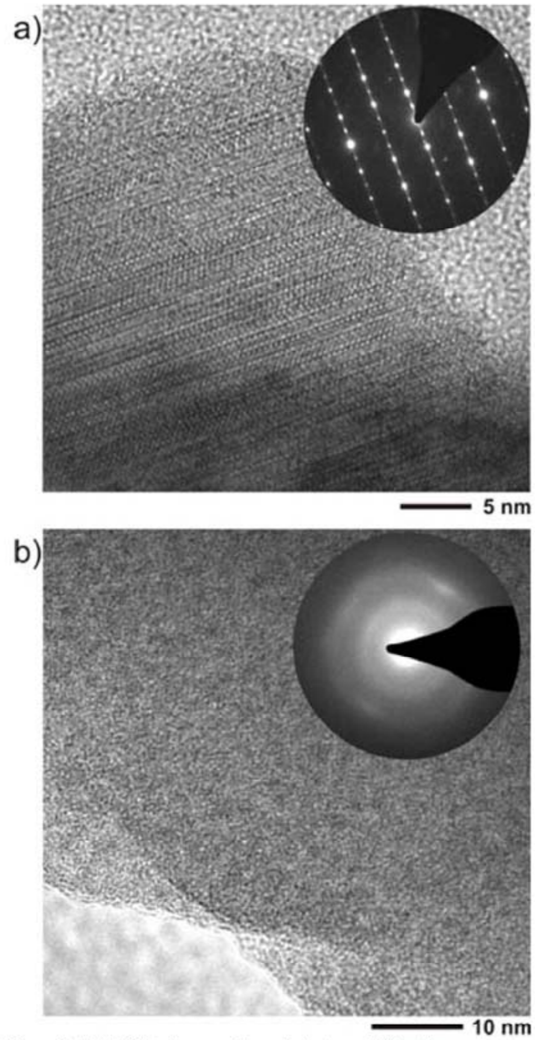

Figure 3. HRTEM micrographs and electron diffraction patterns (inset) of the components **W** (a) and **X** (b).

When irradiating **X** for a long-term with the dose usually applied for HRTEM no changes of the amorphous structure can be detected. However, a massive dose with an increase of the current density by factor 40 compared to the normal value can be adjusted by removing the condenser aperture. Under such conditions crystalline nanoparticles were evaporated from the amorphous precursor (cf. figure 4), while the remaining target material for electron bombardment stays amorphous. On closer inspection it becomes apparent that the diameter of the nanoparticles is determined by the distance from the irradiated area of the precursor (see figure 4).

Next to the precursor a percolation of larger particles is observed, while more and more separated and smaller particles occur with increasing distance, see insets in figure 4. Generally, the particle sizes appear uniform inside areas with the same distance from the precursor, e. g. for large distances of several microns reduced sizes below 2 nm are dominant.

According to electron diffraction and HRTEM, all of the particles formed by electron beam impact are crystalline; however, EDX data indicates strong fluctuations of the composition, particularly concerning the In : S ratio. Moreover, the presence of faceted and non-faceted nanoparticles calls for a separation into distinct species.

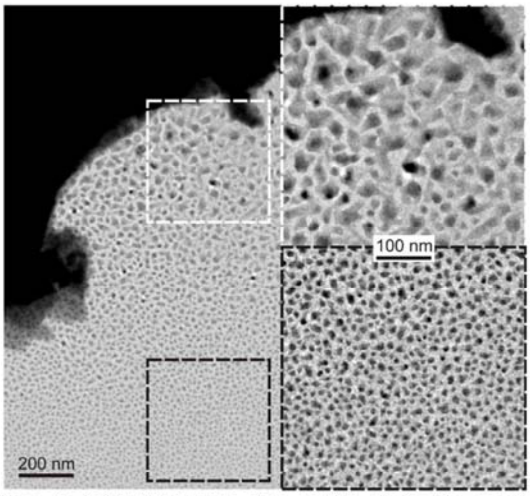

Figure 4. Bright-field image of a particle of **X** after massive electron beam impact with enlarged sections showing the characteristic particle size distribution next (top) and apart the particle edge (bottom).

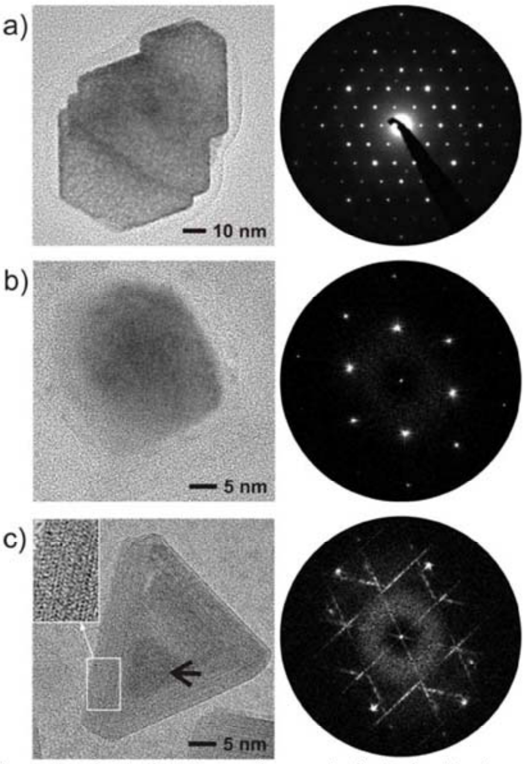

Figure 5. a) Bright-field image of a crystal of α-In_2S_3 with electron diffraction pattern (both zone axis [110]); b) Indium nanoparticle with FFT of the image, zone axis [111]; c) Core-shell structure with a crystalline core of indium and shells of an indium sulfide. Inserted: enlarged section, see marks, attached FFT of the image.

The faceted crystals (e. g. figure 5a) were determined as binary phases In-S, which show electron diffraction patterns that can be assigned to the spinel-type α-In_2S_3. The non-faceted particles were identified as pure indium, cf. FFT in figure 5b for a particle aligned in zone axis orientation [111] (d(101) = 2.75 Å, d(110) = 2.32 Å, calculated values based on [29]: 2.72 Å, 2.30 Å). Additionally EDX data proves the increase of the indium content, as evidenced by the spectra recorded on point 3 marked in figure 6.

Interestingly, the ratio In : S of the sulfur containing species is frequently found to be larger than one which is in contradiction with the nominal composition known for crystalline In-S phases (note that the phase described as "In_5S_4" [37] is truly $SnIn_4S_4$ [38]). This discrepancy is rationalized by the fact that all of the latter particles exhibit a core-shell morphology made by indium (core) and a binary In-S phase (shell), respectively. The shape of the shell resembles simple polygons folded around the core; see for instance the triangular shape depicted in figure 5c. However, the cores frequently take off-center positions as demonstrated by the enlarged section in figure 6, bottom. The atomic structure of the shells is characterized by prominent disorder of layered structural motifs as can bee seen in the enlarged section in figure 5c. Thus, the FFTs calculated inside square areas of the shell exhibit lines of diffuse intensity, and the complete FFT contains a set of parallel lines. The pattern formed by the diffuse lines depends on the overall shape of the shell, and an example is the hexagonal diffuse pattern from the triangular particle in figure 5c. Spatially resolved nanoprobe-EDX analyses on the core and the shell do not separate the constituents due to their superposition. However, as illustrated in figure 6 the quantification of the spectra recorded next to points 1 and 2 demonstrates the reversal of the In : S ratio, i. e. the ratio is larger and smaller than 1 when transmitting the core area (point 1: In : S ~ 1.33) and the shell (point 2: In : S ~ 0.85), respectively.

*3.2.2. Sample obtained after rapid pyrolysis for 5 s (**RP5**).* When annealing the pristine material rapidly for five seconds, **W** and **X** still represent the major components, and again **X** can be decomposed by the in-situ evaporation experiment with the results described above (the evaporation of core-shell nanocrystals). Moreover a third component (**Y**) can be identified forming aggregates of amorphous nanoparticles, cf. figure 7. The EDX analyses (four point measurements) indicate an atomic ratio of Cu : In : S = 3.56(3) : 34.36(24) : 62.08(20) and the presence of larger amounts of carbon, maybe produced by the decomposition the precursor material. Note that according to the EDX data the Cu-content of **Y** with respect to **X** is decreased.

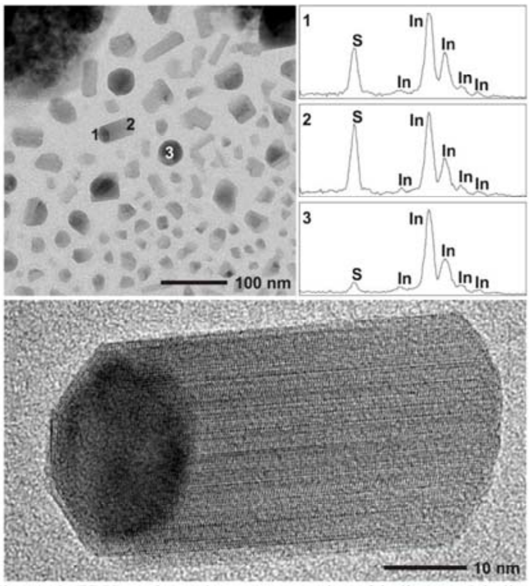

Figure 6. EDX performed on a composite of indium and indium sulfide (points 1 and 2) and indium (point 3, stray intensity from S in the surrounding), see text. Bottom: enlarged view of the composite.

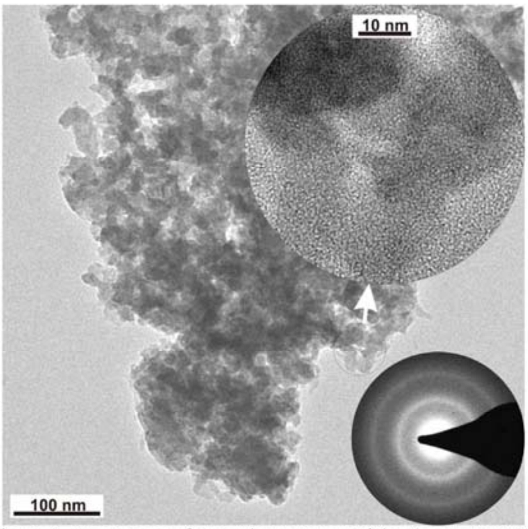

Figure 7. Aggregates of amorphous nanoparticles (component **Y**) after rapid thermal decomposition for five seconds. Bright-field image with enlarged cutout and electron diffraction pattern.

The amorphous structure is well seen in the enlarged section of figure 7 and in the attached electron diffraction pattern. The broad rings with diffuse intensity represent the most prominent two-body correlations of graphite carbon; however, related diffraction patterns can also be expected for amorphous In_2S_3. In the latter case the diameter of the rings of 3.18 Å and 1.89 Å would correlate with the values expected for the crystalline structure of α-In_2S_3 of d(311) and d(440) with 3.25 Å and 1.90 Å, respectively [29].

*3.2.3. Sample obtained after rapid pyrolysis for 10 s (**RP10**).* After more extended times of thermal annealing, all components were found to be crystalline. However, the size distribution of the particles is clearly split. Larger particles (**Z1**) of micron size coexist with nanocrystals (**Z2**) (see figure 8a). Diffraction patterns recorded inside selected areas containing both species can be indexed assuming a spinel-type structure with the metrics reported for cubic α-In_2S_3, see the indices specified in figure 8. This finding suggests that both species are crystallizing in this structure type.

The chemical compositions of the species show significant fluctuations as indicated by large values of the variances, however, as a clear trend the copper content of **Z2** (Cu : In : S = 4 : 35 : 61) was found to be larger than for **Z1** (Cu : In : S = 1 : 38 : 61). Normalizing to the S content, the empirical formulas of **Z1** and **Z2** are $Cu_{0.05}In_{1.87}S_3$ and $Cu_{0.2}In_{1.73}S_3$ respectively, thus the compounds are non-stoichiometric indium sulfides with composition close to In_2S_3. This gives an additional evidence to confirm that the structure of these compounds is cubic (α-In_2S_3), as reported in [32]. Note, that the low copper content does not change the lattice parameters with respect to pure α-In_2S_3 in a way which can be identified via electron diffraction. Actually, the structure of **Z2** can be characterized by focusing on aggregates or single nanoparticles. In this case, the electron diffraction patterns and FFTs match with those expected for the cubic spinel-type structure of α-In_2S_3. For instance, the particle seen in the center of figure 8b is oriented close to zone axis [110] as proven by the d-values determined from the FFT.

With the aid of tilting experiments and HRTEM, the single crystalline particles of **Z1** can be assigned to the cubic spinel-type structure too. The diffracted intensity convincingly matches the calculated one, particularly when selecting the precession mode instead of the fixed beam mode, cf. figure 9.

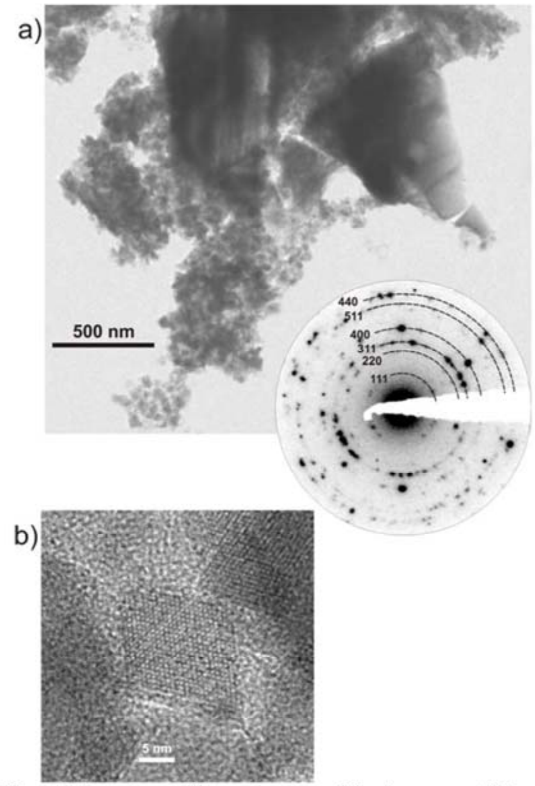

Figure 8. Large crystallites and nanoparticles (component **Z1** and **Z2**, respectively) of a ternary phase Cu-In-S. a) Bright-field image; b) Diffraction pattern recorded on an selected area containing **Z1** and **Z2** and enlarged section showing a faceted nanoparticle of Cu-In-S (spinel-type, zone axis close to [110]).

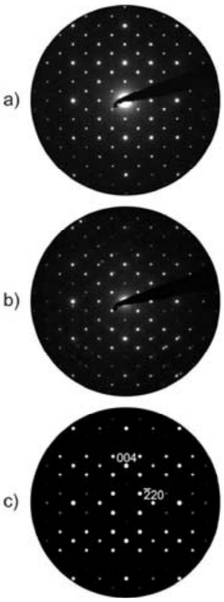

Figure 9. SAD (a) and PED (b) pattern recorded on component **Z1**, c) simulated PED pattern (precession angle: 3°, thickness 30 nm) based on the structure of α-In_2S_3, zone axis [110].

The HRTEM micrographs of figure 10 were recorded next to a thin edge of a particle in the zone axis orientation [110]. The experimentally observed contrasts are well reflected by those of the inserted simulated micrographs, even for strong underfocus conditions, e.g. Δf = -130 nm (figure 10, bottom). In case of Δf = -45 nm the imaging conditions of the Scherzer focus are approximated, i. e. the black spots represent high values of the projected potential and thus correlate with the indium atoms.

3.3. UV-vis spectroscopy

The determination of the optical band gap E_g of the sample **RP10** was done applying the Kubelka-Munk method using the UV-visible reflectance spectrum of a powdered sample. For this purpose α^2/s^2 is plotted against the energy, with α being the absorption coefficient and s the scattering coefficient [39]. In the Kubelka-Munk plot for **RP10** two absorption steps with edge energies at 1.3 eV and 2.2 eV can be identified (figure 11). These values are close to the corresponding E_g of single crystals of $CuIn_5S_8$ (1.31 eV) [40] and β-In_2S_3 (2 eV) [41].

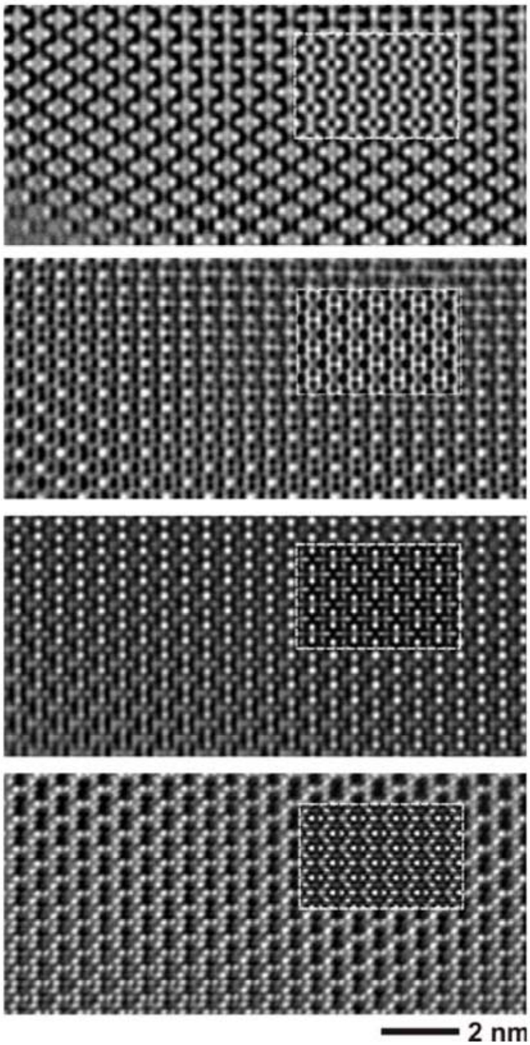

Figure 10. HRTEM performed on component **Z1**. Zone axis [110], parameters for inserted simulated micrographs: t = 6 nm, and from top to bottom: Δf = +5 nm, Δf = -45 nm, Δf = -85 nm, Δf = -130 nm.

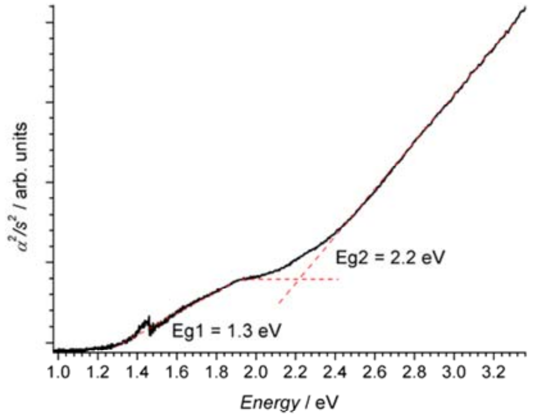

Figure 11. Kubelka-Munk plot for the determination of the optical band-gap of **RP10**. The steps at 1.3 and 2.2 eV correspond to the band-gaps of **Z2** and **Z1** respectively.

It has been reported that doping β-In_2S_3 with different amounts of Cu allows tuning E_g between these two values [42]. In **RP10** the band gap of 1.3 eV can be due to the component with larger Cu content (**Z2**) and the band gap of 2.2 eV should correspond to the one with less Cu content (**Z1**). The small peak in the spectrum around 1.45 eV is due to the change of detector in this region.

3.4. Raman spectroscopy

The Raman spectrum measured for the sample **RP10** can be deconvoluted in 4 peaks that have maxima at 306, 322, 340 and 357 cm^{-1}, as shown in figure 12. In this range β-In_2S_3 presents 3 Raman peaks at 306, 326 and 367 cm^{-1} [43]. There are no reports of the Raman spectrum of α-In_2S_3, nevertheless according to the group theory it should be very similar to the one of β-In_2S_3. In fact, when analyzing the infrared spectra of α- and β-In_2S_3 one can not distinguish a marked difference [43, 44]. Additionally the infrared- and Raman-active modes of β-In_2S_3 at the centre of the Brillouin zone occur in the same range of frequencies, which is relatively narrow, but the differences in frequencies between infrared- and Raman-active modes is sufficiently large to consider that the principle of complementarity is obeyed: modes active in infrared are Raman-inactive [43]. In this way one can assume that the Raman spectra of α- and β-In_2S_3 are very similar. The peaks of **RP10** fit very well with the peaks of In_2S_3; just the peak at around 340 cm^{-1} does not correspond to this material.

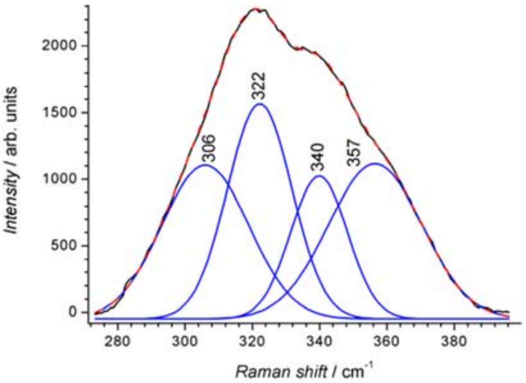

Figure 12. Raman spectrum of ***RP10***. The three deconvoluted peaks at 306, 322 and 357 cm^{-1} fit with the peaks of In_2S_3, and the peak at 340 cm^{-1} is related with the interstitial Cu in the compound.

The additional peak may be caused by the Cu atoms occupying the sites that are normally empty in α-In_2S_3. Actually $CuIn_5S_8$, with cubic structure very similar to α-In_2S_3, exhibits a resonance at around 340 cm^{-1} [45, 46], in the position of the additional peak. The broadness of the Raman peaks of **RP10** is due to the nanocrystalline nature of the material.

4. Conclusions

The thermal decomposition of $Cu_2In_{18}S_{33}(C_{13}H_{28}N_2)_5(H_2O)_x$ on second time scale at elevated temperature yield a complex mixture of compounds with varying Cu : In : S ratios. We demonstrated that the X-ray powder diffractometry of the nano-sized crystals of the sample heated for 10 s at 1000 °C is not the most suitable tool for the identification of the constituents. Moreover, the similarity of the patterns of the known modifications of In_2S_3 and $CuIn_5S_8$ complicates the assignment of distinct phases. Electron microscopy evidences the presence of two distinct crystalline phases both crystallizing in the cubic spinel-type structure. The main difference between these components is the Cu : In : S ratio. Their compositions determined with EDX suggest the presence of ternary cubic Cu-poor phases, i.e., one may view the compounds as Cu-doped cubic In_2S_3 with approximately compositions $Cu_{0.2}In_{1.73}S_3$ and $Cu_{0.05}In_{1.87}S_3$. Both compounds are non-stoichiometric which may be regarded as another hint that the correct symmetry is cubic. The optical band gaps determined by UV-vis reflectance measurements of 1.3 and 2.2 eV clearly indicate that we have a mixture of two phases. *In-situ* conversion by an intense electron beam bombardment of the precursor material and the one obtained after 5 s heat treatment transforms the materials to core-shell Cu-doped In/α-In_2S_3 nanoparticles that are monodisperse at equivalent distances from the heating point.

Further experiments are under way for an optimization of the decomposition procedure reducing the content of amorphous carbon and leading to a homogeneous distribution of the elements over the nano-crystals.

Acknowledgements

The authors would like to thank Prof. Dr. Dr. h. c. mult. A. Simon from the Max Plank institute for Solid State research for enabling the TEM experiments. The support of CONACyT and DAAD is also appreciated.

---

[1] D. K. Nagesha, X. Liang, A. A. Mamedov, G. Gainer, M. A. Eastman, M. Giersig, J. J. Song, T. Ni, N. A. Kotov, *J. Phys. Chem. B* **2001**, *105*, 7490.

[2] Y. Xing, H. Zhang, S. Song, J. Feng, Y. Lei, L. Zhao, M. Li, *Chem. Commun.* **2008**, 1476.

[3] R. Diehl, C. D. Carpentier, R. Nitsche, *Acta Crystallogr.* **1976**, *B32*, 1257.

[4] R. Diehl, R. Nitsche, *J. Cryst. Growth* **1973**, *20*, 38.

[5] N. Barreau, *Sol. Energy* **2009**, *83*, 363.

[6] R. Diehl, R. Nitsche, *J. Cryst. Growth* **1975**, *28*, 306.

[7] T. T. John, M. Mathew, C. S. Kartha, K. P. Vijayakumar, T. Abe, Y. Kashiwaba, *Sol. Energy Mater. Sol. Cells* **2005**, *89*, 27.

[8] N. Kamoun, S. Belgacem, M. Amlouk, R. Bennaceur, J. Bonnet, F. Touhari, M. Nouaoura, L. Lassabatere, *J. Appl. Phys.* **2001**, *89*, 2766.

[9] A. Darga, D. Mencaraglia, Z. Djebbour, A. Migan Dubois, R. Chouffot, J. Serhan, F. Couzinié-Devy, N. Barreau, J. Kessler, *Thin Solid Films* **2009**, *517*, 2423.

[10] B. Asenjo, A. M. Chaparro, M. T. Gutiérrez, J. Herrero, J. Klaer, *Thin Solid Films* **2009**, *515*, 6036.

[11] S. Spiering, L. Bürkert, D. Hariskos, M. Powalla, B. Dimmler, C. Giesen, M. Heuken, *Thin Solid Films* **2009**, *517*, 2328.

[12] B. Asenjo, C. Sanz, C. Guillén, A. M. Chaparro, M. T. Gutiérrez, J. Herrero, *Thin Solid Films* **2007**, *515*, 6041.

[13] S. Buecheler, D. Corica, D. Guettler, A. Chirila, R. Verma, U. Müller, T. P. Niesen, J. Palm, A. N. Tiwari, *Thin Solid Films* **2009**, *517*, 2312.

[14] W. Chen, J. O. Bovin, A. G. Joly, S. Wang, F. Su, G. Li, *J. Phys. Chem. B* **2004**, *108*, 11927.

[15] G. Cao, Y. Zhao, Z. Wu, *J. Alloys Comp.* **2009**, *472*, 325.

[16] X. Cao, L. Gu, L. Zhuge, W. Qian, C. Zhao, X. Lan, W. Sheng, D. Yao, *Colloids and Surfaces A: Physicochem. Eng. Aspects* **2007**, *297*, 183.

[17] R. Jayakrishnan, T. T. John, C. S. Kartha, K. P. Vijayakumar, T. Abe, Y. Kashiwaba, *Semicond. Sci. Technol.* **2005**, *20*, 1162.

[18] Y. He, D. Li, G. Xiao, W. Chen, Y. Chen, M. Sun, H. Huang, X. Fu, *J. Phys. Chem. C* **2009**, *113*, 5254.

[19] Y. Xiong, Y. Xie, G. Du, X. Tian, *J. Mater. Chem.* **2002**, *12*, 98.

[20] D. P. Dutta, G. Sharma, A. K. Tyagi, S. K. Kulshreshtha, *Mater. Sci. Eng. B* **2007**, *138*, 60.

[21] S. H. Choe, T. H. Bang, N. O. Kim, H. G. Kim, C. I. Lee, M. S. Jin, S. K. Oh, W. T. Kim, *Semicond. Sci. Technol.* **2001**, *16*, 98.

[22] J. Tang, G. Konstantatos, S. Hinds, S. Myrskog, A. G. Pattantyus-Abraham, J. Clifford, E. H. Sargent, *ACS Nano* **2009**, *3*, 331.

[23] T. C. Deivaraj, J. H. Park, M. Afzaal, P. O'Brien, J. J. Vittal, *Chem. Mater.* **2003**, *15*, 2383.

[24] M. Calixto Rodriguez, H. Martínez, A. Sanchez Juarez, *Thin Solid Films* **2009**, *517*, 2332.

[25] P. Feng, X. Bu, N. Zheng, *Acc. Chem. Res.* **2005**, *38*, 293.

[26] C. Wang, Y. Li, X. Bu, N. Zheng, O. Zivkovic, C. S. Yang, P. Feng, *J. Am. Chem. Soc.* **2001**, *123*, 11506.

[27] R. Vincent, P. A. Midgley, *Ultramicroscopy* **1994**, *53*, 271.

[28] T. E. Weirich, J. Portillo, G. Cox, H. Hibst, S. Nicolopoulos, *Ultramicroscopy* **2006**, *106*, 164.

[29] H. E. Swanson, R. K. Fuyat, *J. Less-Com. Met.* **1964**, *7*, 17.

[30] G. A. Steigmann, H. H. Sutherland, J. Goodyear, *Acta Crystallogr.* **1965**, *19*, 967.

[31] J. Morales, J. L. Tirado, M. L. Eldrissi Moubtassim, J. Olivier-Fourcade, J. C. Jumas, *Rev. Chim. Min.* **1987**, *24*, 10.

[32] A. Likforman, M. Guittard, A. Tomas, J. Flahaut, *J. Solid State Chem.* **1980**, *34*, 353.

[33] N. Barreau, C. Deudon, A. Lafond, S. Gall, J. Kessler, *Sol. Energy Mater. Sol. Cells* **2006**, *90*, 1840.

[34] N. Barreau, J. C. Bernède, C. Deudon, L. Brohan, S. Marsillac, *J. Cryst. Growth* **2002**, *241*, 4.

[35] B. J. Kooi, W. M. G. Groot, J. T. M. de Hosson, *J. Appl. Phys.* **2004**, *95*, 924.

[36] A. Leen Koh, K. Bao, I. Khan, W. E. Smith, G. Kothleitner, P. Nordlander, S. A. Maier, D. W. McComb, *ACS Nano* **2009**, *3*, 3015.

[37] T. Wadsten, L. Arnberg, J. E. Berg, *Acta Crystallogr.* **1980**, *B36*, 2220.

[38] H. J. Deiseroth, H. Pfeifer, *Z. Kristalogr.* **1991**, *196*, 197.

[39] D. Gal, Y. Mastai, G. Hodes, *J. Appl. Phys.* **1999**, *86*, 37.

[40] A. F. Qasrawi, N. M. Gasanly, *Cryst. Res. Technol.* **2003**, *38*, 1063.

[41] W. Rehwald, G. Harbeke, *J. Phys. Chem. Solids* **1965**, *26*, 1309.

[42] N. Barreau, J. C. Bernède, J. Kessler, in *19th European Photovoltaic Solar Energy Conference*, **2004**, p. 223.

[43] K. Kambas, J. Spyridelis, M. Balkanski, *Phys. Stat. Sol. B* **1981**, *105*, 291.

[44] I. V. Bodnar, A. G. Karoza, E. A. Kudritskaya, A. G. Smirnova, *J. Appl. Spectrosc.* **1997**, *64*, 279.

[45] J. Álvarez-García, A. Pérez-Rodríguez, A. Romano-Rodríguez, J. R. Morante, *J. Vac. Sci. Technol. A* **2001**, *19*, 232.

[46] N. M. Gasanly, S. A. El-Hamid, L. G. Gasanova, A. Z. Magomedov, *Phys. Stat. Sol. B* **1992**, *169*, K115.

Received: ((will be filled in by the editorial staff))

3.4.

In preparation

Synthesis and structural characterization of mixtures of nanocrystalline compounds of the Cu-In-S system, suitable for photocatalytic production of hydrogen using sacrificial reagents

E. Quiroga-González[1], *L. Kienle*[2], *W. Bensch*[1*]

[1] Institute for Inorganic Chemistry of the University of Kiel, Germany
[2] Institute for Material Science of the University of Kiel, Germany

*wbensch@ac.uni-kiel.de

Abstract

Nanocrystalline Cu-In-S phases with compositions very near to $CuInS_2$, $CuIn_3S_5$ and $CuIn_7S_{11}$ were obtained as mixtures under solvothermal conditions. The compounds display different morphologies like nanobelts, nanowalls and aligned microplates. $CuInS_2$ crystallizes as very thin plates which are arranged in a needle-like fashion. The compound $CuIn_3S_5$ consists of plates only some nanometers thick being arranged like the petals of a flower growing from a common point. Finally, $CuIn_7S_{11}$ being the Cu-poorest material, is obtained as nanobelts with an average diameter of individual nanobelts of about 20 nm and lengths up to more than 1 μm. According to electron diffraction patterns and X-ray diffractometry the structures of the two compounds $CuIn_3S_5$ and $CuIn_7S_{11}$ cannot be assigned to known bulk phases of the Cu-In-S system. On the other hand, the well-known chalcopyrite-type $CuInS_2$ occurs as a new morphologic form. The colors of the different phases range from black to orange-red thus covering a large range of band-gaps in the visible range of light. Different proportions of the compounds were obtained varying the amount of sulfur during the synthesis of the mixtures. The mixtures were tested in the photocatalytic production of H_2 by water splitting. The H_2 evolution is comparable to that reported for $CuInS_2/AgInS_2$ applied in solid solution with a wide-gap semiconductor.

1. Introduction

The production of hydrogen by photocatalysis has been widely studied in the last years due to its simplicity, avoiding the use of electricity or the heating by combustion of hydrocarbons [1, 2]. Hydrogen produced from water using sun light is an ideal clean energy source. In this way, the discovery of new and better photocatalysts is imperative for water splitting. Until now more than 130 different compounds have been discovered showing either good catalytic activity for water splitting or the ability to oxidize or reduce water in the presence of an external redox agent [3] which is often called a sacrificial agent. Besides different oxides ranging from the most studied material TiO_2 [4-9] to more complex systems as $PbBi_4Ti_4O_{15}$ [10] or tantalum oxides/tantalates [11, 12] to name just a few, sulfides have been also studied intensively due to their promising band-gaps allowing absorption of visible light. Mainly CdS, ZnS or In based sulfides are investigated as water splitting catalysts [3], but also materials like MoS_2 [13]. Despite the promising band-gap of CdS of 2.4 eV [5-7, 14, 15] this material is not suitable for photocatalytic water splitting because the S^{2-} anions are oxidized by photogenerated holes rather than O^{2-} of H_2O, i.e. the compound is destroyed by the so-called photocorrosion. But supplying a hole scavenger, CdS is a very good photocatalyst for H_2 generation under visible light irradiation. The performance of CdS can be increased using heterostructures like ZnO/CdS [14], ZnS/CdS [15] CdS/CdSe [16], Cu doped CdS [17] or TiO_2/CdS [18]. Despite all these efforts, photocorrosion is still the main problem with CdS containing catalysts.

The theoretical minimum band-gap for water splitting is 1.23 eV [1, 2]. But in addition to this band-gap value, the top of the valance band must be energetically lower than the potential for the O_2/H_2O couple (+1.23 V) and the bottom of the conduction band above the level of 0 V for H^+/H_2. In general, the band structure of a material can be viewed as the thermodynamic requirement to be used for water splitting, but it is not a sufficient condition. A photocatalyst exhibiting activity under visible light should have a band-gap narrower than 3.0 eV. Band-gap engineering is often used to improve the properties of a given material making it suitable for photocatalytic water splitting under visible light conditions.

The ternary sulfide $CuInS_2$ is a very well known material used for photovoltaic applications [19-21], but also presents photocatalytic activity for H_2 production from water [22, 23]. However, the H_2 production is small compared to the yield obtained with wide band-gap semiconductors like CdS [22]. $CuInS_2$ and other narrow band-gap semiconductors like $AgInS_2$ and $AgGaS_2$ have been combined in different proportions with wide band-gap materials like ZnS as solid solutions to obtain different optical bands of photocatalytic activity and to find the optimum [24-26], thus leading to an enhancement of the photocatalytic activity. Often solid solutions are obtained by e.g. co-precipitation like $AgInZn_7S_9$ crystallizing in the wurtzite type structure. This compound may be described as ZnS with a partial substitution of Zn^{2+} by Ag^+/In^{3+}. Such systems motivated us to synthesize mixtures of compounds of the Cu-In-S system that exhibit different optical band-gaps, to cover a wide range of the optical spectrum. Intimate mixtures of only Cu-In sulfides could exhibit comparable photocatalytic properties as the solid solutions mentioned above, and the preparation of such mixed Cu-In-S phases should be easier because they belong to the same ternary system.

Among ternary Cu-In-S compounds, $CuInS_2$ (chalcopyrite structure, tetragonal) [27] and $CuIn_5S_8$ (spinel structure, cubic) [21] are well known and have been obtained as single crystals with good quality. The preparation of compounds in the Cu-In-S system has been achieved by classical high temperature solid state reactions [28] and by deposition of thin films on inert substrates [29, 30]. The synthesis of Cu-In-S compounds using low-temperature methods like the solvothermal approach may lead to the formation of new and metastable compounds showing different crystalline structures which cannot be obtained using classical preparation routes. Additionally, as the solvothermal approach is characterized by multi-component heterogeneous reactions between solid and liquid components [31], the possibility of obtaining multicomponent products is high. The formation of intimate mixtures of different phases in a system like Cu-In-S may be an advantage for photocatalysis because the properties of the individual phases are combined in the product. Indeed the combination of different catalysts as mechanical mixtures may be a promising route as demonstrated for the reforming of gasoline [32].

There have been some attempts to obtain Cu-In chalcogenides by the solvothermal route, and until now nanorods [33, 34], nanoparticles [35], and microspheres [36] were obtained, but their structure and composition is in most cases equal or near to $CuInS_2$. The nanocrystalline morphologies lead to a high surface-to-bulk ratio, what is very desirable in catalysis [2]. However, the study of compounds with other compositions is also desirable.

In this contribution we report about the solvothermal approach for obtaining mixtures of nanocrystalline materials with compositions close to $CuInS_2$, $CuIn_3S_5$ and $CuIn_7S_{11}$, all exhibiting different morphologies. Different proportions of the mentioned compounds have been obtained by varying the amount of sulfur during the syntheses. The optical band-gaps of the compounds determined by UV-Vis spectroscopy range in the visible light spectrum making them suitable for photocatalysis under solar light. The results of preliminary photocatalytic activity investigations are also reported in the manuscript.

2. Experimental details

The starting materials were elemental Cu, In and S. A reproducible mixture of optically identifiable phases was obtained using the following procedure: Cu (0.14 mmol), In (0.54 mmol) and S (0.876 mmol) were mixed with 5 mL of ethylenediamine in a 35 mL Teflon-lined stainless steel autoclave; the sealed vessel was heated at 220 °C for 5 days. After cooling down to room temperature, the product was filtered off, and washed with water, ethanol and acetone. The proportion of the educts Cu:In:S is in this case 1.3:5:8 (Sample S1). Additional experiments were done increasing the proportion of S to 8.5 (sample S2), 9 (sample S3) and 9.5 (sample S4). In all the samples an orange-red and a black phase could be distinguished under optical microscope. In the following the black phase will be named compound C1. After examination in the scanning electron microscope, the orange-red component was found consisting of a red phase and an orange phase labelled C2 and C3 respectively. The manual separation of orange and red crystals is a very difficult task because they are glued together preventing a full separation. The manual isolation of the black component was less difficult but the presence of some orange-red material on the surface could not be avoided.

The morphology of the compounds was analyzed by SEM (ESEM XL30, Philips). For Transmission Electron Microscopy (TEM) observations, the samples were placed on alumina grids which were fixed in a side-entry, double-tilt holder with the tilting limited to a maximum of ± 25° in two directions. High resolution transmission electron microscopy (HRTEM) and selected area electron diffraction (SAED) were performed in a Philips CM30ST (300 kV, LaB_6 cathode). The microscope was equipped with a Spinning Star device (Nanomegas) for applying precession electron diffraction (PED, maximum precession angle: 3°). EDX (energy dispersive X-ray spectroscopy) was performed in the scanning- and nanoprobe mode of CM30ST with a Si/Li-EDX detector (Noran, Vantage System).

The optical band gap of the materials was determined using the Kubelka-Munk method. For this purpose, UV-visible reflection spectra were measured with a Cary5 Varian Techtron UV-vis-NIR spectrometer, which works in the spectral range of 200-3300 nm with 0.05 nm resolution.

For H_2 evolution from water, the catalysts were covered with Pt *in situ* by photodeposition following the procedure described in [26]. An aquous solution containing $Na_2S{\cdot}8H_2O$ and Na_2SO_3 as electron donors (sacrificial reagents) was used for the photocatalytic production of H_2. The whole procedure can be described as follows: 25 mg of a photocatalyst mixture (S1-S4), 3.31 mg of $H_2PtCl_2{\cdot}6H_2O$, 0.27 g $Na_2S{\cdot}8H_2O$ (1.25 mmol) and 0.18 g Na_2SO_3 (1.75 mmol) were mixed in a 5 mL glass vessel containing 2.5 mL of water. The air of the vessel was evacuated and replaced with Ar. The mixture was irradiated with a 250 Watt Long Life Metal-Halogenide lamp, providing a light intensity of 190000 Lux to the vessel, and around 75000 Lux when UV filters were used. The temperature was kept below 40 °C to avoid any evaporation of water. The amount of produced H_2 was quantified with a gas chromatograph Shimadzu GC-14A using Ar as carrier gas.

3. Results and discussion

3.1. Morphology and composition of the materials

The black component from the products (C1) consists of tandems of aligned plates (indicated with arrows in the SEM micrograph Fig. 1a). This material shows signs of self-organization in needles. Structures of aligned plates are not common, and have been usually observed in biominerals like nacre or in seeded grown crystals [37]. The EDX analysis performed in the TEM on several points of the plates gives the empirical formula $Cu_{1.3(0.11)}InS_{2.26(0.15)}$, with the values in parentheses being the estimated standard deviations. The EDX data suggest that the composition of C1 is close to $CuInS_2$.

The compound C2 presents the predominant phase in the orange-red component, consisting of very thin plates of around 4 μm in two dimensions and just some nanometres thick (Fig. 1b). In many instances these plates resemble the petals of a flower, growing from a common point. Some authors refer to thin plates growing over a bulk as "nanowalls" [38, 39], therefore the term nanowalls is adopted to describe C2. The empirical formula of this compound is $CuIn_{2.9(0.09)}S_{5(0.21)}$, i. e. very close to $CuIn_3S_5$. Such a nanowall shape is favourable applying this material as catalyst because the surface-to-bulk ratio is very large.

Besides C2 a fluff-like material C3 consisting of nanobelts (Fig. 1c) is found as the minor product. According to EDX analysis the empirical chemical formula of the nanobelts is $Cu_{1.11(0.38)}In_7S_{10.95(0.9)}$, i.e., C3 is a Cu-poor material.

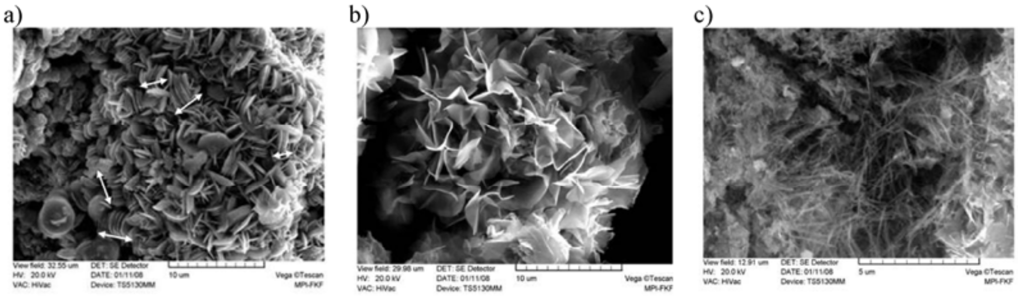

Fig. 1. SEM micrographs of the studied species: a) compound C1 consisting of plate-like crystals with composition $Cu_{1.3(0.11)}InS_{2.26(0.15)}$, b) compound C2 crystallized as "nanowalls" with composition $CuIn_{2.9(0.09)}S_{5(0.21)}$, and c) compound C3 composed of thin nanobelts with composition $Cu_{1.11(0.38)}In_7S_{10.95(0.9)}$.

In preparation

3.2. Structural characteristics

a) TEM investigations

Compounds C2 and C3 are usually found in the same orange-red agglomerates, and as mentioned above, manual separation is not possible. To have a better insight in the morphology and structure of C2 and C3, they were analyzed by TEM. For this purpose the orange-red particles of S1 were used.

Compound C2 is composed of very thin plates transparent to the electron beam even in SEM mode. In contrast to the wedge shape of bulk crystals, the thickness of the nanowalls appears constant within micron-size areas by the constant bright- or dark field contrast. These plates may be regarded as nanowalls that have a clear tendency to roll up (Fig. 2). The rolling axis is indicated with an arrow in the micrograph. Curved surfaces of the nanowalls present strong fluctuations of the high resolution contrast (cf. Fig. 3). The diffuse streaks intersecting in 000 in the FFT of this micrograph (inset in the figure) suggest that the rolled nanowall contains planar defects perpendicular to the plane of the nanowalls. This finding is supported by the parallel stripes seen in the HRTEM micrograph.

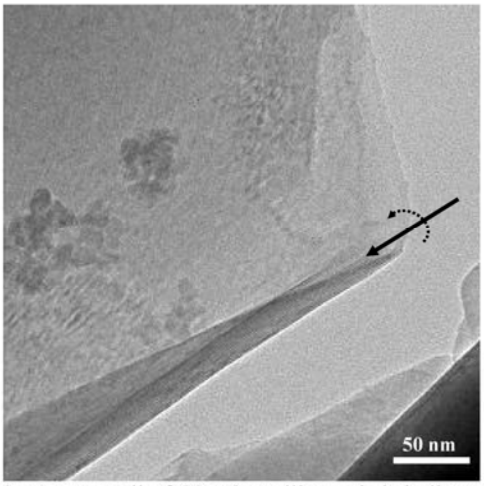

Fig. 2. HRTEM image of a bent nanowall of C2. The rolling axis is indicated with an arrow.

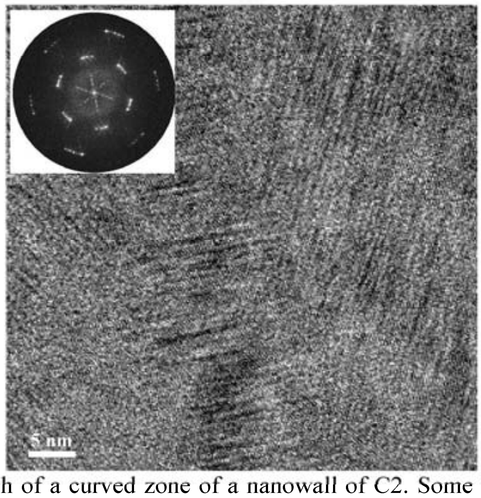

Fig. 3. HRTEM micrograph of a curved zone of a nanowall of C2. Some crystalline domains can be observed. The FFT shown in the inset evidences the existence of planar defects.

Fig. 4a) shows a HRTEM image of a top view of a nanowall with good crystalline quality. The FFT of this image (inset in the figure) evidences a hexagonal symmetry of the nanowalls in the direction perpendicular to the nanowall's plane. However, the reflection intensity distribution in the PED

4

pattern (Fig. 4b) recorded on the same nanowall violates the hexagonal symmetry, and therefore the symmetry must be described as “pseudo-hexagonal”. Additionally, SAED patterns recorded on many nanowalls (e.g. Fig. 5) also point to a second feature of the real structure, namely a rotational disorder of consecutive thin layers stacked along the zone axis. Thus the nanowalls consist of stacked nanometric layers indicating that the compound adopts a layered structure. The rotation angles are frequently random, but in many instances, when the thickness is restricted to a few rotated stacks, it is possible to determine the rotation angles and the number of rotated stacks establishing the nanowall. The low thickness of the stacks is well supported by the absence of dynamic scattering in the electron diffraction pattern. The d-values of the structure of C2 obtained from the circles of the SAED pattern are 3.29, 1.92, 1.66, 1.26, 1.11, 0.97 Å. In case of large rotation angles of a few monolayers in the nanowall, fascinating superposition micrographs are recorded (Fig. 6). The arrangement of the dots highlights the non-periodic appearance of the superposition, and the composite nature of four rotated layers is clearly seen in the FFT of the micrograph (inset in Fig. 6).

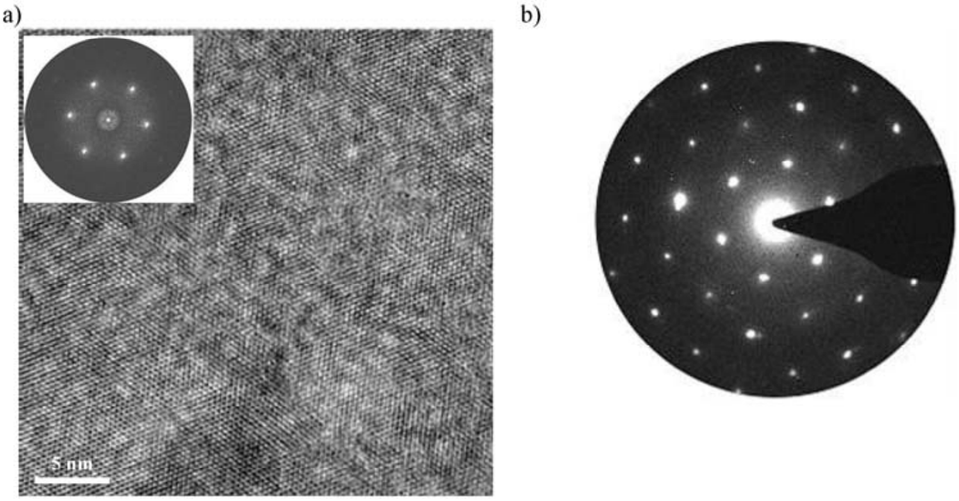

Fig. 4. a) HRTEM micrograph of a flat zone of a nanowall of compound C2. The inset shows the FFT of the micrograph, evidencing the pseudo-hexagonal symmetry of the nanowall. b) PED pattern recorded on the nanowall.

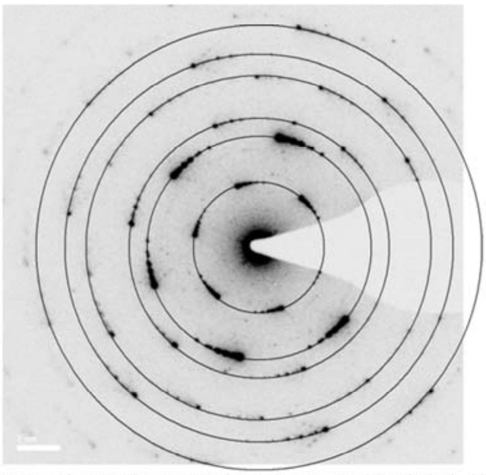

Fig. 5. Typical SAED pattern of rolled nanowalls of C2. A rotational disorder of consecutive thin layers stacked along the zone axis can be identified. Thus the nanowalls consist of stacked nanometric layers. The pattern describes circles that are assigned to the different planes of C2.

In preparation

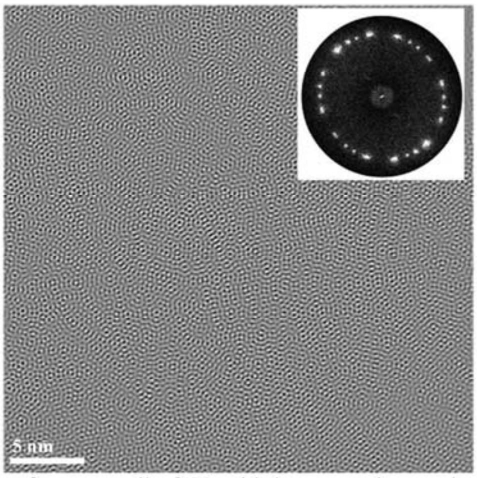

Fig. 6. HRTEM micrograph of a nanowall of C2 with large rotation angles of their composing layers. The inset displays the FFT of the micrograph.

The TEM analysis of compound C3 demonstrates that it is composed of aggregates of "nanobelts" which are randomly arranged (Fig. 7). The average diameter of the single nanobelts is about 20 nm and the lengths vary up to more than 1 µm. The crystallinity of the nanobelts is low and crystal defects are present in the most of them. However, in some cases several aspects of the atomic structure could be determined, for example, the d-values of the structure can be determined from the rings in the SAED patterns (Fig. 8), and the corresponding values are 3.16, 2.93 and 1.90 Å. On the other hand, the observations with HRTEM (Fig. 9) suggest the formation of strings along the axis of the belts. In all cases the repeat unit perpendicular to the axis was about 12.5 Å estimated from the FFT. The analysis of the three different constituents yields a comprehensive picture of the morphology and composition. The evaluation of the ED patterns indicates that C1 is composed of $CuInS_2$ but for the two other constituents the d-values do not match with data reported for any Cu-In-S phase.

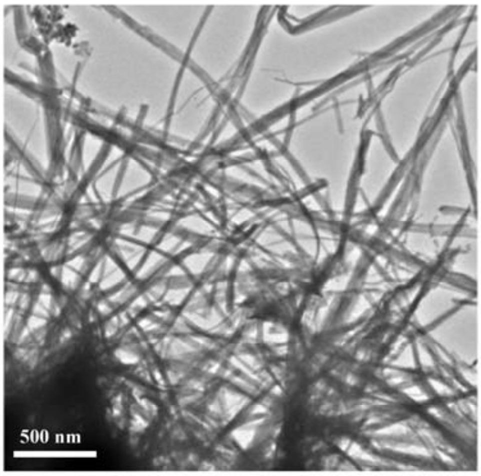

Fig. 7. TEM bright field micrograph of C3 (nanobelts).

6

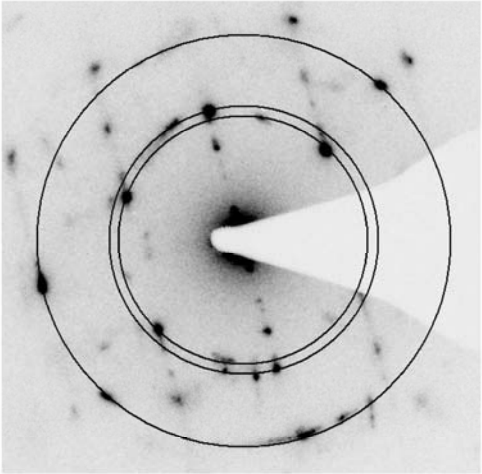

Fig. 8. Typical SAED pattern of C3. The nanobelts present prominent structural defects, but it is possible to calculate the d-values from the identified rings of the pattern.

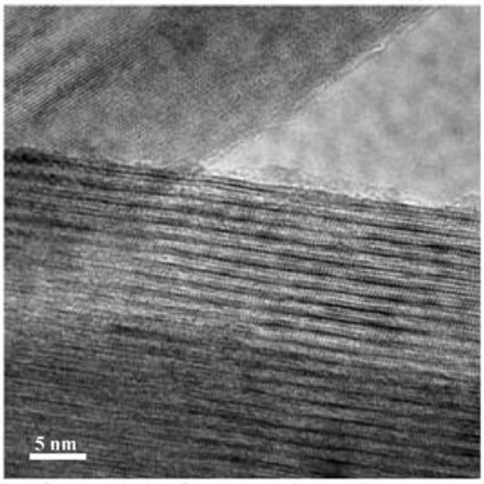

Fig. 9. HRTEM micrographs of a nanobelt of compound C3. The repeat unit perpendicular to the axis of the belts is about 12.5 Å.

b) X-ray powder diffractommetry

The X-ray powder diffractograms of all the samples show the same features, except that the intensity of the reflection at about 7° 2θ increases with increasing amount of S used for the synthesis (Fig. 10). From the mixtures just the biggest agglomerates of C1 could be manually separated. In the X-ray powder diffractogram of this component (Fig. 11) most reflections can be explained with that of the chalcopyrite $CuInS_2$ [40], i.e., the black color and the similarity of the powder pattern suggest that C1 is composed of $CuInS_2$. Some additional reflections with clearly lower intensity are also observed corresponding to some remaining material of C2 and C3 on the surface of the crystals of C1. As explained in the experimental section despite manual separation some contamination of the black crystals could not be avoided.

Taking the X-ray powder diffractogram of the mixture S4 as example, one can see that the positions of the most intense reflections match with the d-values of C2 or C3 obtained from the electron diffraction patterns (Fig. 12). Additionally, the reflection at around 7° 2θ matches well with the interlayer distance of C3. The reflection at around 5.4° 2θ should be due to the layer spacing in C2. The reflections found in the range of 10-26° 2θ are then also due to the layer structures of C2 and C3, and the additional reflections with low intensity mainly correspond to C1.

In preparation

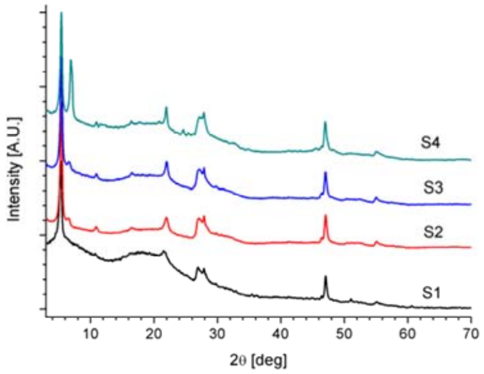

Fig. 10. X-ray powder diffraction patterns of the samples S1-S4. All the diffractograms present the same features, with exception of the reflection at 6.9° 2θ which increases in intensity from S1 to S4.

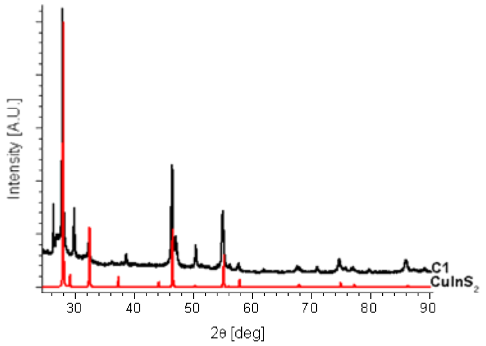

Fig. 11. X-ray powder diffraction pattern of C1. Most reflections fit with that of chalcopyrite CuInS$_2$. The additional reflections with lower intensity correspond to some rests of C2 and C3 on the surface of C1 crystallites.

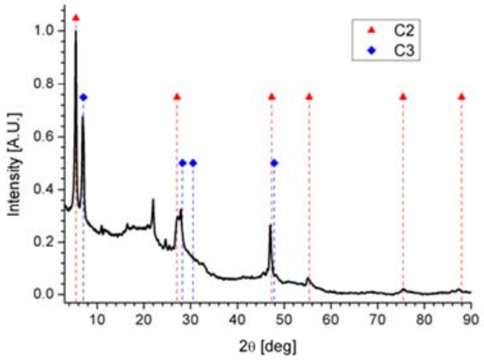

Fig. 12. X-ray powder diffraction pattern of the mixture S4. Some of the reflections are due to the layered structure of C2 and C3, and the others correspond to the main planes of the structures of these compounds. The additional reflections correspond to C1.

The d-values obtained for C2 and C3 cannot be assigned to known phases of the Cu-In-S system, hence these d-values were used to search in the ICSD for a chalcogenide having a similar set of values. The layered chalcogenide Zn$_2$In$_2$S$_5$ was found as a suitable structure candidate for the structure of C2 [41]. Replacing Zn by Cu, charge compensation can be achieved using the formula CuIn$_3$S$_5$. A compound with the Zn$_2$In$_2$S$_5$ structure type has been identified in the In-S system as substitution variant with formula AgGa$_3$In$_2$S$_8$ [42]. On the basis of the structural data of Zn$_2$In$_2$S$_5$, Cu and In atoms were placed on the Zn/In sites according to the ratio Cu:In = 1:3. The comparison of the calculated powder pattern with the experimental diagram shows a reasonable agreement (Fig. 13). The refinement of the cell parameters yields a = 3.862 Å and c = 32.435 Å. A list of the indexed reflections is shown in Table 1. The analysis indicates that C2 may present a new structural modification, unknown for a Cu-In-S compound with composition close to $CuIn_3S_5$. In previous works $CuIn_3S_5$ has been detected as segregation in $CuInS_2$ prepared with excess of In [43], but its crystal structure is not exactly known. Recently the preparation of powders with compositions $CuIn_3S_5$ and $CuIn_7S_{11}$ were reported. For $CuIn_3S_5$ the chalcopyrite type structure with space group P-42c was proposed with lattice parameters a = 5.82 and c = 11.58 Å [44, 45]. Unfortunately, no further structural details were mentioned and the assumptions were not verified e.g. by a Rietveld refinements of the X-ray powder data. The lengths of the axes are surprisingly longer than for $CuIn_3Se_5$ at a = 5.759 and c = 11.537 [46]. For $CuIn_7S_{11}$ a spinel-type structure with a = 10.65 Å was assumed [45] and the structure is not isotypic to that of $CuIn_7Se_{11}$ [47].

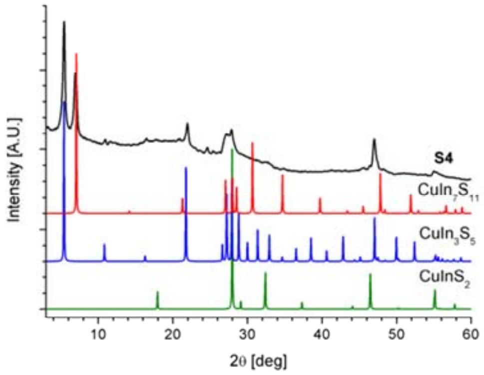

Fig. 13. X-ray powder diffraction pattern of the mixture S4 and the calculated powder diffractograms of $CuInS_2$ and the theoretical $CuIn_3S_5$ and $CuIn_7S_{11}$.

Table 1
Indexed reflections of the electron and X-ray diffraction patterns of C2. The refined position of the reflections and the difference with the experimental data are shown.

d obs [nm]	2θ obs [deg]	h	k	l	2θ calc [deg]	2θ obs-calc [deg]
16.3568	5.398	0	0	2	5.445	-0.0464
8.1356	10.866	0	0	4	10.902	-0.0360
5.3688	16.498	0	0	6	16.384	0.1140
4.0676	21.832	0	0	8	21.905	-0.0723
3.2901	27.080	1	0	2	27.204	-0.1235
19295	47.060	1	1	0	47.024	0.0366
1.6667	55.055	2	0	1	54.938	0.1171
		2	0	2	55.174	-0.1194
1.2600	75.374	2	1	2	75.358	0.0163
1.1100	87.889	2	1	14	87.925	-0.0362
		3	0	3	87.998	-0.1085
0.9700	105.145	1	0	32	105.141	0.0039

The chemical analysis of component C3 yields the composition $Cu_{1.11(0.38)}In_7S_{10.95(0.9)}$. The chemical composition of C3 resembles that of the layered chalcogenide $CuIn_7Se_{11}$ [47]. Using this structure as model, the powder pattern of $CuIn_7S_{11}$ was calculated assuming that the reflections at 7° and 47.8° 2θ of S4 come from the (001) and (110) planes of that compound. The comparison of the calculated powder pattern with the experimental diagram shows also a reasonable agreement (Fig. 13). But due to the partially very broad reflections and the similarity of the calculated powder patterns, a definite decision concerning the crystal structures of C2 and C3 cannot be drawn. More experiments and HRTEM simulations based on models need to be performed for an unambiguous structure analysis.

In preparation

3.3. Optical properties

Black (C1) and red-orange (C2 + C3) products were analysed with UV-vis transmission and reflection measurements to determine the optical band-gaps. From the X-ray powder diffractograms it is known that the amount of C3 is larger in S4. Making a Kubelka-Munk plot for the determination of the band-gap of the red-orange particles of S4 it is possible to identify absorption edges at 2.05 and 2.34 eV (Fig. 14). The particles of S1 having a much smaller amount of C3, only present an absorption edge at 2.05 eV corresponding to C2 (Fig. 15). According to this analysis, the band-gap of 2.34 eV corresponds to C3. The band-gaps of C2 and C3 are much larger than that of $CuIn_5S_8$ (1.31 eV) [48], but close to that of In_2S_3 (2 eV) [49].

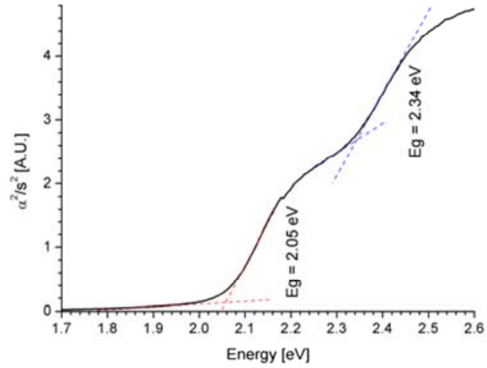

Fig. 14. Kubelka-Munk plot of the red-orange particles (C2+C3) of the product S4. Absorption edges at 2.05 and 2.34 eV can be observed.

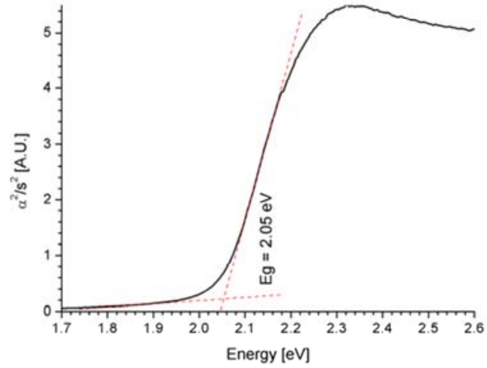

Fig. 15. Kubelka-Munk plot of the red-orange particles of the mixture S1. C2 is the most abundant material in the particles, the absorption edge at 2.05 eV is due to C2.

The strong absorption of C1 in the entire visible and near-infrared spectrum did not allow determining the optical band gap of this material. But it should be in the infrared range, as is the case of the crystalline $CuInS_2$ (~1.5 eV) [50, 51]. It is clear that the mixtures of C1-C3 absorb light in a large range covering from the NIR to the UV region, but being C2 the most abundant compound in the mixtures, the strongest absorption is of light with energies higher than 2.05 eV.

3.4. Photocatalytic activity

To test the mixtures S1-S4 for the photocatalytic production of H_2 from water sacrificial reagents were used, as in the case of $AgInS_2$ with Pt as co-catalyst [24]. The role of sacrificial reagents in photocatalytic reactions can be understood as follows: When the photocatalytic reaction is carried out in aqueous solutions including reducing reagents such as alcohols, S^{2-}, or SO_3^{2-}, the photogenerated holes irreversibly oxidize the reducing reagents instead of water. This side-reaction makes the photocatalyst electron-rich, which reduces the water molecules producing H_2 [2]. The Pt coverage of the catalysts introduces active sites on the surface enhancing the photocatalytic activity [2].

In preparation

A plot of the amount of produced H_2 versus time using the mixtures S1-S4 is shown in Fig. 16. For the catalytic test light of the range 250-600 nm was used. The rate of H_2 evolution is comparable with that of solid solutions of $CuInS_2$ or $AgInS_2$ with wide band gap semiconductors [25, 26], considering the amount of catalyst supplied for the experiment. The largest H_2 evolution is presented by S4, which was prepared with the highest S content during the solvothermal synthesis and contains the largest amount of compound C3. A relative constant evolution rate is exhibited until 40 and 50 min for S3 and S4 respectively, and then it increases, as can be observed in the plots of the derivative of the amount of H_2 with time (Fig. 17). The evolution rate for S1 decreases constantly with time, while for S2 it reaches a maximum at around 35 min and then decreases until no H_2 evolution is observed.

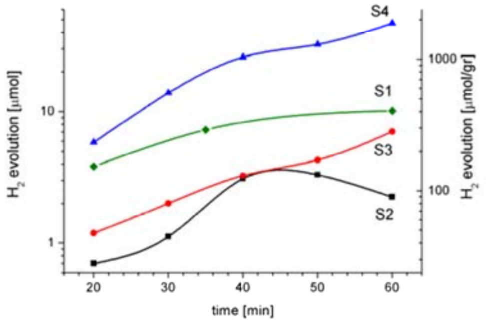

Fig. 16. Plot of the amount of produced H_2 *vs* time for samples S1-S4. The results are reported in µmol and in µmol/gr. For the measurement light of the range 250-600 nm was used.

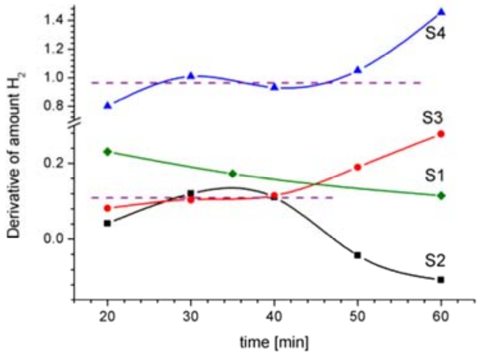

Fig. 17. Plot of the derivative of the amount of produced H_2 *vs* time for samples S1-S4.

Additionally a measurement using a long-pass filter of 515 nm in front of the lamp was performed, cutting the UV components of the excitation light. This test was performed with sample S1. In this case the rate of H_2 evolution is around 9 times smaller than without filter (Fig. 18). One possible reason for this effect is that the long-pass filter narrows the excitation range mainly to energies between 2.05 (band gap of C2) and 2.4 eV (515 nm). When no filter is used energies larger than 2.4 eV are absorbed by the samples (compare Fig. 13) enhancing the photocatalytic activity. It is worthy to mention that during all experiments on photocatalysis no O_2 evolution could be observed due to the use of the sacrificial reagents. In addition, the sacrificial reagents were tested without photocatalyst, and neither H_2 nor O_2 evolution could be detected. As an extra experiment, a powder of $CuInS_2$ prepared under solvothermal conditions was also tested under identical conditions but the amount of H_2 was below the detection limit of the gas chromatograph.

The surface area of the platinated photocatalytic mixtures was analysed using the BET method and the estimated values are 24.4, 13.5, 7.8 and 14.8 m^2/g for S1, S2, S3 and S4 respectively. Obviously, there is no direct correlation between the surface areas with the amount of produced H_2. Nevertheless the specific surface area is an important factor for good photocatalytic properties of the mixtures. Reported solid solutions of sulfide-based photocatalysts have surface areas below 2 m^2/gr [26]. The N_2 adsorption-desorption curves show a hysteresis and the mean pore size ranges between 27 and 56 nm.

In preparation

Obviously, this porosity is caused by packing of the nanoparticles leading to so-called textural porosity.

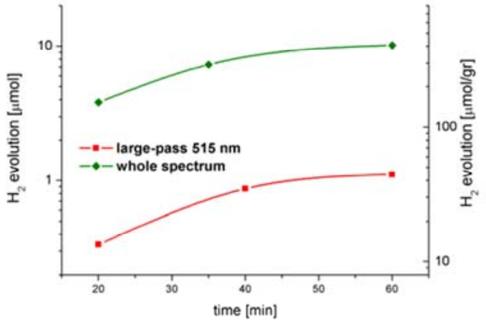

Fig. 18. Plot of the amount of produced H_2 *vs* time for S1. The amount of H_2 was recorded with and without long-pass filter of 515 nm.

The results of the experiments demonstrate that the mixtures of C1, C2 and C3 exhibit good photocatalytic activity for H_2 production from water splitting, but the use of sacrificial reagents is needed to enhance the activity and to avoid the evolution of O_2.

4. Conclusions

The reactions of Cu, In, and S in ethylenediamine under solvothermal conditions led to the formation of three different phases in an intimate mixture. Compound C1 with composition close to $CuInS_2$ is obtained as black piled plates aligned in needles with an optical band-gap in the infrared range. According to X-ray diffractommetry, C1 corresponds to the chalcopyrite $CuInS_2$. Compound C2 (nanowalls) with composition near $CuIn_3S_5$ presents an optical band gap of 2.04 eV and this compound may represent a new structural modification with composition $CuIn_3S_5$. Some evidences are presented that the structure of this compound is related to a hexagonal layered chalcogenide with cell parameters of a = 3.859 Å and c = 32.637 Å. Due to the nanosized nature of the crystals of C2 and intrinsic defects as well as the strong tendency of the nanowalls to roll up an unambiguous structure determination is complicated. Compound C3 (nanobelts) with an empirical chemical formula $Cu_{1.11(0.38)}In_7S_{10.95(0.9)}$ is a Cu-poor material which has a laminar structure exhibiting structural similarities to the layered chalcogenide $CuIn_7Se_{11}$.

The morphology of the compounds is new for ternary compounds of the Cu-In-S system. The optical and morphological properties of the compounds allow their use as mixtures in photocatalysis for the production of H_2. The mixtures were tested as photocatalysts and the results are promising yielding H_2 evolution rates comparable with values reported for solid solutions of narrow and wide band-gap semiconductors.

Acknowledgements

The authors appreciate the support of CONACyT and DAAD. The TEM experiments were performed with the aid of Mrs. Viola Duppel and were enabled by Prof. Dr. Dr. h.c. mult. A. Simon at the Max Planck Institute for Solid State Research.

References

[1] A. Kudo, Pure Appl. Chem. 79/11 (2007) 1917.
[2] A. Kudo, Y. Miseki, Chem. Soc. Rev. 38 (2009) 253.
[3] F.E. Osterloh, Chem. Mater. 20 (2008) 35.
[4] J. Nowotny, C.C. Sorrell, T. Bak, L.R. Sheppard, Solar Energy 78 (2005) 593.
[5] M. Grätzel, Acc. Chem. Res. 14 (1981) 376.
[6] K. Kalyanasundaram, M. Grätzel, E. Pelizzetti, Coord. Chem. Rev. 69 (1986) 57.
[7] M. Ashokkumar, Int. J. Hydrogen Energy 23 (1998) 427.

In preparation

[8] M. Ni, M.K.H. Leung, D.Y.C. Leung, K. Sumathy, Renewable Sustainable Energy Rev. 11 (2007) 401.
[9] A. Fujishima, T.N. Rao, D.A. Tryk, J. Photochem. Photobiol. C 1 (2000) 1.
[10] H.G. Kim, O.S. Becker, J.S. Jang, S.M. Ji, P.H. Borse, J.S. Lee, J. Solid State Chem. 179 (2006) 1214.
[11] H. Kato, A. Kudo, Catal. Lett. 58 (1999) 153.
[12] H. Kato, A. Kudo, Chem. Phys. Lett. 295 (1998) 487.
[13] X. Zhong, Y. Na, F. Wen, G. Ma, J. Yang, D. Wang, Y. Ma, M. Wang, L. Sun, C. Li, Chem. Commun. (2009) 4536.
[14] X. Wang, G. Liu, Z.G. Chen, F. Li, L. Wang, G.Q. Lu, H.-M. Cheng, Chem. Commun. (2009) 3452.
[15] C.J. Xing, Y.J. Zhang, W. Yan, L.J. Guo, Int. J. Hydrogen Energy 31 (2006) 2018.
[16] S. Kambe, M. Fujii, T. Kawai, S. Kawai, F. Nakahara, Chem. Phys. Lett. 109 (1984) 105.
[17] E.N. Savinov, Y.A. Gruzdkov, V.N. Parmon, Int. J. Hydrogen Energy 14 (1989) 1.
[18] H. Fujii, M. Ohtaki, K. Eguchi, H. Arai, J. Mol. Catal. A: Chem. 129 (1998) 61.
[19] T.T. John, M. Mathew, C.S. Kartha, K.P. Vijayakumar, T. Abe, Y. Kashiwaba, Sol. Energy Mater. Sol. Cells 89 (2005) 27.
[20] A. Goosens, J. Hofhuis, Nanotechnology 19 (2008) 424018.
[21] T.J. Savenije, M. Nanu, J. Schoonman, A. Goosens, J. Appl. Phys. 101 (2007) 113718.
[22] K. Kobayakawa, A. Teranishi, T. Tsurumaki, Y. Sato, A. Fujishima, Electrochemica Acta 37/3 (1992) 465.
[23] L. Zheng, Y. Xu, Y. Song, C. Wu, M. Zhang, Y. Xie, Inorg. Chem. 48/9 (2009) 4003.
[24] A. Kudo, I. Tsuji, H. Kato, Chem. Commun. (2002) 1958.
[25] A. Kudo, Int. J. Hydrogen Energy 31 (2006) 197.
[26] I. Tsuji, H. Kato, A. Kudo, Chem. Mater. 18 (2006) 1969.
[27] H.L. Hwang, C.L. Cheng, L.M. Liu, Y.C. Liu, C.Y. Sun, Thin Solid Films 67 (1980) 83.
[28] I.V. Bodnar, I.T. Bodnar, A.A. Vaipolin, Crystal Res. & Technol. 19/12 (1984) 1553.
[29] E. Rudigier, B. Barcones, I. Luck, J.-C. T., P.R. A., R. Scheer, J. Appl. Phys. 95/9 (2004) 5153.
[30] L. Makhova, R. Szargan, I. Konovalov, Thin Solid Films 472 (2005) 157.
[31] L. Engelke, M. Schaefer, F. Porsch, W. Bensch, European Journal of Inorganic Chemistry (2003) 506.
[32] M.A. Mogalis, S.I. Kolesnikov, I.M. Kolesnikov, Chemistry and Technology of Fuels and Oils 42/2 (2006) 133.
[33] T. Nyari, P. Barvinschi, P. Vlăzan, O. Sandru, I. Dékány, 2004 International Semiconductor Conference, Sinaia, Romania, 2004.
[34] J. Xiao, Y. Xie, R. Tang, Y. Qian, J. Solid State Chem. 161 (2001) 179.
[35] W. Du, X. Qian, J. Yin, Q. Gong, Chem. Eur. J. 13 (2007) 8840.
[36] Y. Qi, K. Tang, S. Zeng, W. Zhou, Microporous and Mesoporous Materials 114 (2008) 395.
[37] Z.R. Tian, J.A. Voigt, J. Liu, B. Mckenzie, M.J. Mcdermott, M.A. Rodriguez, H. Konishi, H. Xu, Nature materials 2 (2003) 821.
[38] C.N.R. Rao, V.V. Agrawal, K. Biswas, U.K. Gautam, M. Ghosh, A. Govindaraj, G.U. Kulkarni, K.P. Kalyanikutty, K. Sardar, S.R.C. Vivekchand, Pure Appl. Chem. 78/9 (2006) 1619.
[39] U.K. Gautam, S.R.C. Vivekchand, A. Govindaraj, C.N.R. Rao, Chem. Commun. (2005) 3995.
[40] H. Hahn, G. Frank, W. Klingler, A.D. Meyer, G. Stoerger, Z. Anorg. Allg. Chem. 271 (1953) 153.
[41] H. Haeuseler, A. Cansiz, M. Himmrich, M. Jung, J. Solid State Chem. 74 (1988) 171.
[42] H. Haeuseler, E. Elitok, A. Memo, R. Arzani, Z. Anorg. Allg. Chem. 627 (2001) 1204.
[43] R. Scheer, H.J. Lewerenz, J. Vac. Sci. Technol. A 13/4 (1995) 1924.
[44] N. Khémiri, M. Kanzari, J. Mater. Sci. 44 (2009) 4743.
[45] N. Khemiri, M. Kanzari, Nuclear Instruments and Methods in Physics Research B (2009).
[46] J.M. Merino, M. Di Michiel, M. León, J. Phys. Chem. Solids 64 (2003) 1649.
[47] L.D. Gulay, I.A. Ivashchenko, O.F. Zmiy, I.D. Olekseyuk, Journal of Alloys and Compounds 384 (2004) 121.
[48] A.F. Qasrawi, N.M. Gasanly, Cryst. Res. Technol. 38/12 (2003) 1063.
[49] W. Rehwald, G. Harbeke, J. Phys. Chem. Solids 26 (1965) 1309.

In preparation

[50] V.A. Ivanov, I.A. Viktorov, V.F. Gremenok, Technical physics 47/9 (2002) 1197.

[51] N. Kamoun, N. Jebbari, S. Belgacem, R. Bennaceur, J. Bonnet, F. Touhari, L. Lassabatere, J. Appl. Phys. 91/4 (2002) 1952.

4. Compounds substituting In by Sb

Sulfides or thiometallates containing both In and Sb atoms are scarce. One reason may be the different coordination behavior of the two elements. Indium is always in tetrahedral coordination, as observed in different indium sulfides and thioindates [72, 82], while Sb is mainly coordinated by three S atoms forming a SbS_3 trigonal pyramid [83, 84]. In addition, the Sb(III) centre with the stereochemically active lone electron pair often completes the environment by formation of strong distorted coordination polyhedra and in many cases an enhancement of the coordination number from 3 to 4 or 5, or even to 6 is observed. Thioindates and thioantimonates are prepared under solvothermal conditions and a successful interconnection of InS_4 tetrahedra with SbS_x building units ($x = 3$-6) can only be achieved if soluble species of both elements are formed simultaneously. There are several further synthetic aspects like the surrounding of the dissolved species by the structure directing molecules which may prevent condensation of the primary building blocks. Nevertheless, there is an interest in preparing compounds of the In-Sb-S system to combine the architectures obtained with InS_4 tetrahedra and SbS_x units to obtain new structures which then may present different chemical and physical properties compared to those of the pure thioindates or thioantimonates. Additionally, In is a very costly material and the introduction of Sb in indium sulfides and thioindates could allow obtaining cheaper materials that still present good photoactive properties.

The only known inorganic compounds of the In-Sb-S system are $InSbS_3$ [85] and $In_{1.8}Sb_{0.2}S_3$ (γ-In_2S_3) [59, 61]. Very recently there was one report about a hybrid inorganic-organic compound in this system, namely $[(CH_3CH_2CH_2)_2NH_2]_5In_5Sb_6S_{19}\cdot 1.45H_2O$ [86] synthesized under solvothermal conditions. The structure of this hybrid compound is composed of anionic layers with large windows that allows a rapid and efficient exchange of the organic cations (dipropylammonium, $DPAH^+$) by other ions like Cs^+. It is noted that there are just few reports of compounds of the III-V-VI systems like the thiogallato-antimonates $[Ni(en)_3][Ga_2Sb_2S_7]$ and $[(Me)_2NH_2]_2[Ga_2Sb_2S_7]$ [87].

In the present contribution the new compound $\{[In(C_6H_{14}N_2)_2]_2Sb_4S_8\}Cl_2$ was obtained using the solvothermal synthesis method applying a mixture of $InCl_3$, Sb, S and 1,2 *trans*-diaminocyclohexane (section 4.1). This compound represents the second hybrid inorganic-organic compound in the In-Sb-S system and displays novel structural and thermal properties not observed for thioindates and thioantimonates until now. The structure of the compound consists of two $[In(C_6H_{14}N_2)_2]^{3+}$ complexes interconnected by the $[Sb_4S_8]^{4-}$ anion which acts as a tetradentate ligand. Several compounds with the $[Sb_4S_8]^{4-}$ anion were reported in the literature but in $\{[In(C_6H_{14}N_2)_2]_2Sb_4S_8\}Cl_2$ the thioantimonate(III) anion shows a hitherto never observed connection mode. In-situ X-ray powder diffraction experiments evidenced that the compound shows an highly unusual reversible thermal expansion behavior which until now was only reported for very few compounds. Upon heating, the lattice parameters exhibit unusual uniaxial negative and biaxial positive thermal expansions which are quite different in the temperature regions investigated. The relative negative expansion coefficients for the *a*-axis of $-194\cdot10^{-6}$ K^{-1} (30 – 120 °C) and $-82\cdot 10^{-6}$ K^{-1} (120 – 220 °C) are in the region of so-called colossal thermal expansion. Above about 270 °C the sample starts to decompose and becomes amorphous. Further increase of the temperature leads to crystallization of $InSbS_3$ at 320 °C. When heating the sample above 585 °C Sb starts to be evaporated and a γ-In_2S_3 is formed, which is stable at room temperature when it contains a small amount of Sb.

In additional experiments to replace In by Sb in thiometallates, following similar synthetic conditions as those for the preparation of the thioindate $[Mg(en)_3][In_2S_4]$ led to the crystallization of the thioantimonate(III) $[Mg(en)_3][Sb_4S_7]$ (section 4.2). This is the first time that a complex of an earth-alkaline metal charge-compensates a thioantimonate(III). Many transition metal complex-containing thioantimonates(III) are known, but the structural diversity and properties may be altered using main group cations. In the structure of the compound trigonal SbS_3 pyramids are joined to form an Sb_3S_3 ring. The rings are connected through SbS_3 units yielding an undulated chain anion. Considering so-called secondary Sb-S bonds a layer-like thioantimonate anion is formed. The $[Mg(en)_3]^{2+}$ cations are located between the layers.

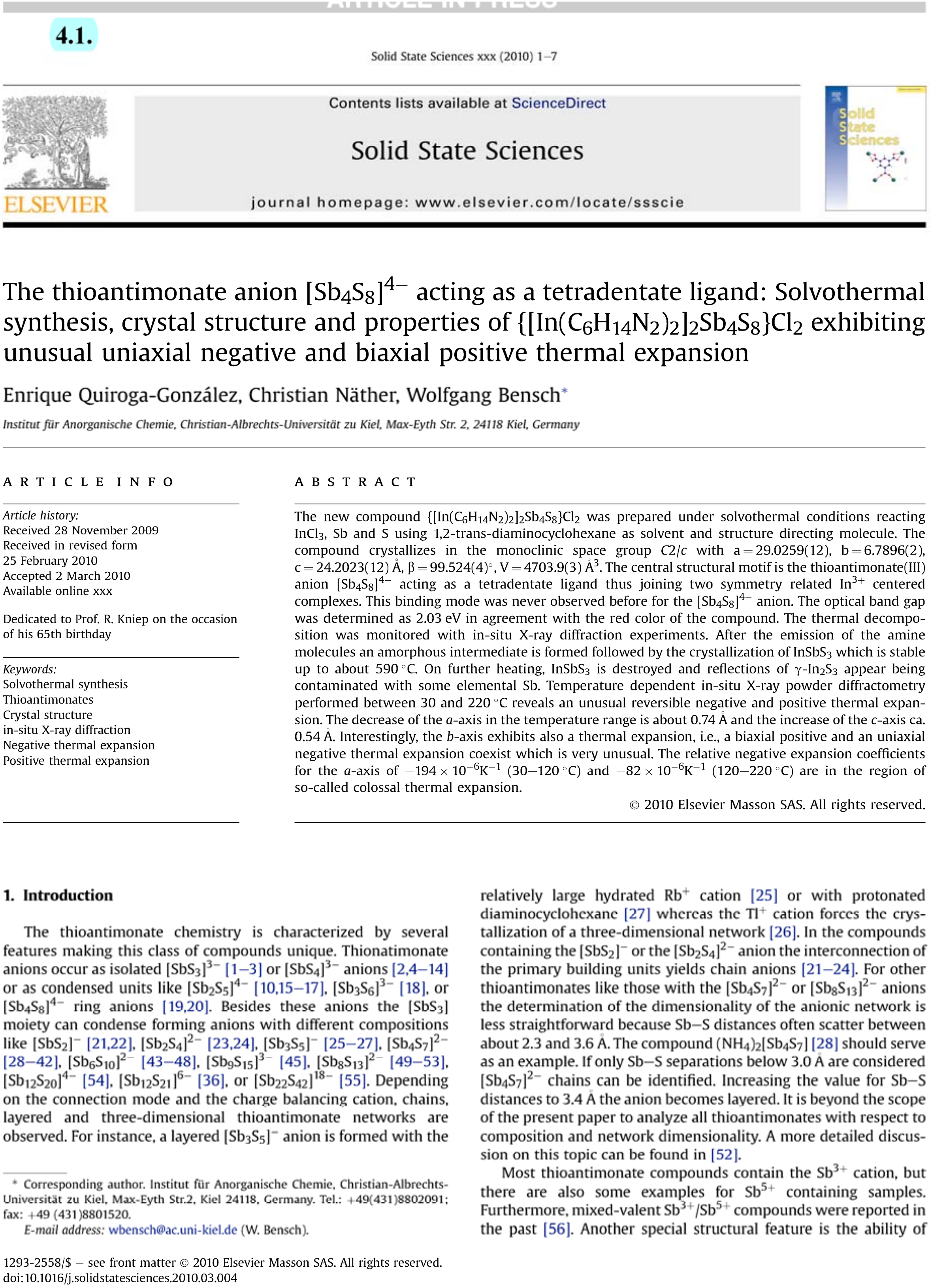

4.1.

Solid State Sciences xxx (2010) 1–7

Contents lists available at ScienceDirect

Solid State Sciences

journal homepage: www.elsevier.com/locate/ssscie

The thioantimonate anion $[Sb_4S_8]^{4-}$ acting as a tetradentate ligand: Solvothermal synthesis, crystal structure and properties of $\{[In(C_6H_{14}N_2)_2]_2Sb_4S_8\}Cl_2$ exhibiting unusual uniaxial negative and biaxial positive thermal expansion

Enrique Quiroga-González, Christian Näther, Wolfgang Bensch*

Institut für Anorganische Chemie, Christian-Albrechts-Universität zu Kiel, Max-Eyth Str. 2, 24118 Kiel, Germany

ARTICLE INFO

Article history:
Received 28 November 2009
Received in revised form
25 February 2010
Accepted 2 March 2010
Available online xxx

Dedicated to Prof. R. Kniep on the occasion of his 65th birthday

Keywords:
Solvothermal synthesis
Thioantimonates
Crystal structure
in-situ X-ray diffraction
Negative thermal expansion
Positive thermal expansion

ABSTRACT

The new compound $\{[In(C_6H_{14}N_2)_2]_2Sb_4S_8\}Cl_2$ was prepared under solvothermal conditions reacting $InCl_3$, Sb and S using 1,2-trans-diaminocyclohexane as solvent and structure directing molecule. The compound crystallizes in the monoclinic space group *C*2/*c* with a = 29.0259(12), b = 6.7896(2), c = 24.2023(12) Å, β = 99.524(4)°, V = 4703.9(3) Å^3. The central structural motif is the thioantimonate(III) anion $[Sb_4S_8]^{4-}$ acting as a tetradentate ligand thus joining two symmetry related In^{3+} centered complexes. This binding mode was never observed before for the $[Sb_4S_8]^{4-}$ anion. The optical band gap was determined as 2.03 eV in agreement with the red color of the compound. The thermal decomposition was monitored with in-situ X-ray diffraction experiments. After the emission of the amine molecules an amorphous intermediate is formed followed by the crystallization of $InSbS_3$ which is stable up to about 590 °C. On further heating, $InSbS_3$ is destroyed and reflections of γ-In_2S_3 appear being contaminated with some elemental Sb. Temperature dependent in-situ X-ray powder diffractometry performed between 30 and 220 °C reveals an unusual reversible negative and positive thermal expansion. The decrease of the *a*-axis in the temperature range is about 0.74 Å and the increase of the *c*-axis ca. 0.54 Å. Interestingly, the *b*-axis exhibits also a thermal expansion, i.e., a biaxial positive and an uniaxial negative thermal expansion coexist which is very unusual. The relative negative expansion coefficients for the *a*-axis of $-194 \times 10^{-6} K^{-1}$ (30–120 °C) and $-82 \times 10^{-6} K^{-1}$ (120–220 °C) are in the region of so-called colossal thermal expansion.

1. Introduction

The thioantimonate chemistry is characterized by several features making this class of compounds unique. Thionatimonate anions occur as isolated $[SbS_3]^{3-}$ [1–3] or $[SbS_4]^{3-}$ anions [2,4–14] or as condensed units like $[Sb_2S_5]^{4-}$ [10,15–17], $[Sb_3S_6]^{3-}$ [18], or $[Sb_4S_8]^{4-}$ ring anions [19,20]. Besides these anions the $[SbS_3]$ moiety can condense forming anions with different compositions like $[SbS_2]^{-}$ [21,22], $[Sb_2S_4]^{2-}$ [23,24], $[Sb_3S_5]^{-}$ [25–27], $[Sb_4S_7]^{2-}$ [28–42], $[Sb_6S_{10}]^{2-}$ [43–48], $[Sb_9S_{15}]^{3-}$ [45], $[Sb_8S_{13}]^{2-}$ [49–53], $[Sb_{12}S_{20}]^{4-}$ [54], $[Sb_{12}S_{21}]^{6-}$ [36], or $[Sb_{22}S_{42}]^{18-}$ [55]. Depending on the connection mode and the charge balancing cation, chains, layered and three-dimensional thioantimonate networks are observed. For instance, a layered $[Sb_3S_5]^{-}$ anion is formed with the relatively large hydrated Rb^{+} cation [25] or with protonated diaminocyclohexane [27] whereas the Tl^{+} cation forces the crystallization of a three-dimensional network [26]. In the compounds containing the $[SbS_2]^{-}$ or the $[Sb_2S_4]^{2-}$ anion the interconnection of the primary building units yields chain anions [21–24]. For other thioantimonates like those with the $[Sb_4S_7]^{2-}$ or $[Sb_8S_{13}]^{2-}$ anions the determination of the dimensionality of the anionic network is less straightforward because Sb–S distances often scatter between about 2.3 and 3.6 Å. The compound $(NH_4)_2[Sb_4S_7]$ [28] should serve as an example. If only Sb–S separations below 3.0 Å are considered $[Sb_4S_7]^{2-}$ chains can be identified. Increasing the value for Sb–S distances to 3.4 Å the anion becomes layered. It is beyond the scope of the present paper to analyze all thioantimonates with respect to composition and network dimensionality. A more detailed discussion on this topic can be found in [52].

Most thioantimonate compounds contain the Sb^{3+} cation, but there are also some examples for Sb^{5+} containing samples. Furthermore, mixed-valent Sb^{3+}/Sb^{5+} compounds were reported in the past [56]. Another special structural feature is the ability of

---

* Corresponding author. Institut für Anorganische Chemie, Christian-Albrechts-Universität zu Kiel, Max-Eyth Str.2, Kiel 24118, Germany. Tel.: +49(431)8802091; fax: +49 (431)8801520.
E-mail address: wbensch@ac.uni-kiel.de (W. Bensch).

1293-2558/$ – see front matter © 2010 Elsevier Masson SAS. All rights reserved.
doi:10.1016/j.solidstatesciences.2010.03.004

thioantimonate anions to form bonds to transition metal cations and transition metal complexes [40,57–71]. Concerning the small thioantimonate anions $[SbS_3]^{3-}$, $[Sb_2S_5]^{4-}$, $[Sb_3S_6]^{3-}$ and $[Sb_4S_8]^{4-}$, there are only few examples where these units act as ligands joining metal cations. The first example for the $[SbS_3]^{3-}$ anion was the compound $[Cr(tren)SbS_3]$ (tren = tris(2-aminoethyl)amine) where the anion acts in a bidentate fashion completing the octahedral environment around the Cr^{3+} cation [2]. Further examples are the compounds $[Cr(tren)]SbS_3 \cdot H_2O$ [72] and $[Cr(trien)]SbS_3$ (trien = triethylenetetramine) [73]. The larger anion $[Sb_4S_8]^{4-}$ was found in $[M(tren)]_2[Sb_4S_8]$ (M = Co, Zn) where the anion acts as a bidentate ligand joining two independent cations using a terminal S atom [15, 65]. Applying an amine like diethylenetriamine or 1,3-diaminopropane which coordinatively saturates the transition metal cation, the isolated $[Sb_4S_8]^{4-}$ anion is observed like in $[Mn(1,3\text{-dap})_3]_2[Sb_4S_8] \cdot 2H_2O$ [20] or $[Ni(dien)_2]_2[Sb_4S_8]$ [19]. Until now, the $[Sb_3S_6]^{3-}$ moiety was only observed in cation–anion isolated compounds like in $[Ni(C_4H_{13}N_3)_2]_3(Sb_3S_6)_2$ [18]. The isolated $[Sb_2S_5]^{4-}$ anion was found in $[Fe(en)_3]_2Sb_2S_5 \cdot 0.55H_2O$ [74] and $[Mn(en)_3]_2Sb_2S_5$ [10]. Very recently we were able to synthesize and characterize the compound $[La(C_4N_3H_{13})_2(\mu_4\text{-}Sb_2S_5)(\mu_3\text{-}SO_4)]_n$ with the $[Sb_2S_5]^{4-}$ anion acting as a tetradentate ligand [13].

It is well documented that In^{3+} prefers a tetrahedral coordination in the presence of S^{2-} anions [75,76]. The aim of the present work was to synthesize compounds consisting of interlinked $[Sb_xS_y]$ and $[InS_4]$ tetrahedra enhancing the structural diversity of the thiometalate chemistry. Instead of such mixed thioantimonate-thioindate compounds the title compound with composition $\{[In(C_6H_{14}N_2)_2]_2Sb_4S_8\}Cl_2$ was obtained containing a tetradentate $[Sb_4S_8]^{4-}$ anion bridging two symmetry related In^{3+} centred InN_4S_2 octahedra. In the manuscript we report on the solvothermal synthesis, crystal structure and properties of this new compound.

2. Results and discussion

The title compound crystallizes in the monoclinic space group C2/c with one unique In atom, two independent Sb atoms and four unique S atoms being located on general positions. There are also two independent 1,2-trans-diaminocyclohexane ligands with all C, N and H atoms located also on general positions. As mentioned in the experimental section, the Cl^- anion is highly disordered, not allowing to find a suitable model for the refinement. The In^{3+} cation is in an octahedral environment of four N atoms of two amine molecules and of two S atoms of the $[Sb_4S_8]^{4-}$ anion (Fig. 1). The $[Sb_4S_8]^{4-}$ anion is constructed by the condensation of two $[SbS_3]^{3-}$ pyramids yielding a $[Sb_2S_5]$ group, and two such groups share a common edge resulting in a Sb_2S_2-ring with a center of inversion in the center of the ring (Fig. 1). The Sb–S bond lengths are between 2.394(5) and 2.566(6) Å and the corresponding S–Sb–S angles are in the range reported in literature [see references cited in Introduction]. We note that the Sb(1)–S(4) separation of 3.606 Å is slightly shorter than the sum of the van der Waals radii of 3.8 Å. The In-N bonds between 2.272(11) and 2.299 (13) Å are in agreement with data given in literature for In^{3+} in an octahedral environment [77]. A search in the Cambridge Structure Database reveals that only two compounds were structurally characterized containing In^{3+} in the environment of four N and two S atoms [78,79]. In these two compounds the In–S bond lengths are between 2.505 and 2.558 Å matching with the values of 2.525(3) and 2.566(6) Å in the title compound (Table 2). The InN_4S_2 octahedron is severely distorted as evidenced by the angles around In^{3+} (Table 2).

The $[Sb_4S_8]^{4-}$ anion in the title compound exhibits a very different bonding pattern of the primary thioantimonate units compared to that observed for $[M(tren)]_2[Sb_4S_8]$ [15,65]. In the latter compounds the thioantimonate(III) anion is constructed by two SbS_3 and two SbS_4 units. The central part of the anion is formed by the two edge-sharing SbS_4 groups yielding a Sb_2S_6 moiety (Fig. 2). The two SbS_3 pyramids are condensed to the central unit through a common edge leaving only two terminal S atoms free for bond formation to the transition metal cation (Fig. 2). The bonding pattern of the anion in $[M(tren)]_2[Sb_4S_8]$ leads to significantly different Sb–S bond lengths and angles around the Sb atoms compared to those found for the $[Sb_4S_8]^{4-}$ anion in the title compound. The Sb–S bonds for the two central Sb atoms range from 2.393 to 2.760 Å, while those in the two SbS_3 pyramids are between 2.378 and 2.468 Å, being comparable with the data observed for the anion in the title compound.

In the unit cell the $\{[In(C_6H_{14}N_2)_2]_2Sb_4S_8\}^{2+}$ cations form rods being approximately directed along [101] (Fig. 3). Along the a-axis the ligands surrounding In^{3+} point face-to-face and this orientation leads to screening of the central thioantimonate in the $\{[In(C_6H_{14}N_2)_2]_2Sb_4S_8\}^{2+}$ cation. The orientation and arrangement of the molecules seem to be forced by N–H···S bonding interactions stabilizing the packing of the constituents. There is one intra-molecular S···H contact (S(3)···N(12) = 3.385 Å; angle S···H–N: 148.7°) and three inter-molecular S···H interactions (S(1)–N(1): 3.530 Å; angle: 166.3°; S(2)–N(1): 3.421 Å; angle: 169.4°; S(3)–N(11): 3.567 Å; angle: 145.8°). The S···H bonding interactions lead to the formation of a three-dimensional network.

The optical band-gap E_g of the compound was determined with diffuse UV–Vis spectroscopy (Fig. 4). The value for E_g of 2.03 eV is in good agreement with the red color and indicates that the title compound is a wide-gap semiconductor.

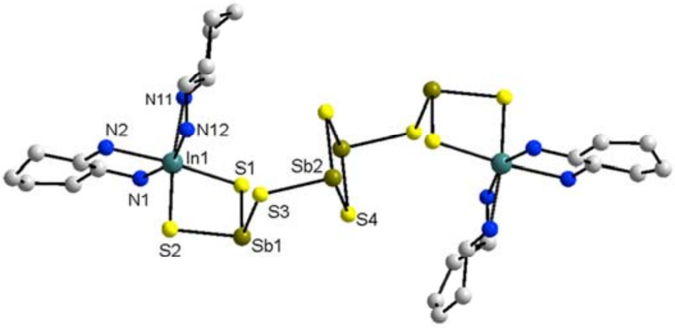

Fig. 1. The cationic moiety in the crystal structure of $\{[In(C_6H_{14}N_2)_2]_2Sb_4S_8\}Cl_2$ together wit atom labelling. Note that not all atoms are labelled and H atoms are omitted for clarity.

Table 1
Selected crystal data and some refinement results for {[In($C_6H_{14}N_2$)$_2$]$_2$$Sb_4S_8$}$Cl_2$.

Formula weight	1429.89
Temperature	293(2) K
Crystal system	Monoclinic
Space group	C2/c
Unit cell dimensions	$a = 29.0259(12)$ Å $b = 6.7896(2)$ Å $c = 24.2023(12)$ Å $\beta = 99.524(4)°$
Volume	4703.9(3) Å^3
Z	4
Density (calculated)	2.019 Mg/m^3
Absorption coefficient	3.611 mm^{-1}
Theta range for data collection	1.42 to 25.66°
Index ranges	−35<=h<=33, −7<=k<=8, −29<=l<=29
Reflections collected	23571
Independent reflections	4441 [$R_{int} = 0.0743$]
Goodness-of-fit on F^2	1.054
Final R indices [$I > 2\sigma(I)$]	R1 = 0.0839, wR2 = 0.2190
R indices (all data)	R1 = 0.0986, wR2 = 0.2311
Largest diff. peak and hole	3.582 and −1.978 e.Å^{-3}

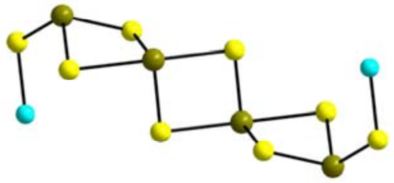

Fig. 2. The [$M_2(Sb_4S_8)$] unit in the compounds [M(tren)]$_2$[Sb_4S_8] [15,65]. Note that only the metal atoms are displayed and the coordinating amines are omitted.

In the Raman spectrum (Fig. 5) several prominent resonances occur, which are partially due to Sb–S vibrations being located between 100 and 400 cm^{-1}. On the basis of literature data [72] the band located at 336 cm^{-1} is tentatively assigned to the stretching vibration of the SbS_3 pyramid. The resonance is relatively broad with shoulders on both the low and high frequency side and may contain more than one such stretching mode. We note that the center of the signal is shifted to a lower value compared to the mode observed in [Cr(tren)SbS_3]·H_2O (tren = tris(2-aminoethyl)amine) [72] where one of the S atoms of the SbS_3^{3-} anion is terminal. In (CuI_2)Cu_3SbS_3 containing an isolated [SbS_3]$^{3-}$ anion two resonances occur at 362 and 339 cm^{-1}. Increasing the number of Sb–S contacts these bands shift to lower frequencies by about 60 cm^{-1} in $MnSb_2S_4$ [80,81]. The weak signal at 287 cm^{-1} may be an indication that the Sb(1) atom has a 3 + 1 environment with one S atom at about 3.60 Å. For [Cr(tren)SbS_3]·H_2O the asymmetric S–Sb–S stretching mode was observed at 285 cm^{-1} with an intensity much higher than that found in the title compound. Due to the somewhat longer Sb–S bonds in the title compound compared to those reported for [Cr(tren)SbS_3]·H_2O this asymmetric stretching vibration may be shifted to lower frequencies occurring as the strong band at 261 cm^{-1}. The assignment of the signals below about 200 cm^{-1} is not unambiguous due to the simultaneous occurrence of lattice vibrations in this energy region. In [Cr(tren)SbS_3]·H_2O the symmetric S-Sb-S bending mode was located at 106 cm^{-1} and the symmetric Sb–S/S/S deformation vibration at 145 cm^{-1}. For the title compound a weak signal at 99 cm^{-1} and a stronger at 142 cm^{-1} may be due to these two modes.

Table 2
Selected bond lengths (Å) and angles (°) for {[In($C_6H_{14}N_2$)$_2$]$_2$$Sb_4S_8$}$Cl_2$. Estimated standard deviations are given in parentheses.

In(1)-N(12)	2.272(11)	In(1)-N(11)	2.299(11)
In(1)-N(1)	2.294(11)	In(1)-N(2)	2.299(13)
In(1)-S(1)	2.525(3)	In(1)-S(2)	2.544(4)
Sb(1)-S(1)	2.411(4)	Sb(1)-S(2)	2.436(4)
Sb(1)-S(3)	2.496(5)	Sb(2)-S(4)	2.394(5)
Sb(2)-S(3)	2.484(5)	Sb(2)-S(4)	2.566(6)
N(12)-In(1)-N(1)	158.6(4)	N(12)-In(1)-N(2)	86.6(5)
N(1)-In(1)-N(2)	75.8(4)	N(12)-In(1)-N(11)	75.7(4)
N(1)-In(1)-N(11)	92.0(4)	N(2)-In(1)-N(11)	90.5(5)
N(12)-In(1)-S(1)	102.9(3)	N(1)-In(1)-S(1)	94.9(3)
N(2)-In(1)-S(1)	170.5(4)	N(11)-In(1)-S(1)	91.8(3)
N(12)-In(1)-S(2)	89.5(3)	N(1)-In(1)-S(2)	103.5(3)
N(2)-In(1)-S(2)	93.4(5)	N(11)-In(1)-S(2)	164.5(3)
S(1)-In(1)-S(2)	86.86(13)		
S(1)-Sb(1)-S(2)	91.98(13)		
S(1)-Sb(1)-S(3)	100.27(15)		
S(2)-Sb(1)-S(3)	93.21(16)		
S(4)-Sb(2)-S(3)	100.23(17)		
S(4)-Sb(2)-S(4A)	90.58(16)		
S(3)-Sb(2)-S(4A)	98.94(17)		
Sb(1)-S(1)-In(1)	89.20(11)		
Sb(1)-S(2)-In(1)	88.21(12)		
Sb(2)-S(3)-Sb(1)	106.08(16)		
Sb(2)-S(4)-Sb(2A)	89.42(16)		

The DTA-TG curves of the thermal decomposition of {[In($C_6H_{14}N_2$)$_2$]$_2$$Sb_4S_8$}$Cl_2$ are displayed in Fig. 6. The first mass loss occurs at $T_{onset} = 270$ °C which is accompanied by an intense endothermic event. Just above the first thermal event a second emission is seen ($T_{onset} = 320$ °C), which is also accompanied by an endothermic peak that is less intense. The intermediate formed at $T > 350$ °C is stable up to about 550 °C and the continuous weight loss above this temperature is due to evaporation of the compound. Making C–H–N analyses of the material after DTA-TG until 700 °C it was found that 2.12 % of carbon remains. Hence it is plausible that Cl (4.72 %) is being released before 350 °C together with most of the amine yielding a total weight loss of 31.3% (the total amount of amine is 30.43%).

An in-situ time resolved X-ray powder diffraction experiment (Fig. 7) was performed to gain more information about the thermal decomposition reaction. Before the decomposition of the material at about 270 °C the most intense reflections shift to larger scattering angles. Above 270 °C, where the amine starts to be eliminated from the compound, no reflection can be seen in the powder pattern indicating amorphization of the sample. At about 320 °C several reflections appear which can mainly be indexed with the structure of $InSbS_3$ [82]. Increasing the temperature to about 590 °C the reflections of $InSbS_3$ disappear and new reflections develop which can be explained on the basis of the formation of antimony stabilized γ-In_2S_3 [83]. The powder pattern of the final product (Fig. 8) shows the reflections of γ-In_2S_3 and a weak reflection of crystalline elemental Sb. The formation of γ-In_2S_3 implies that antimony and sulfur are evaporated at elevated temperatures.

According to the chemical composition of the title compound with the In:Sb:S ratio of 1:2:4, the ternary compound $InSbS_3$ crystallized at the intermediate temperatures must be contaminated at least by Sb and S. But no indications for a crystalline compound composed of Sb and S or reflections of elemental Sb could be found in the powder patterns.

Further in-situ X-ray diffraction experiments were performed investigating the alterations of the lattice parameters of the compound upon heating and cooling. A scan from 30 to 220 °C and back to room temperature of the region of the pattern with the most intense reflections (200), (20-2), (400), and (40-2) is displayed in Fig. 9. Only the position of the (20-2) reflection remains nearly constant during the heating and cooling cycle, whereas the other three reflections exhibit a reversible shift first to higher scattering angles and then back to the starting values upon cooling. These findings indicate a negative thermal expansion of the a-axis and a positive thermal expansion of the c-axis, which almost compensate each other. Powder patterns measured up to

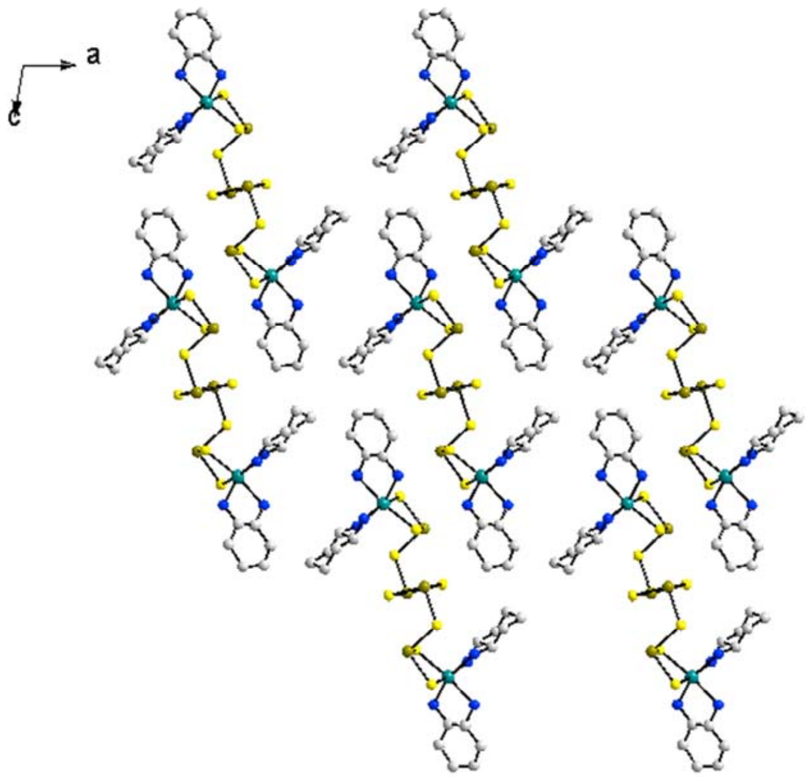

Fig. 3. Arrangement of the $\{[In(C_6H_{14}N_2)_2]_2Sb_4S_8\}^{2+}$ cations. The H atoms are not drawn and the Cl^- anions could not be located.

50° 2θ were used to estimate the lattice parameters applying the Pawley method, and the results are compiled in Table 3. Between 30 and 120 °C the *a*-axis exhibits a decrease of 0.509 Å and the *c*-axis is enlarged by 0.297 Å, whereas the *b*-axis becomes slightly larger by 0.034 Å. The negative thermal expansion coefficient α_a is about -566×10^{-6} Å/K (relative expansion rate α: $-194 \times 10^{-6} K^{-1}$) and the value for α_c is about $330 \cdot 10^{-6}$ Å/K (relative rate α: $136 \times 10^{-6} K^{-1}$). Increasing the temperature to 220 °C the *a*-axis is shortened by 0.235 Å and the *c*-axis is enlarged by 0.238 Å, i.e., the corresponding expansion coefficients are $\alpha_a \approx -235 \times 10^{-6}$ Å/K (relative α: $-82 \times 10^{-6} K^{-1}$) and $\alpha_c \approx 238 \times 10^{-6}$ Å/K (relative α: $97 \times 10^{-6} K^{-1}$). Again the *b*-axis is only slightly affected. The overall decrease of the *a*-axis is about 0.74 Å and the increase of the *c*-axis is about 0.54 Å. All values are extraordinary large compared to data reported in literature (see below). The coexistence of uniaxial negative thermal expansion (*a*-axis) and a biaxial positive thermal

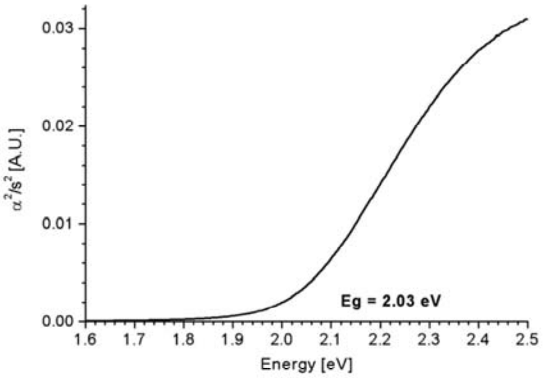

Fig. 4. UV–Vis spectrum of $\{[In(C_6H_{14}N_2)_2]_2Sb_4S_8\}Cl_2$.

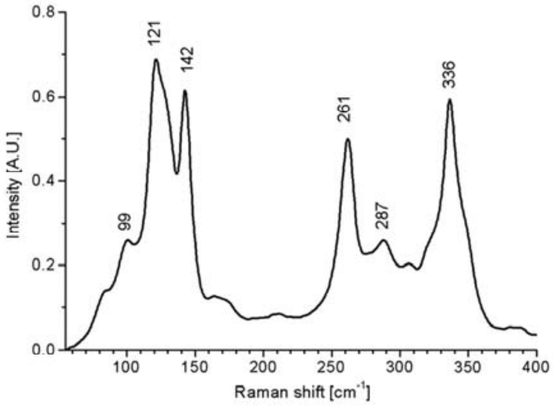

Fig. 5. Raman spectrum of $\{[In(C_6H_{14}N_2)_2]_2Sb_4S_8\}Cl_2$ with the wavenumbers of the main resonances in cm^{-1}.

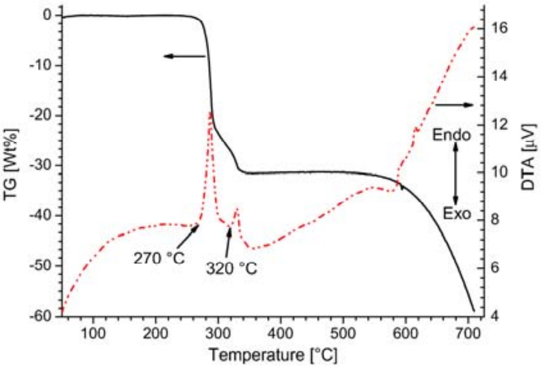

Fig. 6. The DTA-TG curves for $\{[In(C_6H_{14}N_2)_2]_2Sb_4S_8\}Cl_2$ with the onset temperatures of the first two events are indicated.

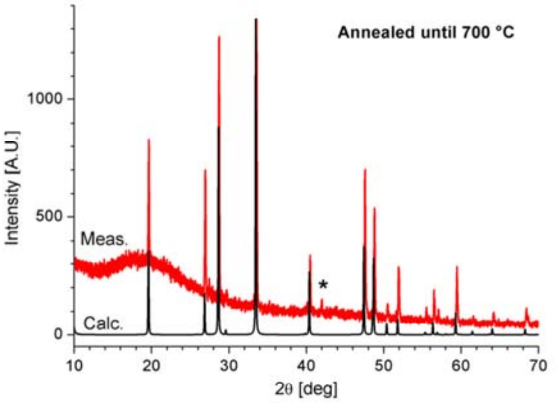

Fig. 8. The X-ray powder pattern of the final decomposition product obtained at 700 °C together with the calculated pattern of γ-In_2S_3. The reflection marked with the asterisk coincides with one of elemental Sb.

expansion (*b*- and *c*-axes) is a very rare case. The axes expand resp. contract roughly to the starting values. The small differences between the data obtained at the beginning and the end of the experiment are caused by reduction of the crystallinity of the sample which may be due to stress exposed by the strong anisotropic thermal behavior. A comparison of the shape of the reflections before and after the heating/cooling cycle shows a small broadening and the development of not well pronounced shoulders. We note that the monoclinic angle β is also affected and decreases upon heating and increases again when the sample is cooled to room temperature. The unit cell volume exhibits a small increase with increasing temperature and nearly approaches the value obtained at the beginning of the experiment.

Very recently a so-called colossal positive and negative thermal expansion (PTE and NTE) was reported for the framework compound $Ag_3[Co(CN)_6]$ [85] and exceptionally large PTE and NTE for an organic sample [86]. For the former compound the relative expansion rates are $150–130 \times 10^{-6}K^{-1}$ and -130 to $-120 \times 10^{-6}K^{-1}$ (temperature range: −257 to 230 °C) for the *a*- and *c*-axes, respectively. For the second compound the coefficient for the PTE reaches the very large value of $515 \times 10^{-6}K^{-1}$ (lowest value: $156 \times 10^{-6}K^{-1}$) and data for biaxial NTE are between $-32 \times 10^{-6}K^{-1}$ and $-204 \times 10^{-6}K^{-1}$ in the relatively narrow temperature range of 110 °C. Comparing the data obtained for the title compound with that of well established uniaxial NTE materials like ZrW_2O_8 ($\alpha = -9 \times 10^{-6}K^{-1}$) [87] or $Cd(CN)_2$ ($\alpha = -20 \times 10^{-6}K^{-1}$) [88] it is obvious that the thermal expansion behavior is highly unusual.

At the present stage of analysis no structural picture is at hand explaining the reversible thermal expansion properties. Single crystal X-ray diffraction experiments at elevated temperatures are planned in the near future which supply the information about structural changes thus explaining the observed behavior.

3. Experimental section

3.1. Sample synthesis

$InCl_3$ (0.313 mmol), Sb (0.627 mmol) and S (1.697 mmol) were mixed with 5 mL of 1,2 trans-diaminocyclohexane in a 35 mL Teflon-lined stainless steel autoclave. The sealed vessel was heated at 190 °C for 10 days. After cooling down to room temperature, the product was filtered off, and washed with water, ethanol and acetone. Red needle-like crystals were obtained in a yield of about 95% based on Sb.

CHNS analysis found : N = 7.51%, C = 18.42%, H = 3.86%,
S = 17.02%
Expected : N = 7.46%, C = 19.20%, H = 3.76%, S = 17.09%

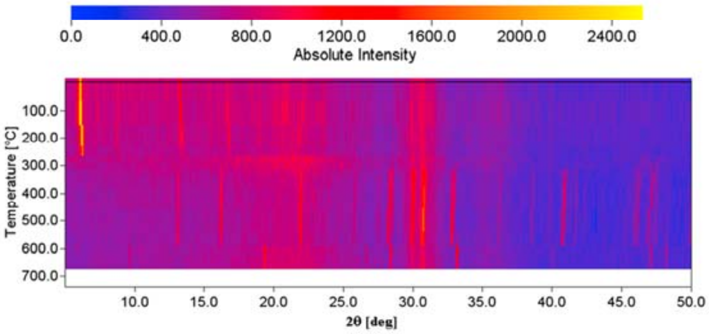

Fig. 7. In-situ X-ray powder patterns recorded during thermal decomposition of the title compound.

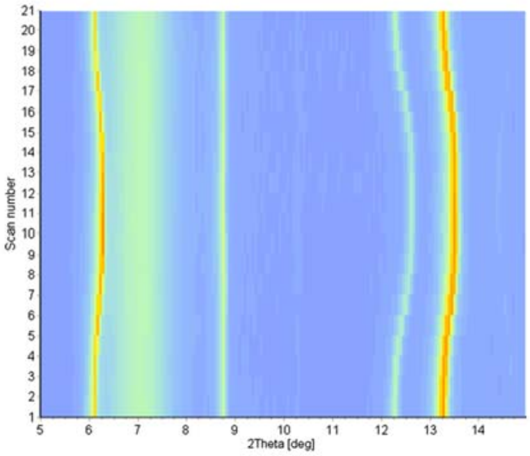

Fig. 9. Temperature dependent X-ray powder pattern of the title compound varying the temperature from 30 °C (step 1) to 220 °C (step 11) and back to 30 °C (step 21) with step size of 20 °C. Reflections from left to right: (200), (20-2), (400), and (40-2). The feature between about 6.5 and 7.5° 2θ is caused by the sample holder.

3.1.1. *Single crystal structure analysis*

The data were measured using an Imaging Plate Diffraction System (IPDS1) from Stoe & CIE with MoK_α radiation). The structure was solved with direct methods using SHELXS-97 [84]. Structure refinement was performed with SHELXL-97 [84]. All non-hydrogen atoms were refined with anisotropic displacement parameters. All hydrogen atoms were positioned with idealized geometry and refined isotropically using a riding model. Relatively large residual electron densities were found in the Fourier map which obviously originates from Cl, but due to a pronounced disorder no suitable structural model could be found. Therefore, the data were corrected for disordered solvent using the SQUEEZE option in Platon. Selected crystal data and results of the structure refinement are shown in Table 1.

However, the presence of Cl in the crystal used for X-ray data collection was proved with EDX (see Fig. S1 in the supporting information). The presence of Cl in the compound was proved with classical chemical analysis. About 25 mg of the sample was dissolved in conc. HNO_3 and to the solution $AgNO_3$ was added giving immediately a white precipitate. Both EDX and X-ray powder diffractometry evidenced that the white powder was AgCl.

Crystallographic data (excluding structure factors) have been deposited with the Cambridge Crystallographic Data Centre as supplementary publication no. CCDC 767530. Copies of the data can be obtained, free of charge *via* www.ccdc.cam.ac.uk/data_request/cif.

Table 3
The lattice parameters obtained at different temperatures using the Pawley approach.

T/°C	a/Å	b/Å	c/Å	β/°	V/Å^3
30	29.129	6.795	24.203	99.93	4718.8
120	28.620	6.829	24.500	99.69	4720.1
220	28.385	6.838	24.738	99.70	4732.9
120	28.696	6.845	24.464	99.79	4735.3
30	29.199	6.790	24.192	100.11	4721.9

3.1.2. *DTA-TG measurements*

DTA-TG measurements were performed in Al_2O_3 crucibles using a STA-409CD thermobalance from Netzsch. The measurements were performed in Al_2O_3 crucibles under a nitrogen atmosphere with a heating rate of 4 K/min.

3.1.3. *X-Ray powder diffractometry*

The homogeneity of the product was checked with X-ray powder patterns, which were recorded on a Stoe STADI P diffractometer (Ge monochromator, *CuKα* radiation, $\lambda = 1.54056$ Å). The in-situ X-ray diffraction experiment was performed in quartz capillary using a graphite-tube furnace. The heating rate was 50 K/min. Temperature dependent X-ray powder patterns were also recorded in the temperature range from 30 to 220 °C in reflection geometry on a PANalytical X'pert-PRO diffractometer in He atmosphere equipped with PIXcel detector. The heating chamber was an HTK1200N of Anton Paar. The step size was 0.00656° with 197.37 s counting time per step. The heating rate was set at 10 °C/min, with 1min. waiting time before measuring the pattern. From step 1 to step 10 of Fig. 9 every step represents an increase of 20 °C in temperature in the range from 30 °C (step 1) until 210 °C (step 10). Step 11 is the scan done at 220 °C. From step 12 to step 21 every step represents a decrease of 20 °C from 210 °C (step 12) to 30 °C (step 21). X-ray powder patterns were also recorded up to 50° 2θ at 30, 120, 220, 120 and 30 °C using the same experimental parameters as mentioned above.

3.1.4. *Raman spectroscopy*

Raman spectra were recorded in the region 100–3500 cm^{-1} with a Bruker IFS 66 Fourier Transform Raman spectrometer (wavelength: 541.5 nm).

3.1.5. *UV/Vis spectroscopy*

UV/Vis spectroscopic investigations were conducted at room temperature using a UV/Vis-NIR two-channel spectrometer Cary 5 from Varian Techtron Pty., Darmstadt. The optical properties of the compound were investigated by studying the UV/Vis reflectance spectrum of the powdered sample. The absorption data were calculated with the Kubelka-Munk relation for diffuse reflectance data. $BaSO_4$ powder was used as reference material.

3.1.6. *Scanning electron microscopy (SEM)/energy dispersive X-ray fluorescence (EDX)*

EDX analyses were done with a Philips ESEM XL30 instrument equipped with an EDAX detector.

Acknowledgements

The authors thank Jannes Ophey for his support performing the XRD measurements. The support of DAAD and CONACyT is appreciated.

Appendix. Supplementary data

Supplementary data associated with this article can be found in the online version, at doi:10.1016/j.solidstatesciences.2010.03.004.

References

[1] H.A. Graf, H. Schäfer, Z. Anorg. Allg. Chem. 414 (1975) 220.
[2] M. Schur, H. Rijnberk, C. Näther, W. Bensch, Polyhedron 18 (1998) 101.
[3] G. Cordier, H. Schäfer, Rev. Chim. Miner. 18 (1981) 218.
[4] H.A. Graf, H. Schäfer, Z. Anorg. Allg. Chem. 425 (1976) 67.
[5] P. Dürichen, W. Bensch, Z. Krist. NCS 212 (1997) 95.
[6] P. Dürichen, W. Bensch, Z. Krist. 211 (1996) 636.
[7] M. Schur, W. Bensch, Acta Cryst. C56 (2000) 1107.

[8] M. Schaefer, L. Engelke, C. Näther, W. Bensch, Z. Anorg. Allg. Chem. 629 (2003) 1912.
[9] R. Stähler, C. Näther, W. Bensch, Acta Cryst. C57 (2001) 26.
[10] D.-X. Jia, Y. Zhang, J. Dai, Q.-Y. Zhu, X.-M. Gu, J. Solid State Chem. 177 (2004) 2477.
[11] D.-X. Jia, Q.-Y. Zhu, J. Dai, W. Lu, W.-J. Guo, Inorg. Chem. 44 (2005) 819.
[12] L. Engelke, C. Näther, P. Leisner, W. Bensch, Z. Anorg. Allg. Chem. 634 (2008) 2959.
[13] J. Lichte, C. Näther, W. Bensch, Z. Anorg, Allg. Chem. 636 (2010) 108.
[14] W.-W. So, B.R. Martin, P.K. Dorhout, Z. Kristallogr. NCS 217 (2002) 302.
[15] R. Stähler, W. Bensch, J. Chem. Soc., Dalton Trans. (2001) 2518.
[16] G. Cordier, H. Schäfer, C. Schwidetzky, Rev. Chim. Miner. 22 (1985) 722.
[17] M. Schaefer, C. Näther, N. Lehnert, W. Bensch, Inorg. Chem. 43 (2004) 2914.
[18] R. Kiebach, F. Studt, C. Näther, W. Bensch, Eur. J. Inorg. Chem. (2004) 2553.
[19] W. Bensch, C. Näther, R. Stähler, Chem. Commun. (2001) 477.
[20] L. Engelke, W. Bensch, Acta Cryst. E59 (2003) m378.
[21] K. Volk, P. Bickert, R. Kolmer, H. Schäfer, Z. Naturforsch. 34b (1979) 380.
[22] H.A. Graf, H. Schäfer, Z. Anorg. Allg. Chem. 414 (1975) 211.
[23] G. Cordier, C. Schwidetzky, H. Schäfer, J. Solid State Chem. 54 (1984) 84.
[24] M. Schur, A. Gruhl, C. Näther, I. Jess, W. Bensch, Z. Naturforsch. 54b (1999) 1524.
[25] K. Volk, H. Schäfer, Z. Naturforsch. 34b (1979) 172.
[26] M. Gostojic, W. Nowacki, P. Engel, Z. Kristallogr. 159 (1982) 217.
[27] L. Engelke, C. Näther, W. Bensch, Eur. J. Inorg. Chem. (2002) 2936.
[28] G. Dittmar, H. Schäfer, Z. Anorg. Allg. Chem. 437 (1977) 183.
[29] G. Dittmar, H. Schäfer, Z. Anorg. Allg. Chem. 441 (1978) 98.
[30] G. Dittmar, H. Schäfer, Z. Anorg. Allg. Chem. 441 (1978) 93.
[31] B. Eisenmann, H. Schäfer, Z. Naturforsch. 34b (1979) 383.
[32] G. Cordier, H. Schäfer, C. Schwidetzky, Z. Naturforsch. 39b (1984) 131.
[33] W.S. Sheldrick, H.-J. Häusler, Z. Anorg. Allg. Chem. 557 (1988) 105.
[34] W. Bensch, M. Schur, Z. Naturforsch. 52b (1997) 405.
[35] M. Schur, W. Bensch, Eur. J. Solid State Inorg. Chem. 34 (1997) 457.
[36] R. Stähler, C. Näther, W. Bensch, J. Solid State Chem. 174 (2003) 264.
[37] M. Schaefer, D. Kurowski, A. Pfitzner, C. Näther, W. Bensch, Acta Crystallogr. E60 (2004) m183.
[38] A. Puls, M. Schaefer, C. Näther, W. Bensch, A.V. Powell, S. Boissiere, A.M. Chippindale, J. Solid State Chem. 178 (2005) 1171.
[39] V. Spetzler, C. Näther, W. Bensch, Z. Naturforsch. 61b (2006) 715.
[40] M. Schaefer, R. Stähler, W.-R. Kiebach, C. Näther, W. Bensch, Z. Anorg. Allg. Chem. 630 (2004) 1816.
[41] R. Kiebach, A. Griebe, C. Näther, W. Bensch, Solid State Sci. 8 (2006) 541.
[42] E. Quiroga-González, C. Näther, W. Bensch, Z. Naturforsch. 64b (2009) 1.
[43] H. Rijnberk, C. Näther, W. Bensch, Monatsh. Chem. 131 (2000) 721.
[44] R. Stähler, C. Näther, W. Bensch, Eur. J. Chem. (2001) 1835.
[45] V. Spetzler, R. Kiebach, C. Näther, W. Bensch, Z. Anorg. Allg. Chem. 630 (2004) 2398.
[46] R. Kiebach, R. Warratz, C. Näther, W. Bensch, Z. Anorg. Allg. Chem. 635 (2009) 988.
[47] R.J.E. Lees, A.V. Powell, D.J. Watkin, A.M. Chippindale, Acta Crystallogr. C63 (2007) m27.
[48] R.J.E. Lees, A.V. Powell, A.M. Chippindale, J. Phys. Chem. Solids 68 (2007) 1215.
[49] K. Volk, H. Schäfer, Z. Naturforsch. 34b (1979) 1637.
[50] X. Wang, F. Liebau, J. Solid State Chem. 111 (1994) 385.
[51] M. Zhang, T.L. Sheng, X.H. Huang, R.B. Fu, X. Wang, S.M. Hu, S.C. Xiang, X.T. Wu, Eur. J. Inorg. Chem. (2007) 1606.
[52] A. Puls, C. Näther, R. Kiebach, W. Bensch, Solid State Sci. 8 (2006) 1085.
[53] X. Wang, T.-L. Sheng, J.-S. Chen, S.-M. Hu, R.-B. Fu, X.-T. Wu, J. Mol. Struct. 936 (2009) 142.
[54] X. Wang, A.J. Jacobson, F. Liebau, J. Solid State Chem. 140 (1998) 387.
[55] R. Stähler, W. Bensch, Z. Anorg. Allg.Chem. 628 (2002) 1657.
[56] R. Stähler, B.D. Mosel, H. Eckert, W. Bensch, Angew. Chem. 114 (2002) 4671 Angew. Chem. Int. Ed. 41 (2002) 4487.
[57] R. Kiebach, W. Bensch, R.D. Hoffmann, R. Pöttgen, Z. Anorg. Allg. Chem. 629 (2003) 532.
[58] M. Schaefer, C. Näther, W. Bensch, Solid State Sci. 5 (2003) 1135.
[59] M. Schur, C. Näther, W. Bensch, Z. Naturforsch. 56b (2001) 79.
[60] V. Spetzler, C. Näther, W. Bensch, Inorg. Chem. 44 (2005) 5805.
[61] V. Spetzler, H. Rijnberk, C. Näther, W. Bensch, Z. Anorg. Allg. Chem. 630 (2004) 142.
[62] M. Schaefer, D. Kurowski, A. Pfitzner, C. Näther, Z. Rejai, K. Möller, N. Ziegler, W. Bensch, Inorg. Chem. 45 (2006) 3726.
[63] L. Engelke, R. Stähler, M. Schur, C. Näther, W. Bensch, R. Pöttgen, M.H. Möller, Z. Naturforsch. 59 (2004) 869.
[64] A. Puls, C. Näther, W. Bensch, Z. Anorg. Allg. Chem. 632 (2006) 1239.
[65] M. Schaefer, C. Näther, W. Bensch, Monatsh. Chem. 135 (2004) 461.
[66] V. Spetzler, C. Näther, W. Bensch, J. Solid State Chem. 179 (2006) 3541.
[67] H.G. Yao, M. Ji, S.H. Ji, R.C. Zhang, Y.L. An, G.L. Ning, Cryst. Growth Design 9 (2009) 3821.
[68] J. Zhou, G.Q. Bian, Q.Y. Zhu, Y. Zhang, C.Y. Li, J. Dai, J. Solid State Chem. 182 (2009) 259.
[69] R. Stähler, W. Bensch, Eur. J. Inorg. Chem. (2001) 3073.
[70] M. Schur, W. Bensch, Z. Naturforsch. 57b (2002) 1.
[71] H.-O. Stephan, M.G. Kanatzidis, J. Am. Chem. Soc. 118 (1996) 12226.
[72] K. Möller, C. Näther, A. Bannwarth, W. Bensch, Z. Anorg. Allg. Chem. 633 (2007) 2635.
[73] P. Vaqueiro, A.M. Chippindale, A.V. Powell, Polyhedron 22 (2003) 2839.
[74] R.J.E. Lees, A.V. Powell, A.M. Chippindale, Polyhedron 24 (2005) 1941.
[75] P. Feng, X. Bu, N. Zheng, Acc. Chem. Res. 38 (2005) 293.
[76] X. Bu, N. Zheng, P. Feng, Chem. Eur. J. 10 (2004) 3356.
[77] D. Pitzschke, W. Bensch, Angew. Chem. 115 (2003) 4525; Angew. Chem. Int. Ed. 42 (2003) 4389.
[78] S. Abram, C. Maichle-Mossmer, U. Abram, Polyhedron 17 (1998) 131.
[79] D.L. Reger, P.S. Coan, Inorg. Chem. 34 (1995) 6226.
[80] A. Pfitzner, D. Kurowski, Z. Kristallogr. 215 (2000) 373.
[81] A. Pfitzner, Chem. Eur. J. 3 (1997) 2032.
[82] H. Paulus, H. Fuess, S. Laminsi, J.K. Kom, Z. Kristallogr. 198 (1991) 125.
[83] R. Diehl, C.D. Carpentier, R. Nitsche, Acta Crystallogr. B32 (1976) 1257.
[84] G.M. Sheldrick, Acta Crystallogr. A64 (2008) 112.
[85] A.L. Goodwin, M. Calleja, M.J. Conterio, M.T. Dove, J.S.O. Evans, D.A. Keen, L. Peters, M.G. Tucker, Science 319 (2008) 794.
[86] D. Das, T. Jacobs, L.J. Barbour, Nat. Mater 9 (2010) 36.
[87] T.A. Mary, J.S.O. Evans, T. Vogt, A.W. Sleight, Science 272 (1996) 90.
[88] A.L. Goodwin, C.J. Kepert, Phys. Rev. B 71 (2005) 140301.

4.2.

Solvothermal Synthesis, Crystal Structure and Properties of $[Mg(en)_3][Sb_4S_7]$ – the First Thioantimonate(III) Containing a Main Group Metal Complex Cation as Structure Director

Enrique Quiroga-González, Christian Näther, and Wolfgang Bensch

Institute of Inorganic Chemistry, Christian-Albrechts-University of Kiel, Max-Eyth-Straße 2,
24118 Kiel, Germany

Reprint requests to Wolfgang Bensch. Fax: +49 431 880-1520. E-mail: wbensch@ac.uni-kiel.de

Z. Naturforsch. **2009**, *64b,* 1312 – 1318; received October 1, 2009

Dedicated to Professor Hubert Schmidbaur on the occasion of his 75th birthday

The new thioantimonate $[Mg(en)_3][Sb_4S_7]$ containing for the first time a $[Mg(en)_3]^{2+}$ cation as structure-directing unit was synthesized under solvothermal conditions applying elemental Mg, $SbCl_3$, S and ethylenediamine. The compound crystallizes in the monoclinic space group $P2_1/c$ with a = 9.9267(6), b = 14.254(1), c = 17.259(1) Å, β = 102.611(7)°, V = 2383.1(3) Å^3, Z = 4. In the structure trigonal SbS_3 pyramids are joined to form an Sb_3S_3 ring. The rings are connected through SbS_3 units yielding an undulated chain anion running along [001]. Considering so-called secondary Sb–S bonds, a layer-like thioantimonate anion is formed. The $[Mg(en)_3]^{2+}$ cations are located between the layers. Relatively short S···H–N contacts suggest hydrogen bonding interactions between the cation and the $[Sb_4S_7]^{2-}$ anion. The compound starts to decompose at about 220 °C. The optical band gap of 2.35 eV is in agreement with the orange color of the crystals. In the Raman spectrum prominent Sb–S resonances are seen between 250 and 400 cm^{-1} which can be assigned to different Sb–S vibrations.

Key words: Thioantimonate, Solvothermal Syntheses, Crystal Structure, Spectroscopic Properties

Introduction

The chemistry of thioantimonates(III) is characterized by a large variety of chemical compositions, primary and secondary building units (SBU) and dimensionalities of the thioantimonate networks. The latter is caused by a very flexible and hierarchical interconnection of the SBU, yielding different dimensionalities of the inorganic network even for a given Sb : S ratio [1 – 3]. An interesting aspect of the thioantimonate chemistry is the occurrence of mixed-valence Sb(III)/Sb(V) compounds like in $[Ni(dien)_2]_2Sb_4S_9$ [4]. Among the different Sb : S ratios observed in thioantimonate(III) compounds, the $[Sb_4S_7]^{2-}$ anion with Sb : S = 1 : 1.75 is the most common one. Until now about 40 compounds containing this anion have been reported [1, 3, 5 – 24]. Of special interest are open-framework thioantimonates with accessible empty voids, cages or holes. If small molecules within the voids in these frameworks can be exchanged, changes of the physical properties may be induced leading to potential applications as sensors, for example [25]. However, the interaction between the structure-directing molecules or cations with the negatively charged thioantimonate networks is strong and thus preventing the removal of the guests without collapse of the structures. An interesting synthetic approach is to pillar layered thioantimonates(III) with organic structure-directing molecules or metal complexes [26]. However, the successful pillaring of the layers depends on different factors like the thermal stability of the pillar under solvothermal conditions.

In the presence of organic ammonium cations S···H hydrogen bonding interactions play an important role. Compared to O···H or F···H bonds the strength of an individual S···H bond is significantly lower, but most thioantimonates(III) with such cations display a large number of such bonds, and therefore they cannot be neglected. Very often, the S···H bonding interaction leads to fully ordered NH_3 groups, and in most compounds the NH_3 group exhibits a special arrangement

0932–0776 / 09 / 1100–1312 $ 06.00 © 2009 Verlag der Zeitschrift für Naturforschung, Tübingen · http://znaturforsch.com

with respect to the S atoms of the thioantimonate network [27–30].

An example for a three-dimensional thioantimonate network is K$_2$Sb$_4$S$_7$ [6]. For most of the [Sb$_4$S$_7$]$^{2-}$-containing compounds the well-known counterion size effect is observed: large cations favor the formation of layers and/or chains. Large organic ammonium cations force the crystallization of layered compounds, and depending on the size and orientation of the cation, large interlayer separations are observed like 6.56 Å for (C$_2$H$_5$NH$_3$)$_2$Sb$_4$S$_7$ [16] or 9.90 Å for (CH$_3$(CH$_2$)$_4$NH$_3$)$_2$Sb$_4$S$_7$ [1]. The solvothermal synthesis method is most suitable for the preparation of thioantimonates(III). Many compounds were obtained using transition metal complexes either as starting material, or they are formed by *in situ* reaction between transition metal cations and the amine supplied as structure director and solvent [31–37]. Until now no thioantimonates(III) containing a main group metal complex cation as structure-directing unit have been reported. In our ongoing work we explored the possibility of using group 2 metal complexes for the synthesis of new thioantimonates(III). In this paper we report the solvothermal synthesis, crystal structure and some selected properties of the first alkaline-earth metal complex-containing thioantimonate(III), Mg(en)$_3$[Sb$_4$S$_7$].

Experimental Section

Synthesis

Mg (0.164 mmol), SbCl$_3$ (0.328 mmol) and S (0.657 mmol) were mixed with 5 mL of ethylenediamine in a 35 mL teflon-lined stainless-steel autoclave. The sealed vessel was heated at 170 °C for 10 d. After cooling to r. t., the product was filtered off and washed with water, ethanol and acetone. Large plate-like orange crystals were obtained in a yield close to 100 % based on Sb. Attempts to synthesize the analogous Ca and Sr compounds were not successful despite a large variation of the reaction parameters. Chemical analysis: calcd. N 9.17, C 8.86, H 2.94, S 23.5; found N 10.1, C 9.39, H 3.03, S 23.79 %.

Single-crystal structure analysis

The data were measured using an Imaging Plate Diffraction System (Stoe & Cie IPDS1) with MoK_α radiation. The structure was solved with Direct Methods using SHELXS-97 [38] and refined with SHELXL-97 [38]. All non-hydrogen atoms were refined with anisotropic displacement parameters. All hydrogen atoms were positioned with idealized geometry and refined isotropically using a riding model. Selected crystal structure data and results of the structure refinement are shown in Table 1.

Table 1. Crystal structure data and refinement results of [Mg(en)$_3$][Sb$_4$S$_7$].

Empirical formula	C$_6$H$_{24}$MgN$_6$S$_7$Sb$_4$
M_r, g mol^{-1}	916.04
Crystal size, mm^{-1}	0.15 × 0.11 × 0.07
Crystal system	monoclinic
Space group	$P2_1/c$
a, Å	9.9267(6)
b, Å	14.254(1)
c, Å	17.259(1)
β, deg	102.611(7)
V, Å^3	2383.1(3)
T, K	170
Z	4
D_calc, g cm^{-3}	2.55
2θ range, deg	5–56
μ (MoK_α), mm^{-1}	5.1
hkl range	−12/13; −18/18; −22/22
Refl. meas. / indep. / R_int	34189 / 5744 / 0.0372
Refl. with $I \geq 2\sigma(I)$	5522
Ref. parameters	218
$R1$ [$I \geq 2\sigma(I)$]/$wR2$ [all data]	0.0294 / 0.0794
Goof	0.970
$\Delta\rho_\text{fin}$ (max/min), e Å^{-3}	1.22 / −1.36

CCDC 752314 contains the supplementary crystallographic data for this paper. These data can be obtained free of charge from The Cambridge Crystallographic Data Centre *via* www.ccdc.cam.ac.uk/data_request/cif.

DTA-TG measurements

DTA-TG measurements were performed in Al$_2$O$_3$ crucibles using a STA-409CD thermobalance (Netzsch). The measurements were performed in Al$_2$O$_3$ crucibles under a nitrogen atmosphere with a heating rate of 4 °C min^{-1}.

X-Ray powder diffractometry

The homogeneity of the product was checked with X-ray powder patterns, which were recorded on a Stoe STADI P diffractometer (Ge monochromator, CuK_α radiation, λ = 1.54056 Å).

Raman spectroscopy

Raman spectra were recorded in the region 100–3500 cm^{-1} with a Bruker IFS 66 Fourier Transform Raman spectrometer (wavelength: 541.5 nm).

UV/Vis spectroscopy

UV/Vis spectroscopic investigations were conducted at r. t. using a UV/Vis-NIR two-channel spectrometer Cary 5 (Varian Techtron Pty., Darmstadt). The optical properties of the compound were investigated by studying the UV/Vis reflectance spectrum of the powdered sample. The absorption data were calculated with the Kubelka-Munk relation for diffuse reflectance data. $BaSO_4$ powder was used as reference material.

Scanning electron microscopy (SEM)/energy dispersive X-ray fluorescence (EDX)

EDX analyses were done with a Philips ESEM XL30 instrument equipped with an EDAX detector.

Elemental analysis

CHN analysis was performed using a Euro EA Elemental Analyzer (Euro Vector Instruments and Software).

Results and Discussion

The title compound crystallizes in the monoclinic space group $P2_1/c$ (Table 1) with all atoms being located on general positions. The primary building units are four trigonal SbS_3 pyramids (Fig. 1). Three SbS_3 units (Sb1, Sb3 and Sb4) share common corners to form a six-membered Sb_3S_3 heteroring. These rings are joined by the $Sb(2)S_3$ pyramids yielding a chain comprised of alternating Sb_3S_3 rings and $Sb(2)S_3$ pyramids running along [001] (Fig. 2). The chain proceeds in a zig-zag-like fashion. The Sb–S bond lengths are between 2.3302(10) and 2.5095(9) Å (Table 2) which are typical for thioantimonates(III) [1 – 26]. The two shortest Sb–S bonds (Sb(2)–S(2): 2.3302(10) and Sb(4)–S(7): 2.3962(9) Å) are observed to the terminal S atoms suggesting stronger bonds. The S–Sb–S angles (Table 2) (86.44(3)–101.76(3)°) indicate a distortion from the ideal trigonal-pyramidal geometry which is often observed in thioantimonate(III) compounds. The chains are arranged in a way that the Sb_3S_3 rings point toward the pocket formed by the $Sb(2)S_3$ pyramid joining two adjacent rings (Fig. 2).

Like in many other thioantimonates(III), the Sb(III) ions in the title compound have next-nearest S neighbors at distances above 3 Å but below the sum of the van der Waals radii of Sb and S of about 3.8 Å. In $[Mg(en)_3][Sb_4S_7]$ the so-called secondary bonds are between 3.061 and 3.582 Å. Considering these weak interactions the coordination environments of Sb(1), Sb(3), and Sb(4) are enhanced to five and six, respectively, whereas Sb(2) is not involved in such contacts (Fig. 3). The resulting $Sb(4)S_6$ unit may be viewed

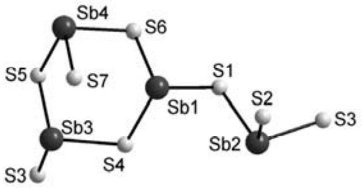

Fig. 1. The primary building units in $[Mg(en)_3][Sb_4S_7]$ with crystallographic labeling scheme used.

Table 2. Selected bond lengths (Å) and angles (deg)[a].

Sb(1)-S(6A)	2.4356(8)	Sb(3)-S(5)	2.4733(9)
Sb(1)-S(1)	2.5011(9)	Sb(3)-S(4)	2.4759(9)
Sb(1)-S(4A)	2.5048(9)	Sb(3)-S(3)	2.5069(9)
Sb(2)-S(2)	2.3302(10)	Sb(4)-S(7)	2.3962(9)
Sb(2)-S(3)	2.4742(9)	Sb(4)-S(5)	2.4969(9)
Sb(2)-S(1)	2.5095(9)	Sb(4)-S(6)	2.4986(9)
S(6A)-Sb(1)-S(1)	87.11(3)	S(7)-Sb(4)-S(5)	94.89(3)
S(6A)-Sb(1)-S(4A)	100.04(3)	S(7)-Sb(4)-S(6)	95.99(3)
S(1)-Sb(1)-S(4A)	93.90(3)	S(5)-Sb(4)-S(6)	91.57(3)
S(2)-Sb(2)-S(3)	99.19(3)	S(5)-Sb(3)-S(4)	99.85(3)
S(2)-Sb(2)-S(1)	101.76(3)	S(5)-Sb(3)-S(3)	86.44(3)
S(3)-Sb(2)-S(1)	93.00(3)	S(4)-Sb(3)-S(3)	91.23(3)
Mg(1)-N(21)	2.193(3)	Mg(1)-N(2)	2.201(3)
Mg(1)-N(1)	2.194(3)	Mg(1)-N(22)	2.218(3)
Mg(1)-N(12)	2.194(3)	Mg(1)-N(11)	2.224(3)
N(21)-Mg(1)-N(1)	91.11(13)	N(12)-Mg(1)-N(22)	94.03(13)
N(21)-Mg(1)-N(12)	98.72(13)	N(2)-Mg(1)-N(22)	94.44(13)
N(1)-Mg(1)-N(12)	168.16(15)	N(21)-Mg(1)-N(11)	94.40(13)
N(21)-Mg(1)-N(2)	167.61(14)	N(1)-Mg(1)-N(11)	93.22(14)
N(1)-Mg(1)-N(2)	78.86(13)	N(12)-Mg(1)-N(11)	79.55(12)
N(12)-Mg(1)-N(2)	92.13(13)	N(2)-Mg(1)-N(11)	93.43(13)
N(21)-Mg(1)-N(22)	78.93(12)	N(22)-Mg(1)-N(11)	170.02(13)
N(1)-Mg(1)-N(22)	94.32(15)		

[a] Symmetry transformations used to generate equivalent atoms: A = $x, -y+3/2, z+1/2$.

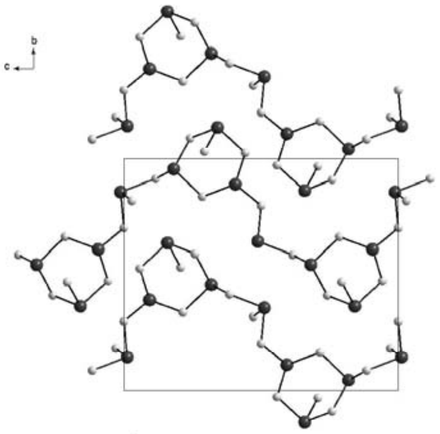

Fig. 2. The $[Sb_4S_7]^{2-}$ chains in the title compound running along [001].

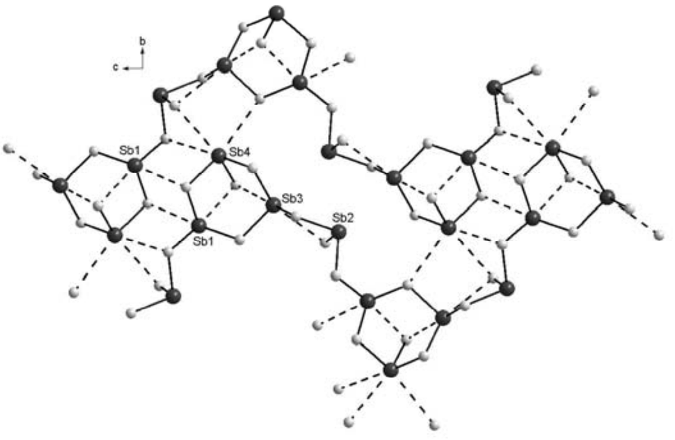

Fig. 3. The thioantimonate anion of $[Mg(en)_3][Sb_4S_7]$ with the so-called secondary Sb–S bonds drawn as broken lines.

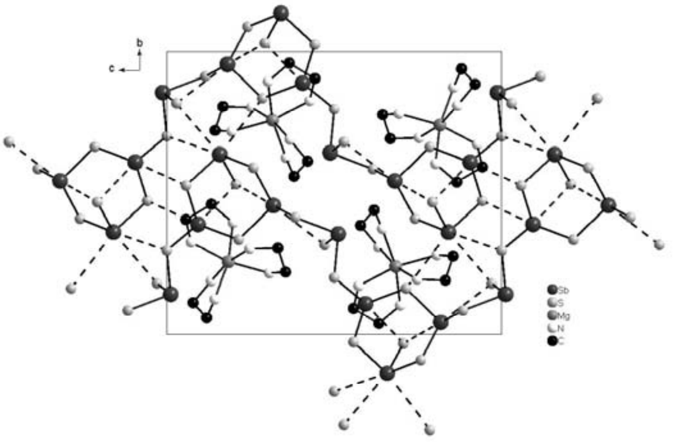

Fig. 4. Arrangement of the $[Mg(en)_3]^{2+}$ cations and the $[Sb_4S_7]^{2-}$ anions. Note that broken lines indicate long Sb–S contacts. H atoms are not shown.

as a strongly distorted octahedron with two short and two long equatorial and one short and one long axial Sb–S distance. The two SbS_5 polyhedra may be described as distorted trigonal bipyramids. These secondary Sb–S bonds join the primary structural units into larger building blocks. The Sb(1)–S(7) (3.0606 Å) and Sb(3)–S(7) (3.0696 Å) contacts transform the Sb_3S_3 ring into a Sb_3S_4 unit with a geometry often called semi-cube, which is a structural motif frequently observed in extended thioantimonate(III) structures.

Moreover, layers extending in the (100) plane are generated by the weak Sb–S contacts. The layered anions are stacked onto each other along [100] with relatively large, nearly rectangular openings composed of eight Sb and eight S atoms (Sb_8S_8) forming tunnels also directed along [100] (Fig. 3). Another special structural feature of the layer is the occurrence of a cluster-like configuration of three Sb_3S_4 semi-cubes (Fig. 3).

The Mg^{2+} cation in the charge-compensating complex $[Mg(en)_3]^{2+}$ is in a distorted octahedral environment of six N atoms of three ethylenediamine molecules, and the conformation of the complex is $\Delta(\lambda\lambda\delta)$. The Mg–N bond lengths (Table 2) range from 2.193(3) to 2.224(3) Å, which are typical values found in the literature [39]. Notably, the $[Mg(en)_3]^{2+}$ unit has only been structurally characterized in two compounds [39]. The N–Mg–N an-

D–H	d(H···A)	⟨D–H···A	d(D···A)	A (symm. operation)
N1–H1B	2.68	127.6	3.32	S2 ($x-1$, $-y+3/2$, $z-1/2$)
N2–H2C	2.51	165.2	3.41	S4
N2–H2D	2.88	125.0	3.49	S3
N11–H11A	2.77	155.8	3.63	S5 ($-x+1$, $y+1/2$, $-z+1/2$)
N11–H11B	2.65	168.2	3.55	S7 ($x-1$, y, z)
N12–H12C	2.77	164.4	3.66	S3
N12–H12D	2.61	155.7	3.47	S7 ($-x+2$, $y+1/2$, $-z+1/2$)
N21–H21C	2.54	167.5	3.45	S2 ($x-1$, $-y+3/2$, $z-1/2$)
N21–H21D	2.65	142.0	3.42	S5 ($-x+1$, $y+1/2$, $-z+1/2$)
N22–H22A	2.82	149.5	3.64	S7 ($-x+2$, $y+1/2$, $-z+1/2$)
N22–H22B	2.68	158.7	3.55	S1 (x, $-y+3/2$, $z-1/2$)

Table 3. Hydrogen bond geometry of $[Mg(en)_3][Sb_4S_7]$. Distances in Å and angles in deg.

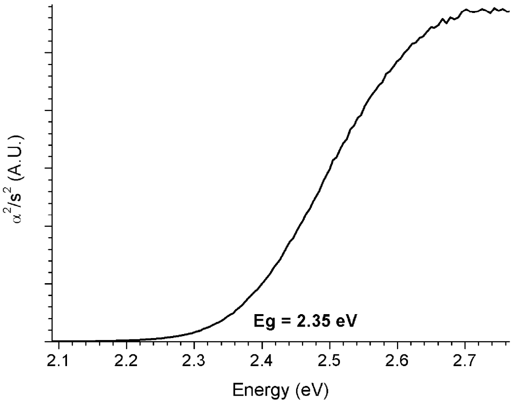

Fig. 5. The UV/Vis diffuse reflectance spectrum of the title compound.

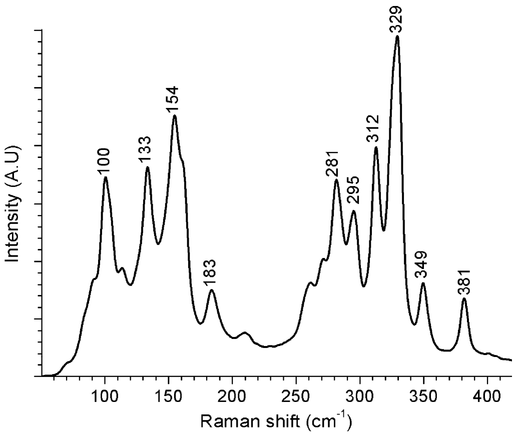

Fig. 6. The Raman spectrum of $[Mg(en)_3][Sb_4S_7]$.

gles indicate a severe distortion with values between 78.86(13) and 170.02(13)°, and *trans* angles of 167.61(14) to 170.02(13)°. In the isostructural compounds $[M(en)_3]Sb_4S_7$ (M = Ni, Fe, Co) the conformation of the cations are either $\Delta(\lambda\lambda\lambda)$ or $\Lambda(\delta\delta\delta)$ [13–15], in contrast to what is observed in the title compound. The $\Delta(\lambda\lambda\lambda)$ or $\Lambda(\delta\delta\delta)$ conformations around the M^{2+} ions also leads to distortions of the octahedral environments with *trans* N–M–N angles of 162–165° for Mn^{2+}, 169–170° for Co^{2+}, and 170–171° for Ni^{2+}.

The $[Mg(en)_3]^{2+}$ cations are positioned between the anionic thioantimonate(III) layers and are located above and below the periphery of the rectangular rings (Fig. 4).

Eleven of the twelve H atoms bonded to N atoms and six out of the seven S atoms are involved in H bonding interactions (Table 3). Although S···H bonds are weak, the large number of such interactions leads to a significant contribution to the stability of the compounds. Transition metal-containing counterions in thioantimonates(III) are very often located and oriented in a way to the anionic network that optimal H bonding interactions are possible. Hence, such cations are mainly located above or below large rings formed by Sb and S atoms. The inter-layer spacing of 6.55 Å in $[Mg(en)_3][Sb_4S_7]$ is very similar to those reported for the isostructural compounds mentioned above (Mn^{2+}: 6.65 Å; Co^{2+}: 6.56 Å; Ni^{2+}: 6.55 Å).

The thermal stability of $[Mg(en)_3][Sb_4S_7]$ was investigated by DTA-TG experiments performed in N_2 atmosphere. Above about 220 °C the emission of the en ligands starts, and the thermal decomposition reaction is accompanied by an intense endothermic signal in the DTA curve. The decomposition is finished at about 350 °C, and in the grey residue only the reflections of Sb_2S_3 could be observed in the X-ray powder pattern. However, since several reflections of MgS and Sb_2S_3 overlap, and the scattering power of Mg is much lower than that of Sb, the presence of MgS in the thermal decomposition product could not be proven unambiguously by powder diffractomery.

The optical band gap of the compound was determined by diffuse UV/Vis reflectance measurements (Fig. 5). The observed value of about 2.35 eV is in good agreement with the orange color of the compound. The metal cation seems to have no significant influence on the optical band gap because similar values were reported for Ni^{2+} (2.35 eV) and Fe^{2+} (2.25 eV), indicating that M^{2+}-based electronic states are not heavily involved in the electronic transition.

The Raman spectrum of the title compound is displayed in Fig. 6. The typical resonances of the SbS_x ($x = 3-6$) stretching vibrations occur between 250 and 400 cm^{-1}. In the present spectrum several intense signals are located in this region. On the basis of literature data [40] the bands located at 349 and 329 cm^{-1} are tentatively assigned to the stretching vibrations of the SbS_3 pyramid. In $(CuI_2)Cu_3SbS_3$ containing an isolated $[SbS_3]^{3-}$ anion these resonances occur at 362 and 339 cm^{-1}, whereas a prominent shift of about 60 cm^{-1} to lower frequencies was reported for SbS_6 and SbS_7 units in $MnSb_2S_4$ [41, 42]. According to the assignment of the bands in the Raman spectrum of $[Cr(tren)SbS_3]\cdot H_2O$ (tren = tris(2-aminoethyl)amine) the resonance at about 281 cm^{-1} may be caused by an asymmetric S–Sb–S stretching mode. The signals at 312 and 295 cm^{-1} may be due to the weak bonding interactions between the Sb(III) ions and the next-nearest S atoms [41, 42]. Resonances located at about 320 and 290 cm^{-1} were explained with the presence of SbS_5 units displaying the typical bonding pattern of three short and two long secondary bonds [41, 42]. As discussed above two Sb atoms in the title compound are in a $3+2$ environment of S atoms, and therefore the two resonances at 312 and 296 cm^{-1} may be caused by these two SbS_5 groups. The signature of the SbS_6 unit may also occur in this region and/or participates in these two low-energy bands. Further assignment of the remaining resonances is difficult because lattice vibrations are also located in the region below about 250 cm^{-1}.

Conclusions

The new thioantimonate(III) $[Mg(en)_3][Sb_4S_7]$ was obtained as orange crystals in almost quantitative yield under solvothermal conditions and represents the first thioantimonate(III) containing a main group metal complex as structure-directing unit. The compound belongs to the group of thioantimonates(III) with an Sb : S ratio of 1 : 1.75 for which the largest number of examples was reported in the literature. The $[Sb_4S_7]^{2-}$-containing compounds can be classified according to their dimensionalities and/or space groups [3]. With the title compound nine structurally characterized $[M(L)][Sb_4S_7]$ (L = ligand) compounds crystallizing in space groups $P2_1/c$ are known. For the compounds containing cations which are surrounded by the less bulky ligand diethylenetriamine a layered thioantimonate network is observed, whereas the more space-demanding $[M(en)_3]^{2+}$ complexes force the formation of a chain anion. Hence, the structure of the title compound is another example supporting the postulated relation between cation size and dimensionality of the thiometalate anion.

Acknowledgement

Financial support by the State of Schleswig-Holstein and the Fonds der Chemischen Industrie is gratefully acknowledged.

---

[1] A. Puls, M. Schaefer, C. Näther, W. Bensch, A. V. Powell, S. Boissière, A. M. Chippindale, *J. Solid State Chem.* **2005**, *178*, 1171 – 1181.

[2] A. Puls, C. Näther, R. Kiebach, W. Bensch, *Solid State Sci.* **2006**, *8*, 1085 – 1097.

[3] H. Lühmann, Z. Rejai, K. Möller, P. Leisner, M.-E. Ordolff, C. Näther, W. Bensch, *Z. Anorg. Allg. Chem.* **2008**, *634*, 1687 – 1695.

[4] R. Stähler, B.-D. Mosel, H. Eckert, W. Bensch, *Angew. Chem.* **2002**, *114*, 4671 – 4673; *Angew. Chem. Int. Ed.* **2002**, *41*, 4487 – 4489.

[5] M. Zhang, T. L. Sheng, X. H. Huang, R. B. Fu, X. Wang, S. M. Hu, S. C. Xiang, X. T. Wu, *Eur. J. Inorg. Chem.* **2007**, 1606 – 1612.

[6] H. A. Graf, H. Schäfer, *Z. Naturforsch.* **1972**, *27b*, 735 – 739.

[7] G. Dittmar, H. Schäfer, *Z. Anorg. Allg. Chem.* **1977**, *437*, 183 – 187.

[8] G. Dittmar, H. Schäfer, *Z. Anorg. Allg. Chem.* **1978**, *441*, 93 – 97.

[9] G. Dittmar, H. Schäfer, *Z. Anorg. Allg. Chem.* **1978**, *441*, 98 – 102.

[10] B. Eisenmann, H. Schäfer, *Z. Naturforsch.* **1979**, *34b*, 383 – 385.

[11] G. Cordier, H. Schäfer, C. Schwidetzky, *Z. Naturforsch.* **1984**, *39b*, 131 – 134.

[12] W. S. Sheldrick, H.-J. Häusler, *Z. Anorg. Allg. Chem.* **1988**, *557*, 105 – 111.

[13] H.-O. Stephan, M. G. Kanatzidis, *Inorg. Chem.* **1997**, *36*, 6050 – 6057.
[14] W. Bensch, M. Schur, *Z. Naturforsch.* **1997**, *52b*, 405 – 409.
[15] P. Vaqueiro, D. P. Darlow, A. M. Chippindale, A. V. Powell, *Solid State Ionics* **2004**, *172*, 601 – 605.
[16] M. Schur, W. Bensch, *Eur. J. Solid State Inorg. Chem.* **1997**, *34*, 457 – 466.
[17] R. Stähler, C. Näther, W. Bensch, *J. Solid State Chem.* **2003**, *174*, 264 – 275.
[18] M. Schaefer, D. Kurowski, A. Pfitzner, C. Näther, W. Bensch, *Acta Crystallogr.* **2004**, *E60*, m183–m185.
[19] V. Spetzler, C. Näther, W. Bensch, *Z. Naturforsch.* **2006**, *61b*, 715 – 720.
[20] M. Schaefer, R. Stähler, W.-R. Kiebach, C. Näther, W. Bensch, *Z. Anorg. Allg. Chem.* **2004**, *630*, 1816 – 1822.
[21] R. Kiebach, A. Griebe, C. Näther, W. Bensch, *Solid State Sci.* **2006**, *8*, 541 – 547.
[22] A. V. Powell, R. J. E. Lees, A. M. Chippindale, *Inorg. Chem.* **2006**, *45*, 4261 – 4267.
[23] F. Q. Huang, J. A. Ibers, *J. Solid State Chem.* **2005**, *178*, 212 – 217.
[24] J. Zhou, J. Dai, G.-Q. Bian, C.-Y. Li, *Coord. Chem. Rev.* **2009**, *253*, 1221 – 1247.
[25] G. A. Ozin, *Supramolecular Chem.* **1995**, *6*, 125 – 134.
[26] R. Kiebach, R. Warratz, C. Näther, W. Bensch, *Z. Anorg. Allg. Chem.* **2009**, *635*, 988 – 994.
[27] L. Engelke, C. Näther, W. Bensch, *Eur. J. Inorg. Chem.* **2002**, 2936 – 2941.
[28] M. Schur, A. Gruhl, C. Näther, I. Jess, W. Bensch, *Z. Naturforsch.* **1999**, *54b*, 1524 – 1528.
[29] M. Schur, W. Bensch, *Z. Naturforsch.* **2002**, *57b*, 1 – 7.
[30] V. Spetzler, H. Rijnberk, C. Näther, W. Bensch, *Z. Anorg. Allg. Chem.* **2004**, *630*, 142 – 148.
[31] R. Kiebach, W. Bensch, R. D. Hoffmann, R. Pöttgen, *Z. Anorg. Allg. Chem.* **2003**, *629*, 532 – 538.
[32] M. Schur, H. Rijnberk, C. Näther, W. Bensch, *Polyhedron* **1998**, *18*, 101 – 107.
[33] M. Schaefer, C. Näther, W. Bensch, *Solid State Sci.* **2003**, *5*, 1135 – 1139.
[34] M. Schaefer, C. Näther, N. Lehnert, W. Bensch, *Inorg. Chem.* **2004**, *43*, 2914 – 2921.
[35] R. Stähler, C. Näther, W. Bensch, *J. Solid State Chem.* **2003**, *174*, 264 – 275.
[36] R. Stähler, W. Bensch, *Z. Anorg. Allg. Chem.* **2002**, *628*, 1657 – 1662.
[37] R. Kiebach, F. Studt, C. Näther, W. Bensch, *Eur. J. Inorg. Chem.* **2004**, 2553 – 2556.
[38] G. M. Sheldrick, SHELXS/L-97, Programs for Crystal Structure Determination, University of Göttingen, Göttingen (Germany) **1997**. See also: G. M. Sheldrick, *Acta Crystallogr.* **2008**, *A64*, 112 – 122.
[39] A. F. Waters, A. H. White, *Aust. J. Chem.* **1996**, *49*, 61 – 72.
[40] K. Möller, C. Näther, A. Bannwarth, W. Bensch, *Z. Anorg. Allg. Chem.* **2007**, *633*, 2635 – 2640
[41] A. Pfitzner, D. Kurowski, *Z. Kristallogr.* **2000**, *215*, 373 – 376.
[42] A. Pfitzner, *Chem. Eur. J.* **1997**, *3*, 2032 – 2038.

5. SRO/SiO_2 multilayers with high Si content

Silicon Rich Oxide (SRO), also known as Silicon Rich Silicon Oxide (SRSO) or off-stoichiometric Silicon oxide, is a multiphase material composed of silicon oxides and Si agglomerates [88, 89]. It is possible to obtain Si nanocrystals (Si-nCs) embedded in a silicon oxide matrix by thermally treating SRO at high temperatures [90]. A typical TEM micrograph of this material is shown in Fig. 6. In the figure one can distinguish crystalline zones (Si-nCs) and amorphous zones consisting of silicon oxides. Si-nCs of less than 5 nm in diameter (the Bohr radius for electrons in crystalline Si [91]) may behave as quantum dots exhibiting quantum confinement in three dimensions. The Si-nCs in SRO are also isolated from other nCs by silicon oxides, a property that distinguishes them from those created by deposition of nanolayers of polysilicon, and such isolated Si-nCs are useful for single electron memories [43]. With the Si quantum dots spaced sufficiently close together, the wave functions of quantum confined carriers in adjacent dots overlap forming a mini-band [92]. For sufficiently broad mini-bands this effectively results in a new semiconductor material with a wider band gap than Si.

Silicon Rich Oxide materials have been prepared using a variety of methods, like sputtering [93, 94], Si implantation in SiO_2 [25, 26], or CVD methods [27, 28, 95, 96]. CVD methods are a simple approach for the deposition of SRO, and have been used for this purpose since some pioneering works in the 1960s [97].

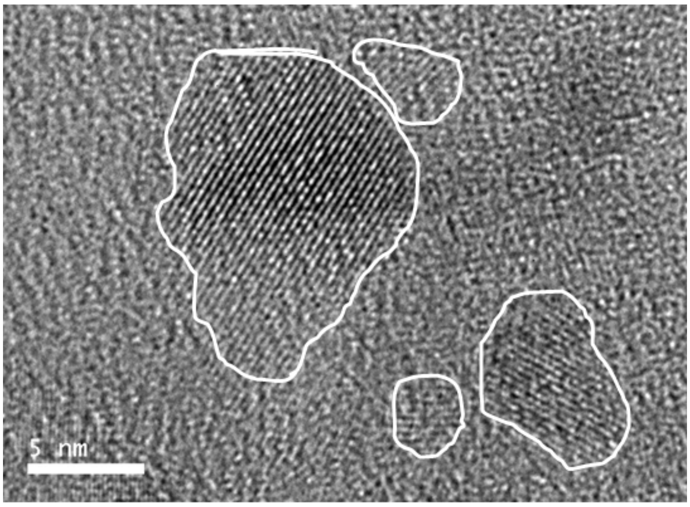

Fig. 6. Typical TEM micrograph of SRO. The enclosed areas are Si-nCs. The atomic layers are seen evidencing the crystallinity of the nano-crystals. The surrounding amorphous material consists of silicon oxides.

SRO materials have been extensively studied due to their photoluminescence (PL) effects in the visible range [29, 30], which are ascribed to quantum confinement effects in the Si agglomerates (commonly nanocrystals) or to defects at the interfaces. The quantum confinement effects in this material have also motivated the research of SRO for application in third generation solar cells [92, 98]. Additionally, SRO samples have been lately been used substituting crystalline Si in Silicon-based devices doped with Er [99, 100]. It has been found that Er emits light with a wavelength of 1.54 μm at room temperature. This wavelength is especially important because it coincides with the absorption minimum in the silica-based optical fibers currently used in optical communications. The temperature quenching of the PL effect from Er is strongly reduced in SRO compared to crystalline Si or silica [94, 100].

Multilayer structures (MLs) and superlattices (SLs) of this material have been also studied with the aim to combine the characteristics of the structures with the properties of SRO. A ML can be simply defined as a tandem of layers of different materials. A SL is a ML that consists of an array of quantum wells separated by very thin barriers. The wells consist of any material, usually crystalline, and the barriers consist of a material with larger band gap (E_g). For example one can prepare SLs of Si ($E_g = 1.1$ eV) and SiO$_2$ ($E_g \sim 8.8$ eV) [101]. A SL presents a series of narrowed allowed and forbidden bands, due to the subdivision of the original Brillouin zone into a series of sub-bands [102]. As the thickness of the barriers is smaller than the electron mean free path, the sub-bands of the quantum wells could align allowing resonant tunneling of carriers [102]. The tunneling process is graphically presented in Fig. 7.

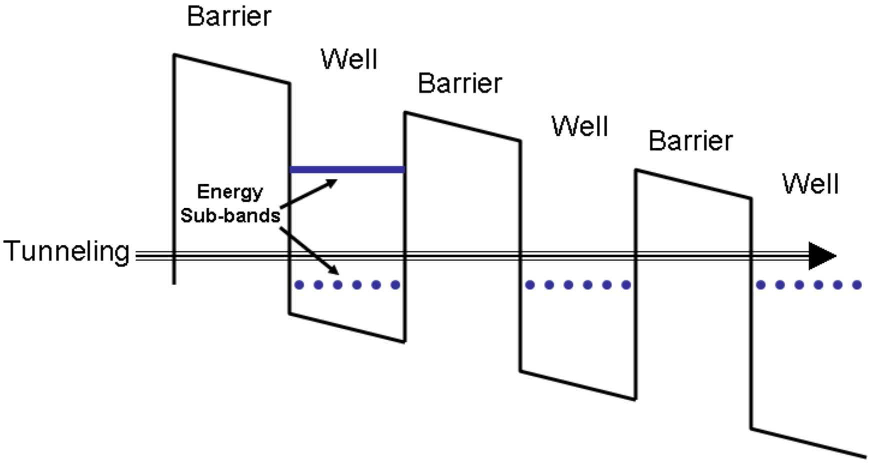

Fig. 7. Energy band diagram of a SL at varying bias conditions to reach energy band alignment and resonant tunneling.

MLs and SLs containing Si-nCs have been intensively studied in the last years, since these structures allow a control of the properties of the nCs related with their size. The size of the Si-nCs can be tuned according with the thickness of the layers [31]. In this way, it is possible to make size-dependent PL studies of the Si-nCs [31]. These structure types composed of SRO have been produced by different methods, but previous to this work no structures have been fabricated by LPCVD.

One of the most important results of the doctoral project has been the deposition and analysis of the first ML structure containing SRO with high Si content prepared by LPCVD (section 5.1). It is a hard task to control the deposition rate of SRO with high Si content and SRO with low Si content at the same temperature. While temperatures higher than 700 °C are needed to deposit SiO_2, polysilicon can be deposited even below 500 °C. This causes a high deposition rate of SRO when it has high Si content, producing films with pronounced roughness. The deposition parameters were adjusted until a layered structure of two independent phases was obtained even with the existing constraints. The structural and compositional characteristics of the ML were discussed on the basis of the results of exhaustive analyses by Secondary Ion Mass Spectroscopy (SIMS), X-ray Photoelectron Spectroscopy (XPS), TEM and Fourier Transformed Infrared spectroscopy (FTIR). These results were the base to produce new MLs.

After this initial study, other MLs were deposited proving the possibility of controlling the size of the Si-nCs with the thickness of the layers (section 5.2). The size of the nCs was determined by TEM and X-ray diffractometry measurements, and additionally a Raman analysis has been used as an alternative approach. Such Raman analysis has not been used before to determine the size of nCs. It consists in analyzing the asymmetry of the Raman peak of crystalline Si, what is much less sensitive to stress or defocusing than other methods which take into account the position or broadness of the peak.

The control of the size of the Si-nCs allowed the deposition of MLs which exhibit PL in the visible range (section 5.3). Even though, the PL signal is just evident in the MLs with Si-nCs smaller than 10 nm and/or content of pure Si in the layers lower than 20 %. It has been proved that these conditions can be also achieved by oxidation of the samples. A detailed analysis of the PL spectra evidences that in all cases the PL emission has the same origin: radiative recombination in the defects of the oxide matrix and of the interfaces between nanocrystals. The interface-related PL depends on the size of the Si-nCs. Such a PL study of MLs containing SRO with high Si content and Si-nCs larger than 5 nm has not been done before. Hence the present study brings much more insight into the emission process of such a system. The origin of the PL in SRO with Si-nC sizes below 4 nm is quite different, and is generally due to direct band to band transitions in Si-nCs due to quantum confinement effects. On the other hand, when no Si-nCs are present the PL emission is due to radiative recombination in defects of the silicon oxides.

5.1.

Phys. Status Solidi A **206**, No. 2, 263–269 (2009) / **DOI** 10.1002/pssa.200824365

physica status solidi a
www.pss-a.com
applications and materials science

Structural characteristics of a multilayer of silicon rich oxide (SRO) with high Si content prepared by LPCVD

E. Quiroga[*, 1], W. Bensch[1], Z. Yu[2], M. Aceves[2], R. A. De Souza[3], M. Martin[3], V. Zaporojtchenko[4], and F. Faupel[4]

[1] Institut für Anorganische Chemie der Universität Kiel, Max Eyth Str. 2, 24116 Kiel, Germany
[2] National Institute for Astrophysics, Optics and Electronics (INAOE), Calle Luis Enrique Erro 1, 72840 Tonantzitla, Pue., Mexico
[3] Institut für Physikalische Chemie, RWTH Aachen University, Landoltweg 2, 52056 Aachen, Germany
[4] Institut für Materialwissenschaft, Technische Fakultät der Universität Kiel, Kaiserstr. 2, 24143 Kiel, Germany

Received 4 September 2008, revised 25 November 2008, accepted 8 December 2008

PACS 62.23.Pq, 68.37.–d, 68.65.Ac, 78.30.Hv, 79.60.Bm, 81.15.Gh

---

[*] Corresponding author: e-mail pesitrama@gmail.com, Phone: +49 431 880 2094

Single layer films and a multilayer structure of SRO (Silicon Rich Oxide) have been prepared by LPCVD (Low Pressure Chemical Vapour Deposition) and characterized by FTIR, SIMS, XPS, TEM and AFM measurements. The stacked structure is composed of alternating layers of SRO with high Si content and SRO with low Si content. The layered structure is confirmed by SIMS and TEM measurements. The composition of the materials is discussed. Besides Si nanocrystals, the existence of agglomerates of silicon oxide with structure close to fused silica and the existence of oxynitrides is evidenced in the films with high Si content.

1 Introduction SRO (Silicon Rich Oxide), also known as off-stoichiometric silicon oxide, is a material composed of Si agglomerates embedded in an oxide matrix. An indication of the Si content in the material is the parameter Ro, which is the ratio of the partial pressure of the precursor gases (for example, N_2O and SiH_4). SRO is an extensively studied material due to its interesting optoelectronic properties, such as photoluminescence in the visible range [1], which is ascribed to quantum confinement effects in the agglomerates of Si (commonly nanocrystals, nc) or to defects at their interfaces. Superlattices (SLs) and multilayer structures (MLs) could exhibit interesting quantum confinement effects too, due to the reduced size of their composing films. There are many reports about nc-Si/SiO$_2$ SLs and MLs that have mostly been prepared by PECVD (Plasma Enhanced Chemical Vapour Deposition) and magnetron sputtering [2–6]. Also epitaxial growth has been used [7]; however, there are just a few reports of MLs prepared by LPCVD [8]. Most of the works present MOS-like structures with embedded nanocrystals [9, 10]. On the other hand, to our knowledge there are no reported multilayer structures based on SRO with a high Si content prepared by LPCVD. LPCVD is a very simple method for film deposition and is thoroughly compatible with Si technology. Furthermore, it permits an easy variation of the silicon content of the deposited layers in a wide range.

In this work, a multilayer structure composed of two different layers of SRO, one with high silicon excess, deposited by LPCVD are studied. FTIR (Fourier Transform Infrared), XPS (X-ray Photoelectron Spectroscopy), SIMS (Secondary Ion Mass Spectroscopy), TEM (Transmission Electron Microscopy) and AFM (Atomic Force Microscopy) measurements were performed in order to study the composition and structural characteristics of the multilayer. In addition, single layers of SRO with the same characteristics as that of the multilayer were studied for comparison.

2 Experimental SRO single layers with Ro = 1 (SRO1) and Ro = 50 (SRO50), and a multilayer structure composed of the stacks of SRO1 and SRO50 were deposited on p-type Si(100) wafers with 30–50 Ω cm resistivity

Table 1 Deposited samples.

sample	layer	thickness (nm)
SRO1	single layer	133
SRO50	single layer	60.8
multilayer	first* layer of SRO50	11
	first layer of SRO1	23
	second layer of SRO50	~21
	second layer of SRO1	~21
	third layer of SRO50	~23

* The layers are numbered parting from the substrate.

by LPCVD at 725 °C, using SiH$_4$ and N$_2$O as the precursor gases. A list of the deposited samples is shown in Table 1. The multilayer is composed of 2 periods of films: 3 barrier layers of SRO50 and 2 well layers of SRO1. The deposition of the multilayer was done varying manually the precursor gases during the deposition.

The microstructure of the samples was studied with TEM measurements (Tecnai F30, 300 kV). Measurements of the roughness of the films were performed with an AFM Autoprobe CP (Park Scientific Instruments) in contact mode, which has a lateral resolution of 0.025 nm and a vertical resolution of 0.0025 nm.

SIMS measurements were performed on a Time-of-Flight SIMS machine (TOF-SIMS IV, IONTOF, Münster). Secondary ions for analysis were produced by bombardment with 15 keV Ga$^+$ ions. Sputter etching of the sample surface was accomplished by bombardment with 1 keV Cs$^+$ ions for negative secondary ion analysis, and with 2 keV Cs$^+$ ions for positive secondary ion analysis (the higher yield of MCs$^+$ secondary ions at 2 keV was more important than the reduced depth resolution). XPS analysis was carried out with an electron spectrometer (Omicron) equipped with a non-monochromated Al Ka source at 0° take off angle. For these measurements, the samples were previously sputtered in a preparation chamber (Omicron Full Lab) bombarding the samples with argon ions with a kinetic energy of 1 keV at an incident angle of 36° for 5 min.

FTIR spectra of the films were measured with a Bruker FTIR spectrometer model V22, which works in the range of 4000–350 cm^{-1} with 2 cm^{-1} resolution.

3 Results and discussion

3.1 TEM and AFM measurements A typical TEM micrograph of SRO1 is shown in Fig. 1. Two phases could be easily distinguished: nanocrystalline Si and amorphous silicon oxide. The material presents good phase separation, and most of the SRO1 film is composed of zones of crystalline Si. Therefore, it can be considered as agglomerates of silicon oxide embedded in a crystalline silicon matrix.

The layered structure of the multilayer can be seen in Fig. 2. According to the TEM micrograph, the total thickness of the multilayer can be estimated to be about 100 nm. The different layers are clearly discernible.

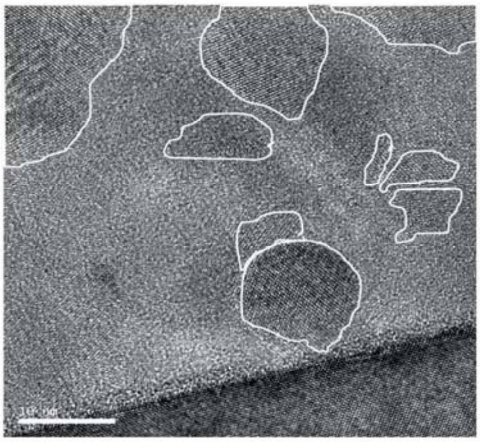

Figure 1 TEM micrograph of SRO Ro = 1. For an easier identification the areas containing Si nanocrystals are enclosed with white lines.

The first layer of SRO50 in the multilayer (from the substrate's side) is very uniform, with a thickness of ~10 nm. On the other hand, the bottom interface of the first layer of SRO1 is very well defined, but its top interface is very rough. This is an indication of the large difference in roughness between the SRO1 and SRO50 films. The large roughness of the SRO1 layer is due to the formation of Si nanocrystals during the deposition process. The layers deposited onto the first SRO1 layer are then relatively rough, but are still easily distinguishable. Figure 3 shows an AFM micrograph of the single SRO1 layer denoting the large roughness of this material.

The mean peak height of the surface bumps is 41 nm and represents ~30% of the total film thickness. The multilayer exhibits a rough surface too (image not shown) with the mean peak height of the surface bumps being 34 nm.

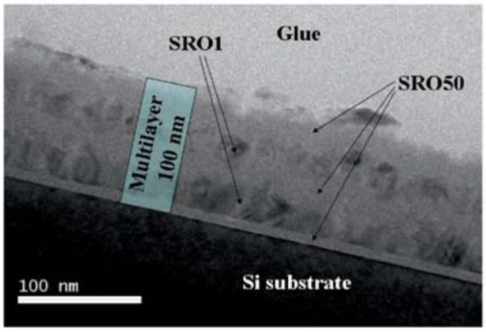

Figure 2 (online colour at: www.pss-a.com) TEM micrograph of the multilayer. The layers of SRO50 are the smooth zones, and the SRO1 layers look like protuberances (Si nanocrystals). The total thickness of the sample is ~100 nm.

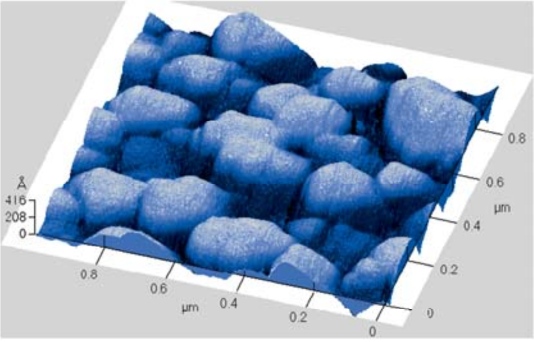

Figure 3 (online colour at: www.pss-a.com) Three dimensional AFM image of the surface of the film SRO Ro = 1. The mean peak height of the surface bumps corresponds to ~30% of the film thickness.

3.2 SIMS measurements Figure 4 shows a ToF-SIMS depth profile of the multilayer. The distribution of O, Si and N were detected from SiO$_2^-$, Si$_2^-$ and SiN$^-$ ions respectively. This does not mean that the sample contains these compounds but indicates the presence of the mentioned elements together in the sample. As expected, the Si$_2^-$ and SiO$_2^-$ signals show variations complementary to each other, again indicating that a layered structure was deposited. Interestingly, the multilayer also contains nitrogen. The SiN$^-$ signal disappears at the interface multilayer/silicon substrate, as happens with the SiO$_2^-$ signal, demonstrating that nitrogen and oxygen are only present in the multilayer. Nevertheless, the intensity of the SiN$^-$ signal is only about 1% of the intensity of the Si$_2^-$ signal.

The low intensity of the SiN$^-$ signal could be an evidence of the small amount of N in SRO1, but without knowing the relative ionisation probabilities of SiO$_2^-$, Si$_2^-$ and SiN$^-$ it is not possible to determine its amount. The N atoms in the multilayer may enhance a possible photoluminescence effect (PL) from the Si nanocrystals in the as-deposited sample [11, 12]. Nevertheless the N content in the present samples is very low and may not have a significant effect on the PL intensity. Eventhough, only PL measurements and analyses will provide the answer to the question how N influences the PL properties. Such PL measurements will be performed in the near future.

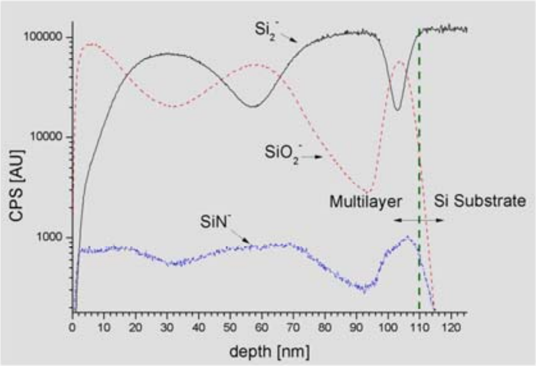

Figure 4 (online colour at: www.pss-a.com) ToF-SIMS depth profile of the multilayer. The elemental distributions of O, Si and N have been detected as Si$_2^-$, SiO$_2^-$ and SiN$^-$.

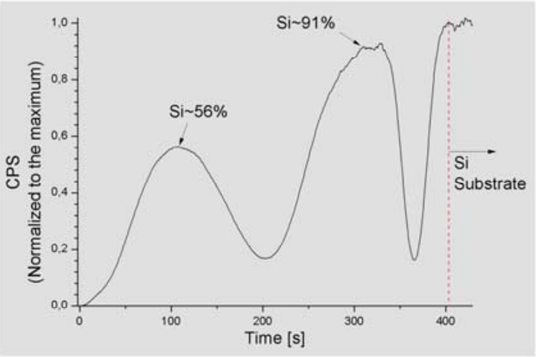

Figure 5 (online colour at: www.pss-a.com) Normalized ToF-SIMS Si$_2^-$ signal as a function of sputter time. The silicon concentration apparently increases, from ~56% of the outer layer of SRO1 to ~91% of the next layer.

Figure 5 shows the normalized Si$_2^-$ signal. From this figure it can be deduced that the Si content is reduced in the outer SRO1 layer. The intensity of the Si$_2^-$ signal from the first SRO50 layer (to the substrate's side), is around 10% compared to that from the Si substrate. As a consequence it can be concluded that the probability to obtain Si$_2^-$ ions from the SRO50 layer is around 10% compared with the probability to obtain such ions from the Si substrate. Since SRO1 presents a very good phase separation and Si nanocrystals represent its major phase (see TEM micrograph), the SIMS Si$_2^-$ signal corresponds mainly to the Si nanocrystals and the matrix effects to obtain it should be less significant. In this way, an approximation of the concentration of Si was made taking into account the maxima of the Si$_2^-$ signal. In the outer SRO1 layer it is about 56%, and it amounts to about 91% in the other layer of the same material. SIMS analysis of positive ions was also carried to confirm the Si profile, since it is far less sensitive to matrix effects. The obtained spectrum (Fig. 6) presents the same behaviour as the one obtained with negative ions, with close values (and much closer when the Si content in the sample is larger) but with a much poorer resolution. Nevertheless, even when the concordance of SIMS measurements of positive and negative ions indicate a good approximation of the Si concentration in SRO1 layers, the exact value can not be determined by this method alone.

The graded concentration of Si in the multilayer may be caused by residual gases in the LPCVD chamber due to the manual variation of the gas flow, which give the opportunity to obtain more silicon oxide. This experimental fac-

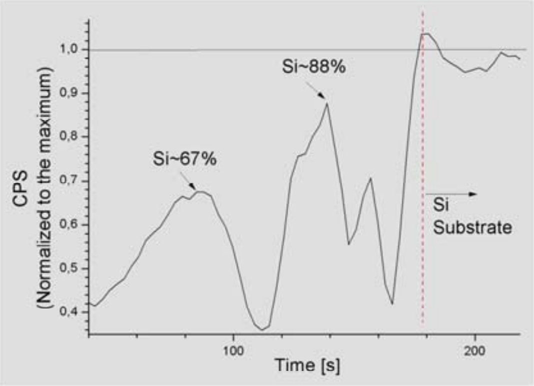

Figure 6 (online colour at: www.pss-a.com) Positive SIMS normalized spectra of the SiCs$^+$ signal (Si is detected in the way of SiCs$^+$ ions). The silicon concentration increase in depth, as was also evidenced with the SIMS of negative ions.

tor must be taken into account if many layers should be deposited.

3.3 XPS measurements In the study of Si oxides by XPS, the oxidation states of Si can be estimated from the chemical shifts of the Si 2p core level line [13, 14]. The Si 2p spectrum of silicon oxides contains contributions of the spin orbit Si 2p$_{1/2}$ and Si 2p$_{3/2}$ lines [13, 15–17] being separated by 0.6 eV. This is an atomic property, practically independent of the chemical environment [15].

In the XPS spectra, each Si 2p core level line occurs at positions corresponding to the energy shifts from the different oxidation states of Si (Si^0, Si^{1+}, Si^{2+}, Si^{3+}, Si^{4+}). The position of the peaks corresponding to Si^0 and Si^{4+} (SiO$_2$) is well known and is easily distinguishable [16]. On the other hand, the peaks related with silicon sub-oxides have been studied at Si/SiO$_2$ interfaces [13, 14, 17, 18], but they cannot be distinguished unequivocally in a complex spectrum composed of different Si oxide species. Hence, a quantitative analysis of such highly convoluted spectra is not straightforward and the results obtained by such fittings sensitively depend on the fitting parameters applied.

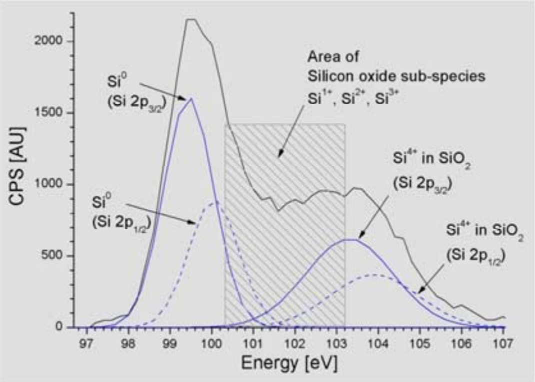

Figure 7 (online colour at: www.pss-a.com) XPS spectrum of SRO1. The peaks of the Si 2p$_{1/2}$ and Si 2p$_{3/2}$ of Si^0 and Si^{4+} were fitted. The existence of sub-oxide species can be noted in the region between Si^0 and Si^{4+}.

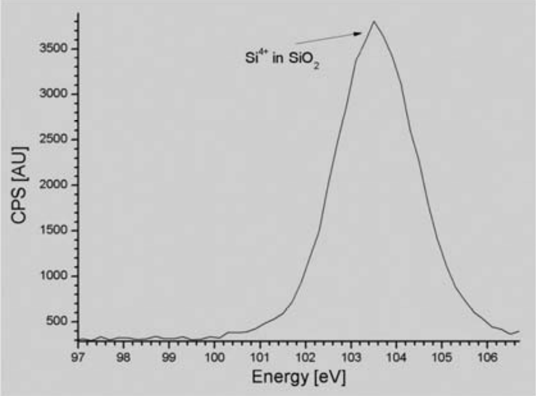

Figure 8 XPS spectrum of SRO50. Just the contribution of SiO$_2$ could be observed in the spectrum.

studied at Si/SiO$_2$ interfaces [13, 14, 17, 18], but they cannot be distinguished unequivocally in a complex spectrum composed of different Si oxide species. Hence, a quantitative analysis of such highly convoluted spectra is not straightforward and the results obtained by such fittings sensitively depend on the fitting parameters applied.

In the XPS spectra, each Si 2p core level line occurs at positions corresponding to the energy shifts from the different oxidation states of Si (Si^0, Si^{1+}, Si^{2+}, Si^{3+}, Si^{4+}). The position of the peaks corresponding to Si^0 and Si^{4+} (SiO$_2$) is well known and is easily distinguishable [16]. On the other hand, the peaks related with silicon sub-oxides have been studied at Si/SiO$_2$ interfaces [13, 14, 17, 18], but they cannot be distinguished unequivocally in a complex spectrum composed of different Si oxide species. Hence, a quantitative analysis of such highly convoluted spectra is not straightforward and the results obtained by such fittings sensitively depend on the fitting parameters applied.

The XPS Si 2p spectrum of the surface of SRO1 is shown in Fig. 7. For elemental Si the signal of the Si 2p$_{3/2}$ line is found at 99.45 eV and that of Si 2p$_{1/2}$ at 100.05 eV, both having a FWHM of 1.2 eV. For Si^{4+} the corresponding signals occur at at 103.3 eV and at 103.9 eV with a FWHM of 2.1 eV for both emissions. The peaks of the Si sub-oxides are located in the region between these two species. As an individual assignment of SiO$_x$ sub-oxides is not unambiguously possible, all the sub-oxides are considered as one group. The amount of sub-oxides was obtained by subtracting the area of the fitted peaks of Si^0 and Si^{4+} from the total area. According to the fitting procedures, the top region of the SRO1 film consists of 50% of elemental Si (Si^0), 34% of SiO$_2$ (Si^{4+}) and 16% of SiO$_x$ (Si^{1-3+}) with $0 < x < 2$. The value of the amount of Si on the surface of SRO1 is very close to the amount of Si in the outer layer of SRO1 in the multilayer. This result is expected, since the concentration of Si is reduced going from the substrate to the top of the samples with deposition time, and the deposition time to obtain SRO1 and the multilayer are similar.

The high amount of silicon sub-oxides in SRO1 is the result of the large amount of Si/SiO$_2$ interfaces that exist in this material. In contrast, in the XPS spectrum of the single SRO50 layer just the contribution of SiO$_2$ could be observed (Fig. 8) evidencing that this material is practically SiO$_2$. Only possible differences in density and the degree of disorder in the Si–O environments within the material compared with a thermal stoichiometric oxide can be expected.

3.4 FTIR spectra Figure 9 shows the FTIR spectra of the samples SRO1, SRO50 and of the multilayer in the range of 900 cm^{-1} to 1300 cm^{-1}. The absorption curves were normalized for clarity. The real peak intensity of sample SRO1 is around 3 times lower than that of the other samples. As can be noted in sample SRO50 just the typical absorptions of SiO$_2$ are evident (peaks B and D).

Peak B located at 1064 cm^{-1} corresponds to the Si–O TO (Transverse Optic) stretching vibration [19–22], and peak D occurring, as a shoulder at 1140 cm^{-1}, corresponds to the Si–O TO asymmetric stretching mode [21, 23]. The position of these bands corresponds to as-deposited Silicon Rich Oxide with low silicon excess [24]. The number of considered bands is consistent with the deconvolution of the peak centred at 1064 cm^{-1} in two peaks, as proposed by some authors studying thin thermal SiO$_2$ films [25, 26].

On the other hand, in the sample SRO1 the absorption peaks A, C and E are evident. Peak A, at 966 cm^{-1}, has been found by some groups as an indication of the existence of nitrogen in Si ingots. The intensity of this peak increases with increasing exposure time of the ingots to N$_2$ atmosphere [27]. Silicon nitride films prepared by nitridation of silica also exhibit this peak [28], and it is explained as the Si–N–Si asymmetric stretching vibration in SiN$_4$ tetrahedra joined via corners with SiO$_4$ tetrahedra. Nevertheless, this vibration has not only been observed on crystalline Si or crystalline silicon oxide, but also on polysilicon films annealed in N$_2$ and is accompanied by oxygen incorporation in the films [29]. As the SRO Ro = 1 is a material close to SIPOS (Semi-Insulating Polysilicon, see TEM results), the idea of oxynitrides in these films is very feasible. Because peak A only appears for SRO1 and not in SRO50, it can be concluded that both materials contain N (as evidenced by SIMS), but only in SRO1 N is bonded to Si in tetrahedral configuration along with oxygen forming a type of oxynitride. The N in SRO50 may be located on interstitial positions, presenting a different bonding configuration since the FTIR spectrum of this material does not show any characteristic peaks of silicon nitrides or oxynitrides.

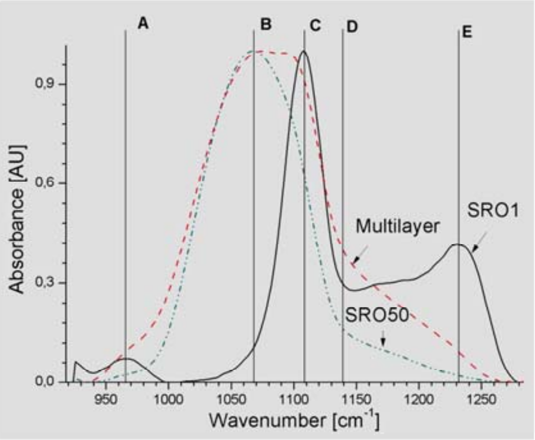

Figure 9 (online colour at: www.pss-a.com) Absorption spectra of the different samples. Five absorption peaks could be identified: A (966 cm^{-1}) related with some N in the films, and peaks B (1064 cm^{-1}), C (1107 cm^{-1}), D (1140 cm^{-1}) and E (1233 cm^{-1}) that are related with Si–O bonds.

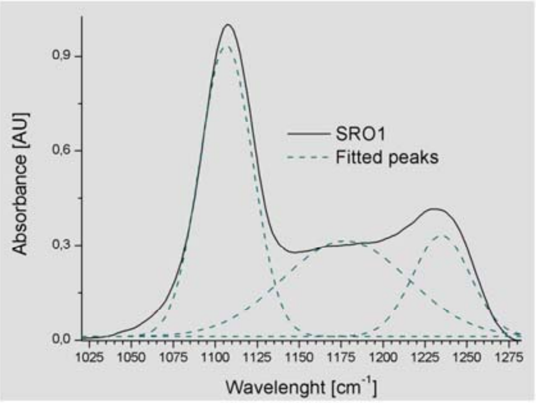

Figure 10 (online colour at: www.pss-a.com) Deconvolution of the absorption spectrum of the film of SRO Ro = 1. Besides the peaks C (1107 cm^{-1}) and E (1233 cm^{-1}) an absorption peak at 1178 cm^{-1} can be observed, which is related to TO Si–O asymmetric stretching vibration.

Peak C being centred at 1107 cm^{-1} in SRO1 occurs on a position which has been reported as interstitial oxygen in Si ingots [30, 31] and at Si/SiO$_2$ interfaces [21]. It has been reported that the TO Si–O stretching vibration of segregated oxygen in polysilicon also produces this absorption peak [29], and actually coincides with the Si–O TO stretching vibration in fused silica [31, 32]. It has been proposed that the interstitial oxygen in Si could adopt a structure close to that of fused silica, but with the Si–O–Si bond angle of around 100°, ascribing then the absorption peak at 1107 cm^{-1} to the TO Si–O stretching vibration [31]. As the SRO Ro = 1 is a material close to SIPOS this absorption peak could be expected.

The deconvoluted IR spectrum of SRO1 (Fig. 10) shows an extra absorption at 1178 cm^{-1} which is blue-shifted by 38 cm^{-1} with respect to the Si–O TO asymmetric stretching vibration of SRO50. This value is very close to the blue-shift of peak C with respect to the TO Si–O stretching vibration of SRO50 (43 cm^{-1}). According to this analysis, peak C and the one located at 1178 cm^{-1} may be caused by TO Si–O stretching vibrations of silicon oxide agglomerates with bonding angles and Si–O bond lengths close to those of quartz. In fact, according to the TEM micrograph of SRO1 in Fig. 1, this material can be considered as agglomerates of silicon oxide embedded in a nanocrystalline silicon matrix. The consideration of two peaks for the Si–O TO vibrations of SRO1 agrees with the number of vibrations found in SiO_2 films with thickness lower than 40 nm [26].

Peak E (at 1233 cm^{-1}) is related to LO Si–O vibrations [26, 33]. LO vibrations are inactive in normal incidence of the IR light, but it has been found that they become active when the particles of silicon oxide have a platelet shape with size <0.36 µm [21, 29, 30]. The agglomerates of silicon oxide in SRO1 are much smaller than this size in all their dimensions, as can be observed in Fig. 1.

The IR spectrum of the multilayer shows all 5 absorption peaks (with peaks A, D and E as shoulders), as can be seen in Fig. 9. Peaks B and C can be identified as the extremes of an asymmetric peak centred at ~1090 cm^{-1}.

The positions of all peaks in the multilayer remain very close to the ones in SRO Ro = 1 and Ro = 50. This evidences that 2 phases coexist in the multilayer, in accordance with the results of TEM and SIMS investigations. The distinction of the two phases is a good indicator that the composing materials do not react with the subsequent layers during the deposition procedure.

4 Conclusion The creation of a multilayer structure of SRO with high Si content by LPCVD has been evidenced by TEM and SIMS measurements. The multilayer is composed of layers of SRO1 and SRO50. A couple of technological constraints have been found to obtain a multilayer by LPCVD: SRO1 presents a high roughness and the amount of silicon in this material diminishes along the layer thickness. A layered structure of two independent phases was obtained even with the existing constraints. All results demonstrate that it is possible to produce layered structures by LPCVD, but the fact that silicon diminishes has to be taken into account.

Si-nanocrystals are the major component of SRO1, and agglomerates of silicon oxide with reduced size are the minor phase. The agglomerates of silicon oxide may have a structure close to fused silica, as evidenced by FTIR. The large amount of silicon sub-oxides found in SRO1 may be due to the large amount of Si/SiO_2 interfaces in this material.

Nitrogen is present in small amounts in the whole multilayer, but it is present as oxynitrides only in the layers of SRO1. Nevertheless the contribution of the oxynitrides to the total composition of SRO1 should be in a very low range. In SRO50 the nitrogen is thought as interstitial.

Acknowledgements The authors appreciate the support from CONACyT and DAAD.

References

[1] D. Berman, M. Aceves, A. Gallegos, A. Morales, L. R. Berriel, J. Carrillo, F. Flores, C. Falcony, C. Domínguez, A. Llobera, M. Riera, and J. Pedraza, Phys. Status Solidi C **1**(S1), S83–S87 (2004).
[2] L. Tsybeskov, Technical Proc. of the 2002 Int. Conf. on Computational Nanoscience and Nanotechnology, Molecular and Nanotechnology (2002), chap. 12, p. 304.
[3] L. Tsybeskov, K. D. Hirschman, S. P. Duttagupta, M. Zacharias, and P. M. Fauchet, Appl. Phys. Lett. **72**(1), 43 (1998).
[4] V. Duzhko and L. Tsybeskov, Appl. Phys. Lett. **83**(25), 5229 (2000).
[5] M. Zacharias, J. Bläsing, and P. Veit, Appl. Phys. Lett. **74**(18), 2614 (1999).
[6] L. Tsybeskov, G. F. Grom, and P. M. Fauchet, Appl. Phys. Lett. **75**(15), 2265 (1999).
[7] G. F. Grom, D. J. Lockwood, J. P. McCaffrey, H. J. Labbé, P. M. Fauchet, B. White, Jr., J. Dlener, D. Kovalev, F. Koch, and L. Tsybeskov, Nature **407**, 358 (2000).
[8] M. Modreanu, E. Aperathitis, M. Androulidaki, M. Audier, and O. Chaix-Pluchery, Opt. Mater. **27**, 1020 (2005).
[9] D. N. Kouvastos, V. Ioanou-Sougleridis, and A. G. Nassiopoulou, Appl. Phys. Lett. **8**(3), 397 (2003).
[10] V. Ioanou-Sougleridis and A. G. Nassiopoulou, J. Appl. Phys. **94**(6), 4084 (2003).
[11] R. López-Estopier, M. Aceves-Mijares, and C. Falcony, in: Proceedings 2006 3rd Int. Conf. on Electrical and Electronics Engineering (ICEEE), Mexico City, Mexico, 2006 (IEEE, 2006).
[12] R. López-Estopier, M. Aceves-Mijares, J. Carrillo, Z. Yu, and C. Falcony, in: Proceedings 2nd Int. Conf. on Electrical and Electronics Engineering (ICEEE) and XI Conference on Electrical Engineering (CIE 2005), Mexico City, Mexico, 2005 (IEEE, 2005), pp. 227–230.
[13] G. Hollinger and F. J. Himpsel, Appl. Phys. Lett. **44**, 93 (1984).
[14] F. J. Grundthaner, P. J. Grundthaner, R. P. Vasquez, B. F. Lewis, and J. Maserjian, Phys. Rev. Lett. **43**(22), 1683 (1979).
[15] F. J. Himpsel, F. R. McFeely, A. Taleb-Ibrahimi, J. A. Yarmoff, and G. Hollinger, Phys. Rev. B **38**(9), 6084 (1988).
[16] F. Verpoort, P. Persoon, L. Fiermans, G. Dedoncker, and L. Verdonck, J. Chem. Soc., Faraday Trans. **93**, 3555 (1997).
[17] P. J. Grundthaner, M. H. Hecht, F. J. Grundthaner, and N. M. Johnson, J. Appl. Phys. **61**(2), 629 (1987).
[18] K. Hirose, H. Nohira, K. Azuma, and T. Hattori, Prog. Surf. Sci. **82**, 3 (2007).
[19] J. Serra, E. G. Parada, P. González, D. Fernández, S. Chiussi, J. Pou, B. León, and M. Pérez-Amor, Surf. Coat. Technol. **80**, 211 (1996).
[20] P. Mandracci and C. Ricciardi, Thin Solid Films **515**, 7639 (2007).
[21] J. Niu, D. Yang, J. Sha, J. N. Wang, and M. Li, Mater. Lett. **61**, 894 (2007).
[22] A. Lehmann, L. Schumann, and K. Hübner, Phys. Status Solidi B **121**, 505 (1984).
[23] F. Ay and A. Aydinly, Opt. Mater. **26**, 33 (2004).
[24] A. Morales, J. Barreto, C. Domínguez, M. Riera, M. Aceves, and J. Carrillo, Physica E **38**, 54 (2007).

[25] I. W. Boyd, Appl. Phys. Lett. **51**(6), 418 (1987).
[26] I. P. Lisovskii, V. G. Litovchenko, V. G. Lozinskii, and G. I. Steblovskii, Thin Solid Films **213**, 164 (1992).
[27] J. Itoh, T. Nozaki, and T. Masui, T. Abe, Appl. Phys. Lett. **47**(3), 488 (1985).
[28] P. S. Lakshminarasimham and P. S. Gopalakrishnan, J. Mater. Sci. Lett. **14**, 1801 (1995).
[29] D. Gupta, B. Awasthy, and S. P. Varma, J. Mater. Sci. **28**, 1488 (1993).
[30] A. Borghesi, M. Geddo, and B. Pivac, J. Appl. Phys. **69**(10), 7251 (1991).
[31] W. Kaiser, P. H. Keck, and C. F. Lange, Phys. Rev. **101**(4), 1264 (1956).
[32] G. Gu, P. P. Ong, and C. Chu, J. Phys. Chem. Solids **60**, 943 (1999).
[33] W. Bensch and W. Bergholz, Semicond. Sci. Technol. **5**, 421–428 (1990).

5.2.

IEEE Proceedings of 10th International Conference on Ultimate Integration of Silicon
Aachen, Germany, 18-20.3.2009

Silicon Rich Oxide with controlled mean size of silicon nanocrystals by deposition in multilayers

E. Quiroga[1*], W. Bensch[1], M. Aceves[2], Z. Yu[2], J. P. Savy[3], M. Haeckel[3], A. Lechner[4]
[1] Institute for Inorganic Chemistry of the University of Kiel. Germany
[2] National Institute for Astrophysics, Optics and Electronics. Puebla, Mexico
[3] Leibniz Institute for Marine Sciences. Kiel, Germany
[4] University of Applied Sciences Regensburg. Germany
E-mail: equiroga@ieee.org

Abstract — **The size of Si nanocrystals in Silicon Rich Oxide has been varied by depositing this material in multilayer arrays. They are possible candidates for one dimensional quantum devices. A study based on TEM, Raman and XRD measurements is presented.**

Keywords — **Silicon Rich Oxide, SRO, Si nanocrystals, size control, multilayer, Raman for size determination.**

I. INTRODUCTION

Silicon nanocrystals (Si-nCs) as porous silicon or embedded in other materials have shown very interesting properties, useful in different fields. Among other properties, Si-nCs exhibit photoluminescence in the visible range, attributed to quantum confinement effects and to defects at the interfaces [1]. Additionally, some studies have been performed to use the nCs as charge storing centers in single buried layers [2, 3] or superlattices of polysilicon [4].

Si-nCs can be created during the deposition of Silicon Rich Oxide (SRO). In this material, also called off-stoichiometric silicon oxide, the Si-nCs grow by segregation of Si and SiO$_2$ faces by thermal treatments [5]. An indicator of the Si content in the material is the parameter Ro, which is the ratio of the partial pressure of the precursor gases (for example, N$_2$O and SiH$_4$) when it is prepared by gas phase deposition methods as CVD (Chemical Vapor Deposition).

Si-nCs in SRO present a three dimensional size confinement, and are also isolated from other nCs by silicon oxides. This last property distinguishes them from those created by deposition of nanolayers of polysilicon, and is useful for single electron charging [6]. Nevertheless, the average crystallite size depends on several factors like temperature, pressure and the ratio Ro.

Here it is proposed a silicon particle size control by deposition of SRO in multilayers, varying just the deposition time. A low Ro value is used to obtain a material close to SIPOS (semi-insulating polysilicon). The multilayers are fabricated by LPCVD (Low Pressure Chemical Vapor Deposition), which is a simple and conventional method allowing the preparation of homogenous and relatively smooth films. TEM, Raman and XRD measurements were performed in order to characterize the samples.

II. EXPERIMENTAL

A. Fabrication

A SRO film with Ro = 1 (SRO1) and two multilayers (M1 and M2) composed of stacks of SRO1 and SRO with Ro = 50 (SRO50) were fabricated by LPCVD at 725°C. The used substrates were p-type Si (100) wafers with 30-50 Ohm-cm resistivity and quartz substrates. The precursor gases were SiH$_4$ and N$_2$O. The deposition of the multilayers was done varying manually the amount of precursor gases during the deposition. As a final step, all the samples were annealed for 3 h at 1100°C in vacuum.

The multilayer M1 consists of 6 layers of SRO50 alternating with 5 layers of SRO1. M2 is composed of 3 layers of SRO50 alternating with 2 SRO1 layers. The deposition times for every layer are listed in Table I.

B. Characterization methods

The microstructure of the samples was studied with TEM (Tecnai F30, 300 kV). XRD (X-ray Diffractometry) measurements were performed with a PANalytical X'PERT-PRO diffractometer in reflection mode, using Cu Kα radiation. Raman spectra were measured with a HORIBA Jobin Yvon LabRam HR, using 532 nm (frequency doubled Nd:YAG) laser excitation, a 100x Olympus objective with 0.9 numerical aperture, and an 1800 groove/mm grating with a spectral resolution of about 1 cm^{-1}. Approximately 10mW laser light was focused on each sample in order to avoid artifacts in the measurements due to heating. The measurements were performed in dark to avoid any interference with light.

TABLE I
DEPOSITION TIMES FOR THE SAMPLES

Sample	Number of layers of SRO50	SRO50 dep. time (min)	Number of layers of SRO1	SRO1 dep. time (min)
SRO1	-	-	1	45
M1	6	14	5	5
M2	3	20	2	10

IEEE Proceedings of 10th International Conference on Ultimate Integration of Silicon
Aachen, Germany, 18-20.3.2009

III. RESULTS AND DISCUSSION

A. TEM observations

SRO1 is a material with characteristics similar to SIPOS (semi-insulating polysilicon) due to its high Si content [7]. Si agglomerates nucleate during the deposition process. After high temperature annealing, well defined Si nanocrystals (Si-nCs) are obtained from the Si agglomerates, as can be observed in Fig. 1. According to the observations on the samples, the nCs are homogenously distributed and their size varies between 10 and 35 nm. The nCs present a random orientation.

Multilayer M2 is well defined (Fig. 2) evidencing the deposition of all the layers. The SRO1 layers in M2 have a thickness of around 22 nm. On the other hand, the layers in M1 cannot be easily identified by TEM, probably due to the high roughness of the SRO1 layers and due to the very thin SRO50 layers. Nevertheless, the SRO1 layers in M1 should be separated by layers of SRO50, even when they are not smooth, since large bright regions of amorphous material (SRO50) are identified by TEM.

B. Raman measurements

Fig. 3 shows the Raman spectra of the samples deposited on quartz substrate. The spectrum of bulk silicon is included for comparison. The Raman peak at 511 cm^{-1} is related to that at 520 cm^{-1} of crystalline Si (c-Si). This peak (Γ'_{25}) is the optical phonon mode in the center of the Brillouin zone [8], but it is slightly shifted due to quantum confinement effects [9]. The peak around 300 cm^{-1} is due to the two phonon 2TA mode of c-Si, and the intensity is enhanced by LA phonons of an amorphous Si (a-Si) phase [8]. Actually, the peak around 480 cm^{-1} occurring as a shoulder corresponds to LO phonons in a-Si [8, 9]. These results suggest that the Si agglomerates in SRO1 are not totally crystallized even after thermal treatments.

The position of the Γ'_{25} line is approximately the same in all the samples, contrary to the expected difference due to different nanocrystal sizes from sample to sample. The position and the width of the Γ'_{25} peak are used by different groups to estimate the Si crystallite size [9 - 12]. But one should keep in mind that both position and width may be strongly affected by stress, roughness, or missfocusing [9]. Therefore, other parameters should be used for a qualitative estimation of the crystalite size.

A broadening of the Γ'_{25} peak on the low wavenumber range being visible as a shoulder is caused by a distribution of crystallite sizes [10]. Hence, the shape of the peak could give an idea of the average crystallite size of Si. The ratio of the left width at half maximum (LWHM) to the right width at half maximum (RWHM) is the asymmetry coefficient C_a. In this work C_a is considered as an indication of the shape of the Γ'_{25} peak. Since C_a is a relative measure of the shape of the Raman peak, it is independent of its absolute width, height or Raman shift, and consequently insensitive against external factors. The values of C_a for the different samples are shown in Table II.

It has been reported that when the Si nanocrystal size decreases, the Γ'_{25} peak broadens [9]. The fact that C_a increases when the deposition time of SRO1 decreases may indicate that the crystal size decreases, as is corroborated in the XRD section.

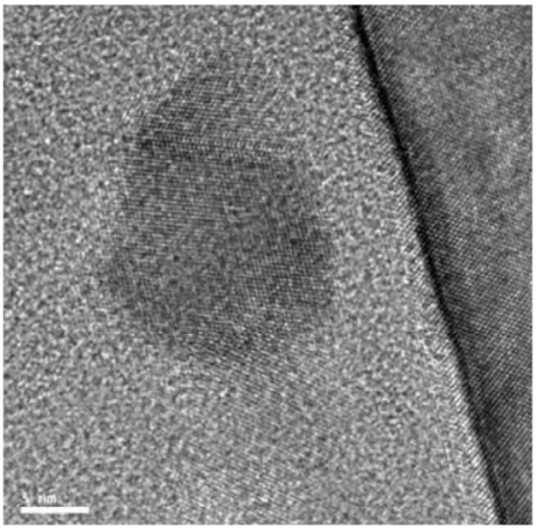

Fig. 1. Typical TEM micrograph of SRO1 in M1. A nanocrystal with diameter of ~20 nm is clearly observed.

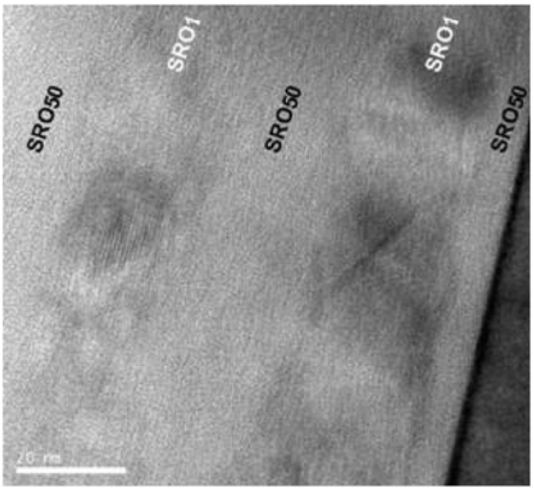

Fig. 2. TEM of M2. The dark zones are layers of SRO1, and the bright ones are layers of SRO50.

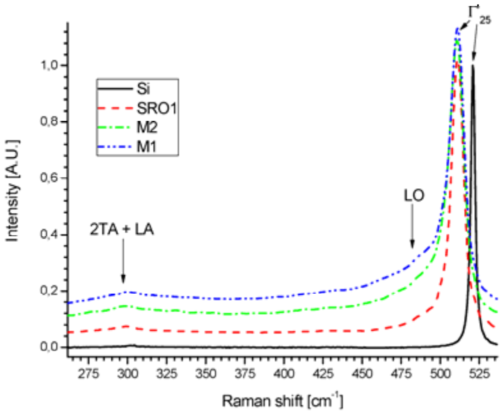

Fig. 3. Raman Spectra of the samples. The spectrum of bulk Si is included for comparison. Three lines related to Si are identified: 2TA and LA (300 cm^{-1}), LO (480 cm^{-1}) and Γ'_{25} (520 cm^{-1} in bulk Si, and 511 cm^{-1} in the rest of the samples).

TABLE II
ASYMMETRY OF THE Γ'_{25} LINE IN THE STUDIED SAMPLES

Sample	SRO1 dep. time (min)	C_a
SRO1	45	1.136
M2	10	1.242
M1	5	1.345

C. XRD measurements

Samples deposited on quartz were used to detect the reflections of Si-nCs, The measurements were performed with long collection times to improve the statistics, but even so, due to the low thickness of the layers the intensity of the reflections is low. Nevertheless, the patterns of all samples evidently present the characteristic reflections of c-Si (111) and (220) at 28° and 47.3° 2θ respectively [13] (see Fig. 4).

Assuming that the samples present a random orientation of nCs, the most intense (111) reflection is taken to calculate the crystallite size. To estimate the size of the coherent scattering domains the Scherrer equation [14] was used:

$$B = \frac{K\lambda}{L\cos\left(\frac{\chi}{2}\right)} \qquad (1)$$

where B is the FWHM of the reflection in radians, K is a constant for which a value of 0.9 is widely accepted assuming spherical particles; λ is the wavelength of incident X-rays (0.1504 nm); χ is the center position of the peak, and L is the crystallite length. The parameters and results of this calculation are summarized in Table III.

According to the data compiled in Table III, the Si nanocrystal size is smaller for shorter deposition times of SRO1, as was also evidenced by the Raman measurements. Fig. 5 shows the relation of the crystallite size with the parameter C_a. In the presented range of nanocrystal sizes the relation seems to be parabolic, but more experiments are needed to probe this tendency and to be able to use this analysis in the estimation of particle sizes.

According to these results it can be concluded that the average size of the Si-nCs in SRO1 (~ 30 nm in thick single films) is limited by the layer thickness. In this way, the size of the nCs can be controlled by tuning the layer thickness.

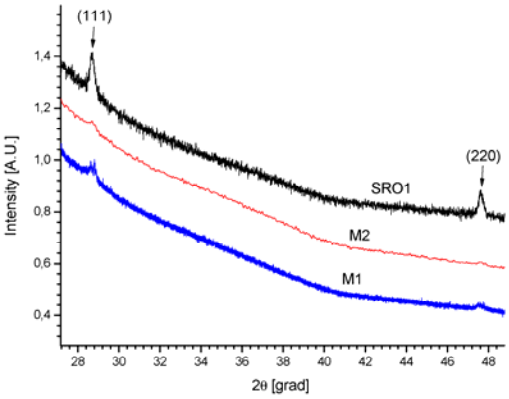

Fig. 4. XRD difractogram of the studied samples. The characteristic reflections of crystalline Si (111) and (220) are identified.

TABLE III
NANOCRYSTAL SIZE

Sample	2θ [grad]	FWHM [grad]	Size [nm]
SRO1	28.69	0.275	29.8
M2	28.71	0.337	24.3
M1	28.73	0.378	21.7

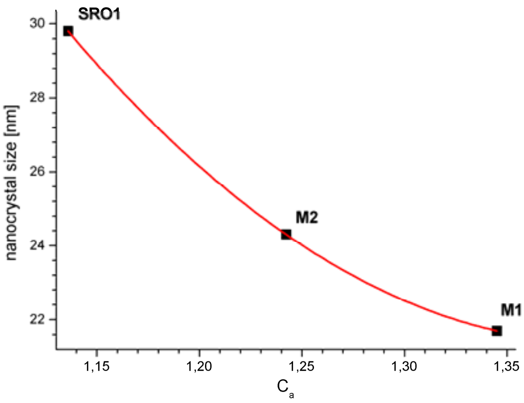

Fig. 5. Relation of the nanocrystal sizes with the parameter C_a.

Additionally, the nCs may tend to be elliptical, since the SRO1 layer thickness in M2 is 22 nm (from TEM) and the average nanocrystal size is 24.3 nm. But this small difference indicates that the shape is almost spherical.

IV. CONCLUSION

The size of Si nanocrystals (Si-nCs) in SRO1 in multilayer arrays depends on the layer deposition time. This is evidenced by studying the asymmetry of the Raman line Γ'_{25} of Si and by XRD. Evaluation of the XRD data allowed a semi-quantitative estimation of the crystallite sizes in different films. Furthermore, the relation of the crystallite size with the asymmetry coefficient C_a seems to be parabolic. Nevertheless, further studies are needed for establishing the analysis of the asymmetry of Raman lines as a tool for the determination of the size of Si-nCs.

The dependency of the Si nanocrystal size on the layer deposition time can be interpreted as a size control, because in one dimension the growth of the nCs is limited by the layer thickness. The nCs are isolated by SiO$_2$ allowing their use in many applications, e.g. as one dimensional quantum devices.

ACKNOWLEDGMENT

The authors appreciate the support from CONACyT and DAAD. Jürgen Kolouch is thanked for his technical collaboration.

REFERENCES

[1] D. Berman, M. Aceves, A. Gallegos, A. Morales, L. R. Berriel, J. Carrillo, F. Flores, C. Falcony, C. Domínguez , A. Llobera, M. Riera, and J. Pedraza "Silicon excess and thermal annealing effects on the photoluminescence of SiO$_2$ and silicon rich oxide super enriched with silicon implantation," *phys. stat. sol. (c)* 1, No. S1, S83– S87 (2004).

[2] D. N. Kouvastos, V. Ioanou-Sougleridis, A. G. Nassiopoulou, "Charging effects in silicon nanocrystals within SiO$_2$ layers, fabricated by chemical vapor deposition, oxidation and annealing," *Appl. Phys. Lett.* 82, No. 3, pp. 397-399, (2003).

[3] V. Ioanou-Sougleridis, A. G. Nassiopoulou, "Investigation of charging phenomena in silicon nanocrystal metal-oxide-semiconductor capacitors using ramp current-voltage measurements," *J. Appl. Phys.* 94, No. 6, pp. 4084-4087, (2003).

[4] E. Quiroga, Z. Yu, M. Aceves, "Charging/discharging effects in nc-Si/SiO$_2$ superlattice prepared by LPCVD" in: Proceedings 2nd International Conference on Electrical and Electronics Engineering (ICEEE) and XI Conference on Electrical Engineering (CIE 2005). Mexico City, Mexico, 2005, pp. 219–222, (IEEE, 2005).

[5] B. Fazio, M. Vulpio, C. Gerardi, Y. Liao, I. Crupi, S. Lombardo, S. Trusso, F. Neri, "Residual crystalline silicon phase in Silicon-Rich-Oxide films subjected to high temperature annealing," *Journal of the electrochemical society* 149, No. 7, pp. G376-G378 (2002).

[6] Z. Yu, M. Aceves, J. Carrillo, F. Flores, "Single electron charging in Si nanocrystals embedded in silicon-rich oxide," *Nanotechnology*, 14, pp. 959–964 (2003).

[7] E. Quiroga, W. Bensch, Z. Yu, M. Aceves, R. A. De Souza, M. Martin, V. Zaporojtchenko, F. Faupel, "Structural characteristics of a multilayer of Silicon Rich Oxide (SRO) with high Si content prepared by LPCVD," *phys. stat. sol. (a).* 206, No. 2, pp. 263-269 (2009).

[8] Y. Ma, X. Liao, G. Kong, J Chu, "Raman scattering of nanocrystalline silicon embedded in SiO$_2$," *Science in China (Series A)* 43, No. 4, pp. 414-420 (2000).

[9] Ch. Ossadnik, S Vepřek, I. Gregora, "Raman Applicability of Raman scattering for the characterization of nanocrystalline silicon," *Thin Solid Films* 337, pp. 148-151 (1999).

[10] S. V. Gaĭsler, O. I. Semenova, R. G. Sharafutdinov, B. A. Kolesov, "Analysis of raman spectra of amorphous-nanocrystalline silicon films," *Physics of the Solid State* 46, No. 8, pp. 1528-1532 (2004).

[11] H. S. Mavi, A. K. Shukla, R. Kumar, S. Rath, B. Joshi, S. S. Islam, "Quantum confinement effects in silicon nanocrystals produced by laser-induced etching and cw laser annealing," *Physics Semicond. Sci. Technol.* 21, pp. 1627-1632 (2006).

[12] B. Li, D. Yu, S. L. Zhang, "Raman spectral study of silicon nanowires," *Physics Semicond. Sci. Technol.* 21, pp. 1627-1632 (2006).

[13] A. Le Donne, S. Binetti, G. Isella, B. Pichaud, M. Texier, M. Acciarri, S. Pizzini, "Structural characterization of nc-Si films grown by low-energy PECVD on different substrates," *Applied Surface Science* 254, pp. 2804-2808 (2008).

[14] A. L. Patterson, "The Scherrer formula for x-ray particle size determination," *Physical Review* 56, pp. 978-982 (1939).

5.3.

Submitted to Thin Solid Films 19.May.2010

Study of multilayer arrays of silicon rich oxide prepared by low pressure chemical vapor deposition for the production of photoluminescence

E. Quiroga-González[1], W. Bensch[1], M. Aceves-Mijares[2*], Z.Yu[3], R. López-Estopier[2], K. Monfil-Leyva[2]

[1] Institute for Inorganic Chemistry of the University of Kiel. Max-Eyth Str. 2. 24118 Kiel, Germany.
[2] National Institute for Astrophysics, Optics and Electronics. Luis Enrique Erro 1, Tonantzintla, Puebla, Mexico.
[3] R&D center, ENN Solar Energy Co. Ltd. 065001 Langfang, China.

*Corresponding author, Email: maceves@ieee.org, tel. +52(222)2470517

Abstract

A study of the structural and compositional properties of multilayer structures containing silicon rich oxide with high silicon content obtained by low pressure chemical vapor deposition is here presented. Different parameters for the preparation of the multilayers have been varied, like Si concentration, the thicknesses of the layers to vary the size of the Si nanocrystals and oxidation temperatures. The possibility of obtaining photoluminescence from the multilayers depends on the fabrication parameters. In all cases the photoluminescence seems to have the same origin: defects in the oxide matrix, and defects in the interfaces between nanocrystals.

PACS: 85.60.Jb, 85.35.Be, 81.15.Gh

1. Introduction

Multilayer structures (MLs) and superlattices of Si/SiO_2 have been receiving much attention in the last years due to the many application possibilities, for example in third generation solar cells [1]. By fabricating tandems of layers of silicon and its oxides using reduced dimension of the silicon layers one can engineer the band gap of Si. These tandems can work as the upper material in the solar cells. In the same way, Si nanocrystals (Si-nCs) embedded in silicon oxides have been used instead of Si in the tandem structures, presenting a three dimensional quantum confinement [2]. The size of the Si-nCs can be tunned according to the thickness of the layers [3].

ML structures with Si-nCs have been also prepared to make size-dependent photoluminescence (PL) studies of the Si-nCs [3]. The layers containing Si-nCs can be prepared by different methods, like implantation of Si in an amorphous matrix (principally SiO_2) [4, 5], and deposition of silicon rich oxides (SRO) [6, 7]. In the case of SRO, also called off-stoichiometric silicon oxide or silicon rich silicon oxide, the Si-nCs grow by segregation of the Si excess from the silicon oxides during thermal treatments at high temperatures [8]. An indicator of the Si content in this material is the parameter Ro, which is the ratio of the partial pressure of the precursor gases (for example, N_2O/SiH_4) when it is prepared by gas phase deposition methods like CVD (Chemical Vapor Deposition). Among CVD methods, the Low Pressure Chemical Deposition (LPCVD) is a very convenient approach for the deposition of SRO films since it allows an exact variation of the Si content and it is a simple and cheap method.

Single layers of SRO with low Si excess usually present PL, but it is product of different effects that can not be easily separated due to large dispersions of the nC sizes. There are some reports on the origin of the PL of Si-nCs in silicon oxides that make a differentiation of the PL caused by quantum confinement effects from the one caused by defects [9], and identify different kinds of defects [10]. Nevertheless there is still some uncertainty at distinguishing the real origin of the PL in each fabrication technique, post thermal treatment and particle size range. For example, in single films

Submitted to Thin Solid Films 19.May.2010

of SiO$_x$ prepared by evaporation the PL is dominated by defects when the annealing temperatures are below 900 °C and it has a component caused by quantum confinement when the temperatures are above 1000 °C [11]. PL due to quantum confinement effects in Si-nCs has also been observed in Si-implanted SiO$_2$ films where the PL peak blue-shifts with oxidation time [5], with the largest particles in these films being about 5 nm. The blue-shift has also been reported in sputtered SRO films when varying the Si-nCs sizes from 5 to 2.7 nm [12, 13]. SRO films prepared by LPCVD present intense PL when they have Si excess (excess compared with SiO$_2$) lower than 8 at% (Ro = 20 – 30), and a weak emission for excess larger than 12 at% (Ro < 10) [6, 14]. One can observe an insignificant blue shift in the PL when going from SRO Ro = 20 to Ro = 30 (particle sizes of around 2.75 nm and no observed particles, respectively), but no shift could be observed when decreasing the Ro to 10 (Si-nCs sizes of around 4.2 nm) [6]. This could be evidence that the PL in this kind of films is dominated by defects.

An evident blue shift in the PL could be observed in evaporated MLs containing Si-nCs when the size of the nanocrystals decreases from 3.2 nm to 2.8 nm [3], an effect that is ascribed to quantum confinement effects. For this kind of study the Si content in the layers containing Si-nCs should be high in order to assure the tuning of the Si-nC sizes with the thickness of the layers.

In the present work it is reported a structural study of MLs containing SRO with high silicon content (Ro < 3) prepared by LPCVD. It is good to mention that ML structures of SRO prepared by LPCVD have been previously reported just by our group [15]. The PL of MLs with SRO with different Si content, different Si-nC sizes, and oxidized at different temperatures are compared in the present study. Transmission Electron Microscopy (TEM), X-ray Photoelectron Spectroscopy (XPS) and ellipsometry were used to study the structural and compositional properties of the MLs. The properties of single layers of SRO were also analyzed in order to know the constituents of the MLs and associate effects.

2. Experimental details

SRO single layers with Ro = 1 (SRO1), Ro = 3 (SRO3), Ro = 30 (SRO30) and Ro = 50 (SRO50), and ML structures composed of stacks of SRO1 (or SRO3) and SRO50 were deposited on p-type Si (100) wafers with 30–50 Ωcm resistivity by LPCVD at 725 °C, using SiH$_4$ and N$_2$O as the precursor gases. A list of the single layers is shown in Table I, and a list of the ML structures is shown in Table II. The MLs, composed of n+1 layers of material 1 (SRO50) and n layers of material 2 (SRO1 or SRO3), were deposited varying manually the precursor gases during the deposition. After the deposition the samples were annealed in N$_2$ at 1100 °C for 3 hr to favor the nucleation of the Si-nCs.

The microstructure of the MLs was studied with TEM measurements (Tecnai F30, 300 kV). A Null ellipsometer Gaertner L117, which operates with a 632.8 nm laser at a fix 70° angle of incidence, was used to obtain the refractive index of the samples. The PL emission spectra were obtained with a spectrofluorometer Jobin Yvon Fluoromax-3 at room temperature; the samples were excited with energy of 280 nm (4.42 eV), and it was used a long-pass filter of 400 nm (3.1 eV) in the detector.

Table I
Single layers

Sample	**Thickness [nm]**
SRO1	133
SRO3	72
SRO30	400
SRO50	60.8

Table II
Multilayers

Sample	Number of periods	Material 1	Material 1 thickness [nm]	Material 2	Material 2 thickness [nm]	Total thickness [nm]
M1	7	SRO50	4	SRO3	4	53
M2	3	SRO50	7	SRO3	8.5	38
M3	5	SRO50	12	SRO1	22	150

The thickness of the layers is an estimated value given for the deposition rate of single films

3. Results and discussion

3.1. Single layers

The composition of SRO30 and SRO50 prepared under similar conditions as in the present case have been already reported in different articles [15, 16]. SRO30 has Si excess of around 6 at% [16]. This Si excess does not form Si-nCs, but is found in the form of amorphous Si sub-oxides [17]. On the other hand, SRO50 is a material with composition very close to stoichiometric SiO$_2$ [15].

To determine the composition of the materials with high Si content (SRO1 and SRO3) XPS analyses were performed in single films of these materials. The Si 2p XPS peak presents a 2p$_{3/2}$ and 2p$_{1/2}$ spin-orbit splitting with the two levels separated by 0.6 eV, thus for every oxidation state of Si there are two peaks [18]. The positions of the peaks corresponding to Si^0 (elemental Si) and Si^{4+} (SiO$_2$) are easily distinguishable in the XPS spectra of SRO1 and SRO3 (Fig. 1a and Fig. 1b respectively), and it is possible to assign them unequivocally according to some reports [18, 19]. The 2p$_{3/2}$ signal of elemental Si is found at around 99 eV with the corresponding 2p$_{1/2}$ line located 0.6 eV at higher energies. The 2p$_{3/2}$ signal of SiO$_2$ is significantly shifted by about 4 eV to higher binding energy and occurs at around 103 eV. The peaks of the Si sub-oxides are located in the region between these two species. As an unambiguous individual assignment of SiO$_x$ sub-oxides is not possible, all the sub-oxides are considered as one group. The amount of sub-oxides in the samples was obtained by subtracting the area of the fitted peaks of Si^0 and Si^{4+} from the total area. The position of the peaks related with silicon sub-oxides has been reported for Si/SiO$_2$ interfaces [18, 20], but they cannot be distinguished unequivocally in a complex spectrum composed of different Si oxide species. Hence, a quantitative analysis of such highly convoluted spectra is not straightforward and the results obtained by such fittings sensitively depend on the fitting parameters applied. According to the deconvolution of the XPS spectra, SRO1 is composed of 72, 12 and 16 at% of elemental Si, SiO$_2$ and SiO$_x$ ($0 < x < 2$), while SRO3 is composed of 20, 34 and 46 at% of those materials respectively. The amount of elemental Si in SRO1 is 3.6 times that of SRO3.

1a)

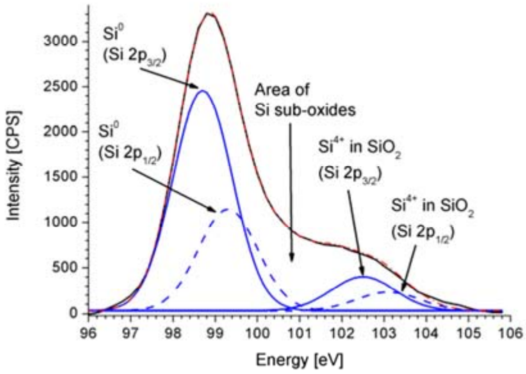

1b)

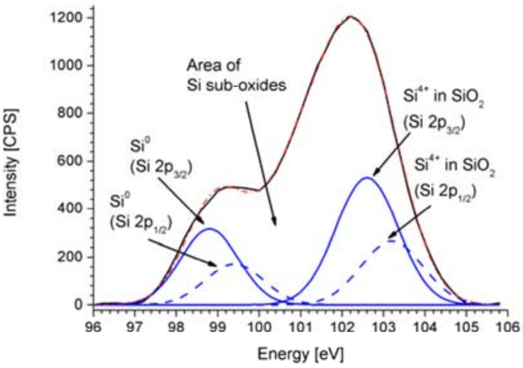

Fig. 1. XPS spectrum of a) SRO1 and b) SRO3. The peaks of the Si 2p$_{1/2}$ and Si 2p$_{3/2}$ of Si^0 and Si^{4+} were fitted. Sub-oxide species are found in the region between Si^0 and Si^{4+}.

When analyzing the PL emission of the SRO single layers, just SRO30 presented a PL signal detectable by the measurement system. This means that neither materials with high Si content (SRO1 and SRO3) nor the one with composition close to SiO$_2$ (SRO50) exhibit detectable PL. The PL spectrum of SRO30 is shown in Fig. 2. This material presents an intense PL peak positioned at around 703 nm.

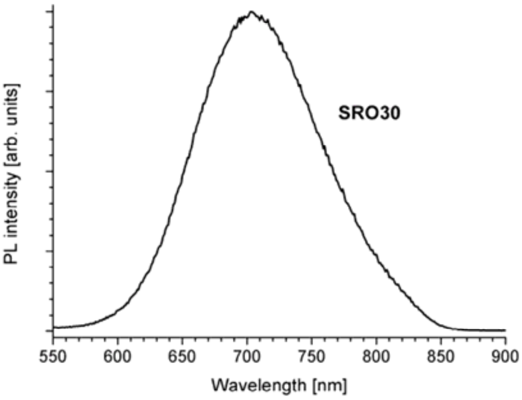

Fig. 2. PL spectrum of SRO30. The PL peak is positioned at 703 nm.

3.2. Multilayers

All MLs were analyzed by TEM, finding that just their first two layers (from the substrate's side) can be easily identified. On top of these layers, the layered structure is less evident due to the increased roughness caused by the SRO1 or SRO3 layers. In this way, one can just observe Si-nCs embedded in an amorphous matrix. Comparing the MLs prepared with SRO3 (M1 and M2) no apparent difference is detected by simple inspection of the micrographs (see Fig. 3 a) and b)). But performing a statistic analysis of the sizes of the Si-nCs a remarkable difference is observed. In M1 most of the Si-nCs have sizes below 4 nm which is the thickness of the SRO3 layers, with an average size of 3.6 nm and mode size between 3.5 and 4 nm (Fig. 4a), i.e., the size of the Si-nCs is limited by the thickness of the layers. This behavior is expected in thin SRO films with high Si contents [21], as is the case of this sample. This could be evidence that the layered structure exists even when it is not clearly observed in the TEM micrographs. In the same way, in the ML M2 all the Si-nCs have sizes smaller than 8 nm (the thickness of the SRO3 layers), and the values are typically below 5 nm (Fig. 4b). The average size in this sample is 4.1 nm.

3a)

3b)

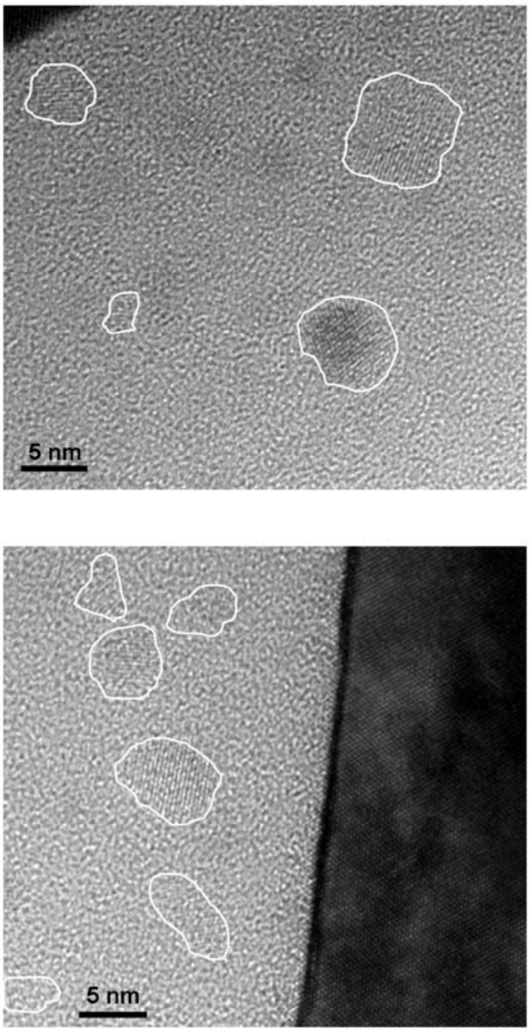

Fig. 3. Typical TEM micrographs of the samples M1 (a) and M2 (b). The black section corresponds to the Si substrate. Some layered sections can be observed in the clear part (enclosed with white lines), corresponding to the Si-nCs. The average sizes of the nCs are 3.6 and 4.1 nm for samples M1 and M2 respectively.

4a)

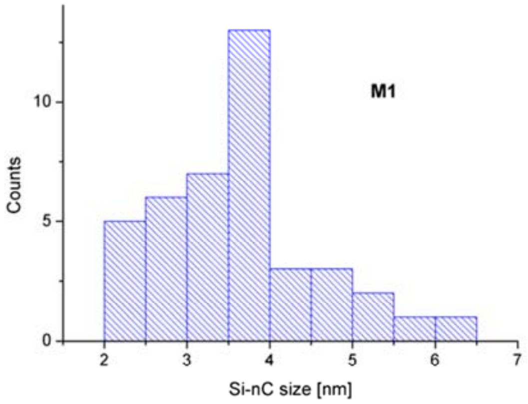

4b)

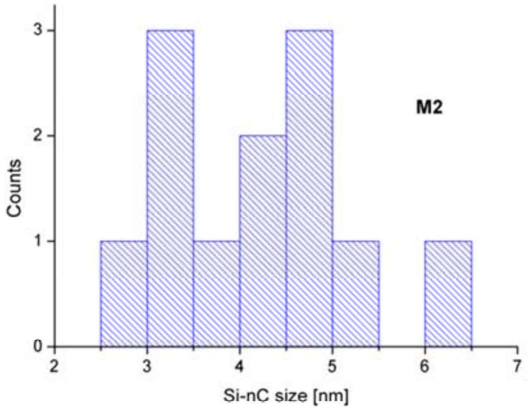

Fig. 4. Distribution of Si-nC sizes in a) M1 and b) M2. In both cases the size of the Si nCs is typically smaller than the thickness of the SRO3 layers (4 and 8 nm respectively).

As in the case of the samples M1 and M2 prepared with SRO3, in the ML synthesized with SRO1 just the first two layers can be easily identified by simple inspection of the TEM micrographs (Fig. 5). Even though, by statistical analysis (Fig. 6) it was determined that the mean Si-nC size is 13.4 nm, with maximum sizes in the range of the expected thickness of the SRO1 layers (22 nm). In this case the size of the Si-nCs is also limited by the thickness of the layers with high Si content (SRO1).

Submitted to Thin Solid Films 19.May.2010

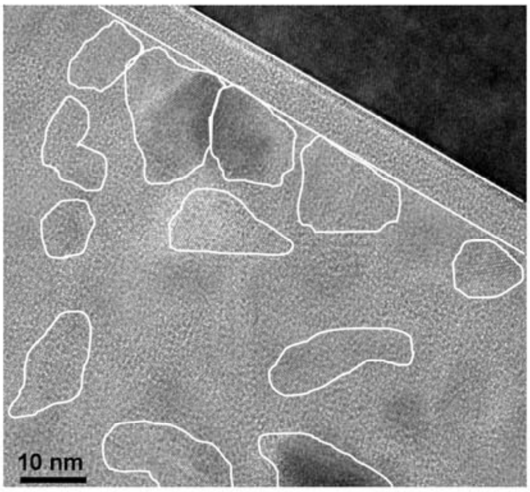

Fig. 5. Typical TEM micrograph of sample M3. The first layer of SRO50 (to the substrate's side) can be easily identified. The average size of the nCs is 13.4 nm.

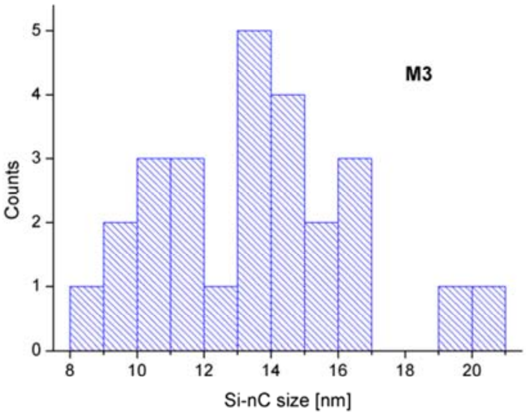

Fig. 6. Distribution of Si-nC sizes in ML M3. All the nCs have sizes below 22 nm (the expected thickness of the SRO1 layers).

The PL spectra of M1 and M2 are shown in Fig. 7a and 7b respectively. M3 does not present any PL signal. The PL of M1 and M2 cannot be originated from the layers of SRO50 since this material does not present PL emission. On the other hand, it cannot be due to direct band-to-band transitions allowed by quantum confinement effects in the nanometric layers of SRO3 since the PL bands of M1 and M2 are at the same position. Because these materials have different Si-nC sizes a blue shift should occur in the PL spectrum of M1 compared with that of M2 if it would be originated from direct band transitions in the Si-nCs. A deconvolution of the PL peaks was performed in order to give possible explanations to the PL. In both cases the PL spectra can be deconvoluted in peaks centred at around 703, 779 and 880 nm (bands A, B and C), as shown in Fig. 7a and 7b.

The PL band A should have the same origin as the PL of SRO30, whose peak is also positioned at 703 nm. As SRO30 do not contain any Si-nCs, the PL in this material should be due to the defects in its sub-oxide matrix. Actually there has been reported just an insignificant blue shift in the PL when going from SRO Ro = 20 to Ro = 30 [6], giving evidence of the defect-related PL. The large number of sub-oxides present in SRO3 should adopt configurations close to the one in SRO30 in the transition area between SRO3 and SRO50 during the deposition of the MLs, allowing the presence of the PL band A.

The positions of the peaks B and C do not change when reducing the size of the Si-nCs, thus these peaks are not due to direct band transitions in the nCs. These PL peaks should then originate from the interfaces between the Si-nCs and the sub-oxide matrix, which is a defect-rich region [22]. The area of the PL peaks B and C increases when reducing the size of the Si-nCs. The sum of areas of the peaks B and C amounts 34.5 % of the total area in M2, while it is 43.9 % in M1. The smaller crystals have larger surface to bulk ratio, so the interface-related PL is of higher intensity. The sample M3 does not present PL properties probably because the nCs in this ML are not small enough for this emission process. Actually, it has been reported that the PL related to the interface depends strongly on the nC size because quantum confinement effects in the nCs are necessary [10]. Due to quantum confinement, the band gap of the Si-nCs increases when their size decreases, and the breakdown of momentum conservation makes the Γ→L and Γ→X transitions pseudo-direct. The defect states are Γ-like, thus, electrons excited from the Si valence band relax to the conduction band edge, from which they tunnel (resonantly) to the defect states and recombine radiatively [23].

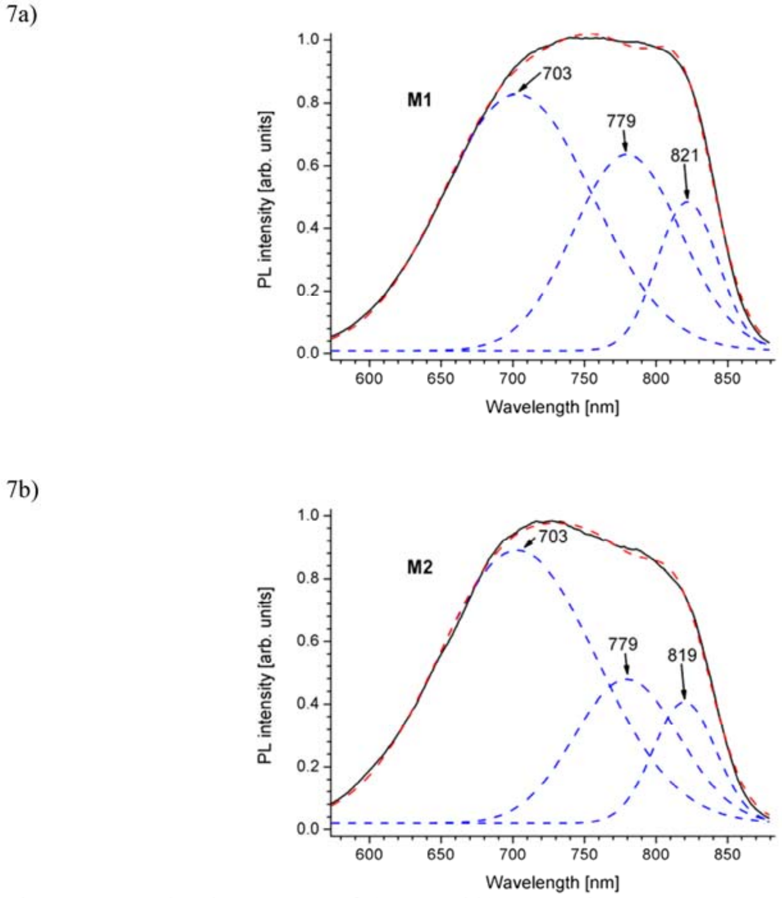

Fig. 7. Deconvoluted PL spectra of a) M1 and b) M2. Both spectra are composed of peaks positioned at around 703, 779 and 880 nm.

Submitted to Thin Solid Films 19.May.2010

3.2. Oxidized multilayers

The ML which did not present PL (M3) was oxidized at different temperatures under dry oxygen in order to analyse the possibility of producing PL. For this purpose, M3 was divided into pieces denoted M3a-d. The oxidation conditions for the samples are listed in Table III.

Table III
Oxidation processes

Sample	**Oxidation conditions**
M3a	60 min 800 °C
M3b	60 min 800 °C + 30 min 900 °C
M3c	60 min 800 °C + 30 min 1000 °C
M3d	60 min 800 °C + 30 min 1100 °C

Like for the non-oxidized layers, a statistical analysis of the Si-nC sizes was also made for the oxidized samples. As expected, the average size of the nCs decreases by increasing the oxidation temperature. This effect can be observed at comparing the distribution of Si-nC sizes of M3a and M3d (Fig. 8a and Fig. 8b respectively). M3a presents nCs with sizes up to 20 nm, with mean size of 13.4 nm. On the other hand, M3d has nCs with sizes typically smaller than 12 nm (see Fig. 8b). According to these results it can be stated that the oxidation level increases upon oxidation temperature, as confirmed by ellipsometric measurements which are discussed below.

8a)

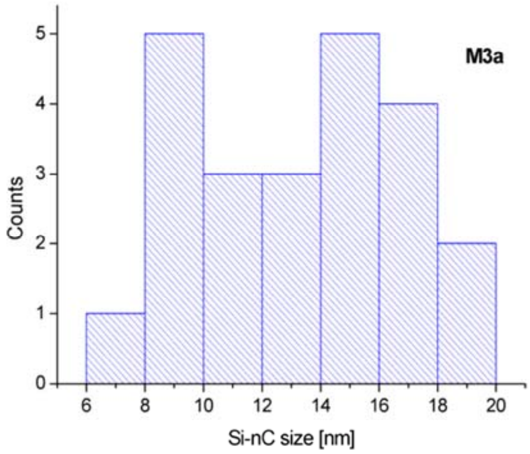

Submitted to Thin Solid Films 19.May.2010

8b)

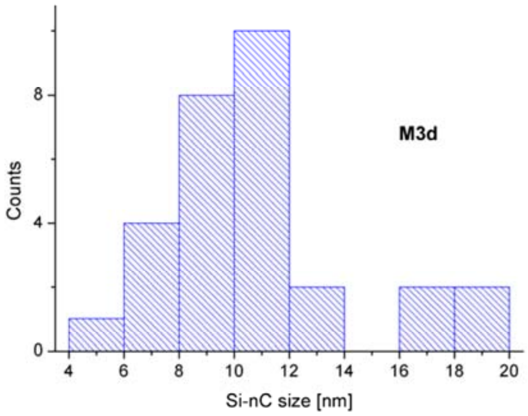

Fig. 8. Distribution of Si-nC sizes in a) M3a and b) M3d. The nC sizes in M3d are typically smaller than 12 nm, contrary to the sizes in M3a, which range between 6 and 20 nm.

The refraction indexes of the oxidized samples, calculated from the ellipsometric measurements, are plotted in Fig. 9. In the plot it can be seen that the refractive index decreases upon oxidation temperature. Considering that the sizes of the Si-nCs and the silicon oxide zones are much smaller than the wavelength of the ellipsometer (632.8 nm), the MLs can be seen as an effective medium with effective refraction index according to the Bruggeman theory [24]. The effective refraction index of the studied material (n_{eff}) is related to the refraction index of each phase (n_{Si} and n_{ox}) as well as to their volume fractions (V_{Si} and V_{ox}). The Bruggeman equation for the two-component system is:

$$V_{Si}\frac{n_{Si}-n_{eff}}{n_{Si}+2n_{eff}} = -V_{ox}\frac{n_{ox}-n_{eff}}{n_{ox}+2n_{eff}} \qquad (1)$$

From this equation is possible to obtain an approximation of the volume fraction of Si-nCs in the MLs if considering that they are composed of Si and SiO$_2$, so that

$$V_{Si} + V_{ox} = 1 \qquad (2)$$

Considering $n_{ox} = 1.46$ and $n_{Si} = 3.85$, the volume fraction of Si-nCs in the different oxidized MLs is around 0.8 (M3a), 0.7 (M3b), 0.6 (M3c) and 0.2 (M3d) respectively. With these results it can be concluded that the oxidation level of the MLs increases when the oxidation temperature increases, i.e., the amount of Si transformed into silicon oxides increases.

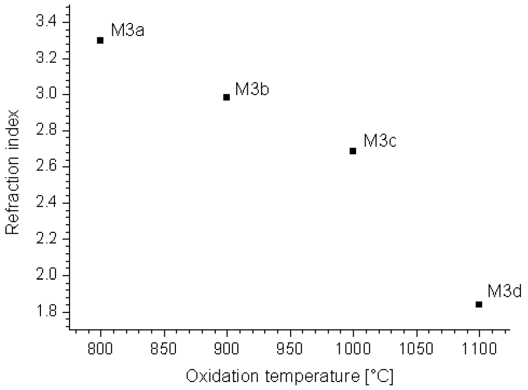

Fig. 9. Dependence of the refraction index on the oxidation temperature. The refraction index tends to that of SiO$_2$ when the oxidation temperature increases, indicating that the volume fraction of the Si-nCs gets smaller.

Among the oxidized samples only the samples M3c and M3d display a PL signal, indicating that they contain Si-nCs with the adequate sizes for the PL emission. The PL emission of M3d is noisy and of low intensity. Even though the spectra of the two samples can be deconvoluted in three peaks found in the same positions as in the not-oxidized samples (703, 779, and ~820 nm), as shown in Fig. 10a and 10b. According to this, the PL in the oxidized samples could have the same origin as in the not-oxidized samples. Upon oxidation the sub-oxides reach a configuration close to the one in SRO30, and the Si-nCs are reduced in size allowing also the interface-related PL.

The sum of the areas of the peaks at 703 and 779 nm (peaks B+C) is 48.6 % of the total area in M3c, while it is 32.4 % in M3d. An explanation for the smaller area of B+C in M3d is that part of the Si-nCs in M3d are fully oxidized, reducing the intensity of the interface-related PL.

10a)

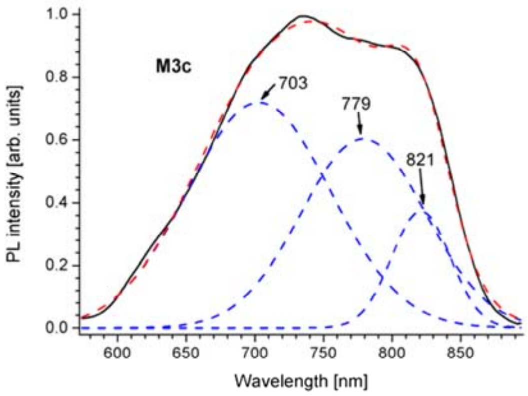

10b)

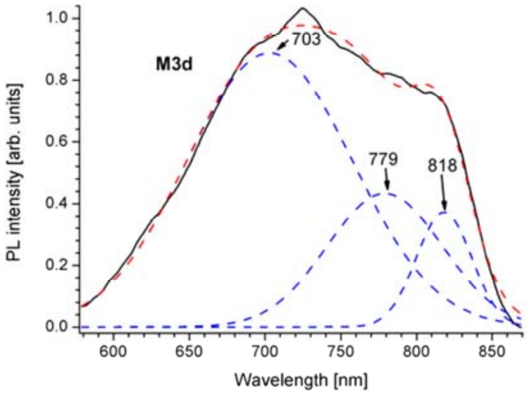

Fig. 10. PL spectra of the oxidized samples a) M3c and b) M3d. The position of the deconvoluted PL peaks is the same as in the not-oxidized samples, confirming that the origin of the PL could be the same in the both cases.

4. Conclusions

ML structures containing SRO with high Si content were prepared. It was demonstrated that the size of the Si-nCs in the structures can be tuned by varying the thickness of the layers. The Si content and Si-nC sizes were also reduced by oxidation. The MLs with smaller Si-nC sizes present PL. It was evidenced that the PL is generated by defects in the oxide matrix, and by defects in the interfaces between nanocrystals. The first emission mechanism is independent of the existence of nanocrystals, as is the case of SRO with Ro = 30. On the other hand, the interface-related PL depends on the size of the Si-nCs. When the Si-nCs have a size at which the band-gap of Si is pseudo-direct (a quantum confinement effect), the excited carriers can tunnel to the interfacial defects, where the radiative recombination takes place.

Aknowledgement

The authors appreciate the support of CONACyT and DAAD. They also thank Pablo Alarcón from INAOE for the technical help for the oxidation of the samples.

References

[1] G. Conibeer, M. Green, R. Corkish, Y. Cho, E.C. Cho, C.W. Jiang, T. Fangsuwannarak, E. Pink, Y. Huang, T. Puzzer, T. Trupke, B. Richards, A. Shalav, K.L. Lin, Thin Solid Films 511-512 (2006) 654.

[2] G. Conibeer, M. Green, E.C. Cho, D. König, Y.H. Cho, T. Fangsuwannarak, G. Scardera, E. Pink, Y. Huang, T. Puzzer, S. Huang, D. Song, C. Flynn, S. Park, X. Hao, D. Mansfield, Thin Solid Films 516 (2008) 6748.

[3] M. Zacharias, J. Heitmann, R. Scholz, U. Kahler, M. Schmidt, J. Bläsing, Appl. Phys. Lett. 80/4 (2002) 661.

[4] H. Coffin, C. Bonafos, S. Schamm, N. Cherkashin, G. Ben Assayag, A. Claverie, M. Respaud, P. Dimitrakis, P. Normand, J. Appl. Phys. 99 (2006) 044302.

[5] M.L. Brongersma, A. Polman, K.S. Min, E. Boer, T. Tambo, H.A. Atwater, Appl. Phys. Lett. 72/20 (1998) 2577.

[6] A. Morales-Sánchez, J. Barreto, C. Domínguez-Horna, M. Aceves-Mijares, J.A. Luna-López, Sensors and Actuators A 142 (2008) 12.

[7] D. Riabinina, C. Durand, J. Margot, M. Chaker, G.A. Botton, F. Rosei, Phys. Rev. B 74 (2006) 075334.

[8] B. Fazio, M. Vulpio, C. Gerardi, Y. Liao, I. Crupi, S. Lombardo, S. Trusso, F. Neri, J. Electrochem. Soc. 149/7 (2002) G376.

[9] K.S. Min, K.V. Shcheglov, C.M. Yang, H.A. Atwater, M.L. Brongersma, A. Polman, Appl. Phys. Lett. 69/14 (1996) 2033.

[10] S. Godefroo, M. Hayne, M. Jivanescu, A. Stesmans, M. Zacharias, O.I. Lebedev, G. Van Tendeloo, V.V. Moshchalkov, Nature Nanotechnology 3 (2008) 174.

[11] Y.C. Fang, Z.J. Zhang, M. Lu, J. Lumin. 126 (2007) 145.

[12] Y. Kanzawa, T. Kageyama, S. Takeoka, M. Fujii, S. Hayashi, K. Yamamoto, Solid State Comm. 102/7 (1997) 533.

[13] L. Khomenkova, N. Korsunska, T. Torchynska, V. Yukhimchuk, B. Jumayev, A. Many, Y. Goldstein, E. Savir, J. Jedrzejewski, J. Phys.: Condens. Matter 14 (2002) 13217.

[14] R. López-Estopier, M. Aceves-Mijares, C. Falcony, 3rd International Conference on Electrical and Electronics Engineering, IEEE, Mexico City, 2006, p. 1.

[15] E. Quiroga, W. Bensch, Z. Yu, M. Aceves, R.A. De Souza, M. Martin, V. Zaporojtchenko, F. Faupel, Phys. Stat. Sol. A 206/2 (2009) 263.

[16] A. Morales, J. Barreto, C. Domínguez, M. Riera, M. Aceves, J. Carrillo, Physica E 38 (2007) 54.

[17] D.J. DiMaria, J.R. Kirtley, E.J. Pakulis, D.W. Dong, T.S. Kuan, F.L. Pesavento, N. Theis, J.A. Cutro, S.D. Brorson, J. Appl. Phys. 56/2 (1984) 401.

[18] F.J. Himpsel, F.R. McFeely, A. Taleb-Ibrahimi, J.A. Yarmoff, G. Hollinger, Phys. Rev. B 38/9 (1988) 6084.

[19] F. Verpoort, P. Persoon, L. Fiermans, G. Dedoncker, L. Verdonck, J. Chem. Soc., Faraday Trans. 93/19 (1997) 3555.

[20] F.J. Grunthaner, P.J. Grunthaner, R.P. Vasquez, B.F. Lewis, J. Maserjian, A. Madhukar, Phys. Rev. Lett. 43/22 (1979) 1683.

[21] E. Quiroga, W. Bensch, M. Aceves, Z. Yu, J.P. Savy, M. Haeckel, A. Lechner, 10th International Conference on Ultimate Integration of Silicon (ULIS 2009), IEEE, Aachen, Germany, 2009, p. 349.

[22] F. Djurabekova, M. Backman, K. Nordlund, Nucl. Instrum. Methods Phys. Res. B 266 (2008) 2683.

[23] B. Averboukh, R. Huber, K.W. Cheah, Y.R. Shen, G.G. Qin, Z.C. Ma, W.H. Zong, J. Appl. Phys. 92/7 (2002) 3564.
[24] M. Khardani, M. Bouaïcha, B. Bessaïs, Phys. Stat. Sol. C 4/6 (2007) 1986.

6. Conclusions and outlook

New thioindates presenting different architectures and compositions have been synthesized under solvothermal conditions. The ones presented in the thesis are the 0-D cationic thioindate $[In(en)_2S]_2 \cdot 2Cl$, the 1-D thioindate $[Mg(en)_3][In_2S_4]$ which is the first one containing an earth alkaline complex, and the thioindate $(C_{13}H_{28}N_2)_5[Cu_2In_{18}S_{33}] \bullet x(H_2O)$ composed of supertetrahedral clusters. The success of obtaining new thioindates demonstrates that the solvothermal approach is a powerful and promising method for the preparation of new compounds with different and unique crystal structures. Such explorative experimental work is necessary for the synthesis of new compounds which may exhibit photoactive properties superior to those of the well established materials. Obviously, the products of the solvothermal syntheses cannot be predicted or planned, and it is a “trial and error” approach which requires a large number of experiments varying several reaction parameters. Once a new compound is obtained, a systematic variation of the synthetic parameters of the chemical system under investigation yields further new compounds which enriches our knowledge about the structural diversity, chemical flexibility and variability of the physical properties of the distinct system which is just explored. Several examples in the present PhD thesis can be regarded as instructive examples for the large potential of the solvothermal synthesis approach.

In further experiments on solvothermal synthesis, three inorganic compounds of the Cu-In-S system have been prepared as mixtures, exhibiting good photocatalytic properties for H_2 production from water using sacrificial reagents. The compounds display new nanocrystal morphologies ranging from flower-like agglomerates of thin nanoplates to nanobelts. The compositions of the three compounds are very near to $CuInS_2$, $CuIn_3S_5$ and $CuIn_7S_{11}$ according to Nano-EDX analyses. In the X-ray powder patterns of the mixtures $CuInS_2$ (chalcopyrite structure type) could be clearly identified, whereas a distinct crystal structure for the remaining two samples is still missing. Despite this drawback, the advantage of the intimate mixture on the photocatalytic H_2 evolution from water decomposition in the presence of sacrificial reagents is obvious. The three samples cover a wide range of optical band-gaps thus they effectively utilize a large wavelengths range of incident light. In the literature such materials of the Cu-In-S system have been usually prepared in solid solutions with wide-band materials when they were used for photocatalysis. Nevertheless the number of such reports is still low.

The new thioindate compounds have been used as single source precursor for the production of different indium sulfides. In this way the materials In_2S_3, Cu-containing In_2S_3, $MgIn_2S_4$ and $CuInS_2$ were obtained with different morphologies depending on the synthetic methods. The applied methods were Pulsed Laser Deposition, rapid pyrolysis and simple thermal decomposition in inert atmospheres. Microcrystalline and nanocrystalline powders or films were prepared. The photoconductive properties of the obtained materials were studied, and some of them were found good candidates for photovoltaic applications. The proposed methods for the preparation of nanocrystals of indium sulfides have been scarcely studied for this material system.

As additional work, with the objective of producing photoconductive materials with lower price, the possibility of substituting the In atoms in thioindates by Sb atoms was tested. These experiments led to the synthesis of the second In-containing thioantimonate $\{[In(C_6H_{14}N_2)_2]_2Sb_4S_8\}Cl_2$.This compound presents an especial connectivity feature of the thioantimonate anion acting as a tetradentate anion. The compound additionally presents reversible negative thermal expansion that is new in the areas of thioindates or thioantimonates. In other experiments where the synthetic conditions to prepare a thioindate were followed to prepare a thioantimonate, the result was the crystallization of the new thioantimonate $[Mg(en)_3][Sb_4S_7]$, which is the first thioantimonate(III) compound containing an earth alkaline complex. In this way it has been evidenced that it is possible to transfer some structural characteristics from thioindates to thioantimonates when they are prepared under similar conditions, opening research opportunities in the synthesis of thiometallate materials.

The second part of the work consisted of the fabrication and characterization of multilayers of SRO (Silicon Rich Oxide) with high Si content and SiO_2 by LPCVD (Low Pressure Chemical Vapor Deposition). Different analytic methods were used to clarify the properties of these structures; multilayers of SRO with high Si content have not been much studied previous to this work. A refining of the deposition conditions was reached through a large number of experiments. This allowed the control of the size of the Si nanocrystals (Si-nCs) embedded in SRO, by varying the size of the layers. During the study of these structures a new method for the determination of the Si-nC sizes by Raman spectroscopy has been proposed. The control of the Si-nC allowed the preparation of multilayers that exhibit photoluminescence in the visible range. This photoluminescence is ascribed to defects in the interfaces between layers and in the silicon oxide matrix. The results in this area give more insight in the preparation of multilayers of SRO by LPCVD, proving that LPCVD is a convenient method for this purpose. On the other hand, the photoluminescence bands of the studied structures are broader compared with other reported multilayers, covering a large range of the visible spectrum. This is caused by the difference in the emission mechanism.

Besides the results presented in this thesis other interesting results were obtained, but due to time and space limitation it was decided not to include these data in the thesis. For example, it was possible to substitute the metal cations of known open framework thioindates allowing a continuous tuning of the optical band-gap depending on the substituting metal cation. This substitution also allowed tuning the energy of the photoluminescence produced by the compound. When introducing Fe interesting magnetic properties are observed, which depend on the degree of Fe substitution. Additionally other In complexes and thioantimonates were prepared and all these results will be published soon.

The results of the thesis can be viewed as the starting point in different areas like the preparation of cationic thioindates or the charge compensation of thioindates with different cations. The preparation of indium sulfides from thioindates by alternative methods like the proposed rapid pyrolysis gives a lot of research opportunities. The preparation of hybrid compounds in the In-Sb-S system also represents a challenging area, because only two compounds containing both In and Sb in a sulfur environment were prepared until now. Additionally much more investigations can be done in the area of photoluminescence of multilayers of SRO, searching for controlling the energy of the emission. The proposed Raman method to estimate the size of the Si-nCs in the multilayers should be supported by additional experiments, and it could become a standard method due to its simplicity and relatively cheap equipment needed.

List of publications

1. **E. Quiroga-González**, W. Bensch, Z. Yu, R. López-Estopier, K. Monfil-Leyva, M. Aceves-Mijares, "Study of multilayer arrays of silicon rich oxide prepared by low pressure chemical vapor deposition for the production of photoluminescence," *Thin Solid Films.* Submitted 19.May.2010.

2. **E. Quiroga-González**, L. Kienle, C. Näther, V.S.K. Chakravadhanula, W. Bensch, "Zero- and one-dimensional thioindates synthesized under solvothermal conditions yielding α-In_2S_3 or $MgIn_2S_4$ as thermal decomposition products," *J. Solid State Chem.* Submitted 28.Apr.2010.

3. **E. Quiroga-González**, L. Kienle, V. Duppel, D. K. Lee, J. Janek, W. Bensch, "In-$CuInS_2$ nanocomposite film prepared by Pulsed Laser Deposition using a single source precursor," *Solid State Sci.* Submitted 28.Apr.2010.

4. **E. Quiroga-González**, L. Kienle, V. Duppel, W. Bensch, "Transmission Electron Microscopy study of Cu-containing spinel-type In_2S_3 nanocrystals prepared by rapid pyrolysis of a single molecular precursor," *Z. Anorg. Allg. Chem.*. Submitted 11.Apr.2010.

5. **E. Quiroga-González**, Christian Näther, Wolfgang Bensch, "The thioantimonate anion $[Sb_4S_8]^{4-}$ acting as a tetradentate ligand: solvothermal synthesis, crystal structure and properties of $\{[In(C_6H_{14}N_2)_2]_2Sb_4S_8\}Cl_2$ exhibiting unusual uniaxial negative and biaxial

positive thermal expansion," *Solid State Sci.* (2010), doi:10.1016/j.solidstatesciences.2010.03.004

6. **E. Quiroga-González**, C. Näther, W. Bensch, "Solvothermal synthesis, crystal structure and properties of $[Mg(en)_3][Sb_4S_7]$ - the first thioantimonate(III) containing a main group complex cation as structure director," *Z. Naturforsch.* 64b (2009), 1.

7. **E. Quiroga**, W. Bensch, M. Aceves, Z. Yu, J. P. Savy, M. Haeckel, A. Lechner, "Silicon Rich Oxide with controlled mean size of silicon nanocrystals by deposition in multilayers," IEEE Proceedings of *10th International Conference on Ultimate Integration of Silicon*, Aachen, Germany, 18-20.Mar.2009. pp. 349-352.

8. **E. Quiroga**, W. Bensch, Z. Yu, M. Aceves, R. A. De Souza, M. Martin, V. Zaporojtchenko, F. Faupel, "Structural characteristics of a multilayer of Silicon Rich Oxide (SRO) with high Si content prepared by LPCVD," *Phys. Stat. Sol. (a)*. 206 (2009), No. 2, 263.

Articles in collaboration

R. Kiebach, A. Morales, K. Monfil, Z. Yu, **E. Quiroga**, M. Aceves-Mijares, "Synthesis of light emitting SiO_x layers with calculable optical properties – a first step to controlled integration of photoluminescente active compounds in silicon based devices," *Smart Nanocomposites*, 1 (2010), No. 1, 41-54.

Conferences

1. **E. Quiroga-González**, W. Bensch, M. Aceves-Mijares, Z. Yu, “Activation of photoluminescence of multilayer arrays of silicon rich oxide by oxidation at different temperatures,” *18th International Vacuum Congress (IVC-18)*, Beijing, China, 23-27. Aug. 2010. Accepted.
2. **E. Quiroga-González**, L. Kienle, W. Bensch, “Zero-dimensional thioindate for the preparation of β-In_2S_3 nanocrystals by pyrolysis,” *International Bunsen Discussion Meeting on Light Harvesting and Solar Energy Conversion*, Stuttgart, Germany, 29-31. Mar. 2010.
3. **E. Quiroga-González**, L. Kienle, D. K. Lee, J. Janek, W. Bensch “Nanocrystalline $CuInS_2$ film with embedded Indium nanoclusters,” *42nd IUPAC Congress*, Glasgow, UK., 2-7. Aug. 2009.
4. **E. Quiroga**, W. Bensch, M. Aceves, Z. Yu, J. P. Savy, M. Haeckel, A. Lechner, “Silicon Rich Oxide with controlled mean size of silicon nanocrystals by deposition in multilayers,” *10th International Conference on Ultimate Integration of Silicon*, Aachen, Germany, 18-20. Mar. 2009.
5. **E. Quiroga**, L. Kienle, W. Bensch, “Nanocrystalline hexagonal phases in the Cu-In-S system synthesized under solvothermal conditions,” *17. Jahrestagung der Deutschen Gesellschaft für Kristallographie*, Hannover, Germany, 9-12. Mar. 2009.

Enrique Quiroga González

PERSONAL INFORMATION

Nationality: Mexican

Gender: male

Date of birth: 22 February 1980

Married

EDUCATION

Oct 2006 – present **PhD in Inorganic Chemistry**
Christian-Albrechts University of Kiel. Kiel, Germany.
Project: Study of photoactive materials based in compounds of the In-S system and in multilayers of SRO/SiO_2.
Advisors: Prof. Dr. Wolfgang Bensch, Dr. Mariano Aceves Mijares.
DAAD-Conacyt scholarship.

Aug 2003 – Oct 2005 **MSc. in microelectronics**
National Institute for Astrophysics, Optics and Electronics. Tonantzintla, Mexico.
Thesis: "Characterization of Si/SiO_2 superlattice prepared by LPCVD."
Advisors: Dr. Zhenrui Yu, Dr. Mariano Aceves Mijares.
Record: 91/100. Conacyt scholarship.

Aug 1998 - May 2003 **BSc. Electronic engineering, specialty in digital systems**
Instituto Tecnológico de Hermosillo. Hermosillo, Mexico.
Record: 95.98/100. Best student of the 1998 class. SEP scholarship.

Aug 1995 – May 1998 **High school**
Centro de Bachillerato Tecnológico Industrial y de Servicios Nº11. Hermosillo, Mexico.
Record: 100/100. Best student of the 1995 class.

EXPERIMENTAL TECHNIQUES

Material preparation
Bulk materials: Solvothermal synthesis.
Thin Films: Low Pressure Chemical Vapor Deposition (LPCVD).

Microelectronic fabrication techniques
Oxidation processes, chemical etching, evaporation of metals, work in clean room.

Basic material analytical skills
XRD, FTIR and Raman spectroscopy, Photoluminescence, AAS, ICP, DTA-TG, XPS, SIMS, EDX, SEM, AFM and TEM. Basic magnetic measurements and corresponding analysis.

Analyses of electrical properties
I-V and C-V. Use of signal generators and oscilloscopes.

SKILLS

Languages

Spanish: Mother language
English: Written and spoken 95%
German: Spoken 80%, written 60%
French: Spoken 40%, Written 30%

IT skills

Extensive knowledge of all Microsoft Office programs. Use of Origin for curve plotting and fitting. Simple numerical simulations with mathematic programs like Maple and Matlab. Programming of PLCs, and basic knowledge of programming in C.

Personal skills

Enthusiastic hard worker, able to work in interdisciplinary environments. Good at working under pressure. Problem solver, driven to succeed with innovative ideas.

PUBLICATIONS

1. **E. Quiroga-González**, W. Bensch, Z. Yu, R. López-Estopier, K. Monfil-Leyva, M. Aceves-Mijares, “Study of multilayer arrays of silicon rich oxide prepared by low pressure chemical vapor deposition for the production of photoluminescence,” *Thin Solid Films*. Submitted 19.May.2010.

2. **E. Quiroga-González**, L. Kienle, C. Näther, V.S.K. Chakravadhanula, W. Bensch, “Zero- and one-dimensional thioindates synthesized under solvothermal conditions yielding α-In_2S_3 or $MgIn_2S_4$ as thermal decomposition products,” *J. Solid State Chem.* Submitted 28.Apr.2010.

3. **E. Quiroga-González**, L. Kienle, V. Duppel, D. K. Lee, J. Janek, W. Bensch, “In-$CuInS_2$ nanocomposite film prepared by Pulsed Laser Deposition using a single source precursor,” *Solid State Sci.* Submitted 28.Apr.2010.

4. **E. Quiroga-González**, L. Kienle, V. Duppel, W. Bensch, “Transmission Electron Microscopy study of Cu-containing spinel-type In_2S_3 nanocrystals prepared by rapid pyrolysis of a single molecular precursor,” *Z. Anorg. Allg. Chem.* Submitted 11.Mar.2010.

5. **E. Quiroga-González**, Christian Näther, Wolfgang Bensch, “The thioantimonate anion $[Sb_4S_8]^{4-}$ acting as a tetradentate ligand: solvothermal synthesis, crystal structure and properties of $\{[In(C_6H_{14}N_2)_2]_2Sb_4S_8\}Cl_2$ exhibiting unusual biaxial negative and uniaxial positive thermal expansion,” *Solid State Sci.* (2010), doi:10.1016/j.solidstatesciences.2010.03.004

6. **E. Quiroga-González**, C. Näther, W. Bensch, “Solvothermal synthesis, crystal structure and properties of $[Mg(en)_3][Sb_4S_7]$ - the first thioantimonate(III) containing a main group complex cation as structure director,” *Z. Naturforsch.* 64b (2009), 1.

7. **E. Quiroga**, W. Bensch, M. Aceves, Z. Yu, J. P. Savy, M. Haeckel, A. Lechner, “Silicon Rich Oxide with controlled mean size of silicon nanocrystals by deposition in multilayers,” *IEEE proceedings of 10th International Conference on Ultimate Integration of Silicon*, Aachen, Germany, 18-20.Mar.2009.

8. **E. Quiroga**, W. Bensch, Z. Yu, M. Aceves, R. A. De Souza, M. Martin, V. Zaporojtchenko, F. Faupel, “Structural characteristics of a multilayer of Silicon Rich Oxide (SRO) with high Si content prepared by LPCVD,” *Phys. Stat. Sol. (a)*. 206 (2009), No. 2, 263.

9. R. Kiebach, A. Morales, K. Monfil, Z. Yu, **E. Quiroga**, M. Aceves-Mijares, "Synthesis of light emitting SiO_x layers with calculable optical properties – a first step to controlled integration of photoluminescente active compounds in silicon based devices," *Smart Nanocomposites*. 1 (2010), No. 1, 41-54.

10. Z. Yu, M. Aceves-Mijares, **E. Quiroga**, R. Lopez-Estopier, J. Carrillo, C. Falcony, "Structural and optical properties of Si/SiO_2 superlattices prepared by low pressure chemical vapor deposition," *J. Appl. Phys.* 100 (2006), 013524.

11. Z. Yu, M. Aceves, A. Luna-López, **E. Quiroga**, R. Lopez-Estopier, "Photoluminescence and single electron effect of nanosized silicon materials" In: Progress in Nanotechnology Research, Nova Science Publishers, Inc., NY, USA. 2007. ISBN: 1-59454-897-8.

CONFERENCES

1. **E. Quiroga-González**, W. Bensch, M. Aceves-Mijares, Z. Yu, "Activation of photoluminescence of multilayer arrays of silicon rich oxide by oxidation at different temperatures," 18th International Vacuum Congress (IVC-18), Beijing, China, 23-27.Aug.2010. Accepted.

2. **E. Quiroga-González**, L. Kienle, W. Bensch, "Zero-dimensional thioindate for the preparation of β-In_2S_3 nanocrystals by pyrolysis," International Bunsen Discussion Meeting on Light Harvesting and Solar Energy Conversion, Stuttgart, Germany, 29-31.Mar.2010.

3. **E. Quiroga-González**, L. Kienle, D. K. Lee, J. Janek, W. Bensch "Nanocrystalline $CuInS_2$ film with embedded Indium nanoclusters," *42nd IUPAC Congress*, Glasgow, UK., 2-7.Aug.2009.

4. **E. Quiroga**, W. Bensch, M. Aceves, Z. Yu, J. P. Savy, M. Haeckel, A. Lechner, "Silicon Rich Oxide with controlled mean size of silicon nanocrystals by deposition in multilayers," *10th International Conference on Ultimate Integration of Silicon*, Aachen, Germany, 18-20.Mar.2009.

5. **E. Quiroga**, L. Kienle, W. Bensch, "Nanocrystalline hexagonal phases in the Cu-In-S system synthesized under solvothermal conditions," *17. Jahrestagung der Deutschen Gesellschaft für Kristallographie*, Hannover, Germany, 9-12.Mar.2009.

6. Z. Yu, M. Aceves, **E. Quiroga**, J. Carrillo, "Resonant tunnelling through nc-Si/SiO_2 superlattices," *Intl. Conference on Microelectronics, MEMS, and Nanotechnology*, Brisbane, Australia, 11-14.Dec.2005.

7. **E. Quiroga**, Z. Yu, M. Aceves, "Charging/discharging effects in c-Si/SiO_2 superlattice prepared by LPCVD," *ICEEE-CIE 2005 Conference*, México City, 7-9.Sep.2005.

LABORAL EXPERIENCE

Oct 2005 – Sep 2006 **Research assistant**

National Institute for Astrophysics, Optics and Electronics. Tonantzitla, Mexico.
My job consisted of the design, installation and test of an LPCVD furnace for microelectronic applications. Additional activities were the preparation of films and their analysis.

Feb 2003 – Jun 2003 **Professional Internship**

Ford Motor Company (Plant of assembling & stamping). Hermosillo, Mexico.

My project consisted of different activities related to the increase of the productivity in the area of maintenance of the department of bodywork.

EXTRA-ACADEMIC ACTIVITIES

Feb 2004 – Nov 2005
Editor and participant writer of the intranet Magazine “La Capirotada” of INAOE.

Feb 2004 – Nov 2005
President of the IEEE (Institute of Electrical and Electronic Engineers) student Branch of INAOE.

Oct 2001 – Oct 2002
President of the student comittee of the Institute of Electronics of *Instituto Tecnológico de Hermosillo* (ITH).

1995 – 2003
Dancer and instructor of Flamenco and Mexican folkloric dance in various dance companies of Hermosillo, Mexico.

References

[1] S. Teske, A. Zervos, O. Schäfer, Greenpeace International and EREC, 2007.

[2] M. Grätzel, Phil. Trans, R. Soc. A 365 (2007) 993.

[3] Y. Akaki, S. Kurihara, M. Shirahama, K. Tsurugida, S. Seto, T. Kakeno, K. Yoshino, J. Phys. Chem. Solids 66 (2005) 1858.

[4] A.F. Qasrawi, N.M. Gasanly, Cryst. Res. Technol. 38/12 (2003) 1063.

[5] E. Bucher, Appl. Phys. 17 (1978) 1.

[6] W. Rehwald, G. Harbeke, J. Phys. Chem. Solids 26 (1965) 1309.

[7] N. Barreau, A. Mokrani, F. Couzinié-Devy, J. Kessler, Thin Solid Films 517 (2009) 2316.

[8] T.T. John, M. Mathew, C.S. Kartha, K.P. Vijayakumar, T. Abe, Y. Kashiwaba, Sol. Energy Mater. Sol. Cells 89 (2005) 27.

[9] N. Zheng, X. Bu, H. Vu, P. Feng, Angew. Chem. 117 (2005) 5433.

[10] A. Kudo, I. Tsuji, H. Kato, Chem. Commun. (2002) 1958.

[11] I. Tsuji, H. Kato, A. Kudo, Chem. Mater. 18 (2006) 1969.

[12] S. Shen, L. Guo, J. Solid State Chem. 179 (2006) 2629.

[13] A. Kudo, Y. Miseki, Chem. Soc. Rev. 38 (2009) 253.

[14] W. Chen, J.O. Bovin, A.G. Joly, S. Wang, F. Su, G. Li, J. Phys. Chem. B 108 (2004) 11927.

[15] G. Cao, Y. Zhao, Z. Wu, J. Alloys Comp. 472 (2009) 325.

[16] X. Cao, L. Gu, L. Zhuge, W. Qian, C. Zhao, X. Lan, W. Sheng, D. Yao, Colloids and Surfaces A: Physicochem. Eng. Aspects 297 (2007) 183.

[17] Y. Xing, H. Zhang, S. Song, J. Feng, Y. Lei, L. Zhao, M. Li, Chem. Commun. (2008) 1476.

[18] C. Wang, Y. Li, X. Bu, N. Zheng, O. Zivkovic, C.S. Yang, P. Feng, J. Am. Chem. Soc. 123 (2001) 11506.

[19] M.A. Green, Prog. Photovolt: Res. Appl. 17 (2009) 183.

[20] M.A. Green, K. Emery, Y. Hishikawa, W. Warta, Prog. Photovolt: Res. Appl. 17 (2009) 85.

[21] W. Guter, J. Schöne, S.P. Philipps, M. Steiner, G. Siefer, A. Wekkeli, E. Welser, E. Oliva, A.W. Bett, F. Dimroth, Appl. Phys. Lett. 94 (2009) 223504.

[22] L.T. Canham, Appl. Phys. Lett. 57 (1990) 1046.

[23] Y. Hirano, F. Sato, N. Saito, M. Abe, S. Miyazaki, M. Hirose, J. Non-Cryst. Solids 266-269 (2000) 1004.

[24] A. Markwitz, M. Rudolphi, B. Barry, H. Baumann, Curr. Appl. Phys. 8 (2008) 395.

[25] H. Coffin, C. Bonafos, S. Schamm, N. Cherkashin, G. Ben Assayag, A. Claverie, M. Respaud, P. Dimitrakis, P. Normand, J. Appl. Phys. 99 (2006) 044302.

[26] M.L. Brongersma, A. Polman, K.S. Min, E. Boer, T. Tambo, H.A. Atwater, Appl. Phys. Lett. 72 (1998) 2577.

[27] A. Morales-Sánchez, J. Barreto, C. Domínguez-Horna, M. Aceves-Mijares, J.A. Luna-López, Sensors and Actuators A 142 (2008) 12.

[28] D. Riabinina, C. Durand, J. Margot, M. Chaker, G.A. Botton, F. Rosei, Phys. Rev. B 74 (2006) 075334.

[29] R. López-Estopier, M. Aceves-Mijares, C. Falcony, 3rd International Conference on Electrical and Electronics Engineering, IEEE, Mexico City, 2006, p. 1.

[30] A. Morales, J. Barreto, C. Domínguez, M. Riera, M. Aceves, J. Carrillo, Physica E 38 (2007) 54.

[31] M. Zacharias, J. Heitmann, R. Scholz, U. Kahler, M. Schmidt, J. Bläsing, Appl. Phys. Lett. 80 (2002) 661.

[32] L. Tsybeskov, K.D. Hirschman, S.P. Duttagupta, M. Zacharias, P.M. Fauchet, J.P. McCaffrey, D.J. Lockwood, Appl. Phys. Lett. 72 (1998) 43.

[33] M. Zacharias, L. Tsybeskov, K.D. Hirschman, P.M. Fauchet, J. Bläsing, P. Kohlert, P. Veit, J. Non-Cryst. Solids 227-230 (1998) 1132.

[34] S. Wolf, R.N. Tauber, Silicon processing for the VLSI era, Lattice Press, Sunset Beach, California, 2000.

[35] A.C. Adams, Dielectric and polysilicon film deposition, McGraw-Hill, New York, 1983.

[36] W. Kern, Semicond. Internat. 8 (1985) 122.

[37] R.S. Rosler, Solid State Tech. 20 (1977) 63.

[38] B.C. Hseih, M.K. Hatalis, D.W. Greve, IEEE Trans. Elec. Dev. 35 (1988) 1842.

[39] E. Sachs, G.H. Prueger, R. Guerrieri, IEEE Trans. Semicond. Manuf. 5 (1992) 3.

[40] F. Martin, F. Bertin, H. Sprey, E. Granneman, Semicond. Sci. Technol. 6 (1991) 1100.

[41] I.H. Cho, N.K. Sung, H.S. Shim, H.H. Ryu, J.H. Ha, W.G. Lee, Thin Solid Films 434 (2003) 69.

[42] E. Quiroga, Z. Yu, M. Aceves, 2nd International Conference on Electrical and Electronics Engineering (ICEEE) and XI Conference on Electrical Engineering (CIE 2005), IEEE, Mexico City, 2005, p. 219.

[43] Z. Yu, M. Aceves, J. Carrillo, F. Flores, Nanotechnology 14 (2003) 959.

[44] T. Ohnishi, K. Shibuya, T. Yamamoto, M. Lippmaa, J. Appl. Phys. 103 (2008) 103703.

[45] D.B. Chrisey, G.K. Hubler, Pulsed Laser Deposition of Thin Films, John Wiley & Sons, 1994.

[46] J.D. Ferguson, G. Arikan, D.S. Dale, A.R. Woll, J.D. Brock, Phys. Rev. Lett. 103 (2009) 256103.

[47] M. Lippmaa, N. Nakagawa, M. Kawasaki, Appl. Phys. Lett. 76 (2000) 2439.

[48] G. Koster, B.L. Kropman, G.J.H.M. Rijnders, D.H.A. Blank, H. Rogalla, Appl. Phys. Lett. 73 (1998) 2920.

[49] A. Ohtomo, H.Y. Hwang, J. Appl. Phys. 102 (2007) 083704.

[50] D.K. Schroder, Semiconductor material and device characterization, John Wiley & Sons, Inc., New York, 1998.

[51] R.H. Bube, Photoelectronic properties of semiconductors, Cambridge University Press, Cambridge, 1992.

[52] Z. Yu, M. Aceves, F. Wang, J. Carrillo, R. Kiebach, K. Monfil, Physica E 41 (2008) 264.

[53] D. McNaught, A. Wilkinson, Compendium of Chemical Terminology, Blackwell Scientific Publications, Oxford, 1997.

[54] B. Krebs, Angew. Chem. Int. Ed. Engl. 22 (1983) 113.

[55] C.L. Bowes, G.A. Ozin, Adv. Mater. 8 (1996) 13.

[56] H. Metzner, M. Brüssler, K.-D. Husemann, H.J. Lewerenz, Physical Review B 44 (1991) 11614.

[57] W.J. Duffin, J.H.C. Hogg, Acta Cryst. 20 (1966) 566.

[58] R. Diehl, C.D. Carpentier, R. Nitsche, Acta Crystallogr. B32 (1976) 1257.

[59] R. Diehl, R. Nitsche, J. Cryst. Growth 20 (1973) 38.

[60] N. Barreau, Sol. Energy 83 (2009) 363.

[61] R. Diehl, R. Nitsche, J. Cryst. Growth 28 (1975) 306.

[62] R. Scheer, H.J. Lewerenz, J. Vac. Sci. Technol. A 13 (1995) 1924.

[63] J. Morales, J.L. Tirado, M.L. Eldrissi Moubtassim, J. Olivier-Fourcade, J.C. Jumas, Rev. Chim. Min. 24 (1987) 10.

[64] L. Gastaldi, L. Scaramuzza, Acta Cryst. B36 (1980) 2751.

[65] H. Hahn, G. Frank, W. Klingler, A.D. Meyer, G. Stoerger, Z. Anorg. Allg. Chem. 271 (1953) 153.

[66] J. Alvarez-García, A. Pérez-Rodríguez, B. Barcones, A. Romano-Rodríguez, J.R. Morante, A. Janotti, S.H. Wei, R. Scheer, Appl. Phys. Lett. 80 (2002) 562.

[67] R. Hoppe, W. Lidecke, F.C. Frorath, Z. Anorg. Allg. Chem. 309 (1961) 49.

[68] H. Schubert, R. Hoppe, Z. Naturforsch. B 25 (1970) 886.

[69] H.J. Deiseroth, Z. Naturforsch. B 35 (1980) 953.

[70] N. Zheng, X. Bu, B. Wang, P. Feng, Science 298 (2002) 2366.

[71] H. Li, A. Laine, M. O'Keeffe, O.M. Yaghi, Science 283 (1999) 1145.

[72] P. Feng, X. Bu, N. Zheng, Acc. Chem. Res. 38 (2005) 293.

[73] I. Dance, K. Fisher, Progr. Inorg. Chem. 41 (1999) 637.

[74] N. Zheng, X. Bu, P. Feng, Angew. Chem. 116 (2004) 4857.

[75] Q. Zhang, X. Bu, L. Han, P. Feng, Inorg. Chem. 45 (2006) 6684.

[76] N. Zheng, X. Bu, H. Lu, L. Chen, P. Feng, J. Am. Chem. Soc. 127 (2005) 14990.

[77] C.L. Cahill, B. Gugliotta, J.B. Parise, Chem. Commun. (1998) 1715.

[78] C. Wang, X. Bu, N. Zheng, P. Feng, Angew. Chem. Int. Ed. 41 (2002) 1959.

[79] C.L. Cahill, J.B. Parise, J. Chem. Soc., Dalton Trans. (2000) 1475.

[80] P. Vaqueiro, J. Solid State Chem. 179 (2005) 302.

[81] J. Zhou, G.Q. Bian, Y. Zhang, Q.Y. Zhu, C.Y. Li, J. Dai, Inorg. Chem. 46 (2007) 6347.

[82] A. Aydinli, N.M. Gasanly, I. Yilmaz, A. Serpengüzel, Semicond. Sci. Technol. 14 (1999) 599.

[83] W.S. Sheldrick, M. Wachhold, Coord. Chem. Rev. 176 (1998) 211.

[84] H. Lühmann, Z. Rejai, K. Möller, P. Leisner, M.E. Ordolff, C. Näther, W. Bensch, Z. Anorg. Allg. Chem. 634 (2008) 1687.

[85] H. Paulus, H. Fuess, S. Laminsi, J.K. Kom, Z. Kristalogr. 198 (1992) 125.

[86] N. Ding, M.G. Kanatzidis, Chem. Mater. 19 (2007) 3867.

[87] M.L. Feng, Z.L. Xie, X.Y. Huang, Inorg. Chem. 48 (2009) 3904.

[88] D. Dong, E.A. Irene, D.R. Young, J. Electrochem. Soc.: Solid State Sci. Tech. 125 (1978) 819.

[89] E. Talbot, R. Lardé, F. Gourbilleau, C. Dufour, P. Pareige, epl 87 (2009) 26004.

[90] B. Fazio, M. Vulpio, C. Gerardi, Y. Liao, I. Crupi, S. Lombardo, S. Trusso, F. Neri, J. Electrochem. Soc. 149 (2002) G376.

[91] Y. Kanemitsu, J. Lumin. 100 (2002) 209.

[92] G. Conibeer, M. Green, R. Corkish, Y. Cho, E.C. Cho, C.W. Jiang, T. Fangsuwannarak, E. Pink, Y. Huang, T. Puzzer, T. Trupke, B. Richards, A. Shalav, K.L. Lin, Thin Solid Films 511-512 (2006) 654.

[93] M.S. Yang, K.S. Cho, J.H. Jhe, S.Y. Seo, J.H. Shin, K.J. Kim, D.W. Moon, Appl. Phys. Lett. 85 (2004) 3408.

[94] C.L. Heng, E. Chelomentsev, O.H.Y. Zalloum, J. Wojcik, P. Mascher, J. Vac. Sci. Technol. A 27 (2009) 101.

[95] G. Mariotto, G. Das, A. Quaranta, G. Della Mea, F. Corni, R. Tonini, J. Appl. Phys. 97 (2005) 113502.

[96] D.N. Kouvastos, V. Ioannou-Sougleridis, A.G. Nassiopoulou, Appl. Phys. Lett. 82 (2003) 397.

[97] R.J. Joyce, H.F. Sterling, J.H. Alexander, Thin Solid Films 1 (1968) 481.

[98] G. Conibeer, M. Green, E.C. Cho, D. König, Y.H. Cho, T. Fangsuwannarak, G. Scardera, E. Pink, Y. Huang, T. Puzzer, S. Huang, D. Song, C. Flynn, S. Park, X. Hao, D. Mansfield, Thin Solid Films 516 (2008) 6748.

[99] Y.R. Jang, K.H. Yoo, J.S. Ahn, C. Kim, S.M. Park, J. Appl. Phys. 106 (2009) 063521.

[100] D. Kuritsyn, A. Kozanecki, H. Przybylinska, W. Jantsch, Phys. stat. sol. (c) 1 (2004) 229.

[101] L. Tsybeskov, G.F. Grom, P.M. Fauchet, J.P. McCaffrey, J.-M. Baribeau, G.I. Sproule, D.J. Lockwood, Appl. Phys. Lett. 75 (1999) 2265.

[102] L. Esaki, Nobel Lecture, 1973.